On the Migratory Behavior of Planetary Systems

On the Migratory Behavior of Planetary Systems

A dissertation presented

by

Rebekah Ilene Dawson

to

The Department of Astronomy

in partial fulfillment of the requirements

for the degree of

Doctor of Philosophy

in the subject of

Astronomy & Astrophysics

Harvard University

Cambridge, Massachusetts

April 2013

Dissertation Advisor: Dr. Ruth Murray-Clay Rebekah Ilene Dawson

On the Migratory Behavior of Planetary Systems

Abstract

For centuries, an orderly view of planetary system architectures dominated the discourse on planetary systems. However, there is growing evidence that many planetary systems underwent a period of upheaval, during which giant planets "migrated" from where they formed. This thesis addresses a question key to understanding how planetary systems evolve: is planetary migration typically a smooth, disk-driven process or a violent process involving strong multi-body gravitational interactions? First, we analyze evidence from the dynamical structure of debris disks dynamically sculpted during planets' migration. Based on the orbital properties our own solar systems Kuiper belt, we deduce that Neptune likely underwent both planet-planet scattering and smooth migration caused by interactions with leftover planetesimals. In another planetary system, β Pictoris, we find that the giant planet discovered there must be responsible for the observed warp of the systems debris belt, reconciling observations that suggested otherwise. Second, we develop two new approaches for characterizing planetary orbits: one for distinguishing the signal of a planets orbit from aliases, spurious signals caused by gaps in the time sampling of the data, and another to measure the eccentricity of a planet's orbit from transit photometry, "the photoeccentric effect." We use the photoeccentric effect to determine whether any of the giant planets discovered by the Kepler Mission are currently undergoing planetary migration on highly elliptical orbits. We find a lack of such "super-eccentric" Jupiters, allowing us to place an upper limit on the fraction of hot Jupiters created by the stellar binary Kozai mechanism. Finally,

we find new correlations between the orbital properties of planets and the metallicity of their host stars. Planets orbiting metal-rich stars show signatures of strong planet-planet gravitational interactions, while those orbiting metal-poor stars do not. Taken together, the results of thesis suggest that suggest that both disk migration and planet-planet interactions likely play a role in setting the architectures of planetary systems.

Contents

Acknowledgments

I am fantastically fortunate to have the opportunity to work on this thesis with my advisor, Ruth Murray-Clay. Among astrophysicists, Ruth is known for elegantly distilling complicated problems into their essential physics. Not only is it a great pleasure and inspiration to work with someone who has this gift, but I have found that she applies this skill to advising as well, identifying talents in me that I never knew I possessed, concocting cures for my weaknesses that I once considered immutable limitations, and helping me identify the most interesting problems to tackle and understand why my results matter. When I go to her for help, she often photographs and then erases a small segment of her equation-packed white board; somehow it is always plenty of space for us to work out a solution to whatever problem I have been stuck on for days. In addition to her thoughtful, effective, and inspiring research advising, Ruth has spent countless hours coaching me in how to give effective presentations, how to do all kinds of order-of-magnitude problems, how to confidently participate in discussions, and how to write clearly, all which I used to regard with dread. It is incredible privilege to be the first PhD student of this advisor-for-the-ages.

Two wonderful "sous-advisors" have also guided me through work included in this thesis. When I wanted to try an observational project, Ruth arranged for me to collaborate on a side project with John Johnson, to whom I am so grateful for taking me on as a remote-advisee. What started as a small side project branched off into several chapters of this thesis, and John taught me so much about observations, statistics, writing, productivity, and channeling scientific creativity. I thank John for also being an incredibly inspirational source of mentoring and encouragement. Second, I was so

lucky to work with Daniel Fabrycky when he was a postdoc at the CfA and collaborate with him on several projects since then. With tireless patience and encouragement, Dan helped me evolve from a student following instructions to a scientist pursuing — with much help — her own ideas. I am grateful to him to pouring time into helping me work through every inkling of an idea I had (or, with his matchless knowledge of the astronomical literature, pointing to me to where an idea had been brought to fruition decades earlier).

I am thankful for the wisdom and benevolence of the Curriculum on Academic Studies in assigning me such a helpful Thesis Advisory Committee. My committee chair, David Charbonneau, is a generous advocate for my work, in ways I often only find out about months after the fact. I am also grateful to Dave for helping me develop teaching skills and confidence. Matt Holman has encouraged my interest in solar and extra-solar systems ever since I was a college senior. I am especially thankful to Matt for his gentle humor and his insightful comments and suggestions on my work, presentations, and proposals. Sean Andrews has talent for giving sensible and profound advice that sticks with me for years and ends up shaping my most important decisions. I am also grateful to him for exuding a calm, non-pressuring encouragement and wish I could have him in the audience every time I give a talk. I am so thankful to Avi Loeb and Debra Fischer for coming on board for my thesis defense. Avi brings so much curiosity and insight to the Q&A session of every talk. I admire Debra so much for all her pioneering work in exoplanets over the past couple decades, and it is such an honor to have her serve as my external examiner.

A number of Harvard and SAO astronomers have made the CfA a nurturing place for me to do my graduate studies. I am so grateful to Margarita Karovska, for so

generously taking the time to mentor me and share her insight and encouragement. I especially thank Irwin Shapiro, David Latham, Allyson Bieryla, Lisa Kaltenegger, Dimitar Sasselov, Scott Kenyon, Brian Marsden (who is greatly missed), and Alicia Soderberg for their kindness, interest, and advice throughout my time here.

One of my favorite things about being at the CfA is interacting with an inspiring set of post-docs and older graduate students. Special thanks to to Darin Ragozzine, Smadar Naoz, Matija Cuk, Sarah Ballard, Kaitlin Kratter, Elisabeth Adams, Sara Gettel, Meredes Lopez-Morales, Stella Offner, Matthew Payne, Joshua Carter, Francois Fressin, Jean-Michael Dessert, David Kipping, Hagai Perets, Konstantin Batygin Jonathan Irwin, Moritz Guenther, Christopher Burke, Andrew Youdin, Ann Mao, Robert Marcus, Gurtina Besla, Sumin Tang, Meredith Hughes, Heather Knutson, Meng Su, Ryan O' Leary, Andrew Friedman, Joey Nielsen, Laura Blecha, Maggie McLean, Jonathan Foster, and Catherine Espelliat for believing in me and sharing your scientific and career advice, baked goods, and gossip. I miss those of you who are no longer at the CfA but know that young-uns elsewhere are now flourishing under your influence.

I have been very happy in graduate school in no small part because I have the best officemate in the world, Ragnhild Lunnan, who entertains, sympathizes, and drinks tea with me, and inspires by example with her brilliance and hard work. Many thanks to my lovely housemates Lauranne Lanz, Tanmoy Laskar, and Merry and my awesome and hilarious Ruthmates Anjali Tripathi, Ana-Maria Piso, and Elisabeth Newton. I am grateful to Katherine Rosenfeld, Courtney Dressing, Wen-fai Fong, Lauren Woolsey, Gongjie Li, Laura Schaefer, and Meredith McGregor for the fun times, and to Zachary Berta, Christina Balkaran, Alexa Hart, Sophia Dai, Diego Munoz, and Sarah Rugheimer for their kindness. Thanks to Yucong Zhu, Maxwell Moe, Dylan Nelson and Li Zeng

for being excellent yearmates and dinner buddies; to Ian Czekala, Greg Synder, Chris Faesi, and Josh Suresh for their friendliness and insights; to Nick Stone, Robert Harris, Bob Penna, Vicente Rodriguez, Greg Green, Paul Torrey, and Bence Beky for making P-building the most entertaining "retirement home" imaginable; to Kirit Karkare, Aaron Bray, Jason Dittman, and Sukrit Ranjan for entertaining me when I return to A-building; to the astro-ph coffee regulars Luke Kelley, Maria Drout, and Sarah Wellons for the fun discussions; to Nathan Sanders, Hope Chen, Eddie Chua, and Doug Ferrer for their sane and calming influence; and to the precious and adorable first years who grew up so fast: Marion Dierickx, Philip Mocz, Kate Alexander, Xinyi Guo, Stephen Portillo, Pierre Christian, Yuan-Sen Ting, George Miller, Fernando Becerra, Zachary Slepian, and Mary Zhang.

I am grateful to my family, to whom this thesis is dedicated, for their love and support: my creative and insightful mother, Emily Dawson; my father, John Dawson, who has done so much to encourage my love of science; and my dear siblings — William, Elliot, and Maggie Dawson — whom I look forward to joining in California this fall. Many thanks to my supportive extended family, especially the Zimets, the O'Neils, the Sakayedas, and the Ginsbergs. Thank you to my delightful and entertaining friends, especially Kathryn Neugent, Ruobing Dong, Amanda Zangari, Katherine Lonergan, Christina Epstein, and Rebecca McGowan.

I am so grateful to Peg Herlithy for all her cheer, support, and kindness throughout my time here. Many thanks to the wonderful Harvard administrators, Donna Adams, Robb Scholten, and Jean Collins, for all their work to keep the department thriving; to the talented Debbie Nickerson and Margaret Carroll for effectively nativating all sorts of financial conundra; and to Peg Hedstrom, Uma Mirani, and Nina Zonnevylle for making

the ITC such a great place to work.

Many thanks to my talented collaborators, Schuyler Wolff, Eric Mukherjee, Timothy Morton, Joshua Winn, Justin Crepp, Andrew Howard, and Roberto Sanchis-Ojeda. It is has been an education to work with you. Special thanks to Joshua Winn for — probably unbeknownst to him — regularly curing my writer's block. Whenever I am starting at an empty LaTeX document, I remind myself, "Josh Winn made the figures for *A Super-Earth Transiting a Naked Eye Star* in one day, and wrote the text on the second day," and it actually helps a lot.

It is a delight to work in the field of exoplanets not only because the profound and inspirational questions we are priviledged to spend our days working on but because it seems to draw an especially thoughtful, generous, and friendly group of people. Special thanks to Eric Ford, Joshua Winn, Hilke Schlicting, Sara Seager, Jack Wisdom, Kevin Schlaufman, Amaury Triaud Will Farr, Fred Rasio, Yoram Lithwick, Eugene Chiang, Geoff Marcy, Paul Kalas, James Graham, Renu Malhotra, Kathryn Volk, Rick Greenberg, Jason Wright, Roman Rafikov, Scott Tremaine, Aristotle Socrates, Subo Dong, Boas Katz, Dong Lai, and Kevin Heng for fun and enlightening discussions and answering many "quick questions." It is always such a pleasure to talk about other planets or our lives on this one with Marta Bryan, Julia Fang, Katherine Deck, Bjoern Benneke, Renyu Hu, Leslie Rogers, Christa Van Lauerhoven, Diana Dragomir, Laura Kreidberg, Kamen Todorov, Christian Schwab, Sharon Wang, Ethan Kruse, Lauren Weiss, Angie Wolfgang, Eric Lopez, Jennifer Yee, Cristobal Petrovich Balbontin, and Chelsea Huang.

I am so grateful to my college advisors and professors for encouraging my intellectual

interests. Richard French first got me involved in research, guided through my undergraduate thesis, and remains a wonderful mentor and collaborator today. Thank you to my inspiring research mentor, Mark Showalter, and to my fantastic academic mentors, Wendy Bauer and Yue Hu. Special thanks to professors Ted Ducas, Glenn Stark, Courtney Lannert, Steve Slivan, Kim McLeod, Liz Young, Robbie Berg, Raymond Starr, and Nat Scheidley, from whom I learned so much. Thank you to Diana Dabby for shaping my philosophy on data through her enormously useful course on signal processing. I am grateful to my tutors at Oxford for their encouragement and high expectations, especially Graeme Smith.

I am grateful to a number of people for helpful comments and discussions on the work presented in thesis. I thank Gurtina Besla, David Charbonneau, Matija Cuk, Matthew Holman, Kaitlin Kratter, David Latham, Renu Malhotra, Diego Munoz, Darin Raggozine, Schuyler Wolff, and Kathryn Volk for helpful discussions related to Chapter 2, and I thank Konstantin Batygin, Daniel Fabrycky, Darin Raggozine, Kathryn Volk, Jack Wisdom, Hal Levison, and an anonymous referee for insightful comments on this chapter. I thank Michael Fitzgerald, Paul Kalas, and Philippe Thebault for β Pictoris insights, and Thayne Currie and an anonymous referee for helpful comments on Chapter 3. I thank Debra Fischer, Andrew Howard, Greg Henry, Barbara McArthur, and Geoff Marcy for helpful discussions related to Chapter 4, and am grateful to helpful comments from anonymous referees, Steven Kawaler, Eric Agol, Christopher Burke, and Scott Tremaine. I am thankful for the helpful feedback from the anonymous referee of the work presented in Chapter 5. I gratefully acknowledge constant guidance from Joshua Winn's pedagogical guide to transiting planets (Winn 2010), and the ministry and fellowship of the Bayesian Book Club. I thank Avi Loeb and the ITC for hosting John

Johnson as part of their visitors program. I thank Sarah Ballard, Zachory Berta, Joshua Carter, Courtney Dressing, Subo Dong, Daniel Fabrycky, Jonathan Irwin, Boaz Katz, David Kipping, Timothy Morton, Norman Murray, Ruth Murray-Clay, Peter Plavchan, Gregory Snyder, Aristotle Socrates, and Joshua Winn for helpful discussions regarding this chapter. Several colleagues provided helpful and inspiring comments on Chapter 5: Joshua Carter (who, in addition to other helpful comments, suggested the procedure described in Chapter 5.3.4), Daniel Fabrycky, Eric Ford, David Kipping, and Ruth Murray-Clay. Special thanks to J. Zachary Gazak for helpful modifications to the TAP code. I thank the anonymous reviewer of Chapter 6 for the helpful and timely report. I thank Zachary Berta, Joshua Carter, Courtney Dressing, Emily Fabrycky, Jonathan Irwin, Scott Kenyon, David Kipping, Maxwell Moe, Norman Murray, Smadar Naoz, and Roberto Sanchis Ojeda for helpful comments and discussions. I am thankful to the anonymous referee of Chapter 7 an insightful report that improved the paper and in particular for advocating more conservative assumptions about the completeness of the *Kepler* pipeline. I am grateful to Smadar Naoz for many enlightening discussions and comments, including opening our eyes to other possibilities in Chapter 7.5, for which I also thank Simon Albrecht and Fred Rasio. Many thanks to Adrian Barker, Rick Greenberg, Renu Malhotra, Francesca Valsecchi, and especially Brad Hansen for tidal insights; to Katherine Deck, Will Farr, Vicky Kalogera, Yoram Lithwick, and Matthew Payne for helpful dynamical discussions; to Will Farr and Moritz Günther for helpful statistical discussions; and to Courtney Dressing and Francois Fressin for *Kepler* assistance. I am grateful to Subo Dong for constructive comments on a draft of Chapter 7. Thanks to Joshua Carter, Boas Katz, Doug Lin, Geoff Marcy, Darin Ragozzine, Kevin Schlaufman, and Aristotle Socrates for helpful comments and to Christophe Burke

and Jason Rowe for helpful discussions of *Kepler* 's completeness for giant planets. Special thanks to J. Zachary Gazak for helpful modifications to the TAP code. I thank Dáithí Stone for making available his library of IDL routines. We are very thankful to Chelsea Huang for provided us with her detrended data for KIC 6805414. I thank the referee of Chapter 8 for the helpful, timely report. My gratitude to John Johnson for many illuminating discussions about the three-day pile-up, the period distribution of giant planets, observational approaches to distinguishing the origins of hot Jupiters, valuable insights on previous collaborations connected to this investigation, and extensive comments. I thank Daniel Fabrycky for many helpful comments, Courtney Dressing for occurrence rate insights, and Subo Dong, Zachory Berta, David Charbonneau, Sean Andrews, Matthew Holman, Jason Wright, and Kevin Schlaufman for useful discussions. I thank B. Scott Gaudi and Andrew Gould for helpful comments and corrections, including alerting me about XO-3-b.

The numerical integrations in this thesis were run on the Odyssey cluster supported by the FAS Sciences Division Research Computing Group. I thank the Research Computing Group for their assistance, especially Paul Edmon.

I gratefully acknowledge support during the 2010-2011, 2011-2012, and 2012-2013 academic years by the National Science Foundation Graduate Research Fellowship under grants DGE 064449, DGE 0946799, and DGE 1144152.

This thesis includes data collected by the *Kepler* mission. Funding for the *Kepler* mission is provided by the NASA Science Mission directorate. I am extremely grateful to the *Kepler* Team for their long and extensive efforts in producing this rich dataset. Some of the data presented in this paper were obtained from the Multimission Archive

at the Space Telescope Science Institute (MAST). STScI is operated by the Association of Universities for Research in Astronomy, Inc., under NASA contract NAS5-26555. Support for MAST for non-HST data is provided by the NASA Office of Space Science via grant NNX09AF08G and by other grants and contracts.

To Emily, John, William, Elliot, and Margaret Dawson

Chapter 1

Introduction

1.1 Divine Animals

"The machinery of the heavens is not like a divine animal but like a clock."
Kepler (1605, quoted by Field 1999).

Planets were once thought to be harmoniously arranged in their orbits, as if by an architect (Titius 1776), and set in motion to follow these orbits with clockwork regularity (Kepler 1605) and "harmony in... motion and magnitude" Copernicus (1543, quoted by Gingerich 1993). In the 18th century, the spacing and co-planarity of planetary orbits inspired the first modern theories of planet formation by Kant and Laplace: a spinning cloud of gas and dusk collapses and flattens into a disk, out of which forms an orderly set of planets on nested orbits. But planetary discoveries over the past few decades have called this peaceful picture into question. Astronomers have found planets orbiting other stars (e.g. Latham et al. 1989) and, in our solar system, a belt of planetary

debris beyond Neptune: the Kuiper belt. Pluto, formerly considered our solar system's smallest planet, is now known to be one of thousands of Kuiper belt objects. To our surprise, the majority of known planetary systems — which are home to 699 extra-solar planets confirmed to date (see Wright et al. 2011 and references therein) — are wild and disorderly. Their planets do not appear to have been merely wound up and set on their orbits like clockwork. Hot Jupiters (Mayor & Queloz 1995; Marcy et al. 1997) orbit at scorchingly small planet-star separations (e.g. WASP-12-b orbits within three radii of its host star, Hebb et al. 2009), where they could not have formed (Rafikov 2006). Many planets have orbits that are highly eccentric and/or misaligned from their host stars' spin axes. Over the course of its highly elongated orbit, HD-80606-b moves from Earth's orbital separation to that of a hot Jupiter Naef et al. 2001). The first planet discovered to be misaligned from its host star's spin axis (and thus from the plane it likely formed in), XO-3-b (Hébrard et al. 2008; Winn et al. 2009b), has a projected obliquity of 37 degrees. Planets have subsequently been discovered on polar and retrograde orbits (see Albrecht et al. 2012 and references therein). Such planetary systems — rather than following like clockwork the circular, co-planar obits they formed on — likely underwent upheaval from their primordial orbits to the orbits we observe today. Even in our solar system, the highly inclined and eccentric orbits of Pluto (Malhotra 1993, 1995) and subsequently discovered Kuiper Belt objects (KBOs) (Jewitt & Luu 1993 found the second, 1992QB1) belie the orderly impression given by our full-fledged planets.

In this thesis, we take the view that planetary systems are more like "divine animals" than Kepler imagined. Environmental pressures and changing conditions influence their behavior and evolution; they struggle and adapt and sometimes survive. The collection of extra-solar planets is frequently described in the literature not as a clock collection

but as a "menagerie" (e.g. Fortney et al. 2006, Siverd et al. 2012). One of the earliest uses of the term was in a review by Lunine (2001), who called out hot Jupiters as having caused a "paradigm shift in our expectations regarding planetary system architectures." However, the paradigm shift from clockwork order to wild beasts was not solely driven by extra-solar discoveries; in fact, some theories of planetary system evolution were first proposed for the solar system (e.g Fernandez & Ip (1984); Malhotra (1993)) and much of the theory regarding extra-solar upheaval is inspired by work on small bodies in the solar system (e.g. Kozai 1962; Goldreich & Tremaine 1980; Goldreich & Rappaport 2003). To fully capture the behavior of these divine animals, we must conduct our zoological fieldwork both at home and abroad.

Here we investigate the migratory behavior of planetary systems, focusing primarily on the giant planet species. Evidently environmental pressures drive many giant planets, including hot Jupiters, to abandon their original habitats, but it remains debated which environmental pressures have the biggest influence. Migration has been proposed to be the result of torques from the gas disks from which planets form (e.g. Goldreich & Tremaine 1980; Ward 1997), angular momentum exchanged via interactions with planetary debris (e.g. Fernandez & Ip 1984), and perturbations by other planets or stars (e.g. Rasio & Ford 1996). (We use "migration" in this thesis as an umbrella term for any process that alters the circular, co-planar obit on which the planet formed.) Thus we currently lack an understanding of a) the typical planetary systems migratory behavior, including whether it was violent or peaceful and b) the diversity of migratory behaviors and how they connect to the present-day orbital and compositional traits of planets we observe. Consequently we are missing the context for interpreting the present-today traits and behaviors of planets we discover (including, for example, how much upheaval a

given planet likely endured in its planetary system). Characterizing migratory behavior is therefore an essential component of characterizing planetary systems and eventually Earth-like planets.

1.2 Evidence of Migratory Behavior from Debris Disks

The first place we look for evidence of migratory behavior is in debris disks. Planetary debris disks hold the pebbles, rocks, and boulders leftover from the era of planet formation. Our own solar system has two debris belts — the asteroid belt, located between Mars and Jupiter, and the Kuiper belt, located beyond Neptune. The first known exodebris disk, orbiting Vega Aumann et al. (1984), was discovered even before the Kuiper belt. Debris disks can play an important role in recording a planetary system's evolution. Like a patch of prairie trampled and marked with hooveprints after a herd of migrating bison has passed through, a planetesimal disk, if present during a planetary system's upheaval, can record signatures of migration. Indeed, our solar system's Kuiper belt was the first evidence for planetary migration, even before the discovery of misplaced hot Jupiters. Kuiper belt objects in mean motion resonances, such as Pluto, are thought to have been captured in these configurations during Neptune's migration (Malhotra 1993). Remnant planetesimal disks may reveal the violent history of planetary systems that appear peaceful in their current configurations or serve as signposts for inclined or eccentric planets (e.g. Formalhaut b, Quillen 2006; Chiang et al. 2009). Here we consider two such cases.

Our solar system's giant planets are thought to have formed packed close together and then underwent migration, with Neptune and Uranus transversing large distances (up to 20 AU). However, it remains debated if the planets were propelled by planet-planet scattering (e.g. Thommes et al. 1999; Levison et al. 2008; Morbidelli et al. 2008; Batygin & Brown 2010; Batygin et al. 2011) or driven by interactions with planetesimals (e.g. Fernandez & Ip 1984; Malhotra 1993; Hahn & Malhotra 2005). The dynamical structure of the Kuiper belt was sculpted the giant planets' migration, especially by Neptune, but there several outstanding problems in interpreting this structure. In Chapter 2, we focus on the "classical" region (from 40-50 AU), where a population of dynamically "hot" high-inclination objects overlies a flat "cold" population with distinct physical properties. Simulations of the solar systems dynamical history, while reproducing many properties of the Belt, fail to simultaneously produce both populations. We seek to account for this dynamical structure based on the solar system's migratory behavior by performing a parameter study for a general Kuiper belt assembly model. This type of model (e.g. Levison & Stern 2001; Gomes 2003; Morbidelli et al. 2008; Batygin et al. 2011) accounts for the different physical properties by forming the hot classical Kuiper belt objects (KBOs) interior to Neptune and delivering them to the classical region, where the cold population forms in situ. We present a new observational constraint that we use to rule out much of parameter space and pin down Neptune's migratory behavior. We demonstrate that planet-planet scattering and smooth migration likely *both* played a role in Neptune's migration behavior.

The extra-solar debris disk, β Pictoris, may also hold signatures of planetary upheaval. A vertical warp in the diskan inclined inner disk extending into a flat outer diskwas long interpreted as the signpost of a planet on an inclined orbit (e.g. Mouillet

et al. 1997; Augereau et al. 2001). The hypothesized planet's orbit was possibly tilted during an early upheaval in the system. Subsequently Lagrange et al. (2009, 2010) discovered, via direct imaging, a planet (β Pictoris b) with a mass and orbital distance suitable for creating this warp. However, when Currie et al. (2011) measured the planets orbit via astrometry, they were surprised to find that it is aligned with the flat outer disk, not the inclined inner disk, and that planet b therefore lacks the inclination to warp the disk. It appeared that the warp that motivated the search for β Pictoris b could not have actually been caused by β Pictoris b, calling into question the utility of disk structure as a signpost of planets. Chatterjee et al. (2011) suggested that another, undetected planet could be responsible. In Chapter 3, we model the sculpting of a debris disk by a planet on an inclined orbit and reconcile the directly imaged planets apparent misalignment with the warped inner disk. We show that β Pictoris b both can and must be responsible for creating the observed warp.

1.3 Characterizing Planetary Orbits

Further evidence of migratory behavior arises not only from debris disks but from planetary orbits themselves, particularly planets on inclined, eccentric, and/or close-in orbits. Here we develop new methods to characterize these planetary orbits, an essential step toward understanding their past migration. Our methods enhance the dynamical information that can be extracted from the two most commons types of exoplanet observations: radial-velocity measurements and transit photometry.

Since the discovery of HD-114762-b by Latham et al. (1989), over 400 exoplanets have been found through the Doppler, or radial-velocity (RV), method, in which the

planets orbit is deduced from its host stars radial motion. Identifying the planets true orbital frequency in the RV data is essential to correctly deriving its properties, including distance from its host star, temperature, mass, eccentricity, and dynamical relations with other planets in the system. But gaps in the RV time sampling cause spurious aliases frequencies that can be confused with the planets orbital frequency, potentially causing a severe mischaracterization. For example, Udry et al. (2007) announced a super-Earth orbiting the M star Gl 581 with an orbital period 83 days, beyond the cold edge of the habitable zone. After more than doubling the number of observations, they determined that the planet's period was actually 67 days, well within the habitable zone, and that the 83 day period was an alias (Mayor et al. 2009). The distinction between an alias and physical frequency was the distinction between a frozen, dead planet and a planet possibly hospitable to life. In Chapter 4, we develop a new approach to distinguish a planets true orbital frequency from spurious alias frequencies. Our approach harnesses knowledge of the observation window function (set by the observation times) to compute a finger-print of expected aliases for each possible orbital frequency, which we then compare to the data. We apply our approach to published data, including super-Earth 55 Cnc e, whose orbital period we revise from 2.8 to 0.74 days, and five other planets with orbital period ambiguities.

The other most common method for discovering and characterizing exoplanets is the transit technique, in which the light from a star dims as a planet passes through our line of sight (e.g. Charbonneau et al. 2000). In Chapter 5, we develop a new approach for measuring a planet's orbital eccentricity from its transit light curve. We created this approach as part of our search for giant planets on highly eccentric orbits, whose connection to planetary migration is motivated further in Section 1.4. The *Kepler*

Mission (e.g. Borucki et al. 2010) — launched in 2009 — is continuously monitoring the brightness of 100,000 stars to search for planetary transits and has discovered an abundance of transiting giant planets. Traditionally, the eccentricities of such planets would be measured through follow-up precise RV measurements. However limited telescope time for *Kepler* follow-up and the faintness of most *Kepler* targets prevent a systematic follow-up of giant planets. We develop a Bayesian method (which we term the photoeccentric effect) to, for the first time, measure an individual planet's eccentricity solely from its transit photometry, allowing us to search for Jupiters on super-eccentric orbits using the *Kepler* light curves, without the need for RV follow-up. We show that our approach enables a tight measurement of large eccentricities for Jupiter-sized planets.

1.4 Distinguishing Giant Planet Migration Mechanisms

We now know of hundreds of giant planets orbiting closer to their stars than the Earth orbits to the sun. Close-in giant planets displaced from their formation location serve as evidence for the prevalence of planetary migration. The nature of this migration remains debated, in particular whether it is a smooth process caused by planet-disk interactions or violent process caused by strong gravitational interactions between the planet and other planets or stars in the system. Hot Jupiters — which orbit within just 0.1 AU of their host stars — are particularly mysterious. The typical hot Jupiter may have migrated smoothly through the proto-planetary disk or, alternatively, been perturbed by a companion onto a highly eccentric orbit, which tidal dissipation shrank

and circularized during close passages to the star. Socrates et al. (2012b) proposed a test for distinguishing models: the latter model should produce a number of super-eccentric hot Jupiter progenitors readily discoverable by the *Kepler* Mission. Using the approach we developed in Chapter 5, we search for the super-eccentric hot Jupiter progenitors expected if giant migration is spurred by multi-body interactions but not if disk migration is responsible. In Chapter 6, we apply our technique to KOI-1474.01, finding that the Jupiter-sized *Kepler* candidate planet has a large eccentricity of 0.8. KOI-1474.01 also exhibits transit timing variations due to a massive outer companion, which may be the culprit responsible for KOI-1474.01s highly eccentric orbit. In Chapter 6, we extend our search to the entire *Kepler* sample and find, surprisingly, a paucity of proto-hot Jupiters on high-eccentricity orbits. We consider observational effects but find that they are unlikely to explain this discrepancy. We discuss whether our results necessarily indicate that disk migration is the dominant channel for producing hot Jupiters and under what circumstances multi-body interactions can still be consistent with our results.

Migration processes must not only produce hot Jupiters but also populate the region from 0.1 to 1 AU. This region is outside the reach of tidal damping forces exerted by the host star but interior to both the ice line and the observed pile-up of giant planets at 1 AU, one of which likely indicates where large, rocky cores can grow and accrete. We call this semi-major axis range the "Valley," because it roughly corresponds to the "Period Valley" (e.g. Jones et al. 2003), the observed dip in the giant planet orbital period (P) distribution from roughly $10 < P < 100$ days. The Valley houses gas giants both on highly eccentric and nearly circular orbits. This bimodality may point to two different migration mechanisms: smooth gas disk migration and migration caused by strong gravitational interactions among planets. If there are two migration mechanisms,

the physical properties of the proto-planetary environment may determine which is triggered. In Chapter 8, we present three new observational trends with metallicity that support this interpretation.

Chapter 2

Neptune's Wild Days: Constraints from the Eccentricity Distribution of the Classical Kuiper Belt

R. I. Dawson & R. A. Murray-Clay *The Astronomical Journal*, Vol. 750, id. 43, 2012

Abstract

Neptune's dynamical history shaped the current orbits of Kuiper Belt objects (KBOs), leaving clues to the planet's orbital evolution. In the "classical" region, a population of dynamically "hot" high-inclination KBOs overlies a flat "cold" population with distinct physical properties. Simulations of qualitatively different histories for Neptune including smooth migration on a circular orbit or scattering by other planets to a high eccentricity have not simultaneously produced both populations. We explore a general Kuiper Belt

assembly model that forms hot classical KBOs interior to Neptune and delivers them to the classical region, where the cold population forms in situ. First, we present evidence that the cold population is confined to eccentricities well below the limit dictated by long-term survival. Therefore Neptune must deliver hot KBOs into the long-term survival region without excessively exciting the eccentricities of the cold population. Imposing this constraint, we explore the parameter space of Neptune's eccentricity and eccentricity damping, migration, and apsidal precession. We rule out much of parameter space, except where Neptune is scattered to a moderately eccentric orbit (e>0.15) and subsequently migrates a distance $\Delta a_{\rm N} = 1 - 6$ AU. Neptune's moderate eccentricity must either damp quickly or be accompanied by fast apsidal precession. We find that Neptune's high eccentricity alone does not generate a chaotic sea in the classical region. Chaos can result from Neptune's interactions with Uranus, exciting the cold KBOs and placing additional constraints. Finally, we discuss how to interpret our constraints in the context of the full, complex dynamical history of the solar system.

2.1 Introduction

Neptune, with its nearly circular and equatorial orbit, may seem straight-laced compared to the oblique, hot, eccentric, and resonant planets in the extra-solar menagerie. But the highly inclined and eccentric orbits of Pluto (Malhotra 1993, 1995) and subsequently discovered Kuiper Belt objects (KBOs) imply that Neptune may have experienced its own "wild days" in the early solar system. During these wild days, Neptune sculpted the KBOs into four main dynamical classes: objects in mean motion orbital resonance with Neptune (the "resonant" population), objects that are currently scattering off

Neptune (the "scattering" population), and two populations of "classical" objects that are currently decoupled from Neptune. One population of classical objects is dynamically "cold," on nearly circular orbits at low inclinations, and the other classical population is dynamically "hot" with a range of eccentricities and inclinations. The cold classicals have distinct physical properties from the hot classicals, including colors (Tegler & Romanishin 2000; Thommes et al. 2002; Peixinho et al. 2008), sizes (Levison & Stern 2001; Fraser et al. 2010), albedos (Brucker et al. 2009), and binary fraction (Stephens & Noll 2006; Noll et al. 2008). A major problem in understanding the formation of the solar system is that, as we will review below, no model of Neptune's dynamical history adequately produces the superposition of hot and cold classicals or accounts for the difference in their physical properties.

Two types of dynamical sculpting models have been developed to explain, in particular, the population of resonant KBOs. Extensive migration models (Malhotra 1993, 1995; Hahn & Malhotra 2005) propose that Neptune migrated outward by 7-10 AU on a nearly circular orbit from its location of formation, capturing objects into resonance as its resonance locations slowly swept through the Kuiper Belt. This type of model generates the resonant and scattering objects and the cold population (unexcited objects that, in this model, formed in situ) but not the hot population. It also does not match the observed inclination distribution within the resonances. Chaotic capture models (Levison et al. 2008), inspired by the Nice model (see Morbidelli et al. 2008, and references therein), propose that Neptune was scattered onto a highly eccentric orbit by other planets during a period of instability (Thommes et al. 1999). Neptune's high eccentricity created a chaotic zone in what is now the classical region, and some objects were caught in resonances when Neptune's eccentricity damped. Chaotic capture

models produce a hot population: objects that formed in the inner disk, subsequently were scattered by Neptune into the classical region, and then decoupled when Neptune's eccentricity damped. These models also produce a resonant population and scattering population. Although some of the objects delivered into the classical region end up on low-eccentricity orbits, we point out that a cold population confined to low eccentricities is not produced. Other variations of the Nice model (e.g. Morbidelli et al. 2008) include an in situ population of cold objects, but, over the course of Neptune's evolution, these objects become excited to higher eccentricities. K. Batygin (2010, private communication[1]) has suggested that fast apsidal precession of Neptune's orbit could prevent Neptune from disrupting the cold classicals during its proposed high-eccentricity period, but it remains to be explored under what circumstances this mechanism would work and how it would affect the hot classicals.

With neither the extensive migration models nor chaotic capture models producing both the hot and cold classicals, the qualitative picture of what happened in the early solar system, including the roles of planet-planet scattering and planetary migration, remains up for debate. It remains a question whether Neptune migrated outward by many AU on a nearly circular orbit, was launched onto an eccentric orbit near its current location, or none of the above. Pinning down Neptune's dynamical history, which should

[1]After the submission of this manuscript, Batygin et al. (2011) presented a model in which Neptune underwent a period of high eccentricity and, due to its fast apsidal precession, could avoid disrupting the cold classicals. Because this paper appeared after the submission of our manuscript, we leave a detailed discussion of its results for future work. However, we note that in the particular simulations they presented, the cold classicals are dynamically excited, inconsistent with the constraints we will establish. In Section 2.5.1, we explore under what circumstances, if any, this could be avoided.

be possible given the constraints from over 500 KBOs with well characterized orbits, would reveal much about the history of our own solar system and about the processes of scattering and migration that shape the architecture of many planetary systems.

Previous models attempted to produce all four dynamical classes of KBOs with 0.5-4 Gyr simulations that included all four giant planets and thousands of massless KBOs (e.g. Hahn & Malhotra 2005; Levison et al. 2008). It has not been computationally feasible to fully explore parameter space with such extensive simulations. Thus it is unclear whether the dynamical history described by a particular model (1) has trouble producing both the cold and hot populations because there is a qualitative problem with the scenario or, alternatively, because the parameters need to be slightly adjusted; and (2) is unique, or whether another, qualitatively different dynamical history would match the observations just as well.

Inspired by previous models, we explore a generalization in which Neptune undergoes all potential combinations of high eccentricity, migration, and/or apsidal precession: "Neptune's wild days." In this generalization, the cold objects form in situ where we observe them today and the hot objects are delivered from the inner disk and superimposed on the cold objects. "Two-origin" models superimposing a hot classical population from the inner disk on top of a cold population firmed in situ (e.g. Levison & Stern 2001; Gomes 2003; Morbidelli et al. 2008) have the advantage of explaining the different physical properties of the hot and cold classicals that were discussed above. The different colors, sizes, and albedos of the two populations are accounted for by their formation in different regions of the solar system's proto-planteary disk under different conditions. For instance, chemical differences may result in different colors for objects formed in the inner versus the outer disk (Brown et al. 2011a). The cold classicals have

a higher binary fraction because any hot classical binaries were likely to have been disrupted when they were scattered from the inner disk to the classical region (Parker & Kavelaars 2010) and because binary capture may have been less efficient in the inner disk (Murray-Clay & Schlichting 2011). However, to date this class of model has not yet been demonstrated to work quantitatively. We consider a generalized two-origin model in which hot classical deliver echoers as a result of scattering by Neptune (rather than due to resonance sweeping as in Gomes 2003). Focusing on the consistency of this class of model with the eccentricity distribution of classical KBOs — unaccounted for by previous model realizations — we explore the parameter space for this generalized model using several alternative tactics:

- Instead of attempting to produce a single model, we fully explore the parameter space of Neptune's eccentricity, semimajor axis, migration rate, eccentricity damping rate, and precession rate to assess the consistency of a collection of dynamical histories with the observations. This approach is general in the sense that previous models (e.g. Malhotra 1995; Levison et al. 2008) are under consideration (corresponding to a particular set of parameters), as well as other regions of parameter space that have not been explicitly considered. We will explore Neptune's inclination and inclination damping rate in a paper currently in preparation (R.I. Dawson and R. Murray-Clay 2012, in preparation). In Section 2.5.4, we clarify how to interpret complex solar system histories in the context of this general model.

- Instead of matching the observations in detail, we focus on matching major qualitative features of the classical KBO eccentricity distribution that are

unaffected by observational bias or by the long-term evolution of the solar system (i.e. the evolution that happens over the ~ 4 Gyr after the planets reach their final configuration). This approach allows us to perform short integrations that end once the planets reach their current configuration.

- Instead of relying solely on numerical integrations, we determine which dynamical processes affect the evolution of the KBOs and place constraints using analytical expressions.

- Instead of modeling all four planets directly, we model only Neptune but allow its orbit to change. We will demonstrate why this approach is sufficient for the problem we are exploring.

Our exploration of parameter space could produce two possible outcomes. If we find regions of parameter space that can deliver the hot objects on top of the cold, these consistent regions will provide constraints for more detailed models. If we rule out all of parameter space, then a new type of model, employing different physical processes, is necessary. Either way, we will identify and quantify what physical processes are responsible for sculpting the eccentricity distribution of the classicals in the generalized model we are treating. We emphasize that, rather than proposing a new model, we are exploring a generalization of Neptune's dynamical history, in which previous models correspond to a particular set of parameters.

In the next Section, we demonstrate that the hot and cold classicals have not only a bimodal inclination distribution, as already well established in the literature, but also distinct eccentricity distributions that were sculpted during Neptune's wild days. We use qualitative features of these eccentricity distributions to establish conservative

criteria that models must meet. In Section 2.3, we establish the framework for our study and argue that, combined with the distinct physical properties of the hot and cold populations, these eccentricity distributions imply separate origins for the cold and the hot classicals. In Section 2.4, we identify, for the classical region, the potential dynamical consequences of Neptune spending part of its dynamical history with high eccentricity — delivery of objects via scattering, secular forcing, accelerated secular forcing near resonances, and a chaotic sea — and present analytical expressions validated by numerical integrations. In Section 2.5, we combine the analytical expressions from Section 2.4 with the conservative criteria established in Section 2.2 to place constraints on Neptune's path, orbital evolution timescales, and interactions with other planets, ruling out almost all of parameter space. We find that Neptune must spend time with high eccentricity to deliver the hot classicals by these processes, but is restricted to one of two regions of (a, e) space while its eccentricity is high. To avoid disrupting the cold objects, Neptune's eccentricity must have damped quickly or the planet's orbit must have precessed quickly while its eccentricity was high. Finally, because Neptune's current semimajor axis is ruled out when Neptune's eccentricity is high, Neptune is constrained to have migrated a short distance after its eccentricity damped. In the final Section, we discuss our results and their implications for the early history of the solar system.

2.2 Constraints from the Observed Eccentricity Distributions of Hot and Cold Classicals

The cold and hot populations are defined by the observed bimodal inclination distribution of classical KBOs (Brown 2001; Gulbis et al. 2010; Volk & Malhotra 2011). They also have distinct eccentricity distributions. The eccentricity distribution of all the observed KBOs is plotted in Figure 2.1. In Section 2.2.1, we present evidence for distinct hot classical and cold classical eccentricity distributions and identify robust qualitative features of the distributions that models of Neptune's dynamical history must produce. In Section 2.2.2 we lay out the observational constraints which we will use for the remainder of the paper. In Section 2.2.3, we assess the robustness of these features by performing statistical tests and considering observational bias.

2.2.1 Evidence for Distinct Hot Classical and Cold Classical Eccentricity Distributions

We wish to use inclinations to separate the cold and hot classicals and then examine the eccentricity distributions of these two populations. Traditionally, the observed cold and hot objects have been separated using one inclination cutoff. However, because of the overlap between the hot and cold components in the bimodal inclination distribution, a single cutoff will necessarily result in the misclassification of hot objects as cold and vice versa. For example, if the classical population follows the model KBO inclination distribution derived by Gulbis et al. (2010) and we were to distinguish between the cold and hot populations using an inclination cut-off $icut = 4°$, 11% of objects with $i < 4°$

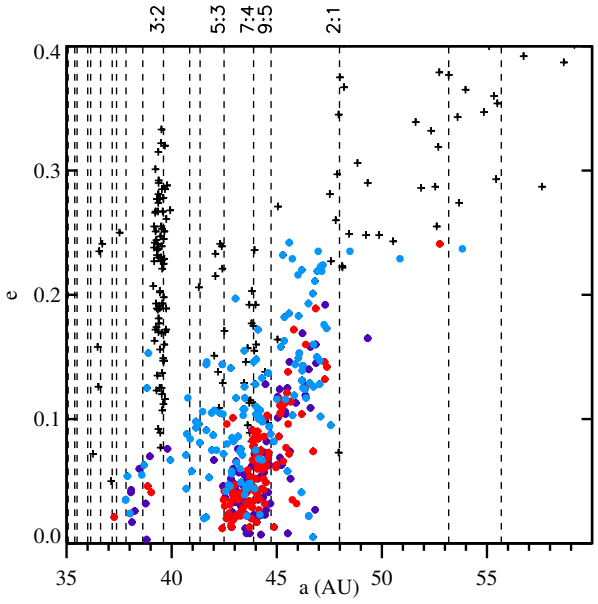

Figure 2.1.—: Orbital eccentricity distribution of Kuiper Belt Objects. The resonant and scattered objects are plotted as black pluses. The classical objects are plotted as colored circles. The red objects have $i < 2°$ and are thus very likely cold classicals. The blue objects have $i > 6°$ and are thus very likely hot classicals. The membership of any given purple object, which has $2° < i < 6°$, is ambiguous (see Figure 2.2). Objects are taken from the Minor Planet Center Database and the Canada-France Ecliptic Plane Survey (CFEPS) and classified by Gladman et al. (2008); Kavelaars et al. (2009); Volk & Malhotra (2011). Dashed lines indicate the location of mean motion resonances with Neptune, which are included up through fourth order.

would be actually be hot objects and 15% of objects with $i > 4°$ would be actually be cold objects. Thus, using $icut = 4°$, 11% of the objects classified as cold would be "contaminated," and 15% of those classified as hot would be contaminated. In Figure 2.2, we plot the "contaminated" fraction over a range of values for *icut* for the cold and hot populations based on three models of the debiased inclination distribution (Brown 2001; Gulbis et al. 2010; Volk & Malhotra 2011). For all three models, less than 10% of the cold classicals are contaminated for $icut < 2°$, while less 3% of the hot classicals are contaminated for $icut > 6°$.

Therefore, instead of using a single *icut*, we divide the classicals into a likely cold population ($i < 2°$), a likely hot population ($i > 6°$), and an ambiguous population ($2° < i < 6°$). We then examine the eccentricity distributions of the likely cold and likely hot populations, which are "uncontaminated" samples. We use the uncontaminated eccentricity distributions to identify major features that models much match. In Section 2.7, we confirm that our results are consistent if we probabilistically include the ambiguous population.

We wish to identify features of the eccentricity distribution that are sculpted during Neptune's wild days, *not* by the long-term stability of the region under the influence of the modern solar system planetary configuration or by observational bias. First we compare the eccentricities of observed likely cold ($i < 2°$) and likely hot ($i > 6°$) objects to the survival map of Lykawka & Mukai (2005), generated from a 4 Gyr simulation. Lykawka & Mukai (2005) generated initial conditions for test particles uniformly filling a cube of (a, e, i) in the classical region: $41.375AU < a < 48.125$ AU, $0 < e < 0.3$, and $0 < i < 30°$. They then performed a 4 Gyr numerical integration including the test particles and the four giant planets (starting on their modern orbits). Then they

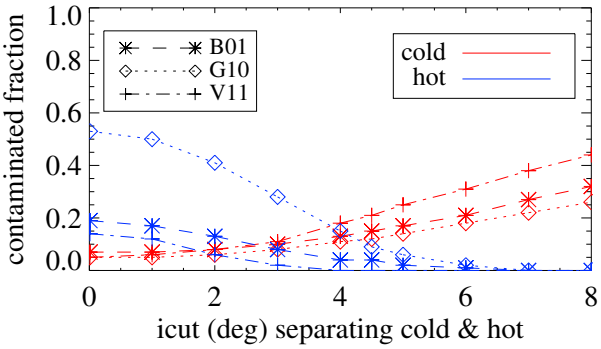

Figure 2.2.—: Fraction of each population "contaminated" by the other group as a function of the cut-off inclination *icut* between the cold and hot population. The dashed lines, labeled B01, are calculated from the inclination distribution defined by Brown (2001); the dotted lines, labeled G10, from the inclination distribution defined by Gulbis et al. (2010); and the dash-dotted lines, labeled V11, from the inclination distribution defined by Volk & Malhotra (2011).

computed the survival rate of test particles in bins of (a, e) and (a, i). In this work, we consider only the eccentricity survival map. This map bins over all inclinations[2]. After 4 Gyr of evolution under the influence of the planets in their current configuration, KBOs with an initially uniform eccentricity distribution would be distributed according to this survival map.

However, rather than following the survival map, the observed cold and hot objects exhibit major distinct features. In Figure 2.3, we plot the sample of observed classical objects from the Minor Planet Center (MPC) and the Canada-France Ecliptic Plane Survey (CFEPS; Kavelaars et al. 2009) on top of the Lykawka & Mukai (2005) stability

[2]We note that at a given semimajor axis, the survival rate does not show a strong dependence on inclination (Lykawka & Mukai 2005, Figure 4, lower panel), except near the ν_8 secular inclination resonance at 41.5 AU, which is devoid of low inclination objects. We do not establish constraints in this region.

map. The cold objects are confined to very low eccentricities. From 42.5 to 44 AU, the cold objects appear to be confined to $e < 0.05$. From 44 to 45 AU, the cold objects appear confined below $e < 0.1$. This confinement of the cold classicals to below the survival limit implies that they were not excited above these levels because if they had been, we would still observe objects at higher eccentricities. Similarly, Kavelaars et al. (2009) found that classical objects with $i < 4.5°$ are restricted to 42.5 AU $< a <$ 45 AU and $e < 0.1$. In contrast, hot objects occupy the upper portion of the survival region and appear uniformly distributed in a from 42 to 47.5 AU. Suggestively, they also appear to be distributed roughly along a scattering line, as if they were scattered into the classical region but did not have time to evolve to low eccentricities before Neptune's eccentricity damped.

2.2.2 Conservative Criteria that Models Must Meet

We use the following major qualitative features to place constraints on Neptune's dynamical history. We consider these criteria "conservative" because they allow for dynamical histories at the very edge of consistency with the observations.

Cold population: confined to low eccentricities of $e < 0.1$ in the region from 42.5 to 45 AU. In the region between 42.5 and 45 AU, the cold objects have eccentricities well below the distribution that follows the survival map. Therefore, Neptune cannot excite the cold classical objects in this region above $e = 0.1$. (We choose this value to be conservative in ruling out regions of parameter space and to match Kavelaars et al. (2009), but it appears that cold objects with semimajor axes less than 44 AU are confined below $e < 0.05$, a tighter constraint.) We indicate this threshold as a solid

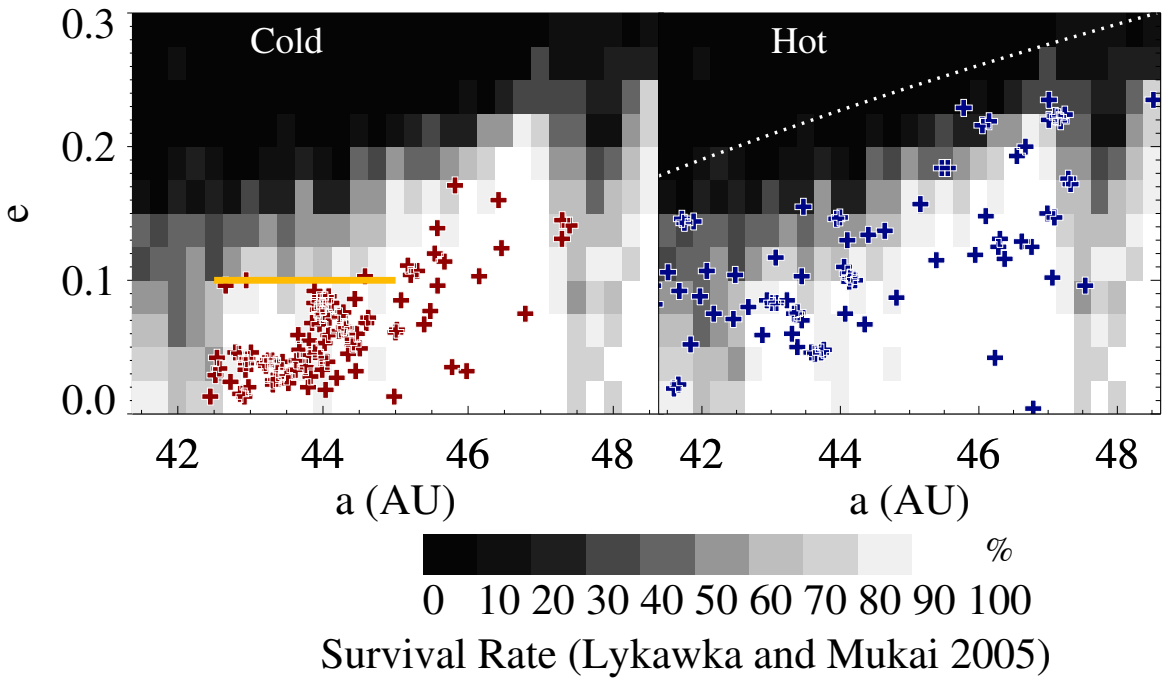

Figure 2.3.—: Observed (plus symbol) eccentricity distributions of cold classicals with $i <^{\circ} 2$ (left) and hot classicals with $i > 6^{\circ}$ (right), plotted over the survival map of Lykawka & Mukai (2005). In the left panel, the cold classicals between 42.5-44 AU are confined to $e < 0.05$, well below the survival limit in this region, while cold classicals between 44-45 AU are confined to $e < 0.1$, also below the survival limit. In the right panel, the hot classicals occupy the upper portion of the survival region. We plot $e = 0.1$ from 42.5 to 45 AU as a solid yellow line in the left panel. The dashed line in the right panel, periapse $q = 34$ AU, indicates an approximate upper threshold of long-term survival, which we will use in Sections 2.5.2 and 2.5.3. Classical objects are taken from the Minor Planet Center Database and the Canada-France Ecliptic Plane Survey (CFEPS; Kavelaars et al. 2009) and are classified by Gladman et al. (2008), Kavelaars et al. (2009), and Volk & Malhotra (2011).

yellow line in Figure 2.3.

Hot population: delivered to the upper survival region with $q > 34$ AU out to 47.5 AU. The observed hot objects occupy the upper portion of the survival region. Therefore, a consistent dynamical history should allow some objects to reach this region. It is not necessary for the transported objects to reach very low eccentricities, only low enough to survive under the current planetary configuration. We set the criterion that the hot classicals must be delivered to periapse $q > 34$ AU (dashed line in Figure 2.3) from 42 A to 47.5 AU, the edge of observed population.

2.2.3 Assessing the Robustness of the Observed Features

In determining which major features serve as constraints on the dynamical history of the solar system, we address several complications:

1. The inclinations of objects vary over time (Volk & Malhotra 2011).
2. The inclination cut-off between the hot and cold classicals is model dependent.
3. Proper elements are more robust than the observed instantaneous elements.
4. The features in the eccentricity distributions might be the result of random chance or small number statistics.
5. The eccentricity distributions may be impacted by observational bias.

The first complication is addressed by Volk & Malhotra (2011). They find that, at any given time, only 5% of objects will be inconsistent with their original

inclination-based classification of hot versus cold. Therefore we expect the major qualitative features we identify to hold despite variations in the inclinations of some objects

The second complication is that the cut-off inclination between the hot and cold classicals depends on the parameters and form of the model for the bimodal inclination distribution. The three models we consider (Brown 2001; Gulbis et al. 2010; Volk & Malhotra 2011) each use the functional form of $\sin i$ multiplied by a Gaussian but use different widths and cold/hot fractions. They also use different planes for the inclination: Brown (2001) defines the inclination with respect to the ecliptic plane, Gulbis et al. (2010) with respect to the mean plane of the Kuiper Belt, and Volk & Malhotra (2011) with respect to the invariable plane. However, despite these differences, $i < 2^\circ$ and $i >^\circ 6$ are robust cut-offs for establishing an uncontaminated cold and hot population, respectively, for each of the three models. In regards to the functional form of the model, Volk & Malhotra (2011) find that the high-inclination component is not well-described by a Gaussian, and Fabrycky & Winn (2009) argue that the most robust generic functional form for a distribution of inclinations is a Fischer distribution. However, the discrepancies between different functional forms are strongest for classifying objects in the intermediate, overlapping portion of the bimodal inclination distribution (K. Volk 2011, private communication), so we argue that our approach of definitively classifying only the "uncontaminated" low and high inclination objects is robust.

Regarding the third complication, the stability map of Lykawka & Mukai (2005) is formulated in terms of instantaneous eccentricity and inclination, but the most robust, non-varying formulation of the orbital elements are the proper, or free, elements. However, none of the model inclination distributions are formulated in terms of the

proper inclination, nor is the stability map of Lykawka & Mukai (2005) formulated in the proper elements. To compare "apples to apples," we use the instantaneous orbital elements in the plots in this section. We use the proper elements in Section 2.7 and find that the observational features we identify (Section 2.2.2) still hold.

Addressing the fourth complication, in Section 2.7, we confirm that the confinement of the cold population to low eccentricities is statistically significant. For the hot population, we only impose the constraint that the models must deliver them to the long-term stable region (Section 2.2.2); we will demonstrate that this loosely formulated restriction ends up imposing strong constraints on Neptune's dynamical history.

Ruling Out Observational Bias through Statistical Tests

We would not expect observational bias (the final complication) to cause the cold classicals to appear to confined to low eccentricities; KBO searches are more likely to preferentially observe high-eccentricity (i.e. small periapse) objects of a given semimajor axis. However, to ensure that the features on which we base our constraints (Section 2.2.2) are not created by observational bias, we perform the following test to see if observational bias could generate them:

1. We begin by generating a simulated sample of objects uniformly distributed in (a, e). We set the inclinations to follow the unbiased inclination distribution of the classicals, as modeled by Gulbis et al. (2010).

2. Then we use the stability map of Lykawka & Mukai (2005) to transform this simulated sample following a uniform eccentricity distribution into a sample following the eccentricity distribution shaped by the four giant planets under their

current configuration. We call this process "filtering." For each simulated object, we obtain a predicted survival rate from the (a, e) stability map of Lykawka & Mukai (2005). Then we select a uniform random number between 0 and 1. If the randomly selected number is less than the predicted survival rate, we include the object in our sample. Note that since the survival rates of Lykawka & Mukai (2005) are given as a range (e.g. $10 - 20\%$, $90 - 100\%$), we repeated this entire test (i.e., steps 2-4) three times, once using the minimum of each range, once using the mean of each range, and once using the maximum of each range. As expected, the resulting eccentricity distribution had higher (lower) eccentricities when we used the maximum (minimum) each range but the major features we identified still held. The simulated population in Figure 2.4 uses the mean. Next we transformed the "survival-rate filtered" sample from step 2 into an observed sample:

3. We randomly assign each object an H magnitude[3] between 6 and 8.

4. Then we apply the L7 Survey Simulator for the well-characterized CFEPS. (Kavelaars et al. 2009).

5. We compare the final simulated distribution to the subset of objects that were detected by CFEPS (Kavelaars et al. 2009) (Figure 2.4). Figure 2.4 is analogous to Figure 2.3. It includes the simulated distribution (circles) and only the subset of KBOs observed by CFEPS. The simulated distribution is not confined to $e < 0.1$ from 42.5 to 45 AU, confirming this feature of the observed eccentricity distribution does not result from observational bias. Note also that simulated hot objects are

[3]An alternative method, randomly drawing the H magnitudes from observed classical CFEPS objects, yielded results that were qualitatively the same.

found at lower eccentricities than observed.

2.3 Framework

Our representation of the observations in Figure 2.3 highlights the problem with theories of a single origin for the hot and cold objects. How could a single origin produce both a cold population confined to low eccentricities and a hot population, with different physical properties and inclinations, dwelling above at high eccentricities? In Section 2.3.1, we explain why a single origin scenario is unlikely. In Section 2.3.2, we describe a scenario, which we will consider throughout the rest of the paper, in which the cold population formed in situ and the hot population formed in the inner disk and was transported to the classical region. In Section 2.3.3, we explain why is it reasonable to place constraints on Neptune's history using the evolution of the KBOs only during Neptune's wild days, and in Section 2.3.4 we discuss the possibility of alternative scenarios of Kuiper Belt assembly.

2.3.1 Ruling out a Single Origin for the Hot and Cold Classicals

A single origin for the hot and cold populations seems unlikely. If the cold and hot classicals formed together in the classical region, where they are observed today, it is difficult to imagine a process that would excite the hot population while leaving the cold population confined to low eccentricities. Hahn & Malhotra (2005) proposed a scenario in which the classical region has been pre-excited. However, this scenario does not produce a population of cold classicals confined to low eccentricities. Moreover, if both

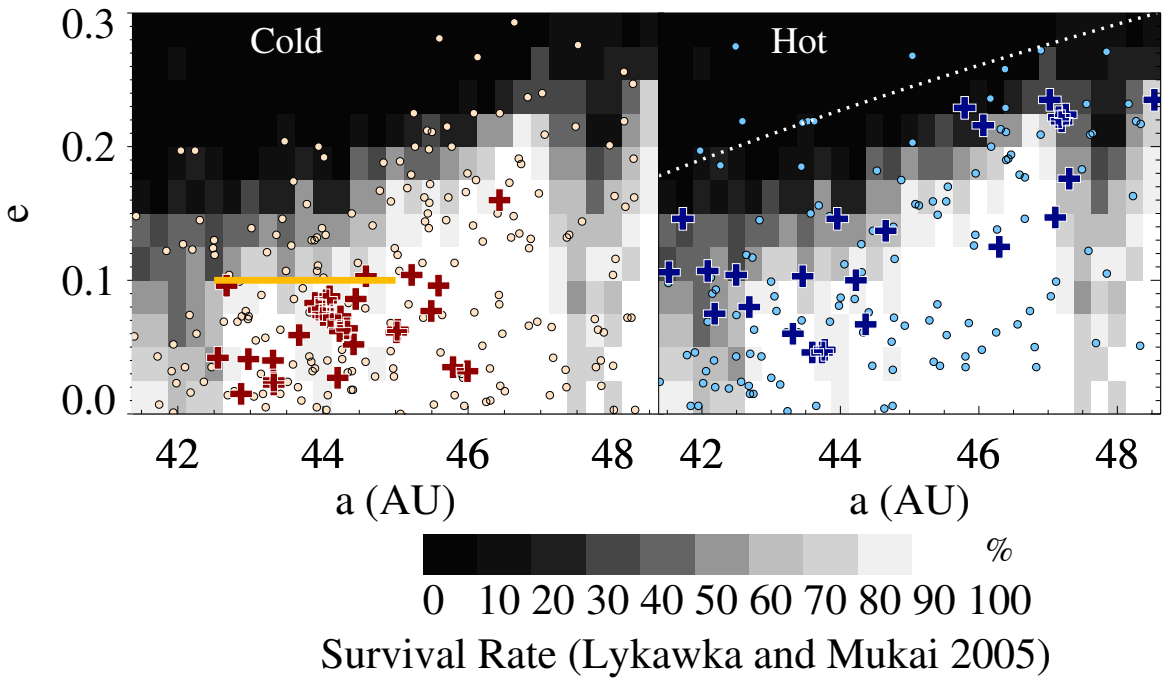

Figure 2.4.—: CFEPS objects only. Plotted over the survival map of Lykawka & Mukai (2005) are predicted (circle) and observed (plus) distributions of cold classicals with $i < 2°$ (left) and hot classicals with $i > 6°$ (right). The predicted classicals are the distribution expected from a uniform (a, e) distribution, filtered by the survival map and put through the CFEPS Survey Simulator of Kavelaars et al. (2009) (see the text for further detail). The observed classicals are those observed by CFEPS. In the left panel, the cold classicals between 42.5 and 44 AU are confined to $e < 0.05$, well below the survival limit, while cold classicals between 44 and 45 AU are confined to $e < 0.1$, also below the survival limit in this region. We plot $e = 0.1$ from 42.5 to 45 AU as a solid yellow line in the left panel. In the right panel, the hot classicals occupy the upper portion of the survival region. The dashed line indicates an approximate upper threshold of long-term survival, which we will use in Sections 2.5.2 and 2.5.3.

the cold and hot classicals were transported from the inner disk, it seems unlikely that a common deposition process would place the cold classicals solely at low eccentricities. Levison & Morbidelli (2003) and Levison et al. (2008) propose scenarios in which both the hot and cold classicals are transported from the inner disk.

In the scenario of Levison & Morbidelli (2003), the cold classicals were pushed outward by the 2:1 resonance and dropped during stochastic migration, while the hot classicals scattered off of Neptune. The feasibility of this mechanism depends on the size distribution of planetesimals, because the migration needs to be stochastic in order to drop objects from resonance. When Neptune scatters a planetesimal inward and the planetesimal is ejected by Jupiter, Neptune experiences a net gain in angular momentum and migrates outward. If the planetesimals are small, this is a smooth process, but if they are large, it is a jumpy, stochastic process, in which KBOs can be dropped from resonance. See Murray-Clay & Chiang (2006) for a detailed exploration of stochastic migration; they conclude that planetesimal-driven migration cannot generate the necessary stochasticity unless a large fraction of planetesimals formed very large. This constraint merits a fresh look in light of new planetesimal formation models (see Chiang & Youdin 2010, and references therein). However, even if extreme planetesimal properties allowed this mechanism to work, objects dropped from the 2:1 resonance would have a range eccentricities, not be confined solely to low eccentricities. Therefore this mechanism holds more potential for producing the hot population than the cold population.

In the scenario of Levison et al. (2008), the cold classicals are objects that, like the hot classicals, were scattered into the Kuiper Belt by an eccentric Neptune but, unlike the hot classicals, evolve down to low eccentricities in regions near resonances.

However, this mechanism would create a range of eccentricities for the cold classicals and thus would have trouble producing the confined eccentricities of the region of 42.5 AU $< a <$ 45 AU (Figure 2.3). They do find some correlation between a particle's final inclination and its initial semimajor axis in one of their simulations (Levison et al. 2008, Figure 11, panel (b)), which may be able to partially account for a difference in physical properties between low and high inclination objects. However, transporting the cold classicals from the inner disk is not consistent with the finding by Parker & Kavelaars (2010) that wide binaries — of which the cold population contains a number — cannot survive transportation from the inner disk to the classical region.

The Eccentricity Distribution was not Sculpted Solely by a Different Stability Threshold in the Past

One might wonder whether the observed confinement of the cold classicals (Figure 2.3) is the result of a smaller stability region than exists today, as if the cold classicals follow an ancient scattering line. However, there are numerous "hot" objects with $i > 6°$, as well as ambiguous objects with $2° < i < 6°$, in the region from 42.5 to 45 AU that have high eccentricities, right up to the modern stability limit. To create the observed distribution, one would need a mechanism that removes all objects with high eccentricities and $i < 2°$ while leaving a) objects with low eccentricities and $i < 2°$, and b) objects with a range of eccentricities and $i > 2°$. Therefore, it seems unlikely that this mechanism could produce both the hot and cold populations. We note that such a scenario could take place before Neptune transports the hot classicals. However, such initial sculpting would not affect the constraints we will place, which Neptune still needs to obey during the hot classical transport phase.

2.3.2 Colds in Situ, Hots Transported from the Inner Disk

Thus, throughout the rest of paper, we consider the general scenario — also discussed in Morbidelli et al. (2008) — in which the hot objects are transported to the classical region from the inner disk and the cold objects form in situ in the classical region. The cold objects must not be dynamically excited, as quantified by the criterion we established in Section 2.2.2. In Figure 2.5, we show a conceptualization of this model. This general scenario encompasses previous models and allows Neptune to undergo any potential combination of high eccentricity, migration, and/or apsidal precession with a range of initial eccentricities and semimajor axes. If our constraints do not rule out all of parameter space for this model, it may be possible to produce both the hot and cold classical population. Otherwise, a major physical process is missing from current models.

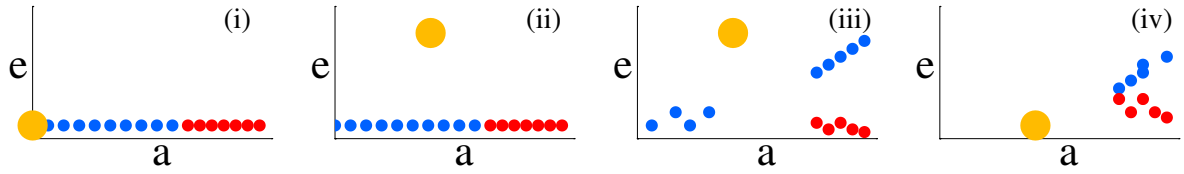

Figure 2.5.—: Conceptual framework. (i) The hot classicals (blue) form in the inner disk and the cold classicals (red) form in the outer disk. (ii) Neptune is scattered onto a high-eccentricity orbit through its interactions with other planets. (iii) Neptune scatters the hot objects into the classical region without disrupting the cold ones. (iv) Neptune's large eccentricity damps, leaving the cold classicals confined to low eccentricities.

For now, we can think of Neptune as having a high eccentricity at one location after undergoing planet-planet scattering. Our results hold in more complicated scenarios as well, as we will describe in Section 2.5.4.

2.3.3 The Case for Considering Short-term Evolution

We have chosen features (Section 2.2.2) that are not shaped by the long-term survival of KBOs under the current solar system planetary configuration. Therefore, we can focus on modeling the processes that affect these features during the interval of Neptune's wild days instead of treating the entire 4 Gyr. We model these processes analytically in Section 2.4 and validate our analytical expressions using numerical integrations.

Unless otherwise specified, the integrations are performed as follows. We perform the integrations using the *Mercury 6.2* hybrid symplectic integrator (Chambers 1999), an N-body code that allows massless test particles. We employ an accuracy parameter of 10^{-12} and a step size of 200 days and impose (if applicable) the migration and damping of Neptune's orbit through user-defined forces and velocities. Migration and damping follow the following forms:

$$\begin{aligned} a_{\rm N} &= (a_{\rm N})_f + ((a_{\rm N})_0 - (a_{\rm N})_f) \exp\left(-t/\tau_{a_{\rm N}}\right) \\ e_{\rm N} &= (e_{\rm N})_0 \exp\left(-t/\tau_{e_{\rm N}}\right), \end{aligned} \tag{2.1}$$

where $a_{\rm N}$ is the semimajor axis of Neptune at time t, $(a_{\rm N})_0$ is the initial semimajor axis, and $(a_{\rm N})_f = 30.1$ AU is the final semimajor axis. At time t, the eccentricity of Neptune is $e_{\rm N}$; Neptune's initial eccentricity is $(e_{\rm N})_0$. The forced evolution of Neptune's orbit is implemented through modifications to *Mercury 6.2*, described in detail in the Appendix of Wolff et al. (2012). The migration and damping are parametrized by timescales $\tau_{a_{\rm N}}$ and $\tau_{e_{\rm N}}$ respectively, which we specify in the text in the applicable cases. When specified, Neptune is forced to undergo apsidal precession using an artificial stellar oblateness force, built into *Mercury 6.2*, that we modified to apply only to Neptune, parameterized

by a J_2 coefficient chosen to produce the correct precession rate. Unless otherwise noted, Neptune is the only planet included in the integration. The KBOs are modeled as 600 massless test particles with initial a evenly spaced between 40 and 60 AU and initial $e = i = 0$. The migration, damping, and apsidal precession are not applied to the KBOs, only to Neptune.

2.3.4 Alternative Scenarios for Kuiper Belt Assembly

The purpose of this paper is to explore whether the generalized scenario described here can even work, i.e. whether it is ever possible to transport the hot classicals from the inner disk to the classical region without disrupting an in situ cold population. Yet alternative scenarios exist that do not fit within this framework, such as the additional planet beyond Pluto proposed by Lykawka & Mukai (2008) and others. Furthermore, we will describe in the conclusion how additional constraints could rule out the generalized model we consider. In that case, development of alternative scenarios would be necessary. Obviously, the constraints we will place do not necessary hold for a scenario that is not encompassed by our general model.

2.4 Physical Processes Resulting from Neptune's High Eccentricity

We begin our analysis by describing the physical processes that can impact the Kuiper Belt if Neptune's eccentricity is high. First we consider how classical KBOs reach the classical region. In our generalized model (Figure 2.5), the cold classicals form in situ

and hot classicals are delivered by Neptune from the inner disk. Once the hot and cold objects are in the classical region, both evolve in response to an eccentric Neptune. A tension arises between need of hot objects for Neptune to be eccentric — to deliver them into the classical region and to allow them to evolve to low eccentricities once they arrive — and the undesirable excitation of cold objects when Neptune is eccentric. In this Section, we lay out analytical expressions for how KBOs evolve in response to an eccentric Neptune and use this theory to transform our observational constraints into comprehensive constraints on Neptune's orbit during its high eccentricity period. We will employ these constraints on Neptune's orbit in Section 2.5 to rule out much of parameter space.

2.4.1 Delivery into the Classical Region

In the generalized model we explore, Neptune may be scattered outward from the inner solar system onto a highly eccentric orbit. After this occurs, Neptune's new orbit crosses the orbits of some planetesimals in the inner disk (see Figure 2.5), which scatter off the planet. This mechanism can potentially deliver hot objects from the inner disk into the classical region.

The region into which Neptune can scatter objects is defined by the planet's semimajor axis $a_{\rm N}$ and eccentricity $e_{\rm N}$. Neptune can scatter objects outward to periapses $q = a(1-e)$ between Neptune's periapse $r_{p,{\rm N}} = (a_{\rm N} - a_{\rm H})(1-e_{\rm N})$ and apoapse $r_{a,{\rm N}} = (a_{\rm N} + a_{\rm H})(1+e_{\rm N})$. In Figure 2.6, we show examples of the region into which Neptune can scatter KBOs for two sets of parameters $(a_{\rm N}, e_{\rm N})$. We have adjusted $r_{p,{\rm N}}$ and $r_{a,{\rm N}}$ to include the Hill sphere radius, $a_{\rm H}$ (~ 1 AU), the distance from Neptune at which

Neptune's gravity overcomes the Sun's tidal gravity. Particles that enter Neptune's Hill sphere will be scattered and, if they are scattered outward into the classical region, will reach – under the approximation that the scattering location becomes the particle's new periapse – a given semimajor axis a with eccentricities between $1 - r_{p,\mathrm{N}}/a$ and $1 - r_{a,\mathrm{N}}/a$.

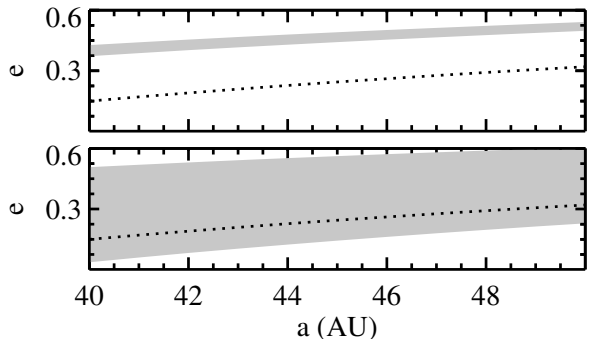

Figure 2.6.—: Region into which Neptune can scatter particles for $a_{\mathrm{N}} = 24, e_{\mathrm{N}} = 0.02$ (top), a typical initial condition for extensive migration models, and $a_{\mathrm{N}} = 28.9, e_{\mathrm{N}} = 0.3$ (bottom), which is the initial condition for Run B in Levison et al. (2008). The dashed line marks the upper threshold of long-term survival, as indicated in Figure 2.4.

Implications of Scattering for the Cold Classicals

If Neptune's apoapse $r_{a,\mathrm{N}}$ is large enough, the planet can potentially impinge into the cold classical region, scattering the objects there. However, we find in practice that if Neptune's eccentricity damps within the constraints we will place, then cold objects are never excited up to the scattering line, which moves upward as Neptune's eccentricity damps. In Section 2.5.1, we will return to this issue for the special case of Neptune undergoing fast apsidal precession.

2.4.2 Secular Forcing

Secular forcing has a strong effect on the behavior of KBOs during the potential period when Neptune's eccentricity is high. (See Murray & Dermott 2000 for a pedagogical description of first order secular theory outside of mean motion resonance.) On a timescale of a million years, a cold object is excited to a higher eccentricity via Neptune's secular forcing. (The direct forcing from the other planets on the KBO is negligible and the other planets only affect the KBOs via Neptune, as we will demonstrate in Section 2.4.2). A hot object that is scattered into the classical region also experiences secular forcing, which can decrease its eccentricity so that its orbit no longer crosses Neptune's. Hot or cold, an object's eccentricity is a vector combination of its forced eccentricity — set by Neptune's eccentricity, Neptune's semimajor axis relative to the object's, and Neptune's apsidal precession rate — and of the object's free eccentricity, which is set by its initial condition before Neptune is scattered to a high eccentricity. The object's free eccentricity precesses about the forced eccentricity at the secular frequency $g_{\rm KBO}$. Therefore, as we will demonstrate, a cold object has a well-defined excitation time and amplitude, and a hot object will have a minimum eccentricity it can reach after being scattered into the classical region. Thus while Neptune's eccentricity is high, secular forcing potentially is an important mechanism for exciting the cold objects and stabilizing the hot ones. As we will show, when Neptune's eccentricity damps quickly, the orbits of the KBOs are "frozen" near the eccentricities they reached through secular evolution.

Basic Secular Evolution

First we define expressions for the secular evolution of a test particle under the influence of a planetary system containing only Neptune and the Sun. The components of the particle's eccentricity vector are $h = e\sin\varpi$ and $k = e\cos\varpi$, where ϖ is the particle's longitude of periapse. Secular forcing by Neptune causes h and k to evolve as (to first order in e and $e_{\rm N}$):

$$\begin{aligned} h &= e_{\rm free}\sin(g_{\rm KBO}t+\beta) + e_{\rm forced}\sin(\varpi_{\rm N}) \\ k &= e_{\rm free}\cos(g_{\rm KBO}t+\beta) + e_{\rm forced}\cos(\varpi_{\rm N}) \end{aligned} \tag{2.2}$$

where

$$\begin{aligned} e_{\rm forced} &= \frac{b^{(2)}_{3/2}(\alpha)}{b^{(1)}_{3/2}(\alpha)} e_{\rm N} \\ \alpha &= \frac{a_{\rm N}}{a} \\ g_{\rm KBO} &= \alpha b^{(1)}_{3/2}(\alpha)\frac{m_{\rm N}}{m_\odot}\frac{n}{4} \end{aligned} \tag{2.3}$$

The constants $e_{\rm free}$ and β are determined from the initial conditions, and the particle's forced eccentricity is $e_{\rm forced}$. Here, $\varpi_{\rm N}$ is the longitude of periapse of Neptune, $e_{\rm N}$ is the eccentricity of Neptune, and α is the ratio of Neptune's semimajor axis to that of the particle, all of which are assumed to be constant. The functions b are standard Laplace coefficients (see Murray & Dermott 2000). The secular frequency of the KBO is $g_{\rm KBO}$, $m_{\rm N}$ is the mass of Neptune, $m_\odot$ is the mass of the Sun, $n = (Gm_\odot/a^3)^{1/2}$ is the particle's mean motion, and G is the universal gravitational constant.

Consider a cold object with $e = 0$ at $t = 0$. In our approximation, Neptune, having been scattered by the other giant planets, effectively instantaneously appears and imparts a forced eccentricity of $e_{\rm forced}$. From these initial conditions, $e_{\rm free} = e_{\rm forced}$. Then, the KBO's forced eccentricity vector remains fixed and the object's total free eccentricity vector precesses about the forced eccentricity. Thus its total eccentricity varies sinusoidally from $e = 0$ to $e = 2e_{\rm forced}$ on a timescale set by $g_{\rm KBO}$.

A hot object scattered into the classical region, in contrast, has an eccentricity e at $t = 0$. The magnitude of its free eccentricity is a value between $\max(0,\, e - e_{\rm forced})$ and $e + e_{\rm forced}$, depending on the initial location of its periapse relative to Neptune's. Over a timescale set by $g_{\rm KBO}$, its total eccentricity oscillates. Depending on the initial conditions, it may reach an eccentricity low enough so that its orbit no longer crosses Neptune's and/or so that it is stable under the current configuration of the giant planets.

An example of the secular evolution of cold objects "going up" and hot objects "going down" in eccentricity is shown in Figure 2.7, highlighting the tension between the evolution of hot objects to low eccentricities and the evolution of cold objects to high eccentricities. The cold objects (red) begin with $e = 0$ (see Section 2.3.3 for a general description of the integrations we performed.) The hot objects in the integration (blue) all begin with $e = 0.2$ and $\varpi = \varpi_{\rm N} + \pi/3$, for the purposes of illustrating secular evolution[4]. As time progresses through three snapshots, the cold objects become excited and the hot objects reach low eccentricities. The analytical model from Equation (2.2) matches well except near mean motion resonances, where the secular evolution is much

[4]As shown in Section 2.4.1, a real hot object can only be scattered to a certain region of (a, e) space in the classical region, and its eccentricity and periapse are actually correlated

faster than predicted. We also overplot a more accurate analytical expression that includes a resonant correction term, which we will derive in Section 2.4.2.

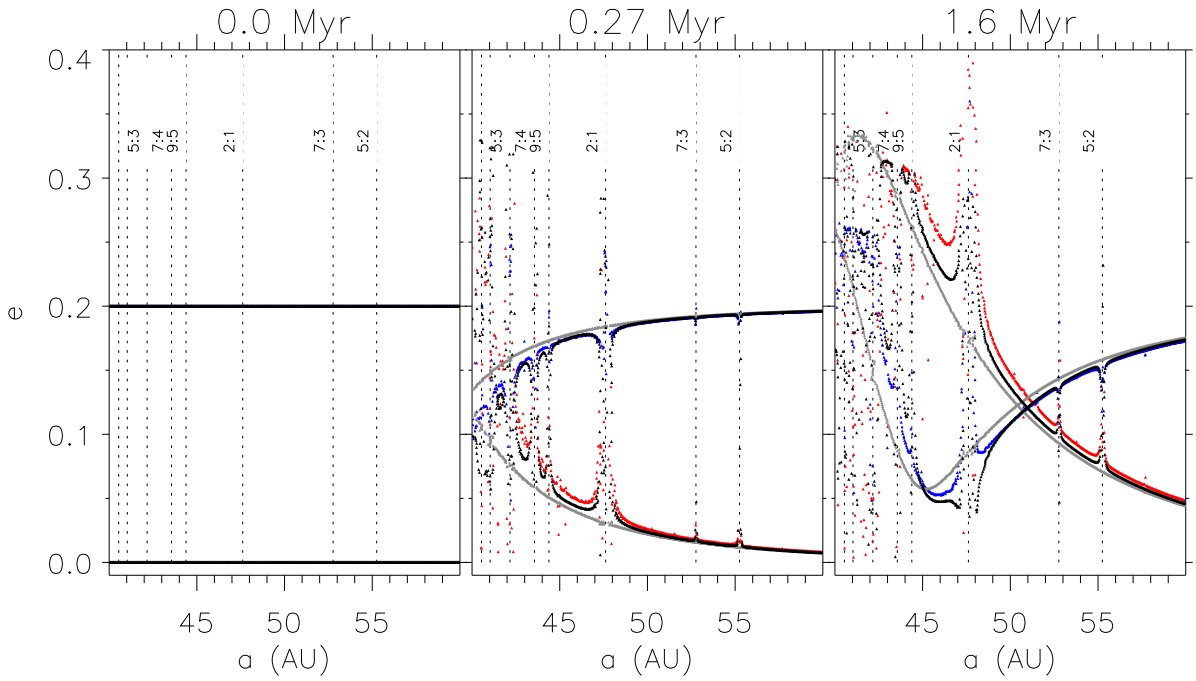

Figure 2.7.—: Numerical integration ($a_N = 30, e_N = 0.2$) shows cold objects (red) secularly evolving to high eccentricities and hot objects (blue) to low eccentricities. The gray is our analytical model without the resonance correction terms (Equation 2.2) and the black, which matches much better near the resonances, includes resonance terms (Equation 2.4).

We note that throughout the paper, we perform numerical integrations of objects with initial semimajor axes out to 60 AU to give a better conceptual picture of the secular excitation. Moreover, depending on where the initial population was truncated in the solar system's planetesimal disk, it is possible that additional classical KBOs will be discovered beyond 48 AU in the future, and we would like to make testable predictions. Finally, the integration results should be interpreted as examples: since we cannot show

a figure for every possible combination of parameters for Neptune, we plot out to 60 AU to let the reader imagine the results if Neptune's semimajor axis were smaller.

Refined Secular Expression

The secular expression in Section 2.4.2 is valid to first order in eccentricity, neglects the effects of orbital resonances, and applies in the case in which Neptune's orbit does not apsidally precess. However, these neglected effects can significantly alter a secularly evolving KBO's behavior:

1. Neptune's high eccentricity makes terms of order $e_{\rm N}^2$ (ignored in deriving Equation 2.2) non-negligible. As we will show, these extra terms result in a faster secular forcing frequency of the KBO.

2. Proximity to mean-motion resonances with Neptune significantly alters the secular frequencies of KBOs (as shown for other solar system bodies in Hill 1897; Malhotra et al. 1989; Minton & Malhotra 2011). Following Malhotra et al. (1989), we incorporate resonance correction terms, described in Section 2.8.1. These resonance correction terms are very important for objects *near* resonance but not valid for objects librating in resonance (we are not considering resonant objects in this paper[5]).

3. As Neptune's eccentricity is damped, the particle's forced eccentricity goes to zero. If the damping occurs over a timescale $\tau_{e_{\rm N}}$ shorter than the secular oscillation

[5]It has been claimed (e.g. Levison et al. 2008) that the entire classical region from the 3:2 to the 2:1 resonance is full over overlapping resonances. However, in Section 2.4.5 we will demonstrate that Neptune's high eccentricity alone does not cause resonance overlap in the classical region.

time, the particle's eccentricity is frozen at approximately the value it reaches at the eccentricity damping time. If the damping occurs over a longer timescale, the particle's eccentricity evolves to its initial free eccentricity.

4. Apsidal precession of Neptune alters the forced eccentricity, keeping it low when Neptune precesses quickly. It also alters the oscillation timescale of the total eccentricity, because now both the free and forced eccentricity are precessing.

5. Migration alters the secular frequencies and shifts the locations of the resonances.

Based on these considerations, we modify the standard expression (Equation 2.2) for the secular evolution of a test particle's h and k under the influence of an eccentric Neptune to incorporate these effects.

$$\begin{aligned} h &= e_{\text{free},0}\sin(g_{\text{KBO}}t+\beta_0)+\bar{e}_{\text{forced}}\sin(\varpi_{\text{N},0}+\dot{\varpi}_{\text{N}}t) \\ k &= e_{\text{free},0}\cos(g_{\text{KBO}}t+\beta_0)+\bar{e}_{\text{forced}}\cos(\varpi_{\text{N},0}+\dot{\varpi}_{\text{N}}t) \end{aligned} \tag{2.4}$$

$$g_{\text{KBO}} = (1+\frac{f_5}{f_2}e_{\text{N}}^2)\alpha b_{3/2}^{(1)}(\alpha)\frac{m_{\text{N}}}{m_\odot}\frac{n}{4}+\epsilon\delta g_{\text{KBO}} \tag{2.5}$$

$$\delta g_{\text{KBO}} = \alpha(Cxe_{\text{N}}^{x-1})^2\frac{m_{\text{N}}}{m_\odot}n \tag{2.6}$$

$$\bar{e}_{\text{forced}} = \sin(\min(g_{g_{\text{KBO}}}\tau_{e_{\text{N}}},\pi/2))\frac{g'_{\text{KBO}}}{\dot{\varpi}_{\text{N}}-g_{\text{KBO}}}e_{\text{N}}(t) \tag{2.7}$$

$$g'_{\text{KBO}} = -(1+\frac{f_{10}}{f_{11}}e_{\text{N}}^2)\ \alpha b_{3/2}^{(2)}(\alpha)\frac{m_{\text{N}}}{m_\odot}\frac{n}{4} \tag{2.8}$$

Compare Equation (2.4) to Equation (2.2). The form is the same but Equation (2.4) has several key differences and new variables, that we will proceed to discuss and define throughout the remainder of this subsection. One distinction is that several quantities

that were fixed in Equation (2.2) (i.e., $\varpi_{\rm N}, \alpha, e_{\rm N}$) can now vary with time. Additionally, we have incorporated corrections for Neptune's high eccentricity and for the potential proximity of the KBO to mean motion resonance with Neptune. The impact of the time-varying $e_{\rm N}$ is the most complicated, so we leave it for last.

As our first correction, we allow the longitude of pericenter of Neptune, $\varpi_{\rm N}$, to precess. Neptune's precession adds an extra term $\dot{\varpi}_{\rm N}$ to Equation (2.4) (where we rewrite $\varpi_{\rm N}$ as a linear function of time: $\varpi_{\rm N,0} + \dot{\varpi}_{\rm N} t$) and to Equation (2.7), in analogy to the standard secular theory for the four-planet case. We note that the other giant planets impact the secular evolution of the KBOs indirectly by causing Neptune's eccentricity to precess (see Section 2.4.2 for discussion).

The precession rate $\dot{\varpi}_{\rm N}$ has the same role (and same place, in the denominator of the forced eccentricity) in the just-Neptune secular theory as in the standard four-planet secular theory (Section 2.8.2) for the particle except that we are specifying Neptune's evolution via $\dot{\omega}_{\rm N}$ instead of constructing a secular theory for the planets that produces a particular $\dot{\omega}_{\rm N}$. When $\dot{\varpi}_{\rm N}$ is large, the effective forced eccentricity $e_{\rm forced} = |\bar{e}_{\rm forced}|$, defined below, remains low because the forced eccentricity is inversely proportional to the precession rate for $|\dot{\varpi}_{\rm N}| \gg |g_{\rm KBO}|$ (Equation 2.7).

When Neptune migrates, α changes with time. In Wolff et al. (2012), we found that migration occurs in three regimes, relative to the eccentricity damping timescale $\tau_{e_{\rm N}}$: fast, comparable, and slow. When Neptune's migration timescale $\tau_{a_{\rm N}}$ is slow relative to the damping time, the secular evolution of the KBOs effectively takes place as if Neptune remains at its initial location. When Neptune's migration is fast relative to the damping time, the secular evolution of the KBOs effectively takes place as if Neptune

were always at its final location. In the intermediate case, in which $\tau_{e_N} \sim \tau_{a_N}$, modeling the secular evolution at the location Neptune reaches after half a damping time is a fair approximation. In this work, we therefore use a fixed α, which should be chosen according to these principles for a given evolution of Neptune. Figure 2.8, which we will describe after discussing our treatment of Neptune's eccentricity, provides an example showing that this approach is effective.

Before considering the impact of e_N varying with time, we discuss the correction terms for Neptune's high eccentricity and for resonances. The correction terms for Neptune's high eccentricity do not change the form of the secular evolution. We have applied a correction term, $\frac{f_5}{f_2}e_N^2$, in our expression for g_{KBO} (Equation 2.5), and another such factor, $\frac{f_{10}}{f_{11}}e_N^2$, in g'_{KBO} (Equation 2.8), which is another eigenfrequency. These terms are derived, the f factors (which are of order unity) defined, and their necessity demonstrated in Section 2.8.

Proximity to resonance changes the secular frequency g_{KBO} (Equation 2.5), as described by Malhotra et al. (1989). Orbital resonances greatly increase the secular forcing frequency because terms in the disturbing function that depend on the resonant angle can no longer be averaged over. The amplitude of the resonant correction term ϵ is defined in Section 2.8 and depends on how close the particle is to the location of mean-motion resonance. The frequency, δg_{KBO}, defined in Equation (2.6), depends on the order of the resonance x and a constant C, of order unity, that is different for each resonance. See Figure 2.7 for a demonstration of the resonance correction terms.

Finally, we turn to the impact of eccentricity damping, which alters e_N. Instantaneously, the KBO has the eccentricity components $h = e \sin \varpi = e_{free} \sin \phi +$

$\bar{e}_{\rm forced} \sin \varpi_{\rm N}$ and $k = e \cos \varpi = e_{\rm free} \cos \phi + \bar{e}_{\rm forced} \cos \varpi_{\rm N}$, where $\phi = g_{\rm KBO}\ t + \beta$. However, now the forced eccentricity vector $(\bar{e}_{\rm forced} \cos \varpi_{\rm N}, \bar{e}_{\rm forced} \sin \varpi_{\rm N})$ is changing. We have already accounted for the apsidal precession, but now the magnitude of the forced eccentricity vector is changing as well. When $e_{\rm forced}$ does not change, $e_{\rm free}$ is a constant determined by initial conditions. This remains true when $e_{\rm forced}$ evolves slowly compared to the secular forcing time of the KBO. Otherwise, $e_{\rm free}$ changes. Instead of allowing both $e_{\rm free}$ and $e_{\rm forced}$ to change with time, we use $e_{\rm free,0}$ and define an "effective" forced eccentricity, $|\bar{e}_{\rm forced}|$ (Equation 2.7). The "effective" forced eccentricity changes with time proportionally to $e_{\rm N}$. Throughout the rest of the paper, we will refer to $e_{\rm free,0}$ as $e_{\rm free}$ and the "effective" forced eccentricity as $e_{\rm forced}$. The "effective" forced eccentricity includes a factor $\sin(\min(g_{g_{\rm KBO}} \tau_{e_{\rm N}}, \pi/2))$. When Neptune's eccentricity damping timescale is long compared to the KBO's secular oscillation period (i.e. $g_{\rm KBO} \tau_{e_{\rm N}} > \pi/2$), the particle's total eccentricity damps to its initial free eccentricity, $e_{\rm free,0}$, and this factor is unity. However, when Neptune's eccentricity damps quickly, the particle's total eccentricity damps to a value near the eccentricity it reached after one damping time. The empirical correction factor allows us to model the particle's behavior without altering the form of the secular evolution. This empirical factor provides a match to the integrations (see Figure 2.8).

The modified secular theory, Equation (2.4), matches the integrations even when damping and migration are included (Figure 2.8). Figure 2.8 shows an example of a case in which $\tau_{e_{\rm N}} = 0.3$ Myr is shorter than its migration timescale, $\tau_{a_{\rm N}} = 5$ Myr. (See Section 2.3.3 for a description of how we implemented the damping and migration of Neptune's orbit.) In the top row, Neptune undergoes eccentricity damping from $e = 0.3$ at constant semimajor axis 28 AU. In the middle row, Neptune migrates from 28 AU

to 30 AU on a timescale $\tau_{a_{\rm N}} = 5$ Myr, without its eccentricity damping. Unlike any other model in this paper, we use a time-dependent $\alpha(t)$ for the analytical model. In the bottom row, Neptune undergoes both damping and migration, but we plot again the same analytical model as in row 1, in which Neptune undergoes only eccentricity damping (no migration). The model over plotted in row 3, even though it in no way includes the effects of migration, matches well. When the migration is slow compared to the damping, the change in the secular frequency $g_{\rm KBO}$ is negligible over the timescale during which Neptune's eccentricity is high. It is as if Neptune's eccentricity damps while Neptune remains at its initial $a_{\rm N}$. Thus when the migration is slow compared to the damping timescale, we can model the KBOs' secular evolution as if Neptune's eccentricity damps while Neptune remains in place.

Figure 2.8.—: Secular excitation of cold classicals when Neptune undergoes eccentricity damping and/or migration. In the top row, Neptune's eccentricity damps with $\tau_{e_N} = 0.3$ Myr, and the planet does not migrate; secular theory, including damping (Equation 2.4), is plotted in black. In the middle row, Neptune migrates outward on the timescale $\tau_{a_N} = 5$ Myr, and its eccentricity does not damp. The secular theory, including migration (Equation 2.4), is plotted in black. The scattered points in the final panel are objects that have undergone accelerated forcing near resonances as the resonances swept through. The bottom row displays a numerical integration including both eccentricity damping and migration, on the same timescales as above, but the analytical model overplotted in black is the same as in row 1.

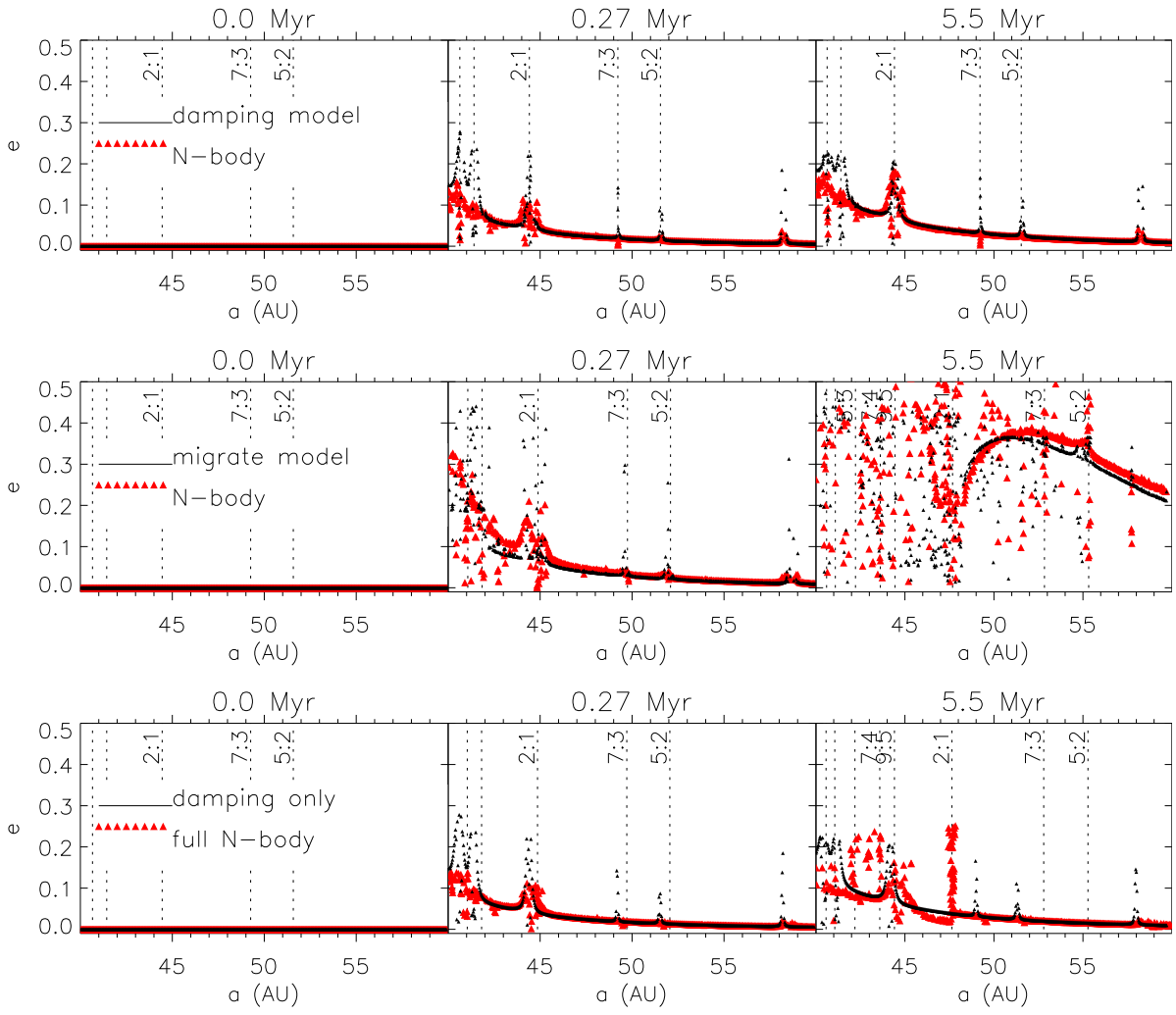

Figure 2.8.—: Continued

Effects of Other Planets

Our approach of modeling only Neptune, undergoing a range of orbital histories that would be caused by interactions with the other giant planets and with the solar system's planetesimal disk, is sufficient because the other planets primarily affect the KBOs only indirectly, through influencing Neptune. The influence on the Kuiper Belt of a single, apsidally precessing Neptune matches the influence of multiple planets in both integrations and theory.

An illustrative case is shown in Figure 2.9. The initial conditions for the particles are the same as in Figure 8, and Neptune has $a_{\rm N} = 28$ and $e_{\rm N} = 0.2$. The top panel (four planets) and middle panel (just Neptune undergoing precession) are very similar, keeping the objects at lower eccentricities than in the bottom panel (just Neptune, no precession). Thus precession must be included in the parameter space exploration, and including precession successfully accounts for the influence of the other giant planets. We note that in the time of the snapshot (1.4 Myr), the particles have secularly evolved to have eccentricities large enough so that their orbit, at the proper orientation, could intersect Neptune's. In cases in which Neptune precesses (top two panels), the objects are scattered by Neptune as Neptune's orbit precesses to intersect the orbits of the KBOs with eccentricities above the scattering line. The cut-off is at 45 AU because, interior this location, particles are secularly evolving quickly due to their proximity to resonance and have thus reached high eccentricities, allowing them to scatter. In the final panel, the particles are not scattered because Neptune's orbit does not precess to intersect the orbits of the particles.

The other planets matter in that they affect Neptune, but their direct effect on the

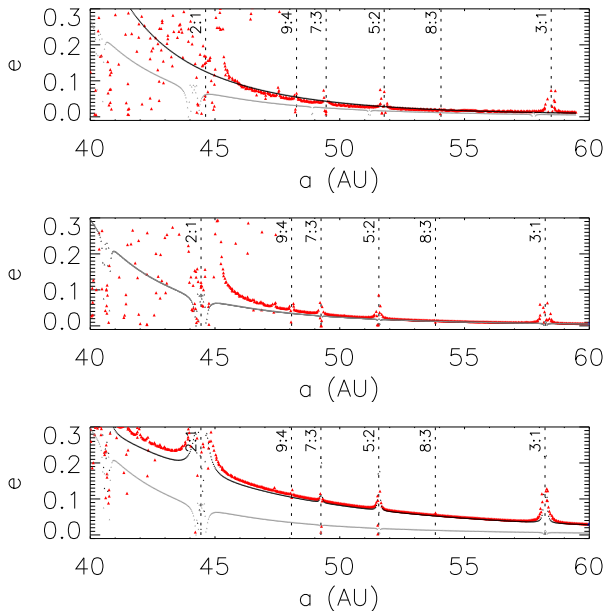

Figure 2.9.—: Other giant planets affect the cold classicals indirectly by causing apsidal precession of Neptune. Top panel: snapshot (1.4 Myr) from an integration including four planets (with initial conditions $a = 5.2$ AU, $e = 0.05$, $i = 1.3°$ for Jupiter, $a = 9.54$ AU, $e = 0.06$, $i = 2.49°$ for Saturn, and $a = 16$ AU, $e = 0.05$, $i = 0.773°$ for Uranus). Middle panel: same for integration including just Neptune undergoing apsidal precession with a period of 1.6 Myr. Bottom panel: same for integration including Neptune not undergoing precession. The black line in the top plot is the first-order multi-planet secular theory (i.e. without the extra resonant correction terms or higher order e_N terms we included for the just-Neptune theory) (Murray & Dermott 2000). The gray line on each plot is the analytical expression from the middle panel for comparison, computed using single planet secular theory, including precession (Equation 2.4). The black line in the bottom panel does not include precession. Note the scattering in the top two panels interior to the 2:1 resonance.

KBOs is negligible. Their main effect is to cause precession of Neptune. Interactions between Uranus and Neptune, if they closely approach the 2:1 resonance while Neptune's eccentricity is high, cause additional effects that we discuss in Section 2.4.5. These effects can also be modeled using only Neptune, with appropriate orbital variations.

Treating only Neptune reduces the number of free parameters, allowing a more thorough exploration of the restricted space. The constraints we will develop can be applied to more extensive models that include the other giant planets. See Section 2.8.2 for a mathematical discussion of how the full four-planet secular theory reduces to the just-Neptune case.

Constraints from Secular Excitation of Cold Objects

It follows from the expressions in Section 2.4.2 that the excitation of the cold classicals happens on timescales of millions of years (or shorter near resonances) with an amplitude and timescale that depend on Neptune's semimajor axis, eccentricity, eccentricity damping timescale, migration rate, and precession rate. Complementarily, hot objects scattered into the classical region can evolve to lower eccentricities on similar timescales.

The observations require that the cold classicals not be excited above $e > 0.1$ in the region 42.5 AU $< a <$ 45 AU, as demonstrated in Section 2.2. From Equations (2.4) and (2.5) derived in Section 2.4.2, it follows that the cold classicals will not be excited above $e > 0.1$ at a given location if (CONSTRAINT 1):

$$\sin(\min(g_{\rm KBO}\tau_{e_{\rm N}}, \pi/2))|\frac{g'_{\rm KBO}}{\dot{\varpi}_{\rm N} - g_{\rm KBO}}|e_{\rm N} < 0.1 \tag{2.9}$$

Thus there are three possible regimes to "preserve" an in situ population of cold classicals through Neptune's wild days:

1. The eccentricity of Neptune is small enough that the region's forced eccentricity, proportional to $e_{\rm N}$, is below 0.1 (i.e. $|\frac{g'_{\rm KBO}}{\dot{\varpi}_{\rm N}-g_{\rm KBO}}|e_{\rm N} < 0.1$)

2. Neptune's periapse precesses quickly enough that the region's forced eccentricity, inversely proportional to $\dot{\varpi}_{\rm N}$, is below 0.1 (i.e. $\dot{\varpi}_{\rm N}$ is large).

3. The eccentricity of Neptune damps quickly enough that the objects are not excited above 0.1 (i.e. τ_e is small).

2.4.3 Effects of Post-scattering Secular Evolution on Hot Objects

Hot objects that have been scattered into the classical region from the inner disk (Section 2.4.1) will undergo secular evolution when they arrive in the classical region. They will reach a given semimajor axis a in the classical region with eccentricities between $1 - r_{a,N}/a$ and $1 - r_{p,N}/a$. Not all of these eccentricities are consistent with stable orbits over 4 Gyr (Figure 2.3). If a particle is scattered to a high eccentricity above the stable region, under certain conditions — if $\tau_{e_{\rm N}}$ is not too fast and Neptune imparts a forced eccentricity that is large enough relative to the particle's free eccentricity — the particle can reach a region of long-term survival through secular evolution.

In Figure 2.10, we show two examples of KBOs that are scattered into the classical region from an integration resembling Levison et al. (2008) Run B. In this integration, Neptune begins with $a_N = 28.9$ AU, $e_{\rm N} = 0.3$. Its eccentricity damps on a timescale

of $\tau_e = 2$ Myr, and it undergoes migration to 30.1 AU with $\tau_a = 10$ Myr. Uranus begins with $a = 14.5$ and $e = 0$ and also undergoes migration, to 19.3 AU, on the same timescale. Jupiter and Saturn begin with $a = 5.2$ AU, $e = 0.05$ and $a = 9.6$ AU, $e = 0.05$ respectively and do not undergo migration or eccentricity damping. The integration includes 24,000 test particles, half of which (following Levison et al. 2008) begin in the region from 20-29 AU with $e = 0.2$ and half of which begin in the region from 29 - 34 AU with $e = 0.15$. The two example particles shown were among the group of particles found in the stable classical region in this integration after 4 Gyr and exhibit typical behavior. The particles are scattered into the classical region above the region of survival (Figure 3; below dotted line in right panel) but secularly evolve down into the stable region. After 4 Gyr, the particles remain in this location. Neither of these example objects is librating in an orbital resonance.

Therefore, Neptune's apoapse $r_{p,N}$ must be large enough so that the hot classicals reach the region of long-term survival either immediately or can evolve there before the eccentricity of Neptune damps, after which the eccentricity of the particle is frozen.

However, the post-scattering evolution depends strongly on $\varpi - \varpi_{\rm N}$. Particles are not actually scattered to orbits with independent, random $\varpi - \varpi_{\rm N}$. This is because, by definition, after each scattering, the particle's new orbit fulfills the condition that at θ, the angle at which the orbit of the particle and the orbit of Neptune intersect, $r = r_N$:

$$\frac{a(1-e^2)}{1+e\cos(\theta-\varpi)} = \frac{a_{\rm N}(1-e_{\rm N}^2)}{1+e_{\rm N}\cos(\theta-\varpi_{\rm N})} \tag{2.10}$$

This is important because once the particle is scattered, it begins to undergo secular oscillations and the initial phase of the oscillation, β_0 (Equation 2.4), depends on $\varpi - \varpi_{\rm N}$.

Since in the classical region, most of the particle's orbit is outside of Neptune's

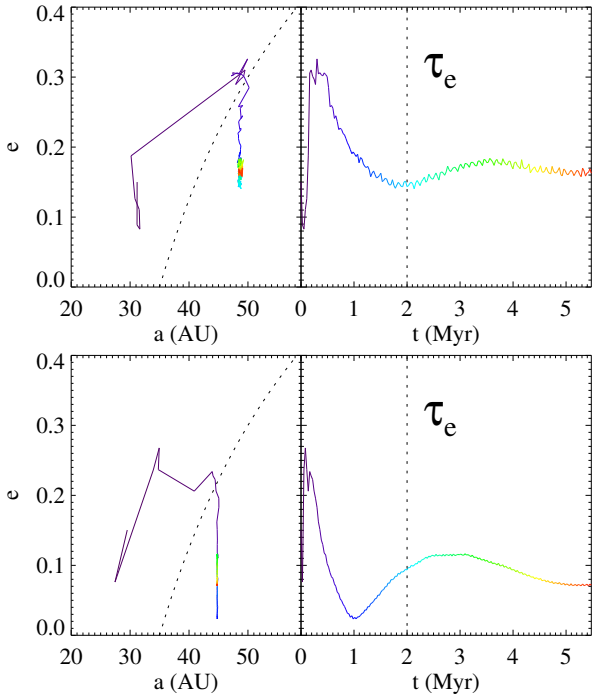

Figure 2.10.—: Secular evolution can deliver hot objects into the classical region. Evolution of two example particles (top and bottom) for the first 6 Myr of an 4 Gyr integration resembling Levison et al. (2008) Run B. Left: path of objects in (a, e) space. The color varies from purple (beginning of the integration) to red (6 Myr). The dashed line indicates the scattering line $q = 35$. Right: evolution of the particle's eccentricity versus time. The dashed line indicates one e-folding time, $\tau_{e_{\rm N}} = 2$ Myr, for the damping of Neptune's eccentricity.

orbit, the orbits will intersect close to the particle's periapse, i.e. the interior part of its orbit, so $\theta \approx \varpi$. When $\theta = \varpi$, Equation (2.10) simplifies to:

$$q = a(1-e) = \frac{a_{\rm N}(1-e_{\rm N}^2)}{1 + e_{\rm N}\cos(\varpi - \varpi_{\rm N})} \tag{2.11}$$

and thus ϖ maps exactly to the particle's post-scattering periapse q. For example, particles scattered to the minimum $q = r_{p,N}$ have $\varpi - \varpi_{\rm N} = 0$, while particles scattered to the maximum $q = r_{a,\rm N}$ have $\varpi - \varpi_{\rm N} = \pi$. Particles scattered to an intermediate $q = a_{\rm N}(1-e_{\rm N}^2)$ have $\varpi - \varpi_{\rm N} = \pm\pi/2$.

In Figure 2.11, we plot the longitude of periapse relative that of to Neptune $\varpi - \varpi_{\rm N}$ versus periapse q of test particles that were scattered in an integration we performed. The $\varpi - \varpi_{\rm N}$ is from the first (3000 yr) timestep after the particle's scattering. The integration lasted for 1 Myr and included Neptune, with $a_{\rm N} = 30$ AU and $e_{\rm N} = 0.3$, and 11,600 test particles evenly-spaced in semimajor axis from 29-34 AU, with $e = 0.15$. The $\varpi - \varpi_{\rm N}$ values are well-matched by Equation (2.11).

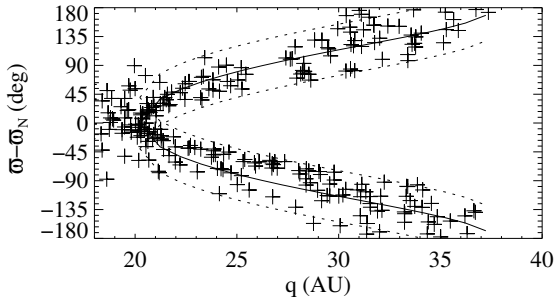

Figure 2.11.—: Longitude of periapse relative to Neptune $\varpi - \varpi_{\rm N}$ of a particle's orbit after being scattered by Neptune into the region $a > 40$ AU maps to the particle's new periapse distance q. The particles from the integration are plotted as pluses and the solid line is Equation (2.11). The dashed lines are the solid line shifted by $\pm 40°$.

The secular evolution of the particle after its scattering will depend on its semimajor axis, eccentricity, and longitude of pericenter relative to Neptune's (Equation 2.2). In particular, from Equation (2.2), it follows that the initial rate of change of the particle's eccentricity depends on $\varpi - \varpi_{\rm N}$. By calculating the particle's total eccentricity $e = \sqrt{h^2 + k^2}$, differentiating with respect to time, and evaluating the time derivative at $t = 0$, we find:

$$\dot{e}(t=0) = -e_{\rm N} \sin(\varpi - \varpi_{\rm N}) \alpha b^{(2)}_{3/2}(\alpha) \frac{m_{\rm N}}{m_\odot} \frac{n}{4} \tag{2.12}$$

An analogous expression follows from Equation (2.4).

Along a scattering line q, the KBOs do not have random ϖ but ϖ close to the value dictated by Equation (2.11). Thus the particles scattered to the minimum $q = r_{p,N}$, which have $\varpi - \varpi_{\rm N} = 0$, and maximum $q = r_{a,{\rm N}}$, which have $\varpi - \varpi_{\rm N} = \pi$, are turning over in their secular evolution cycles ($\dot{e} = 0$). However, particles scattered to an intermediate $q = a_{\rm N}(1 - e^2_{\rm N})$, which have $\varpi - \varpi_{\rm N} = \pi/2$, will be decreasing in eccentricity at the maximum rate in the cycle.

Moreover, the particle's free eccentricity also depends on $\varpi - \varpi_{\rm N}$:

$$e^2_{\rm free} = \bar{e}^2_{\rm forced} + (e(0))^2 - 2e(0)\bar{e}_{\rm forced} \cos(\varpi - \varpi_{\rm N}) \tag{2.13}$$

where $e(0)$ is the KBO's eccentricity at $t = 0$.

Thus $\varpi - \varpi_{\rm N}$ sets not only the particle's initial phase in its secular evolution cycle but also the amplitude of its free eccentricity. The particles with the phase to achieve the lowest possible total eccentricity ($e_{\rm free}$ close to $e_{\rm forced}$) may not initially be evolving downward in their cycle. Therefore, in order to calculate the minimum time for a particle to reach the stable region we consider all values of $\varpi - \varpi_{\rm N}$.

Thus particles with $\varpi - \varpi_{\rm N} = 0$ and $\varpi - \varpi_{\rm N} = \pi$ have the smallest and largest free eccentricities respectively, while those with $\varpi - \varpi_{\rm N} = \pm\pi/2$ have an intermediate value. Unfortunately for particles trying to reach low eccentricities, the ones with largest free eccentricity ($\varpi - \varpi_{\rm N} = \pi$) are initially going up (i.e. e is increasing).

From numerical integrations (Figure 2.11), it appears that the maximum deviation in $\varpi - \varpi_{\rm N}$ as a function of q from Equation (2.11) is $\pm 40^\circ$ for conditions relevant to Neptune and the classical region KBOs (due to the fact that θ in Equation (2.10) is not always exactly ϖ). In setting the initial conditions for the secular evolution of scattered particles, we employ this mapping between $\varpi - \varpi_{\rm N}$ and the particle's q, including the uncertainty.

Thus the criterion for delivering the hot classicals developed in Section 2.2.2 requires that:

CONSTRAINT 2: Neptune's apoapse is large enough ($r_{a,\rm N} > 34$ AU) so that particles are immediately scattered into the stable region, or Neptune imparts an $e_{\rm forced}$ large enough relative to $e_{\rm free}$ so that it is possible for particles with semimajor axes in the range 42.5-47.5 AU to evolve to $q > 34$ AU in less than $\tau_{e,N}$.

This constraint ensures that it is possible for at least some hot objects in the region from 42.5 to 47.5 AU to be delivered into the region of longterm stability.

2.4.4 Accelerated Secular Forcing Near Resonances

When two bodies are near resonance, the secular eccentricity forcing happens on a much faster timescale. This effect has been recognized as the cause of Saturn and Jupiter's

fast precession, which Hill (1897) attributed to their period ratios being near 5:2. More recently, Minton & Malhotra (2011) recognized that the 2:1 resonance also contributes to Jupiter and Saturn's fast precession and Malhotra et al. (1989) identified the classical Uranian satellites' proximity to resonance as the cause of their deviation from their predicted ephemerides.

For the cold objects, the accelerated secular forcing near resonance quickly excites the eccentricities of these objects (as seen in Figure 2.7) , disrupting the confinement of the cold population. Near resonance, the correction term, $\epsilon\delta g_{\rm KBO}$, to $g_{\rm KBO}$ is large (Equation 2.5). Thus the secular frequency $g_{\rm KBO}$ is very high. If resonances overlay the cold classical region at early times, Neptune's eccentricity would have to damp on unrealistically short timescales to fulfill CONSTRAINT 1 (Equation 2.9). As shown in Figure 2.8, the objects near resonance remain dynamically disrupted even after Neptune's eccentricity damps. Since the cold objects in the region 42.5 AU $< a <$ 45 AU are confined to low eccentricities (Section 2.2.2), they cannot have been excited by accelerated secular forcing near resonance while Neptune's eccentricity was high.

CONSTRAINT 3: Resonances cannot overlie the region 42.5 AU $< a <$ 45 AU while Neptune's eccentricity is high. This constraint is a special case of CONSTRAINT 1 (Equation 2.9) and is quantified in Section 2.5.1.

For the hot objects, accelerated secular forcing near resonance can drive down their eccentricities once they have been scattered into the classical region. Figure 2.12, inspired by Figure 3 of Levison et al. (2008), shows two example integrations of particles beginning at large eccentricities and evolving down to smaller eccentricities. The initial conditions (panel i) match those in Levison et al. (2008), Figure 3 (their top left panel).

The snapshots in panels (ii) and (iii) are after 1.4 Myr. The integration in panel (ii) includes all four giant planets. Neptune has initial conditions $a_{\rm N} = 30$ AU and $e_{\rm N} = 0.2$, and the other planets have their modern orbital elements. The integration in panel (iii) is the same except without Uranus. The particles are undergoing secular evolution, as demonstrated by their vertical paths in (a, e) space (a does not change under secular evolution) and their eccentricity oscillations (panel iv). If Uranus is present near the 2:1 resonance with an eccentric Neptune, the evolution of the particles is chaotic (panel ii), as we will discuss in more detail in Figure 2.4.5. For objects capable of reaching low eccentricities through secular evolution (Equation 2.13), proximity to resonance significantly decreases the delivery time. Fast secular evolution near resonances can also assist in capturing objects into resonance, in addition to the previously identified mechanisms of chaotic capture (Levison et al. 2008) and smooth migration (Malhotra 1995).

2.4.5 Chaotic Sea: No Additional Constraints

When Neptune's eccentricity is large, the resonances are widened and potentially overlap in what Levison et al. (2008) describe as a "chaotic sea." Levison et al. (2008) argue that this region extends to the 2:1 resonance when Neptune's eccentricity is $e_{\rm N} > 0.15$. We have investigated the circumstances for chaos and reached several conclusions, which we will state and then justify:

1. Even when widened by Neptune's high eccentricity, the resonances between the 5:3 and 2:1 do not overlap except for particles at high eccentricities.

2. Variations in Neptune's semimajor axis on timescales of order a KBO libration

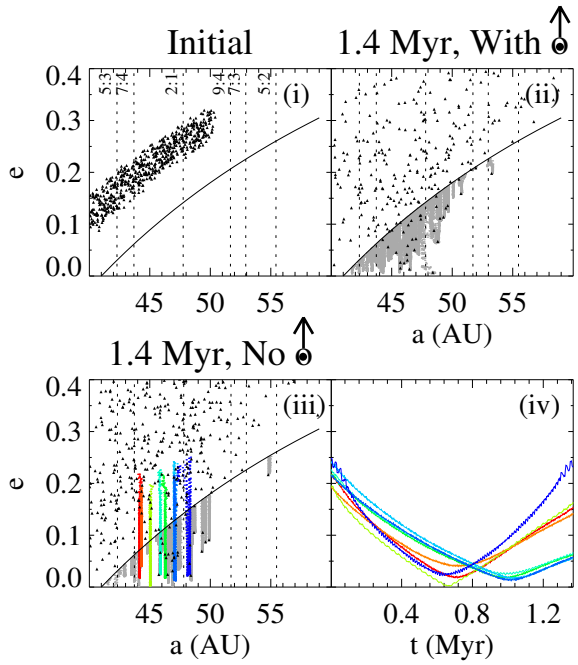

Figure 2.12.—: Objects scattered into the classical region undergo re-scattering and secular evolution. Panel (i): Initial conditions of the particles. Panel (ii): Positions of the particles (black circles) after 1.4 Myr (compare to the middle row of Levison et al. (2008), Figure 3) in an integration including all four giant planets. The gray is the cumulative region visited by the particles. Panel (iii): Same for an integration without Uranus. The colors show the paths of a few selected particles. Panel (iv): Eccentricity oscillations for particles corresponding to panel (iii).

time combine with widened resonances to cause a chaotic region.

3. The existence and extent of the chaotic region depend on the details of Neptune's interactions with Uranus.

4. The potential for chaos does not impose immediate additional constraints beyond those described in the previous subsection (Section 2.4.2). We will show that we can still model just Neptune, taking into account its potential evolution under the influence of the other giant planets.

Just Neptune: No Chaotic Sea

In addition to examining each particle individually, a qualitative way to distinguish between: 1) a chaotic sea, and 2) particles secularly evolving until they are scattered, is to plot the individual paths of a collection of particles through (a, e) space (Figure 2.13). First we consider an integration that includes only Neptune (row 1). Each starting at $e = 0$, the particles move straight upward vertically in (a, e) space until they reach the scattering line (solid black line, $e = 1 - r_{a,\mathrm{N}}/a$), rather than moving horizontally and vertically as they would in a chaotic sea.

In integrations including just Neptune, with or without apsidal precession, the eccentricity of an initially cold particle grows secularly until its orbit crosses Neptune's at $e > 1 - r_{a,\mathrm{N}}/a$. For a particle at 42.5 AU, when $a_{\mathrm{N}} = 30$ AU and $e_{\mathrm{N}} = 0.2$, this threshold is $e > 0.15$. After reaching this threshold, the particle then undergoes scattering events. Even particles near resonances evolve secularly, with the increased secular frequency defined by Equation (2.5). These particles appear separated from the coherent excitation of the other cold particles (Figure 2.7) because they undergo secular evolution so quickly

and because the secular oscillation rate depends quite steeply on semimajor axis near resonance. It appears that, for particles that begin at low eccentricities, the resonances do not overlap even when $e_{\rm N} = 0.2$. Therefore the constraints from 2.4.2 hold in the just-Neptune case, even when the planet is precessing.

Neptune, Jupiter, and Saturn: No Chaotic Sea

Adding Jupiter and Saturn in their current configurations does not generate a chaotic sea (Figure 2.13, row 2). The particles continue to move upward in (a, e) space until they reach the scattering line. The behavior is not qualitatively different from the just-Neptune case.

Neptune and Uranus: Chaotic Sea

However, when Uranus is added on its current orbit, a chaotic sea appears in the classical region, extending up to the 9:5 resonance (Figure 2.13, row 3). In the chaotic regime, individual particles exhibit chaotic jumps in their eccentricity. Some cross from one resonance to another. They move horizontally, as well as vertically, in (a, e) space.

Why does adding Uranus create the chaotic sea? Neptune and Uranus exhibit anti-correlated variations in their semimajor axes associated with proximity to their 2:1 resonance. For the configuration considered here, the periodicity of this variation is about 10^4 years, and the amplitude for Neptune is about 0.2 AU. This timescale is of order the typical libration time of a resonant KBO in the classical region. We performed additional integrations in which we modified *Mercury6* to turn off the gravitational interaction between each KBO and any planet except Neptune. The behavior was

Figure 2.13.—: Paths of particles in (a, e) space provides a qualitative probe of the existence of a chaotic sea; the solid line indicates the scattering line. The locations of the resonance centers are plotted as dashed lines; in the case in which Neptune's semimajor axis changes (i.e. in rows 3 and 4), the minimum and maximum centers are plotted. We integrated 200 massless test particles, each starting with $e = 0$, for 6 Myr under the influence of a subset of planets. Neptune, present in each integration, begins with $a_{\rm N} = 30, e_{\rm N} = 0.2$. Row 1: the top panel is an integration with just Neptune, precessing with a period of 4 Myr. The chaotic sea is not present: particles evolve secularly upward in (a, e) space until they reach the scattering line. Row 2: the behavior of the particles in this integration, which also includes Jupiter and Saturn at their current locations, is qualitatively similar: no chaotic sea. Row 3: in this integration — which includes Jupiter, Saturn, and Uranus at their current locations — the chaotic sea appears, extending up to about 45 AU, just past the 9:5 resonance. Instead of a straight upward path, the particles move from left to right as well. Row 4: the chaotic sea is also present in this integration, which includes just Neptune but with its semimajor axis oscillating with a period of 12,400 yr and amplitude 0.2 AU, as it does under the influence of Uranus in row 3. Values for a and e are in barycentric coordinates.

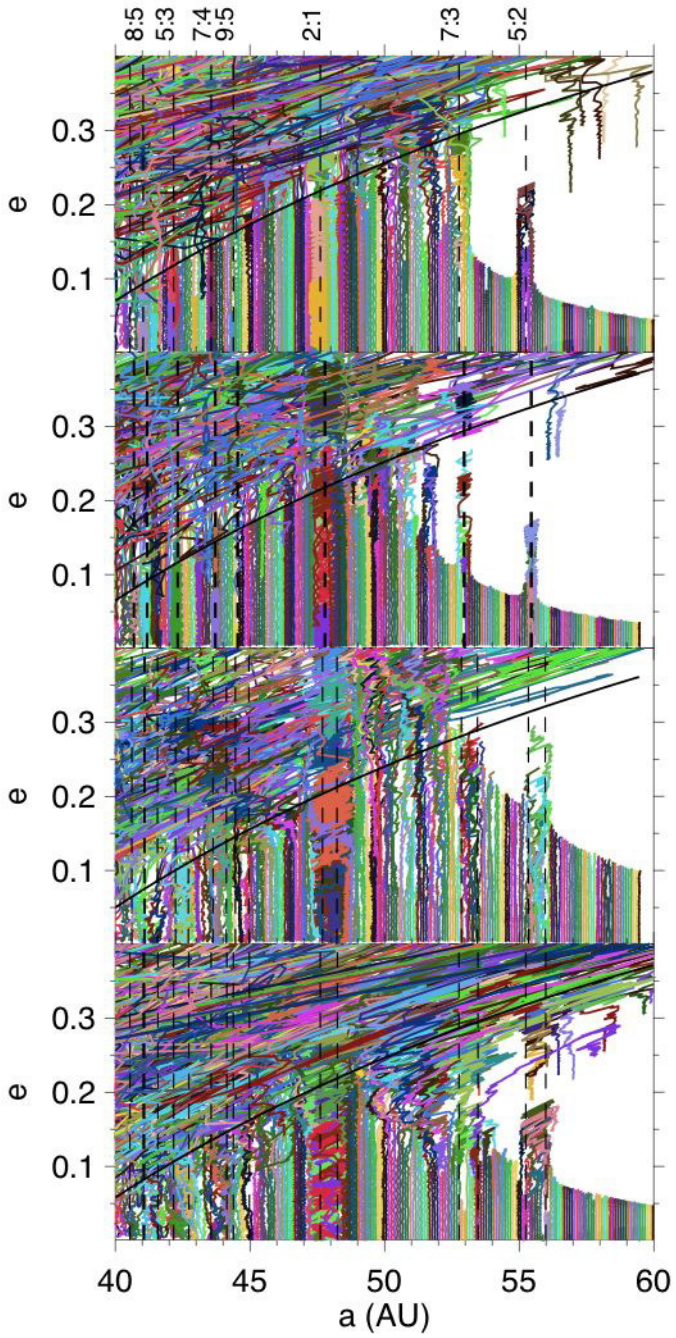

Figure 2.13.—: Continued

qualitatively the same as that shown in Figure 2.13, row 1, suggesting yet again that the other giant planets only affect the KBOs indirectly through their impact on Neptune's orbit. We performed integrations that include just Neptune, no other giant planets, with its semimajor axis oscillating with a period of 12,400 yr and amplitude 0.2 AU. The behavior was the same as in the four planet case, and the chaotic sea was present (Figure 2.13, row 4). Evidently this strong periodicity in Neptune's orbital variations, which is driven by Uranus and which moves the locations of the resonances on timescales of order a KBO libration time, causes the chaotic sea.

We note that in the case in which Uranus is excluded (Section 2.4.5, Figure 2.13, row 2), Neptune's semimajor axis is perturbed on orbital timescales (165 years) by Saturn and Jupiter, with an amplitude of 0.02 AU. This small-amplitude perturbation in $a_{\rm N}$, on a timescale two orders of magnitude shorter than the resonant timescale of KBOs, does not create a chaotic sea. The chaotic sea appears to be limited to particular dynamical histories in which Neptune and Uranus are strongly interacting through the 2:1 resonance. A thorough exploration of these histories are beyond the scope of this paper, but may provide additional constraints.

The chaotic sea appears to extend to 45 AU, just past the 9:5 resonance. This region between the 3:2 and 9:5 resonances is already forbidden to overlie today's cold classical region because the secular precession rates are extremely fast there (Section 2.4.4), so — in the case of the cold classicals — the potential for chaos adds no additional constraints. We notice that 45 AU coincides with the current edge of the cold classical region. In our interpretation, this is a coincidence. We also note that Levison et al. (2008) found that the chaotic sea extended to the 2:1. Because the chaos depends on the interactions between Uranus and Neptune, we expect that this difference may be due to different

initial conditions for Uranus. Moreover, their interpretation that the chaotic sea extends to the 2:1 is based on the fact that the cumulative region visited by the particles extends to the 2:1 (Levison et al. 2008, Figure 3). An alternative interpretation is that chaotic sea extends only to the 9:5 but that particles beyond this location are close enough to either the 9:5 or the 2:1 resonance to quickly reach low eccentricities through secular evolution, which is faster in regions near resonances.

Our constraints based on secular evolution (Section 2.4.2) are conservative. The chaotic sea cannot revive a region of parameter space which we have excluded, but it can rule out additional regions. If oscillations in Neptune's semimajor axis caused by interactions with Uranus are large enough, the chaotic sea may extend beyond the 9:5 resonance, which would impose additional constraints. For example, if the chaotic sea extended to the 2:1 resonance, the region of parameter space for Neptune with $e_{\rm N} > 0.1$ between 28-29 AU (which we will demonstrate is viable in Section 2.5.1, Figure 2.15), in which the cold classical region is sandwiched between the 9:5 and the 2:1 resonance, would no longer preserve the low eccentricities of cold classicals.

Another effect of the oscillations in Neptune's semimajor axis is to effectively widen the resonances. This effect could potentially cause more KBOs at the edge of, but not within, the chaotic sea (for example, KBOs just beyond the 2:1 resonance) to experience fast secular evolution due to proximity to orbital resonance (Section 2.4.4). Thus even more parameter space could be ruled out. We do not explicitly take this into account because the oscillations in Neptune's semimajor axis depend on the particular configuration of Neptune and Uranus.

Our constraints are a starting point for more extensive integrations, which will

require careful consideration of the interactions between Neptune and Uranus. We note that, for illustrative purposes, we have used the current semimajor axis and eccentricity of Uranus and current semimajor axis of Neptune in these explorations, but the existence and extent of the chaotic sea depends on their particular orbital configuration — especially their proximity to the 2:1 resonance — during Neptune's wild days.

2.4.6 Summary

By modeling the four dynamical processes that result from Neptune's high eccentricity — scattering (Section 2.4.1), secular forcing (Section 2.4.2-2.4.3), accelerated secular forcing near resonances (Section 2.4.4), and a chaotic sea (Section 2.4.5) — we have translated the conservative criteria imposed by the observed eccentricity distributions of the hot and cold classicals (Section 2.2.2) into the following constraints:

- Neptune's apoapse must be large enough to deliver hot objects to the longterm-stable classical region immediately ($r_{a,\mathrm{N}} > 34$ AU) or e_{forced} must be large enough (relative to e_{free}) to evolve the particle's e to < 0.3 in less than Neptune's eccentricity damping time $\tau_{e_{\mathrm{N}}}$

- The final value for the eccentricities of planetesimals in the region from $42.5\ \mathrm{AU} < a < 45\ \mathrm{AU}$ must be less than $e = 0.1$: $\sin(\min(g_{\mathrm{KBO}}\tau_{e_{\mathrm{N}}}, \pi/2))\frac{g'_{\mathrm{KBO}}}{\dot{\varpi}_{\mathrm{N}} - g_{\mathrm{KBO}}} e_{\mathrm{N}} < 0.1$ (or the forced eccentricities must be kept below 0.1 by fast precession).

- Resonances cannot overlie the region $42.5\ \mathrm{AU} < a < 45\ \mathrm{AU}$ while Neptune's eccentricity is high.

Thus Neptune's eccentricity must be high in order to deliver hot objects to the classical region and yet will disrupt the cold objects quickly unless Neptune's high eccentricity damps quickly or the planet's orbit apsidally precesses quickly. In all cases, mean motion resonances with Neptune cannot overlie the region 42.5 AU $< a <$ 45 AU while Neptune's eccentricity is large.

2.5 Results: Constraints on Neptune's Dynamical History

Applying the constraints developed in Section 2.4, we place constraints on parameters of Neptune during its dynamical history. First, we consider separately which parameters of Neptune preserve an in situ cold population (Section 2.5.1) and which allow delivery the hot classicals (Section 2.5.2). In Section 2.5.3, we combine those constraints and determine which parameters of Neptune allow the planet to simultaneously preserve the cold classicals while delivering the hot classicals. In Section 2.5.4, we interpret these parameter constraints in light of Neptune's full dynamical history. We present example integrations illustrating the constraints in Section 2.5.5.

The combined constraints will offer answers to the following questions about Neptune's dynamical history:

- Could Neptune have been scattered to a high-eccentricity orbit?
- If so, how quickly did dynamical friction damp Neptune's eccentricity?
- How far did Neptune migrate in the protoplanetary disk?

- If both damping and migration occurred, what were their relative timescales?

2.5.1 Regions of Parameter Space that Keep Cold Objects at Low Eccentricities

In Section 2.5.1, we identify which regions of parameter space fulfill CONSTRAINT 1 (Equation 2.9), preserving the cold classicals below $e < 0.1$ (as summarized in Section 2.4.6), without including the effects of orbital resonances or precession. In Section 2.5.1, we incorporate CONSTRAINT 3, the effects of orbital resonances. Finally, in Section 2.5.1, we consider the special case of fast precession.

Constraints on Neptune's Eccentricity and Damping Time

We begin by identifying regions of parameter space where, for a given semimajor axis of Neptune $a_{\rm N}$, Neptune's eccentricity $e_{\rm N}$ is small enough or its damping time $\tau_{e_{\rm N}}$ is short enough to avoid excessively exciting the cold classicals. In this subsection, we neglect the effects of resonances and assume zero precession of Neptune's orbit. in Figure 2.14 reveals the two two main regions of parameter space.

1. In the contoured region (high $e_{\rm N}$), we plot contours of maximum eccentricity damping time as a function of $(a_{\rm N}, e_{\rm N})$ that fulfill the criteria set by CONSTRAINT 1 (Equation 2.9). We calculate the maximum eccentricity damping time by considering the equation in CONSTRAINT 1 for a particle at 42.5 AU, where the secular evolution is fastest (excluding resonances). This map of $(a_{\rm N}, e_{\rm N})$ illustrates constraints on how quickly Neptune's eccentricity must damp — in order to avoid

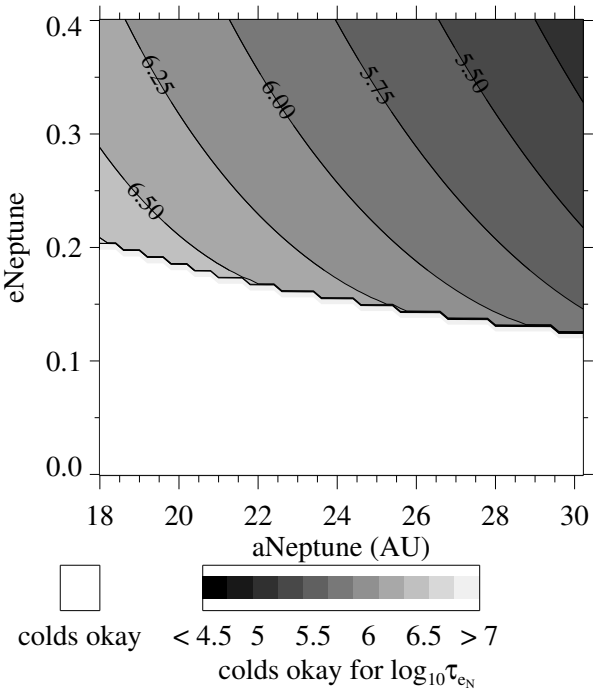

Figure 2.14.—: Constraints on Neptune's parameters to preserve the forced eccentricities of KBOs below $e_{\rm forced} = 0.1$ in the region from 42.5 to 45 AU, where $a_{\rm Neptune} = a_{\rm N}$ and $e_{\rm Neptune} = e_{\rm N}$ are spelled out for clarity. The white region indicates parameters of Neptune that keep $e_{\rm forced} < 0.1$, no matter how long the damping time. The gray regions are contours of the maximum allowed $\log_{10} \tau_{e_{\rm N}}$ (where $\tau_{e_{\rm N}}$ is in years), neglecting orbital resonances and assuming Neptune's orbit has zero precession, to fulfill CONSTRAINT 1 (Equation 2.9).

exciting the cold classicals above the level we observe — when Neptune occupies a particular region of $(a_{\rm N}, e_{\rm N})$ space.

2. In the white region, Neptune's eccentricity is small enough that the forced eccentricity of the cold classicals never exceeds $e_{\rm forced} = 0.1$ and thus the damping time can be arbitrarily long. As shown in Wolff et al. 2012, in the regime of slow damping, the particle's eccentricity damps to its free eccentricity which, for a KBO beginning with $e = 0$, is equal to $e_{\rm forced}$.

We will present several more such plots throughout the paper. Note that we plot only eccentricities up to $e_{\rm N} = 0.4$, corresponding to a $r_{p,N} = 18$ AU for $a_{\rm N} = 30$ AU. Above this value, corrections for Neptune's high eccentricity beyond what we already included would be necessary, and one also worries about the orbit of Neptune crossing the orbit of Uranus, which is currently situated at 19 AU. However, the constraints we have developed could be considered for larger $e_{\rm N}$.

The criteria in this subsection hold when the secular excitation times are not affected by proximity to resonance.

Constraints on Neptune's Dynamical History, including the Effects of Resonances

In regions near orbital resonance with Neptune, KBOs undergo significantly faster secular evolution, as demonstrated in Section 2.4.2. Here we incorporate the resonance correction terms for the secular excitation times. in Figure 2.15, analogous to Figure 2.14, we plot contours of eccentricity damping time as a function of $(a_{\rm N}, e_{\rm N})$ that fulfill the criteria set by CONSTRAINT 1 (Equation 2.9) . We calculate the damping time of

Neptune's eccentricity, τ_e for which 80% of initially cold objects in the region 42.5 AU $< a <$ 45 AU remain below $e = 0.1$. Note the key difference between the two figures: in Figure 2.14, τ_e varied smoothly through $(a_{\rm N}, e_{\rm N})$ space, but in Figure 2.15, there are dark regions where the eccentricity damping time is substantially reduced due to resonances overlying the classical region.

The damping times are unrealistically short for parameters of Neptune for which resonances overlie the cold classical region. Neptune is unlikely to have spent substantial time with high eccentricity in these $a_{\rm N}$ ranges. Ford & Chiang (2007) find that a Neptune-mass planet at 20 AU with an eccentricity of 0.3 undergoes eccentricity damping on $\tau_{e_{\rm N}} = 0.6$ Myr to 1.6 Myr (depending on whether Neptune's orbit intersects the planetesimal disk at pericenter/apocenter or at quadrature) if the surface density σ of planetesimals is 1 g/cc. This is roughly the surface density needed to grow planetesimals in the region of Neptune (Kenyon & Luu 1998). Since $\tau_{e_{\rm N}} \propto \sigma^{-1}$, it is unlikely to be less than 0.1 Myr (10^5 yr), an order of magnitude faster than the $\tau_{e_{\rm N}}$ calculated by Ford & Chiang (2007). With resonances incorporated, certain regions cannot satisfy CONSTRAINT 1 (Equation 2.9) in the zero precession case without un-physically low values of $\tau_{e_{\rm N}}$. CONSTRAINT 3 is a qualitative statement of this result. Thus by applying CONSTRAINT 1, including resonances, we recover CONSTRAINT 3.

Incorporating the resonance correction terms, we plot the maximum $\tau_{e_{\rm N}}$ as a function of the KBO's semimajor axis for several combinations of $a_{\rm N}$ and $e_{\rm N}$ (Fig 2.16). The maximum eccentricity damping time is larger for lower eccentricities, as shown for several illustrative values of $e_{\rm N}$ in the top panel. The dips where $\tau_{e_{\rm N}}$ approaches 0 correspond to regions of the Kuiper Belt near mean motion resonances where the secular excitation time is very short. The dips are wider when Neptune's eccentricity is

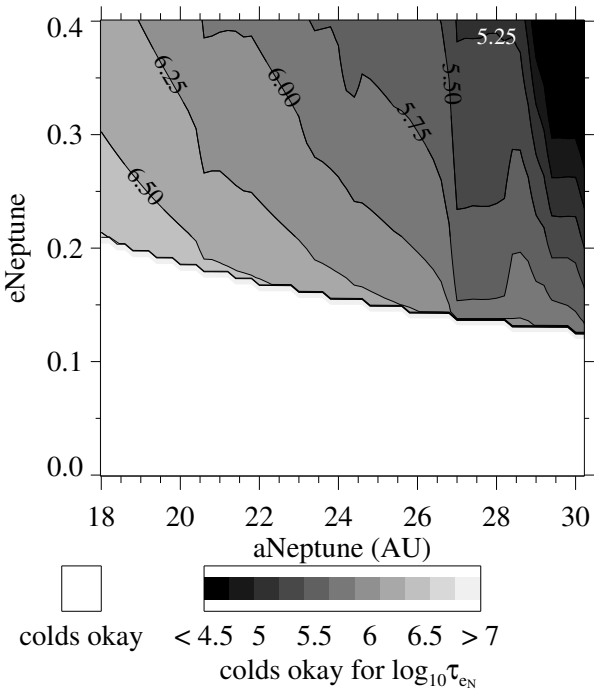

Figure 2.15.—: Contours of $\log_{10} \tau_{e_{\rm N}}$ (where $\tau_{e_{\rm N}}$ is in years), from the constraint that the small bodies be preserved below $e < 0.1$ in the region from 42.5 to 45 AU, where $a_{\rm Neptune} = a_{\rm N}$ and $e_{\rm Neptune} = e_{\rm N}$ are spelled out for clarity. The white region indicates where Neptune's eccentricity is small enough that the forced eccentricity of the cold classicals never exceeds $e = 0.1$. Note that the dark regions are forbidden to Neptune; in these regions, the resonances overlie the cold classical region, exciting the cold classicals to high eccentricities on timescales less than $10^{4.5}$ years. The constraints in this plot correspond to the situation in which at least 80% of the particles in the region from 42.5 to 45 AU are confined below $e < 0.1$.

higher. When these dips overlie the cold classical region from 42.5 AU $< a <$ 45 AU, the damping time requirement is un-physically short. In the bottom panel, we see how the resonances shift with Neptune's semimajor axis. At $a_{\rm N} = 30$ AU, several resonances overlie the cold classical region. When $a_{\rm N} = 28$ AU, the resonances are shifted interior and the cold classical region is sandwiched between two resonances, the 9:5 and the 2:1. For $a_{\rm N} = 27.5$ AU (not shown), the 2:1 resonance would be on top of the cold classicals. When $a_{\rm N} = 26$ AU, all the major resonances are interior to the cold classical region.

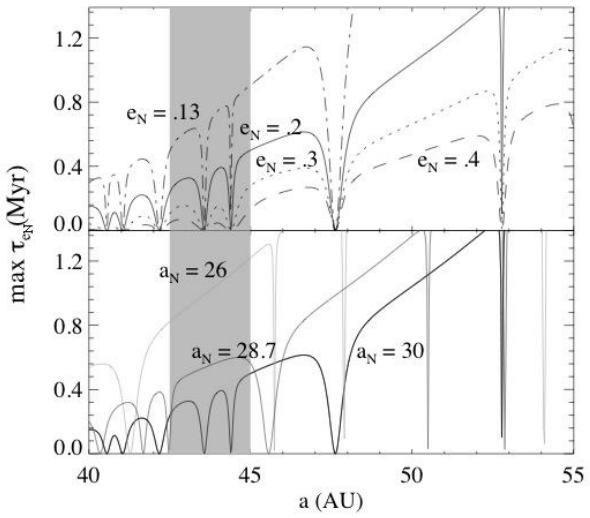

Figure 2.16.—: Maximum eccentricity damping time $\tau_{e_{\rm N}}$ (abbreviated τ_e) to preserve the cold classicals at $e < 0.1$, as a function of a KBO's semimajor axis for illustrative parameters of Neptune. The gray region is the cold classical region (42.5 AU $< a <$ 45 AU). Top panel: maximum eccentricity damping times for: $a_{\rm N} = 30$ and $e_{\rm N} = 0.4$, 0.3, 0.2, and 0.13. Bottom panel: times for $a_{\rm N} = 30, 28.7, 26$ for $e_{\rm N} = 0.2$.

Special Regimes of Fast Precession

In this subsection, we explore the special case of fast precession. Batygin et al. (2011) first suggested that if Neptune were to precess sufficiently quickly, the cold classical population would remain unexcited because fast precession lowers the forced eccentricity (Equation 2.5). In Figure 2.17, we plot the forced eccentricity as a function of the particle's semimajor axis for a range of precession rates when $a_{\rm N} = 30$ AU, $e_{\rm N} = 0.3$. Thus $\tau_{e_{\rm N}}$ in the allowed region can be arbitrarily long if the precession period is sufficiently short. A precession period of 0.9 Myr keeps $e_{\rm forced} < 0.1$ in the cold classical region for these parameters of Neptune (compare to the current g_8 precession period of 2 Myr). However, an even faster apsidal precession period for Neptune may be required if not only secular evolution but scattering and/or chaos excites the cold classicals.

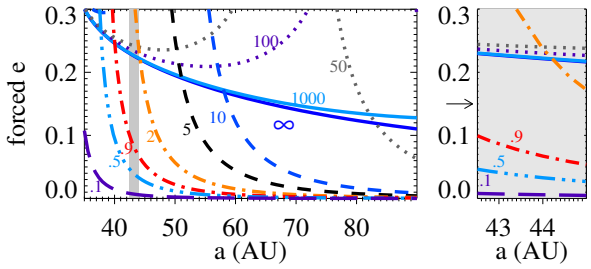

Figure 2.17.—: Forced eccentricity vs semimajor axis for a range of precession rates, for $e_{\rm N} = 0.3, a_{\rm N} = 30$. The forced eccentricity stays below 0.1 in the region 42.5 AU $< a <$ 45 AU for $2\pi/\dot{\varpi} < 0.9$ Myr

Unlike in the case of fast damping (Section 2.4.1), in the case of fast precession, scattering cold KBOs by Neptune may impose an important constraint. In the case of fast precession (and slow damping), even though the KBO's eventually evolve to $e_{\rm free}$ once Neptune's eccentricity damps, the KBO can reach a maximum value of $e_{\rm max} = 2e_{\rm forced}$ while $e_{\rm N}$ is still high. Thus the KBO is vulnerable to being scattered. For example,

for$a_{\rm N} = 30$ AU, $e_{\rm N} = 0.3$, a KBO at 42.5 AU can be scattered if it reaches $e > 0.08$. Thusthe KBO needs $e_{\rm forced} < \frac{1}{2}0.08 = 0.04$ to avoid being scattered, requiring a fast precession period of 0.4 Myr for Neptune.

Chaos (Figure 2.13) can still excite the cold classicals even if their forced eccentricity is low. In this case, resonances cannot overlie the cold classical region if Neptune's semimajor axis oscillates strongly due to interactions with Uranus (Section 2.4.5). Therefore, if the chaotic sea is present, the dark regions in Figure 2.15 are still forbidden.

Figure 2.18 demonstrates how fast precession caused by Neptune's interaction with the other planets is unable to keep the cold objects at low eccentricities in resonance regions. We performed two integrations; in each of which Neptune has $a_{\rm N} = 30.06$ and $e_{\rm N} = 0.2$, and 600 test particles begin with $e = 0$. The first integration (top panel) includes the other three giant planets, on their current orbits; they cause Neptune to undergo apsidal precession with a period of 1.2 Myr. In the second integration, Neptune is forced to precess at this rate without any other planets included (see Section 2.3.3 for details on the implementation). We plot the maximum eccentricity reached by each particle. In the top panel, chaos has dynamically disrupted particles that were preserved at low eccentricities by fast precession in the bottom panel (i.e. in the region interior to 45 AU).

Unfortunately, the most obvious configuration that causes fast precession — Neptune and Uranus near their 2:1 resonance — also causes large oscillations in Neptune's semimajor axis. The larger the oscillations in Neptune's semimajor axis, the wider the chaotic sea. Although Batygin et al. (2011) suggest that a massive planetesimal disk could contribute to fast precession, this precession rate would be

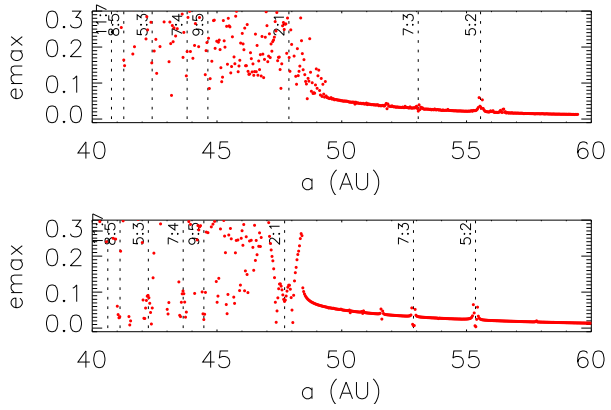

Figure 2.18.—: If fast precession is caused by Neptune's interactions with Uranus, chaos can disrupt the confinement of the cold classicals. Top panel: maximum eccentricity reached by each particle during a 1.6 Myr integration including all four giant planets. Despite fast precession, objects interior to the 2:1 resonance are excited to high eccentricities. Bottom panel: maximum eccentricity when just Neptune precesses at the same rate (period of 1.2 Myr) as in the four-planet case.

roughly $\frac{m_{\rm disk}}{m_\odot} n_{\rm N}$, where $n_{\rm N}$ is Neptune's orbital frequency. Thus a disk mass of roughly 60 Earth masses would produce a precession period of 0.9 Myr. Therefore, it is unlikely that the planetesimal disk alone could produce sufficiently fast precession. When Neptune is in the region from 28-29 AU – and the classical region is sandwiched between the 9:5 and 2:1 resonance – oscillations in Neptune's semimajor axis due to resonant interactions with Uranus could cause a chaotic sea that extends into this "sandwich" region. Thus fast precession may fail for parameters for which fast damping has the possibility of working.

We will present a contour map for Neptune's precession rate, analogous to Figure 2.15, in Section 2.5.3.

2.5.2 Constraints on Transporting the Hot Objects to the Classical Region

Now we consider which parameters of Neptune will allow the transport of the hot objects from the inner disk into the classical region. We consider the full range of (a, e) into which Neptune can scatter objects from the inner disk and the resulting secular oscillations of the objects once they reach the classical region. We calculate a *minimum* eccentricity damping time as a function of $(a_{\rm N}, e_{\rm N})$ by requiring that particles can reach the stability region defined by $q > 34$ AU (CONSTRAINT 2). The "minimum time" (contoured) is the time at which it is possible for objects in 50% of semimajor axes intervals, $\Delta a = 0.063$ AU, to reach this stable region.

Figure 2.19, a map of constraints on Neptune's parameters that deliver the hot objects, illustrates that there are three outcomes for the transport of hot objects:

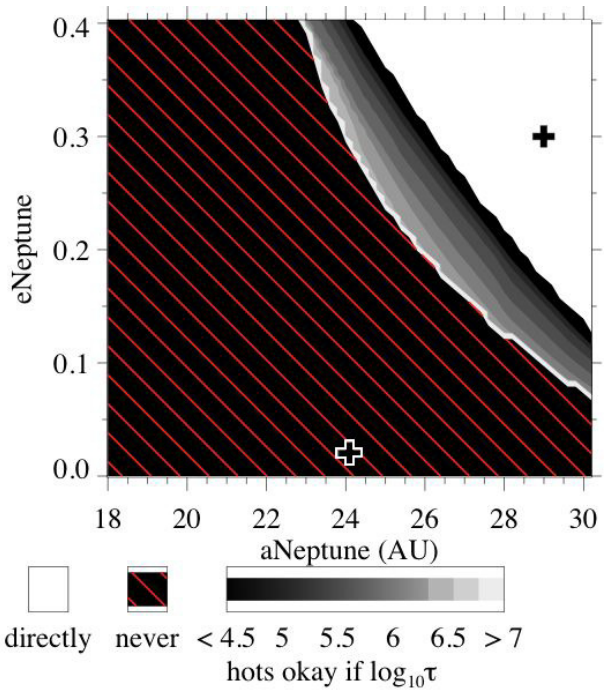

Figure 2.19.—: Parameter space of Neptune consistent with delivering the hot objects from the inner disk to the classical region, where $a_{\rm Neptune} = a_{\rm N}$ and $e_{\rm Neptune} = e_{\rm N}$ are spelled out for clarity. The white region in the upper right is where particles are immediately scattered into the stable region, $q < 34$ AU. The bottom left region (black with red stripes) is where particles can never reach the stable region because their forced eccentricity is too small relative to their free eccentricity. In the contoured region (middle), particles can secularly evolve into the stable region after being scattered if Neptune's eccentricity remains high for long enough. The contours represent the minimum time (see the text) for any scattered KBOs to evolve into the stable region. The pluses mark the conditions of the top panel and the bottom panel of Figure 2.6, which illustrates the region into which Neptune can scatter objects for two sets of illustrative parameters.

1. White region: If $r_{a,\mathrm{N}}$ is sufficiently large, some objects are scattered into the stable region. This criterion can be quantified as $r_{a,\mathrm{N}} = a_{\mathrm{N}}(1 + e_{\mathrm{N}}) > 34$ AU.

2. Black region with red stripes: If $r_{a,\mathrm{N}}$ is too small, the KBOs are scattered into a region that is not stable over 4 Gyr and their forced eccentricity is too small (relative to e_{free}) to allow them to secularly evolve down into the stable region. This second outcome can be understood from Equation (2.2). If the forced eccentricity is small, the free eccentricity will be close to the particle's initial (large) eccentricity after scattering. Thus the free and forced eccentricity vectors cannot destructively cancel to achieve a low total eccentricity.

3. Middle region with gray-scale timescale contours: For intermediate values of $r_{a,\mathrm{N}}$, the particles are scattered above the stable region (i.e. to eccentricities too large for stability) but can secularly evolve down into the stable region if Neptune's eccentricity damping timescale is long enough. The time contours refer to the minimum time (defined above) for particles to secularly evolve to the stable region. We note that, because the analytical model is only first order in the KBO's eccentricity, the timescales in the intermediate region may be in error by up to a factor of two (see Section 2.4.2 for discussion). However, the particles most relevant for this scenario — those rapidly declining in eccentricity — are matched with substantially smaller error. We also note that this regime (Outcome 3) is a narrow region of parameter space and that most parameters for Neptune fall within one of the two regimes above.

The minimum values for $(a_{\mathrm{N}}, e_{\mathrm{N}})$ in the intermediate range of $r_{a,\mathrm{N}}$ has a messy

analytical solution. The minimum eccentricity a particle can achieve is:

$$e_{\min} = (e_{\text{free}}^2 + e_{\text{forced}}^2 - 2e_{\text{free}}e_{\text{forced}})^{1/2} \tag{2.14}$$

Combining with Equation (2.11) and (2.13), for a given a_{N} one can solve for the cutoff e_{N}, below which particles cannot evolve into the long-term stable region.

Effects of Resonances and Chaos

As shown in Section 2.5.1, the secular forcing near resonance is much faster than in regions outside of resonance. Here we address the effects of resonances for the three outcomes we discussed above:

1. If $r_{a,\text{N}}$ is sufficiently large, some objects are scattered directly into the stable region. CONSTRAINT 2 ($q > 34$ AU) can always be met in this region, regardless of secular evolution, so we consider this region to always work for the hot classicals. Mean motion resonances can make this already-allowed region even better, allowing even more objects to reach the stable region.

2. If $r_{a,\text{N}}$ is small, objects are scattered to eccentricities that are too large to allow the objects to reach the stable region, even through fast secular evolution near resonance. Although fast secular evolution near resonance lets objects reach their minimum eccentricity (Equation 2.14), unfortunately all the objects have minimum eccentricities too large for long-term stability.

3. In the intermediate regime (the small contoured strip of parameter space in Figure 2.19 that does not deliver the hot classicals "directly" or "never"), objects are not scattered directly to the stable region but can reach the stable region through

secular evolution, including fast secular evolution near resonances. Without resonances, the secular evolution timescale at 47.5 AU (the largest KBO semimajor axis) sets the minimum timescale over which Neptune needs to maintain its high eccentricity. However, because of fast secular evolution near resonance, the timescale is actually set by the largest KBO semimajor axis unaffected by proximity to resonance. Thus the minimum timescale is shorter (i.e. Neptune can damp more quickly) than if we neglected the effects of resonances. In practice, the secular evolution time is not a steep function of the particle's semimajor axis (Wolff et al. 2012, Figure 4). We created another version (not shown) of Figure 2.19 without including the effects of mean motion resonances. We required objects at 47.5 AU to be able to reach $e < 0.3$, because this would ensure that objects interior of 47.5 would also reach the stable region. The results were qualitatively the same, with some slightly longer minimum times.

Now we consider whether objects that are actually *in* resonance, as opposed to being *near* resonance, could be more easily delivered to the classical region than our constraints would imply. Although we did not explicitly take into account objects actually librating in resonance, we argue that, as a by-product, our constraints include this effect. When Neptune's eccentricity is low or its semimajor axis places no strong resonances in the classical region, objects actually-in-resonance with Neptune occupy a very small portion of phase space. In the opposite situation, in which Neptune's eccentricity is high and strong resonances are present in the classical region, the parameters for Neptune are already in Outcome 1 above ("directly" scattered). For example, the initial conditions used to create the Figure 3 of Levison et al. (2008) are part of this region. The constraints we will place in this region will come only from the cold objects.

Potentially the 2:1 resonance could "sweep" the classical region, rapidly evolving transported objects into the stable region, as Neptune migrates. Moreover, resonances sweeping the region could deliver hot objects to the stable region via orbital chaos. However, neither of these scenarios would be consistent with preserving the cold classicals. Because the hot objects span the whole region from 42.5 AU $< a <$ 47.5 (Figure 3, right panel), the 2:1 resonance would have to sweep all the way through this range, exciting the cold classicals (as would the 9:5 resonance as it passes 42.5 AU). Moreover, if interactions of Neptune and Uranus created a chaotic sea (Section 2.4.5), the cold classicals would be dynamically disrupted. Therefore, the location of resonances do not provide additional constraints or possibilities for the transport of hot classicals.

Effects of Precession

Precession has several effects on delivery of the hot classicals:

1. Before the eccentricity of Neptune damps, precession allows Neptune to scatter more objects from the inner disk. If a KBO in the region near Neptune is on an eccentric orbit, the orbit of Neptune and the small body will not necessary cross, depending on the relative positions of their periapses. But if Neptune's periapse quickly precesses, Neptune's orbit may come to intersect additional KBO orbits.

2. As an object secularly evolves after being transported to the classical region, its longitude of periapse varies. Hence, precession of Neptune's orbit changes the likelihood that the object will be scattered again before it reaches the long-term survival region. We note that the likelihood of scattering depends on the *relative* precession rates of Neptune and the object.

3. If the precession rate is fast enough, it decreases the forced eccentricity. The magnitude of the particle's free eccentricity is given by Equation (2.13). For particles with quickly decreasing eccentricity ($\varpi - \varpi_{\rm N} = \pi/2$) (Equation 2.12), a reduction in $e_{\rm forced}$ decreases the amplitude of the free eccentricity. Thus fewer particles scattered above the stable region are ever able to reach it. Certain $(a_{\rm N}, e_{\rm N})$ that allowed particles to evolve into the stable region, when Neptune was not quickly precessing, will no longer work.

4. The precession of the forced eccentricity allows particles that are evolving down into the stable region via secular oscillation to reach the region more quickly. This effect changes the timescales for objects evolving to the stable region.

Thus precession can either help or hurt the transport of hot objects into the classical region, depending on the particular combination of parameters.

Scattering Efficiency of the Hot Objects

The number of hot objects that reach the stable region depends on the surface density of planetesimals in the inner disk, the eccentricity damping timescale of Neptune, and Neptune's precession rate. A faster precession rate evidently delivers more objects to the classical region, but objects are also more likely to exit the classical region via subsequent frequent scatterings, resulting in a steady state flux. Perturbations from other planets could increase the efficiency by increasing Neptune's precession rate and causing additional perturbations to the inner disk. We leave a more detailed exploration of the scattering efficiency for future work.

However we contrast the inefficient process of transporting the hot objects into

the classical region to the highly efficient preservation of the cold objects, i.e. all the cold objects stay in the classical region but few hot objects are transported there. Such a discrepancy might be possible if the inner disk is much denser than the outer disk. A dense inner disk is consistent with the short eccentricity damping timescales we are finding (Section 2.5.1), because the damping rate scales with the surface density of planetesimals (Ford & Chiang 2007). A dense inner disk and rarefied outer disk may explain why Neptune ceased its planetesimal-driven migration when it reached 30 AU (see Levison & Morbidelli 2003, for the suggestion that the planetesimal disk was truncated at 30 AU). However, the low number of cold objects poses a problem for their formation, as we will discuss in Section 2.6.

2.5.3 Combined Constraints from Both Hot and Cold Objects

We placed constraints on parameters of Neptune that preserve the confinement of cold objects to low eccentricities (Section 2.5.1) or allow the transportation of the hot objects from the inner disk into the classical region (Section 2.5.2),. These constraints are useful separately, and they confirm in situ formation as a feasible origin for the cold objects and transport from the inner disk as a feasible origin for the hot objects. In this Section, we investigate which parameters permit the combination of these two origins, producing both a cold and a hot population. This may be possible if there is overlap between the parameter space that preserves the cold classicals (Section 2.5.1) and the parameter space that transports the hot classicals (Section 2.5.2).

In Figure 2.20, we combine the constraints from the hot and cold classicals. First, as a function $(a_{\rm N}, e_{\rm N})$ we plot the contours for the maximum eccentricity damping time

necessary to keep the cold classicals at $e < 0.1$ in the region from 42.5 to 45 AU. In the white region, Neptune's eccentricity is low enough such that the final eccentricities of the cold objects will be below 0.1, no matter how long the damping timescale. Then we overplot red, diagonal stripes in the region where Neptune cannot deliver the hot classicals, neither by direct scattering nor post-scattering secular evolution. In creating this region, we took into account the sliver of parameter space (Figure 2.6, contoured region) for which Neptune cannot scatter objects directly into the region $q > 34$ AU but for which objects can evolve into the stable region through secular evolution. We compare the time required for the hot objects to reach the long-term stable region to the maximum eccentricity damping time to preserve the cold classicals. In most cases, Neptune's eccentricity must damp before any hot objects reach the long-term stable region. From all these considerations, there is only a small region of parameter space where Neptune can deliver the hot classicals (no red, diagonal stripes) while fast secular evolution near resonances does not quickly excite the cold classicals (light regions).

The allowed region in $(a_{\rm N}, e_{\rm N})$ space, in which the hot objects can be transported without disrupting the cold population, is bounded by a strip extending from (23 AU, 0.4) to (30 AU, 0.10) on the left and (27.5 AU, 0.4) to (30 AU, 0.2) on the right. To the top right of this strip, the series of resonances extending from the 5:2 to the 9:5, widened by Neptune's high eccentricity, are on top of the cold classical region. Within this bounding strip is a forbidden region near $a_{\rm N} = 27.5$ AU, at which the 2:1 resonance overlies the cold classical region.

Based on the considerations above, lower limits can be placed on Neptune's migration timescale while Neptune's eccentricity is high. During Neptune's period of high eccentricity, Neptune's migration timescale must be slow enough to keep Neptune

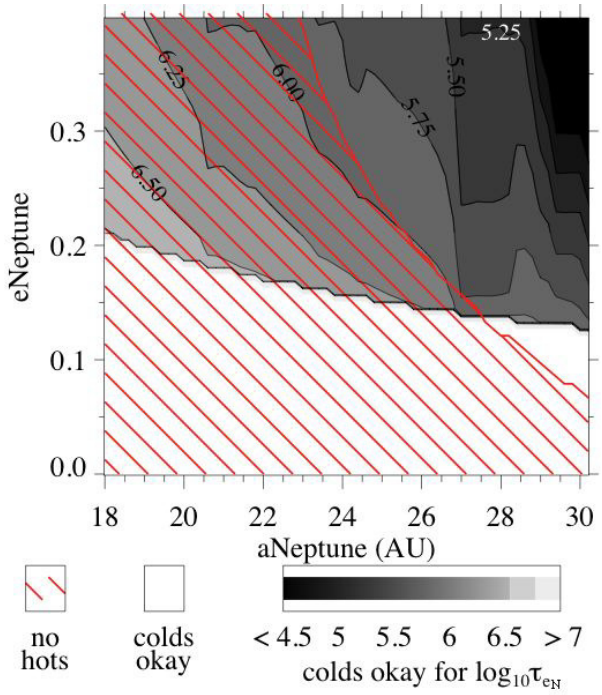

Figure 2.20.—: Combined constraints from the hot and cold classicals when the cold classicals are preserved by Neptune damping quickly, where $a_{\rm Neptune} = a_{\rm N}$ and $e_{\rm Neptune} = e_{\rm N}$ are spelled out for clarity. The contours refer to the maximum eccentricity damping time $\log_{10} \tau_{e_{\rm N}}$ (where $\tau_{e_{\rm N}}$ is in years) for Neptune in this region to avoid excessively exciting the cold classicals. In the white region, the forced eccentricity imparted by Neptune in the region from 42.5 to 45 AU is below 0.1. In the red, diagonally striped region, Neptune cannot transport the hot objects to the classical region, defined as $q > 34$ AU from 42 to 47.5 AU.

in a region that will not quickly excite the cold classicals. Neptune should not spend substantial time with high eccentricity near $a_{\rm N} = 27.5$ AU or $a_{\rm N} = 30$ AU, lest resonances disrupt the classical region. Thus Neptune is constrained to migrate no more than a few AU during Neptune's eccentricity damping time. Because of the discrete ranges of consistent semimajor axes, when resonances are accounted for, a "damp first and then migrate" scenario is consistent with preserving the cold classicals, while a "migrate first and then damp" scenario is not.

In Figure 2.21, we plot analogous constraints for the special case of fast precession. The contours represent the precession rate of Neptune necessary to keep $e_{\rm forced}$ sufficiently low (Equation 2.7). In all cases, the KBOs' forced eccentricities must be below $e_{\rm forced} < 0.1$ (CONSTRAINT 1). We impose an additional constraint to avoid the scattering of cold particles as they reach their maximum eccentricities of $e_{\rm max} = 2e_{\rm forced}$. We require $e_{\rm max}$ must be below the scattering line at the inner edge of the cold classical region: therefore $e_{\rm forced} < \frac{1}{2}(1 - q_{a,{\rm N}}/42.5)$. For large values of Neptune's apoapse $q_{a,{\rm N}}$, this constraint is stricter than $e_{\rm forced} < 0.1$. This constraint may, in fact, be too strict because if a cold classical KBO is scattered by Neptune, it is more likely to scattered out of the classical region altogether than to end up between 42.5 AU $< a <$ 45 AU at an eccentricity too large to be consistent with the observations but small enough to survive over 4 Gyr. We leave a detailed investigation into the role of scattering in the case of fast precession for future work. The red, diagonally striped region is where hot objects cannot reach the long-term stable region.

Next we consider the constraints for delivering the hot classicals. For each $(a_{\rm N}, e_{\rm N})$, we calculate whether objects can be directly scattered into the region $q > 34$ AU. If not, we assume Neptune imparts a forced eccentricity small enough to be consistent with

the constraints above for keeping the cold classicals unexcited (i.e., $e_{\rm forced} = 0.1$, or, if smaller, $e_{\rm forced} < \frac{1}{2}(1 - q_{a,\rm N}/42.5)$) and determine whether the hot object can reach the stable region through secular evolution, using Equation (2.14). If Neptune cannot directly scatter objects into the stable region and if objects secularly evolving cannot reach $q > 34$ AU in more than 50% of semimajor axis intervals, $(a_{\rm N}, e_{\rm N})$ is not consistent with delivering the hot objects. In the cases where fast precession is necessary to keep the cold classicals confined to low eccentricities, hot classicals scattered into the region have the same low forced eccentricities; therefore, they do not experience significant secular evolution down into the classical region but remain at their post-scattering eccentricities.

Finally, in blue vertical stripes, we overplot ranges of $a_{\rm N}$ for which the centers of one or more resonances of fourth order or lower lie in the cold classical region from 42.5 to 45 AU. These $a_{\rm N}$ are not necessary forbidden, but chaos can occur if Neptune's eccentricity is high and interactions with Uranus cause oscillations in $a_{\rm N}$.

Though we are applying constraints that are lenient and conservative in ruling out regions of parameter space, a substantial fraction of parameter space is ruled out. The following scenarios have not been ruled out and may work, depending on the details of the interactions between Uranus and Neptune. In both of these scenarios, resonances cannot overlie the region of 42.5 AU $< a <$ 45 AU.

- Short τ_e and large $r_{p,N}$: An eccentric Neptune transports objects into the classical region until its eccentricity damps, which occurs quickly enough that the cold classicals are not excited (Figure 2.20).

- Fast $\dot{\varpi}_{\rm N}$ and large $r_{p,N}$: An eccentric, quickly precessing Neptune transports objects into the classical region and its quick apsidal precession keeps the forced

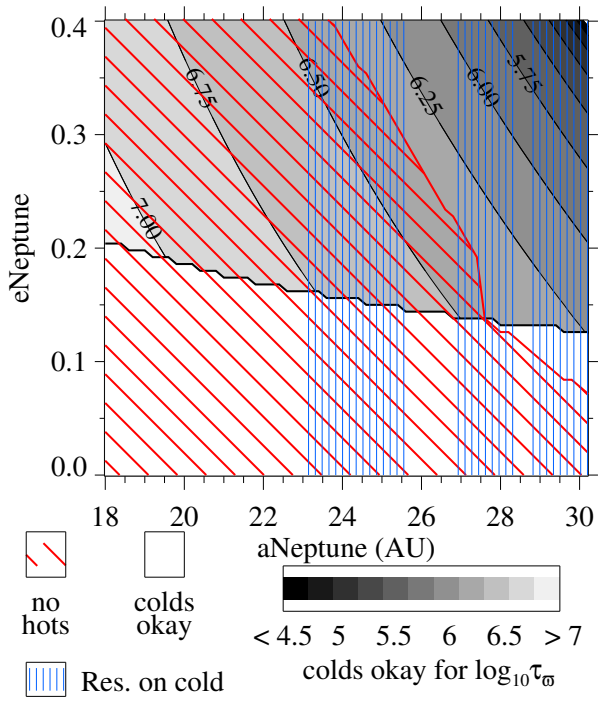

Figure 2.21.—: Combined constraints from the hot and cold classicals when the cold classicals are preserved by Neptune precessing quickly, where $a_{\rm Neptune} = a_{\rm N}$ and $e_{\rm Neptune} = e_{\rm N}$ are spelled out for clarity. The contours refer to the maximum precession period $\tau_{\varpi} = 2\pi/\dot{\varpi}_{\rm N}$ for Neptune to avoid excessively exciting the cold classicals. Neptune must precess fast enough to keep $e_{\rm forced} < 0.1$ and, when Neptune intrudes into the region, $e_{\rm forced} < \frac{1}{2}(1 - q_{a,{\rm N}}/42.5)$. In the white region, the forced eccentricity imparted by Neptune in the region from 42.5 to 45 AU is below 0.1 (and below $\frac{1}{2}(1 - q_{a,{\rm N}}/42.5)$, even when Neptune does not precess). In the red, diagonally-striped region, Neptune cannot transport the hot objects into the stable classical region, defined as $q > 34$ AU from 42.5 to 47.5 AU. The blue, vertically striped regions denote $a_{\rm N}$ for which the center of a resonance, of fourth order or lower, lies in the region from 42.5 to 45 AU. These regions are not necessary forbidden (see the text).

eccentricity of the particles low, preserving the cold classicals (Figure 2.21).

In principle, an intermediate $r_{p,N}$ could deliver hot objects to high eccentricities ($e > 0.3$) in the classical region but allow them to evolve to lower eccentricities ($e < 0.3$) before the cold objects are excited. In practice, we found the timescales are not compatible: if the eccentricity damps quickly enough to preserve the cold classicals from secular excitation, there is not time for hot objects to secularly evolve down into the Belt. However, for parameters of Neptune for which hot objects are scattered directly in the stable region, secular evolution can allow the objects to reach even lower eccentricities, especially the objects undergoing fast secular evolution near resonances.

Therefore, in practice, the consistent dynamical histories are ones in which Neptune has a large enough apoapse to transport hot objects immediately into the stable region, with its eccentricity damping quickly enough or precessing quickly enough so that the cold classicals remain at low eccentricities consistent with the observations.

2.5.4 Interpretation of Constraints in Light of Neptune's Full Dynamical History

The goal of this paper is to determine which parameters for Neptune allow the planet to deliver the hot classicals from the inner disk into the classical region without dynamically disrupting the in situ cold classicals. Throughout its dynamical history, Neptune must satisfy the constraints presented here to avoid excessively exciting the cold classicals (Section 2.5.1). At some point, Neptune must also spend time in a region of parameter space where it can also deliver the hot classicals (Section 2.5.3). We clarify that Neptune

did not necessary form at the location where hot classical delivery takes place or arrive there after undergoing a single, instantaneous scattering. Before and after hot classical delivery, Neptune can potentially spend time in any region of parameter space as long it obeys our constraints against not excessively exciting the cold classicals. The constraints developed here, which can serve as a "road map" for Neptune's path through parameter space, hold for realistic models that include multiple scatterings and have a straightforward interpretation.

In the context of the Nice model, Neptune may have undergone a series of scatterings, spending time at a variety of spots in $(a_{\rm N}, e_{\rm N})$ space. In each of these spots, Neptune must obey the constraints we place to avoid disrupting the cold classicals. Perhaps the scattering occurs quickly compared to the excitation time for the cold classicals. If not, Neptune could pre-excite the cold classicals (but only to below the observational limit) before it reaches a region where it can deliver the hot classicals. In imposing our conservative constraints, we are assuming that the cold classicals begin with $e = 0$, but if they are pre-excited, the constraints will be stricter.

Another possibility is that Neptune may spend a long time at a location where it creates a very small region of stability in the classical region, clearing out most of the cold classicals. This is a potential solution to the mass efficiency problem, which we will discuss in Section 2.6. However, as shown in Section 2.3.1, Neptune cannot deliver the hot classicals in this regime. Therefore, after this period has ended, when Neptune is delivering the hot classicals, the constraints we will place on not exciting the cold classicals will hold.

The scattering(s) Neptune undergoes are quick changes in its orbit. After its period

of high eccentricity ends – or during a temporary period of low eccentricity – Neptune can undergo slow evolution, including slow migration and slow damping of its (now small) eccentricity. The KBOs will maintain their free eccentricities throughout this slow evolution. If Neptune's eccentricity were excited very gradually, on a timescale much longer than the secular evolution times of the cold classicals, the cold classicals would keep their initial low free eccentricities. However, we expect the excitation of Neptune's eccentricity via scatterings to take place on a timescale shorter than millions of years (e.g. Thommes et al. 1999).

We have ruled out much of parameter space with the constraints that Neptune cannot excite the cold objects above $e = 0.1$ and must be able to deliver at least a few hot objects to $q > 34$ AU in the region from 42-47.5 AU. We note that we are "ruling out" parts of parameter space where Neptune cannot deliver the hot objects without disrupting the cold, not "ruling out" that the planet can ever spend time there (see above). In Figure 2.22, we look for greater consistency with the observations (Figure 2.3): a forced eccentricity less than 0.075 for the cold objects and $q_N > 36$ AU (meaning that a hot object could be scattered to an eccentricity as low as 0.24 at 47.5 AU). The parameter space shrinks where Neptune can deliver the hot objects without disrupting the cold (i.e. light gray regions with no red, diagonal constraints). Over-plotted on this figure is an example (arrows) of Neptune's path through parameter space. In this example, Neptune first undergoes multiple scatterings, spending a short enough time at each $(a_{\rm N}, e_{\rm N})$ to avoid exciting the cold classicals. Then it reaches 28 AU with an eccentricity of 0.3; here it delivers the hot classicals, as its eccentricity damps quickly enough to avoid exciting the cold classicals. Then it migrates at a low-eccentricity to its current location.

On this figure, we overplot some parameters as symbols. For the triangles and circles, we will show example integrations in Section 2.5.5. The pluses are parameters taken from the literature. The plus at $a_{\rm N} = 20, e_{\rm N} = 0.02$ marks the initial condition of Hahn & Malhotra (2005), from which Neptune undergoes migration to its current location. Neptune remains in a region that is white (never excites the cold classicals) but also red, diagonal striped (does not deliver the hot classicals); thus this simulation maintained the low eccentricities of the cold classicals but did not deliver the hot classicals. The plus at $a_{\rm N} = 28.9, e_{\rm N} = 0.3$ indicates the initial condition for Levison et al. (2008), Run B. In this part of parameter space, Neptune can deliver the hot classicals, which were indeed produced by this simulation. However, Neptune's eccentricity damped on a timescale of $\tau_e = 2$ Myr, too slow to avoid exciting an in situ cold population.

2.5.5 Example Integrations Illustrating Constraints

Example integrations illustrating the constraints we have derived are shown in Figure 2.23 and 2.24. Each integration lasts for 1.6 Myr unless otherwise noted (see Section 2.3.3 for a general description of the integrations). In addition to the 600 test particles in the region from 40-60 AU, we add 59600 test particles in the region from 18-38 AU, each with initial $e = i = 0$, representing the inner planetesimal disk from which the hot classicals are scattered.

The parameters for the four integrations shown in Figure 2.23 are plotted in the parameter space map in Figure 2.22 as circles and correspond to regions of parameter space where Neptune cannot both deliver the hot objects and keep the cold objects at low eccentricities. In row 1, Neptune is at $a_{\rm N} = 24, e_{\rm N} = 0.02$ and undergoes no

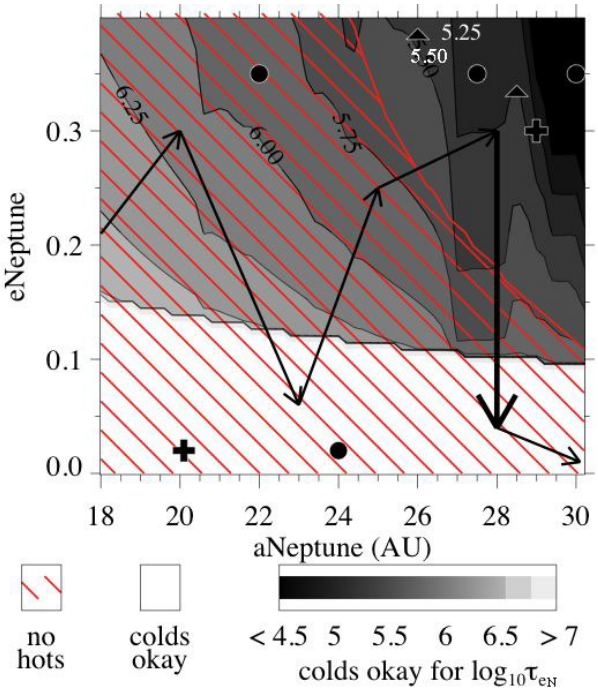

Figure 2.22.—: Combined constraints from the hot and cold classicals, where $a_{\rm Neptune} = a_{\rm N}$ and $e_{\rm Neptune} = e_{\rm N}$ are spelled out for clarity. The contours refer to the maximum eccentricity damping time $\log_{10} \tau_{e_{\rm N}}$ (where $\tau_{e_{\rm N}}$ is in years) for Neptune in this region to avoid excessively exciting the cold classicals. The constraints are stricter than in Figure 2.20. In the white region, the forced eccentricity imparted by Neptune in the region from 42.5 to 45 AU is below 0.075. In the red, diagonal striped region, Neptune cannot transport the hot objects to the classical region, defined as $q > 36$ from 42.5 to 47.5 AU. The arrows are a schematic illustration of an example of Neptune's path through parameter space as it undergoes multiple scatterings, having its eccentricity damped, or being re-scattered, on the contoured timescale to avoid excessively exciting the cold classicals. The pluses mark the initial conditions from Hahn & Malhotra (2005) (bottom) and Levison et al. (2008) (top). The circles are the parameters for example integrations shown in Figure 2.23 and the triangles for example integrations shown in Figure 2.24.

eccentricity damping. The cold classicals remain confined to low eccentricities, but the hot classicals are delivered to high eccentricities and cannot secularly evolve down to lower eccentricities. For the same reason (i.e. that Neptune's apoapse is too small), the hot classicals are also not delivered in row 2 ($a_{\rm N} = 22, e_{\rm N} = 0.35$). The damping timescale in this integration is longer (2 Myr) than half a secular evolution time, so the eccentricities of the cold objects converge to the forced eccentricities, which are above 0.1. This integration lasts 6 Myr. In the third row ($a_{\rm N} = 27.5, e_{\rm N} = 0.35, \tau_e = 0.2$ Myr) and fourth row ($a_{\rm N} = 30.06, e_{\rm N} = 0.35, \tau_e = 0.2$ Myr), the hot classicals are delivered but the cold classicals are excited by fast secular evolution near resonances.

Figure 2.23.—: Examples of four numerical integrations that violate the constraints established (Figure 2.20). The blue and red triangles are the positions of particles at the end of the integration. The red triangles are cold objects which began in the region from 40 to 50 AU with $e = 0$. The blue triangles are hot objects which began in the inner disk interior to 38 AU. The small triangles have eccentricities above the region of long-term stability (dashed line in Figure 2.3) and thus are not expected to survive over 4 Gyr. The yellow line indicates $e = 0.1$ and the shaded gray region is 42.5 AU $< a <$45 AU, where the cold classicals are observed (Figure 2.3) to be confined to low eccentricities. The parameters for Neptune in each integration are: $a_{\rm N} = 24, e_{\rm N} = 0.02$,no eccentricity damping (top row), $a_{\rm N} = 22, e_{\rm N} = 0.35, \tau_e =$2 Myr (row 2), $a_{\rm N} = 27.5, e_{\rm N} = 0.35, \tau_e = 0.2$ Myr (row 3), $a_{\rm N} = 30, e_{\rm N} = 0.35, \tau_e = 0.2$ Myr (row 4). The snapshots are at times 1.6 Myr, 6 Myr, 1.6 Myr, and 1.6 Myr.

The parameters for the two integrations shown in Figure 2.24 are plotted in the parameter space map in Figure 2.22 as triangles and correspond to a set of parameters in

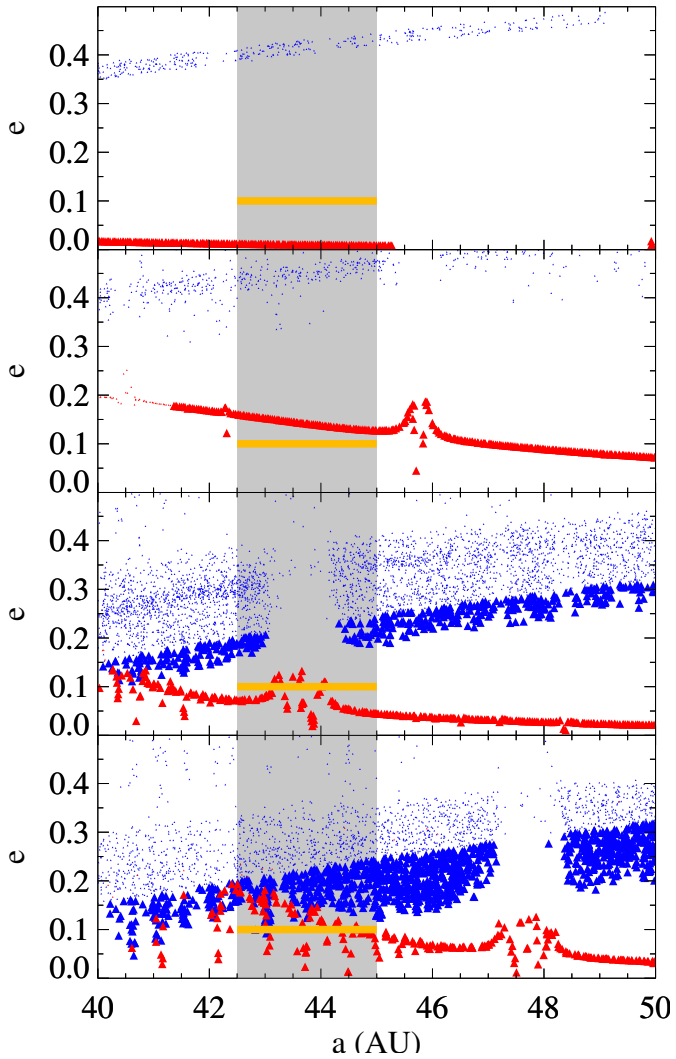

Figure 2.23.—: Continued

each of the two viable regions of parameter space. In both cases, Neptune can deliver the hot classicals. Moreover, since it is in a region of parameter space where no resonances overlie the region of 42.5 AU $< a <$ 45 AU, and since its eccentricity damps quickly enough to obey our constraints, the cold classicals remain at $e < 0.1$. In the top panel, we plot the observed objects from Figure 3 for comparison. In the middle panel, the 2:1 resonance is interior to the cold classical region. In the bottom panel, the cold classicals are sandwiched between two regions where the cold classicals are excited by fast secular evolution near resonance.

2.6 Discussion

Through an exploration of parameter space (Section 2.5) combined with conservative criteria from the observed eccentricity distributions of classical KBOs (Section 2.2.2), we reach the conclusion that most parameters for Neptune are inconsistent with both delivering a hot population from the inner disk and preserving a cold population formed in the outer disk. We have explored the full parameter space for a generalized model — in which Neptune undergoes some combination of high eccentricity, migration, and/or precession and delivers the hot objects on top of the cold — that encompasses the previous "chaotic capture" and "extensive migration" models and accounts for the different physical properties of the hot and cold classicals. We have found that the generalized model remains viable only in two restricted regions of parameter space: Neptune is scattered onto an eccentric orbit with a semimajor axis in one of two ranges, 24-27 AU (so that the 2:1 resonance is interior to 42.5 AU) or 28-29 AU (so that the region from 42.5 to 45 AU is sandwiched between the 9:5 and the 2:1 resonance).

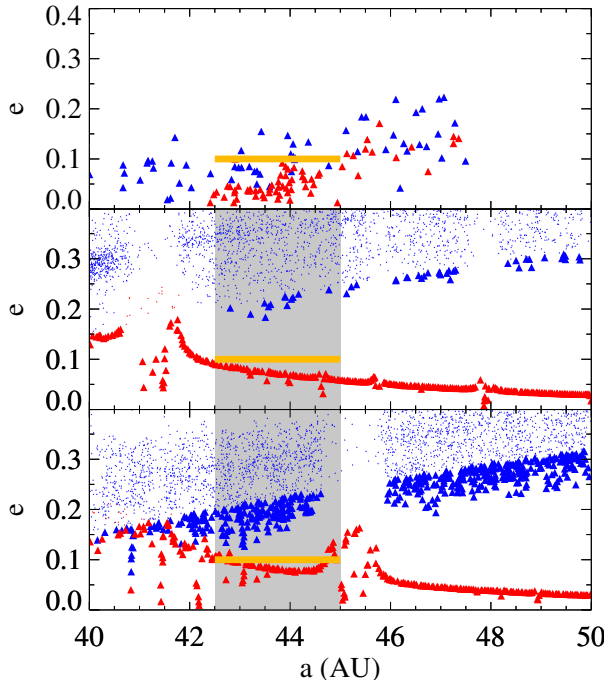

Figure 2.24.—: Examples of two integrations that obey the constraints established (Figure 2.20). The top row shows the observed objects from Figure 2.3 for comparison. In rows 2 and 3, blue and red triangle are the positions of particles at the end of the integration. The red triangles are cold objects which began in the region from 40 to 50 AU with $e = 0$. The blue triangles are hot objects which began in the inner disk interior to 38 AU. The small triangles have eccentricities above the region of long-term stability (dashed line in Figure 2.3) and thus are not expected to survive over 4 Gyr. The yellow line indicates $e = 0.1$ and the shaded gray region is 42.5 AU $< a <$45 AU, where the cold classicals are observed (Figure 2.3) to be confined to low eccentricities. The parameters for Neptune in each integration are: $a_{\rm N} = 26, e_{\rm N} = 0.38, \tau_e = 0.33$ Myr (second row) and $a_{\rm N} = 28.5, e_{\rm N} = 0.33, \tau_e = 0.25$ Myr (third row).

Although $a_{\rm N} = 30$ AU appears feasible on the parameter space plots for $e_{\rm N} \sim 0.15$, in this region "strips" are excited by overlying resonances and the hot objects are far from low enough. Neptune scatters the hot objects from the inner disk into the stable classical region where we observe them. Because Neptune's eccentricity damps or the planet's orbit precesses quickly, Neptune does this without exciting the cold objects above their observed eccentricities. Because Neptune is confined to one of these two particular regions, mean motion resonances — which would quickly excite the cold classicals through accelerated secular forcing and/or chaos — do not, while Neptune's eccentricity is high, overlie the region where we observe the cold classicals confined at low eccentricities today. Most likely, once Neptune's eccentricity damps, it migrates on a circular orbit to its current location, a migration distance of $\Delta a_{\rm N} = 1$-6 AU.

Our constraints should be interpreted in light of Neptune's full dynamical history, which may include multiple scatterings of Neptune and/or excitation/sculpting of the cold classical region before Neptune delivers the hot classicals. Throughout its path through parameter space, Neptune must obey our constraints on not excessively exciting the cold classicals. Whatever the prior early evolution, Neptune must eventually spend time in a region of parameter space where it can deliver the hot classicals while its eccentricity damps or precesses quickly enough — or Neptune is re-scattered quickly enough– to avoid exciting the cold classicals. Then it can proceed to its current location via additional scatterings or migration, maintaining an eccentricity low enough to continue to avoid exciting the cold objects.

The viable regions of parameter space are qualitatively and quantitatively different from the previous models that did not produce the observed eccentricity distributions. Compared to the Malhotra (1995); Hahn & Malhotra (2005) model, Neptune undergoes

a period of high eccentricity and migrates a shorter distance (< 6 AU, as opposed to 7-10 AU). The most significant differences from the Levison et al. (2008) model are that the cold population forms in situ, that a fast damping (0.4 Myr as opposed to 3 Myr) or precession rate is required, and that resonances, rather than being the mechanism for creating the cold population by overlapping to create a chaotic sea, cannot overlie the cold classical region while Neptune's eccentricity is high.

Another key finding is that the "chaotic sea" that may have existed in the classical region during Neptune's wild days (Levison et al. 2008) would not have been caused solely by Neptune's high eccentricity but by oscillations in Neptune's semimajor axis due to its near-resonant interactions with Uranus. Thus the exact dynamical configuration of Uranus and Neptune controls the extent and existence of a chaotic zone. Configurations of these two planets in which their interactions are especially strong might rule out the region of parameter space of 28 AU $< a_{\rm N} <$ 29 AU during Neptune's high eccentricity period, which corresponds to the classical objects being sandwiched between the 9:5 and the 2:1. A detailed investigation of the effects of the interactions between Uranus and Neptune will likely provide additional constraints on the dynamical history of the solar system. The conditions for the chaotic sea not to disrupt the cold classicals may rule out additional parameter space but will not open up more.

There is a major outstanding problem with forming the cold classicals in in situ: unsettlingly, the current surface density of cold classicals is thought to be too low for the in situ formation of the $100 - 1000$ km objects we observe (Stern & Colwell 1997; Kenyon & Luu 1998). One potential explanation is that the population has lost substantial amount of mass to collisions and subsequent removal by radiation forces. Another potential resolution is that, given that the physics of planetesimal formation is

currently poorly understood, it may be possible to form such large objects at such low surface densities (if some major physical process is missing from our understanding of planetesimal formation). Finally, as discussed in Section 2.5.4, the cold classical region may have been depleted by scattering before the period of hot classical delivery. Though none of these potential solutions have been validated, in situ formation of the cold classicals remains viable due to their distinct physical properties.

Our results are intended to provide constraints for extensive numerical integrations that include all the giant planets, have tens of thousands of test particles, and last for the age of the solar system. We established conservative criteria in order to confidently rule out regions of parameter space; the remaining regions are potentially viable but may be ruled out by additional constraints, including those that depend on the details of the configuration of giant planets. We have focused on the classical KBOs in this paper and have not tried explicitly to match the distribution of resonant KBOs. We expect resonant objects to be produced, within the parameter space we constrained, by a combination of migration (Malhotra 1995), chaotic capture (Levison et al. 2008), and, a new mechanism identified here as being important, fast secular evolution to low eccentricities of hot objects delivered near resonance followed by capture. Detailed matching of the resonant population is beyond the scope of this paper but will likely tighten our constraints.

The scattered disk population may also provide additional constraints on Neptune's dynamical history. Within the generalized model we have explored, these objects originate in the inner disk and are scattered out to beyond 48 AU, or within 48 AU at higher eccentricities and inclinations than the classical objects. If the scattered and hot objects have the same origin, any model must correctly produce their relative number. The scattered disk also contains a number of objects beyond 50 AU occupying high-order

mean motion resonances. Lykawka & Mukai (2007) found that in order to produce these resonant objects, Neptune must undergo migration after the Kuiper Belt has been pre-excited out to 50 AU. Our constraints may be consistent with this requirement, since we find that Neptune's eccentricity should damp before it migrates to its current location and that, in one allowed region, unexcited objects are sandwiched between objects excited by fast secular evolution, extending out to the edge of the 2:1 resonance. We leave detailed explorations of constraints from the population of resonant objects in the scattered disk for future work.

The fast damping of Neptune's eccentricity would imply frequent planetesimal scatterings and thus a high surface density of planetesimals in the vicinity of its orbit. Fast precession would imply strong interactions with the other giant planets (or a high surface density disk). Either way, the dynamical histories of Neptune that produce the hot and cold KBOs are very different from the peaceful disk formation that was the paradigm until 15 years ago. The most viable regions of parameter space we identified imply that Neptune underwent a period of high eccentricity but, mercifully for the spared planetesimals that are today's cold classicals, Neptune's "wild days" were over soon.

2.7 Statistical Significance of the Hot and Cold Classical Eccentricity Distributions

In addition to the qualitative assessment performed in Section 2.2, we also conduct statistical tests of the significance of the confinement of the cold population. We perform the one-dimensional Kolmogorov-Smirnov (KS) test with the null hypothesis that the

observed distribution is consistent with being drawn uniformly in a and e and then filtered by the survival map (Lykawka & Mukai 2005). We perform the test separately in two regions, $42 < a < 44$ AU and $44 < a < 45$ AU, because the survival map is different in these two regions. Note that we use 42 AU instead of 42.5 AU in order to increase the sample size. We created the survival map distribution from an initial distribution uniformly spaced in $e < 0.3$ with the "stability map filter" method described in Section 2.2.3 for three assumed survival rates: bottom of the range, middle of the range, and top of the range. We increased the number of objects in the survival map distribution until the results converged, which meant we had to use 10,000 objects post stability map filtering. First, for the observed distribution, we compared to the observed "likely cold" objects with $i < 2°$. The resulting probabilities that the observed distribution is consistent with a population shaped only by long-term stability are summarized in Table 2.1.

Table 2.1:: Probability from KS test comparing observed cold objects with $i < 2°$ from Minor Planet Center (Gladman et al. 2008; Volk & Malhotra 2011) to "survival map" distribution. "Low," "mid," and "high" refer to the bottom, middle, and top of the 10% survival range used by Lykawka & Mukai (2005). For example, for the survival range of $50 - 60\%$, low, middle, and high would indicate that $50\%, 55\%$, and 60% of particles in that (a, e) cell survive. See Section 2.2.3 and Section 2.7 for details.

	sample size	low	mid	high
42 AU $< a <$ 44 AU	38	10^{-7}	10^{-8}	10^{-8}
44 AU $< a <$ 45 AU	13	0.004	0.002	0.001

Then we created five alternative samples of cold objects. Instead of choosing objects

with $i < 2°$ for inclusion in the cold sample, we selected a uniform random number between 0 and 1 for each observed object. If the number was less than the probability that the object is cold (based on the distribution of Gulbis et al. (2010)), we included it in the sample. Using the Brown (2001) distribution of inclinations instead of the Gulbis et al. (2010) did not significantly affect our results. The resulting probabilities are summarized in Table 2.2.

Table 2.2:: Probability from KS test comparing probabilitistically-selected observed cold objects to "survival map" distribution.

	sample size	low	mid	high
42 AU $< a <$ 44 AU				
	60	10^{-8}	10^{-10}	10^{-11}
	64	10^{-10}	10^{-11}	10^{-13}
	69	10^{-10}	10^{-12}	10^{-13}
	67	10^{-9}	10^{-11}	10^{-12}
	69	10^{-11}	10^{-12}	10^{-14}
44 AU $< a <$ 45 AU	31	10^{-5}	10^{-5}	10^{-6}
	33	10^{-5}	10^{-5}	10^{-6}
	30	10^{-4}	10^{-5}	10^{-6}
	32	10^{-4}	10^{-5}	10^{-5}
	29	10^{-5}	10^{-6}	10^{-6}

Based on these results, the orbital distribution of observed objects is not consistent with our null hypothesis. The confinement of cold objects to low eccentricities is formally statistically significant.

Then we repeated the tests using only the CFEPS objects. Instead of using the survival map distribution, we took the survival map distribution and applied the CFEPS Survey Simulator. We assumed either H magnitudes uniformly distributed between 6 and 8 or randomly selected from the observed classical objects, and the results were insensitive to this choice. First we used the "likely cold" objects with $i < 2°$. The resulting probabilities are summarized in Table 2.3.

Table 2.3:: Probability from KS test comparing observed CFEPS cold objects to survey-simulated "survival map" distribution.

	sample size	low	mid	high
42 AU $< a <$ 44 AU	12	0.13	0.06	0.04
44 AU $< a <$ 45 AU	11	0.09	0.06	0.03

Then we created five alternative samples of cold objects, as described above for Table 2. The resulting probabilities are summarized in Table 2.4.

These probabilities using the small sample of CFEPS objects are low, supporting our conclusion that the cold objects are confined to low eccentricities, but this result is statistically marginal. However, we would not expect the observed objects in the full MPC sample to preferentially have lower eccentricities (indeed, in Figure 2.4, the Survey-Simulated survival map distribution follows the survival map closely), so, given our results for the full MPC sample, we expect the significance to increase as the CFEPS sample size becomes larger.

An alternative statistical test is the Anderson-Darling test, which is more sensitive to the tail of the distribution. However, even though we took measures to avoid

Table 2.4:: Probability from KS test comparing observed CFEPS cold objects to survey-simulated "survival map" distribution.

	sample size	low	mid	high
42 AU $< a <$ 44 AU				
	20	0.01	0.003	0.002
	25	0.001	0.0004	0.0002
	20	0.01	0.003	0.002
	20	0.01	0.003	0.002
	22	0.001	0.0003	0.0001
44 AU $< a <$ 45 AU	16	0.03	0.01	0.005
	20	0.009	0.004	0.001
	20	0.009	0.004	0.001
	19	0.01	0.005	0.002
	18	0.02	0.007	0.003

contamination, there are likely to be "contaminating" objects in the observed cold objects that are actually hot. Therefore we do not necessarily want to give the outliers higher weight, so we judge that the KS test is more robust for this purpose. Using the Anderson-Darling test, we obtained similar results in the cases with large sample sizes and somewhat higher probabilities in the low sample size cases.

2.7.1 Proper Elements

We now consider the free, or proper, elements of the observed KBOs, which have been computed for a subset of KBOs by Knežević & Milani (2000); Knezevic et al. (2002); Knežević & Milani (2003). The free elements precess about the forced values, which are set by the current configuration of the giant planets, and thus provide a better window to the history of the solar system than the instantaneous orbital elements. In Figure 2.25, we plot the proper element eccentricities and inclinations of observed KBOs on top of the survival maps of Lykawka & Mukai (2005), which are formulated in terms of instantaneous eccentricity and inclination. Qualitatively, we see the same features as in Figure 2.3 and Figure 2.4: the cold classicals (red squares) are confined below $e < 0.1$ in the region from 42.5 to 45 AU. Throughout the region, the hot objects (blue triangles) occupy the upper portion of the stability region.

We repeat the same statistical tests (Table 2.5 and 2.6) as above for the subset of observed KBOs that have computed proper elements. We use the proper inclinations to classify the objects with $i < 2$ as cold. For the second test, for which the sample is probabilistically-selected, we use the inclination distribution from Volk & Malhotra (2011), which considers the inclinations with respect to the invariable plane. The results

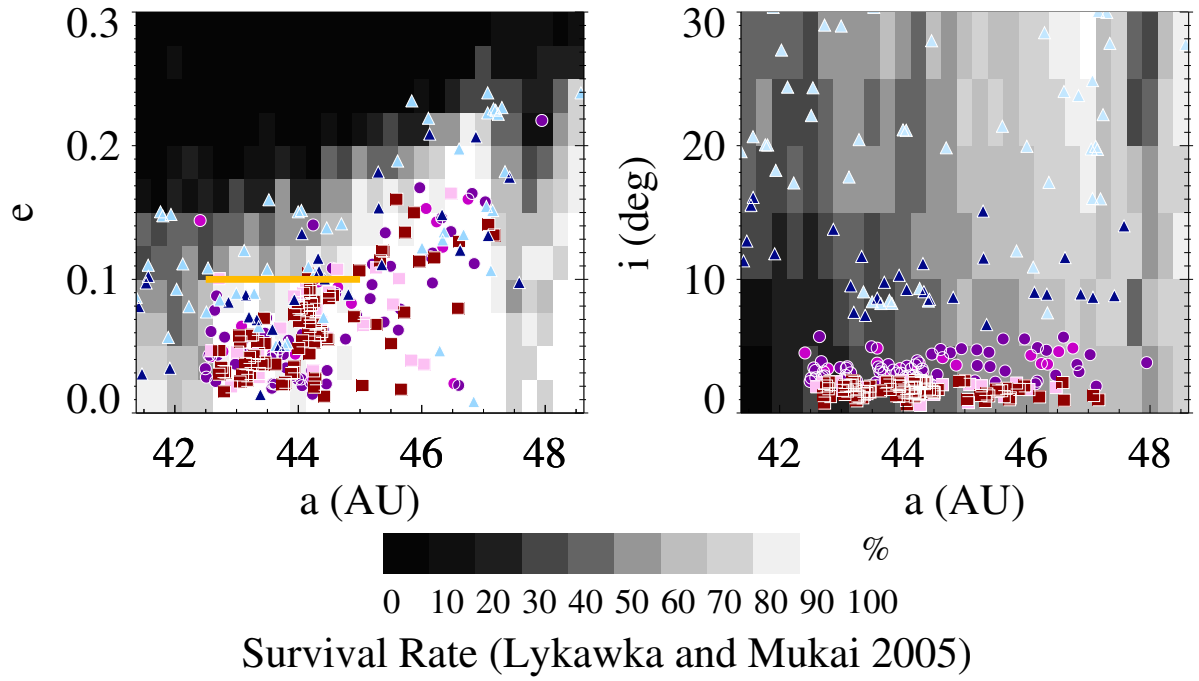

Figure 2.25.—: Plotted over the survival maps of Lykawka & Mukai (2005) are the proper eccentricity (left) and proper inclination (right) distributions of the observed classical KBOs. Note that the survival map uses instantaneous orbital elements. The red squares are objects with $i < 2°$ and are thus very likely cold classicals. The blue triangles have $i > 6°$ and are thus very likely hot classicals. The membership of any given purple circle ($2° < i < 6°$) is ambiguous. These inclinations are now defined using the proper elements. The light red squares, light blue triangles, and light purple circles, respectively, are objects for which proper elements have not been computed, and thus we plot their instantaneous elements. Classical objects are taken from the Minor Planet Center Database and classified by Gladman et al. (2008) and Volk & Malhotra (2011). Proper elements were computed by Knežević & Milani (2000); Knezevic et al. (2002); Knežević & Milani (2003). The yellow line indicates our conservative criterion for preserving the cold classicals.

are consistent with the those from the instantaneous orbital elements above. We caution that we are comparing the proper eccentricities of observed objects to a stability map of instantaneous eccentricities. This comparison should be repeated when a stability map formulated in terms of proper elements becomes available.

Table 2.5:: Probability from KS test comparing observed proper eccentricities cold objects with $i < 2^\circ$ from Minor Planet Center (Gladman et al. 2008; Volk & Malhotra 2011) to "survival map" distribution.

	sample size	low	mid	high
$42 < a < 44$ AU	35	10^{-8}	10^{-9}	10^{-9}
$44 < a < 45$ AU	25	0.002	0.0006	0.0003

2.8 Derivation of Secular Theory

In Section 2.8.1, we derive additional factors that we include in the secular theory (Section 2.4.2). In Section 2.8.2, we consider the secular forcing due to other planets besides Neptune and demonstrate that, for KBOs, the secular forcing due to all four planets reduces to the forcing by a precessing Neptune.

2.8.1 Derivation of Additional Terms

In Section 2.4.2, we relegated to this section the derivation of several additional terms in the modified secular theory. In Section 2.8.1, we derive the factors proportional to $e_{\rm N}^2$ that appear in the extra factors used in Equation (2.5) and (2.8) as coefficients to $e_{\rm N}^2$. In

Table 2.6:: Probability from KS test comparing probabilistically-selected observed cold objects (using proper elements) to "survival map" distribution.

	sample size	low	mid	high
$42 < a < 44$ AU				
	58	10^{-12}	10^{-14}	10^{-14}
	54	10^{-10}	10^{-11}	10^{-12}
	55	10^{-11}	10^{-13}	10^{-13}
	51	10^{-12}	10^{-13}	10^{-14}
	49	10^{-10}	10^{-11}	10^{-12}
$44 < a < 45$ AU	40	10^{-5}	10^{-6}	10^{-6}
	37	10^{-4}	10^{-4}	10^{-5}
	39	10^{-4}	10^{-5}	10^{-5}
	37	10^{-4}	10^{-4}	10^{-5}
	36	10^{-4}	10^{-5}	10^{-6}

Section 2.8.1, we follow Malhotra et al. (1989) to derive resonance correction terms.

High Order Eccentricity Terms

The basic secular theory includes only the lowest order eccentricity terms. However, when Neptune's eccentricity is high, terms containing $e_{\rm N}^2$ are no longer negligible. Therefore $g_{\rm KBO}$ and $\bar{e}_{\rm forced}$ must be modified. Here we define the extra terms and factors used in Equation (2.5), which come from additional terms in the disturbing function (see Chapter 7 of Murray & Dermott 2000, for a standard derivation). The disturbing function has the form, up to second order, of:

$$R = n^2 a^2 \frac{m_{\rm N}}{m_\odot}[e^2(f_2 + f_5 e_{\rm N}^2 + f_6 e^2) + \cos(\varpi - \varpi_{\rm N}) e e_{\rm N}(f_{10} + f_{11} e_{\rm N}^2 + f12 e^2) + \cos(2(\varpi - \varpi_{\rm N})) e^2 e_{\rm N}^2 f_{17}] \tag{2.15}$$

Fully incorporating all e and $e_{\rm N}$ to second order would modify the functional form of the secular theory. However, if we treat $e_{\rm N}$ as a constant, we can modify the f_2 term in the secular forcing frequency $g_{\rm KBO}$ to $f_2 + f_5 e_{\rm N}^2$ (Equation 2.5) and the f_{10} term in the forced eccentricity to $f_{10} + f_{11} e_{\rm N}^2$ (Equation 2.8). Because the form of the secular evolution Equation (2.2) is derived by differentiating R with respect to the particle's h and k, treating $e_{\rm N}$ as a constant does not modify the form of the secular evolution equations but simply adds extra correction factors. The f factors are defined in Appendix B of Murray & Dermott (2000). The success and necessity of these extra terms is illustrated in Figure 2.26.

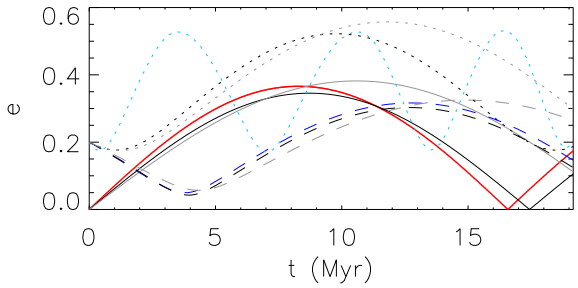

Figure 2.26.—: Evolution of several example particles illustrating the necessity of the additional e_N^2 terms. The colored lines, each representing one of three particles, are the output of a numerical integration in which Neptune has $e_N = 0.3$. Each particle has a different linestyle. The black curve is the analytical model with higher order e_N terms incorporated (Equation 2.4) while the gray curve is the analytical model that neglects these higher order terms (Equation 2.2). For each particle, the black curve matches better than the gray curve. When the particle itself has a high eccentricity, depending on its initial phase, the frequency of the analytical model matches well (purple) or is off by a factor of up to two (cyan worst case scenario). The discrepancy between the analytical model and the numerical integration output at some phases for high eccentricity particles is the result of the approximation which is only to lowest order in the particle's eccentricity. Fortunately, the most favorable case for delivering the hot classicals — an initial periapse that results in the particle's eccentricity sharply decreasing — is that for which our analytical model performs best.

Modification Near Resonances

Proximity to resonance modifies the secular frequencies. Following Malhotra et al. (1989), we define the resonance-correction terms C and ϵ in Equations (5) and (6). Malhotra et al. (1989) developed equations for a pair of moons near first order resonance. Instead of a pair of moons, we treat a massless KBO and Neptune, and we include resonances above the first order.

Resonances add additional important terms to the disturbing function, R. The factor C in Equation (6) is proportional to the coefficient of the direct part of the disturbing function, with argument $(j+x)\lambda - j\lambda_{\rm N} - x\varpi_{\rm N}$, where x is the order of the resonance. Since the coefficients of this part of the disturbing function R are proportional to $e_{\rm N}^x$, and since $\dot{h} \propto \frac{\partial R}{\partial h}$ and $\dot{k} \propto \frac{\partial R}{\partial k}$, a factor of $x e_{\rm N}^{x-1}$ comes in (Equation 6), which was not explicitly included in Malhotra et al. (1989) because they treated only the $x = 1$ case. The factor C for each order x is tabulated in Table 2.7. These coefficients were taken from the expansion of the disturbing function in Appendix B of Murray & Dermott (2000).

The factor ϵ in Equation (2.5) depends on the proximity to resonance. Extending Malhotra et al. (1989) to resonances of arbitrary order, we obtain:

$$\begin{aligned} \omega &= j n_N - (j+x) n (1 + \frac{m_{\rm N}}{m_\odot}(1 + \alpha \frac{d}{d\alpha}) b_{1/2}^{(0)}) \\ \epsilon &= \frac{3}{2}\frac{m_{\rm N}}{m_\odot}(j+x)^2 \frac{1 + \frac{m_{\rm N}}{m_\odot}\alpha(1 + \frac{7}{3}\alpha\frac{d}{d\alpha} + \frac{2}{3}\alpha^2\frac{d^2}{d\alpha^2})b_{1/2}^{(0)}}{(\omega/n)^2} \end{aligned} \tag{2.16}$$

where n_N is the mean motion of Neptune and n is the mean motion of the particle.

The $n:1$ resonances have indirect terms not explicitly included in Malhotra et al.

Table 2.7:: Coefficients for Equation (6).

x	C
1	$\frac{1}{2}(-2(j+x)-\alpha\frac{d}{d\alpha})b_{1/2}^{(j+x)}(\alpha)$
2	$\frac{1}{8}((-5(j+x)+4(j+x)^2)+(-2+4(j+x))\alpha\frac{d}{d\alpha}$ $+\alpha^2\frac{d^2}{d\alpha^2})b_{1/2}^{(j+x)}(\alpha)$
3	$\frac{1}{48}((-26(j+x)+30(j+x)^2-8(j+x)^3)+(-9+27(j+x)-12(j+x)^2)\alpha\frac{d}{d\alpha}$ $+(6-6(j+x))\alpha^2\frac{d^2}{d\alpha^2}-\alpha^3\frac{d^3}{d\alpha^3})b_{1/2}^{(j+x)}(\alpha)$
4	$\frac{1}{384}((-206(j+x)+283(j+x)^2-120(j+x)^3+16(j+x)^4)+(-64+236(j+x)$ $-168(j+x)^2+32(j+x)^3)\alpha\frac{d}{d\alpha}$ $+(48-78(j+x)+24(j+x)^2)\alpha^2\frac{d^2}{d\alpha^2}+(-12+8(j+x))\alpha^3\frac{d^3}{d\alpha^3}$ $+\alpha^4\frac{d^4}{d\alpha^4})b_{1/2}^{(j+x)}(\alpha)$

(1989) (R. Malhotra, private communication). However, the only relevant $n:1$ resonance in the region of the Kuiper Belt we are studying is the $2:1$ resonance and its indirect terms result in expressions that, when incorporated above, are directly proportional to the mass of the KBO and thus assumed to be negligible.

2.8.2 Effects of Other Planets

In the case of multiple planets, the forced eccentricity of a small body on an external orbit is given by (Murray & Dermott 2000):

$$h_0 = -\sum_{i=1}^{N} \frac{\nu_i}{A - g_i} \sin(g_i t + \beta_i)$$
$$k_0 = -\sum_{i=1}^{N} \frac{\nu_i}{A - g_i} \cos(g_i t + \beta_i) \tag{2.17}$$

where

$$\nu_i = \sum_{j=1}^{N} A_j e_{ji}$$
$$A_j = -n \frac{1}{4} \frac{m_j}{m_\odot} \alpha_j b_{3/2}^{(2)}(\alpha_j)$$
$$A = \sum_{j=1}^{N} n \frac{1}{4} \frac{m_j}{m_c} \alpha_j b_{3/2}^{(1)}(\alpha_j) \tag{2.18}$$

where the particle's forced eccentricity $e_{\rm forced} = \sqrt{h_0^2 + k_0^2}$ and g_i and e_{ji} are the eigenfrequencies and eigenvector components of the planetary system. We compare Equation (2.17) with Equation (7). For KBOs in the classical region, Neptune's orbits dominates A, the precession rate of the particle's free eccentricity. The precession rate of a particle's free eccentricity due to Neptune alone agrees with the four-planet case to within 30%. Thus $A \approx g_{\rm KBO}$. Neptune dominates the ν_i term, and thus the four-planet secular theory reduces to the single-planet secular theory with an extra $g_i = \dot{\varpi}_{\rm N}$ term for Neptune's precession. Therefore the four planet Equation (2.17) reduces to Equation (7). The quantity ν_i corresponds to $g'_{\rm KBO} e_{\rm N}(t)$, g_i corresponds to $\dot{\varpi}_{\rm N}$, and A corresponds to $g_{\rm KBO}$. The extra sin term in Equation (7) is an empirical factor to account for eccentricity damping and is discussed in detail in the main text. This conclusion is consistent with the result of Chiang & Choi (2008) that the current forced eccentricities of the KBOs are largely determined by Neptune's orbit.

Chapter 3

On the Misalignment of the Directly Imaged Planet β Pictoris b with the System's Warped Inner Disk

R. I. Dawson, R. A. Murray-Clay, & D. C. Fabrycky *The Astronomical Journal*, Vol. 743, id. L17, 2011

Abstract

The vertical warp in the debris disk β Pictoris – an inclined inner disk extending into a flat outer disk – has long been interpreted as the signpost of a planet on an inclined orbit. Direct images spanning 2004-2010 have revealed β Pictoris b, a planet with a mass and orbital distance consistent with this picture. However, it was recently reported that the orbit of planet b is aligned with the flat outer disk, not the inclined inner disk, and

thus lacks the inclination to warp the disk. We explore three scenarios for reconciling the apparent misalignment of the directly imaged planet β Pictoris b with the warped inner disk of β Pictoris: observational uncertainty, an additional planet, and damping of planet b's inclination. We find that, at the extremes of the uncertainties, the orbit of β Pictoris b has the inclination necessary to produce the observed warp. We also find that if planet b were aligned with the flat outer disk, it would prevent another planet from creating a warp with the observed properties; therefore planet b itself must be responsible for the warp. Finally, planet b's inclination could have been damped by dynamical friction and still produce the observed disk morphology, but the feasibility of damping depends on disk properties and the presence of other planets. More precise observations of the orbit of planet b and the position angle of the outer disk will allow us to distinguish between the first and third scenario.

3.1 Introduction

The β Pictoris debris disk is a rich system, with observational features resulting from the interplay of gravity, radiation pressure, collisions, infalling comets, sculpting by planets, and the physical properties of the gas, dust, and rocks that comprise the disk. In the quarter-century following its discovery (Smith & Terrile 1984), β Pictoris has epitomized young planetary systems, amenable to state-of-the-art observations and to modeling of planetary formation processes. For a review, see Vidal-Madjar et al. (1998).

A striking vertical warp in the β Pictoris disk, at approximately 85 AU from the star, appears in optical and near-infrared images (e.g. Heap et al. 2000; Golimowski et al. 2006). Mouillet et al. (1997) and Augereau et al. (2001) demonstrated that a perturbing

planet on an inclined orbit could produce the warp, whose distance constrains the posited planet's mass and position. A decade later, Lagrange et al. (2009, 2010) discovered, via direct imaging, β Pictoris b, a planet consistent with producing the warp, if correctly inclined relative to the disk.

However, Currie et al. (2011) – stitching together recent (Quanz et al. 2010; Bonnefoy et al. 2011) data and newly reduced data (collected by Lagrange et al. 2010) – recently measured the planet's astrometric orbit and reported it to be, surprisingly, misaligned with the warp. They urged revisiting whether planet b could produce the warp and suggested an undiscovered additional planet as an alternative culprit.

Here we explore three scenarios to reconcile the apparent misalignment of planet b with β Pictoris's warped inner disk. In Section 3.2, we model an inclined planet sculpting a planetesimal disk. Then (Section 3.3), we consider the first scenario: within the extremes of the observational uncertainties, β Pictoris b has the inclination to produce the warp. In Section 3.4, we evaluate the possibility that another planet created the warp; however, we find that the presence of planet b on a flat orbit prevents another object from creating the observed warp. In Section 3.5, we explore the third possibility: planet b had a higher inclination in the past, created the warp, and then its inclination damped. Thus we suggest (Section 3.6) that planet b produced the warp, whether or not its orbit is currently aligned with the warped inner disk.

3.2 Model of a Debris Disk Sculpted by an Inclined Planet

Figure 3.1.—: Snapshot (8 Myr) from an N-body simulation and an analytical model of an inclined planet sculpting an initially flat planetesimal disk. Top: Planetesimal inclinations vs. semi-major axis. The red lines indicate the planet's inclination i_p and $2i_p$. The orange, blue, and black line is composed of triangles, each marking the inclination of a corresponding planetesimal in the middle panel. The planetesimals are color-coded: orange triangles have completed an oscillation, blue are just reaching their maximum inclination, and black are still at low inclinations. We use our analytical model (eqn. 3.1) to calculate the dashed gray line. Middle: Projected positions of the planetesimals. Lower: Same as middle using the analytical model; it reproduces the N-body simulation well. Compare these two lower panels to images of the disk, such as those shown in Heap et al. (2000), Fig. 8 and Golimowski et al. (2006), Fig. 5.

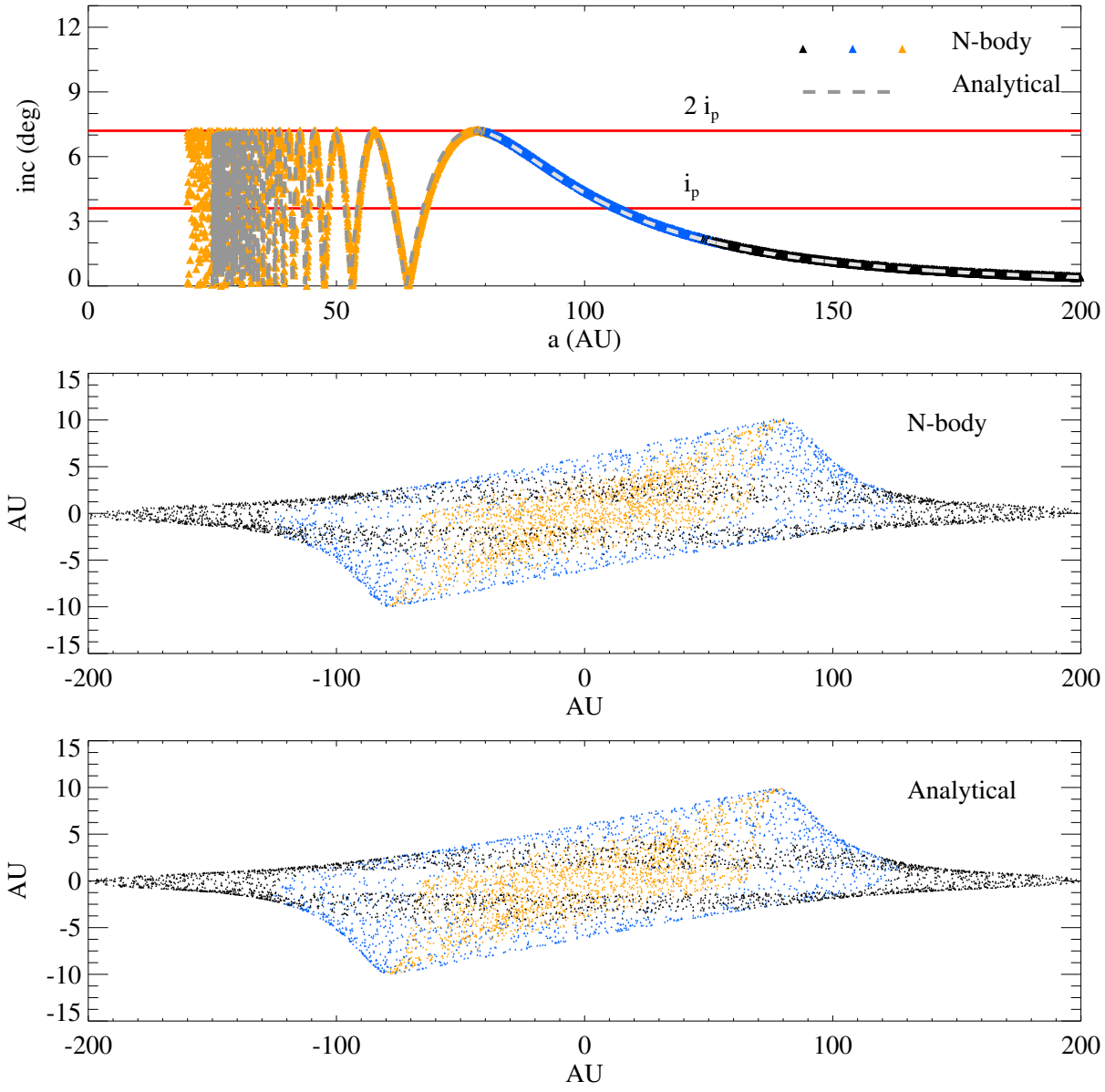

Figure 3.1.—: Continued

The warping of the β Pictoris debris disk by a planet on an inclined orbit results from the secular evolution of the disk's component planetesimals. The planet secularly forces the disk, causing the planetesimals to oscillate about the planet's inclined plane. Planetesimals in an initially flat disk (inclination $i = 0$ relative to the plane of the flat outer disk) reach a maximum i of twice the planet's inclination i_p. The oscillation frequency decreases with the planetesimal's semi-major axis: in a young system like β Pictoris, the inner planetesimal disk – which secularly evolves quickly — is centered on the planet's inclined plane, while the outer disk – which secularly evolves slowly – is still near its initial low inclination. Thus secular evolution produces an inclined inner disk aligned with the planet's inclined plane, a flat outer disk, and a warped feature, extending to $2i_p$, at the distance, $a_{\rm warp}$, where planetesimals are just reaching their maximum inclination. This distance constrains the disk's evolution time and the perturbing planet's mass and location. In Fig. 3.1, we plot the final inclinations and projected positions from an N-body simulation of an initially flat planetesimal disk sculpted by a planet on an inclined orbit. Each of 6000 test-particle planetesimals begins with $e = i = 0$, a semi-major axis a between 20-200 AU, and a random periapse, longitude of ascending node, and mean anomaly. The planet has the observed mass ($m_p = 9 m_{\rm Jupiter}$) and semi-major axis ($a_p = 9.5$ AU) of β Pictoris b, and $i_p = 3.6°$; the star has mass $m_* = 1.75 m_{\rm sun}$. We used the *Mercury* 6.2 (Chambers 1999) hybrid integrator with a step size of 200 days over a timespan of 8 Myr. The system's age, 12^{+8}_{-4} Myr (Zuckerman et al. 2001), minus the planet formation time, $< 3 - 5$ Myr (Hernández et al. 2007; Currie et al. 2009), imply that warp production likely began 3-20 Myr ago. We choose the viewing orientation to make both the outer disk and the planet's orbit edge-on, as observed.

3.2.1 Planetesimal inclination evolution

Secular evolution times set the warp's position: at the pointy part, planetesimals, in the midst of their first cycle about the planet's inclined plane, are just reaching their maximum $2i_p$ (blue triangles, Fig. 3.1). The components p and q of the planetesimal's instantaneous inclination, $i = \sqrt{p^2 + q^2}$, evolve as:

$$\begin{aligned} p &= i_{\text{free}} \sin(ft + \gamma) + p_{\text{forced}} \\ q &= i_{\text{free}} \cos(ft + \gamma) + q_{\text{forced}} \\ f &= -\frac{n}{4}\frac{m_p}{m_*}\alpha\bar{\alpha}b^{(1)}_{3/2}(\alpha) \end{aligned} \tag{3.1}$$

where

$$\alpha = \begin{cases} a/a_p, & a < a_p; \\ a_p/a, & a > a_p; \end{cases}$$
$$\bar{\alpha} = \begin{cases} a/a_p, & a < a_p; \\ 1, & a > a_p. \end{cases} \tag{3.2}$$

The function b is a standard Laplace coefficient (Murray & Dermott 2000), and $n = (Gm_*/a^3)^{1/2}$ is the planetesimal's mean motion. When a single inclined planet forces an initially cold disk, the forced plane, with inclination $i_{\text{forced}} = \sqrt{p^2_{\text{forced}} + q^2_{\text{forced}}}$, is the inclined plane of the perturbing planet, i_p, relative to the flat outer disk. Thus a planetesimal's inclination, initially at $i = 0$, oscillates as:

$$i = 2i_p|\sin(ft/2)| \tag{3.3}$$

3.2.2 Constraining the Sculpting Planet's Orbit

The disk reaches its maximal vertical extent, $z_{\rm warp}$, at $a_{\rm warp}$. From eqn. 3.3, the warp's secular oscillation frequency f is related to the disk's evolution time τ by $f\tau = \pi$, constraining the mass and semi-major axis of the perturbing planet:

$$\pi/\tau = \frac{n_{\rm warp}}{4}\frac{m_p}{m_*}\alpha_{\rm warp}\bar{\alpha}_{\rm warp}b^{(1)}_{3/2}(\alpha_{\rm warp}) \tag{3.4}$$

and the perturbing planet's inclination is separately constrained by:

$$\tan(2i_p) = \frac{z_{\rm warp}}{a_{\rm warp}} \tag{3.5}$$

Our eqn. 3.4 is equivalent to the warp condition in Mouillet et al. (1997), Section 5 and Augereau et al. (2001), Section 1.2, derived from tidal theory. Additionally, Mouillet et al. (1997) modeled the disk's evolution using hydrodynamic simulations. However, using the secular equations above, we can not only constrain the parameters of a perturbing planet but produce the time-evolving disk morphology (e.g. Fig. 3.1, panel 3), facilitating comparisons to observations without simulations.

The warp-revealing visual observations measure the light scattered by *dust*, likely produced by recent collisions of the planetesimal parent bodies. These dust grains are subject to radiative pressure, which induces larger, eccentric orbits relative to their parent bodies. Thus radiation pressure effectively increases the distance of the warp by a factor of $\sim 1/(1-2\beta)$, where β is the ratio of the radiation forces to gravitational forces (see Chiang et al. 2009). For example, if $\beta = 0.2$, a warped disk of parent bodies extending only to 50 AU creates an observed warp at 85 AU. In Fig. 3.2, we plot curves of a_p vs. m_p that produce a warp at 85 AU (eqn. 3.4) for $\beta = 0$ and $\beta = 0.2$. Dust-generating collisions affect the parent bodies' orbits by damping $i_{\rm free}$. However, the

largest parent bodies in the collisional cascade, which recently experienced their first collision and have not had $i_{\rm free}$ significantly damped, set the maximum vertical extent of the warp.

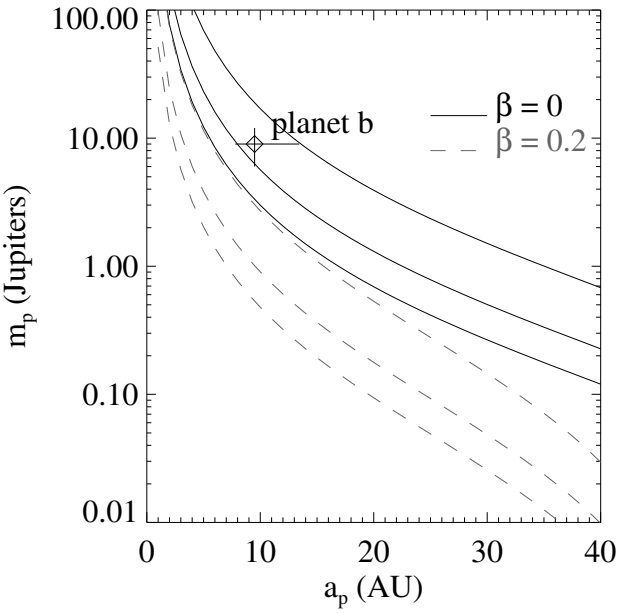

Figure 3.2.—: Three curves (solid) of (a_p, m_p) that produce a warp at 85 AU for (top to bottom) τ = 3, 9, 17 Myr. A planet with properties above the lowest curves significantly impacts the warp evolution over the system lifetime. Equivalent curves for observed dust grains with radiative forcing parameter $\beta = 0.2$ are plotted in dashed grey. Increasing β decreases the warp distance in the planetesimal parent population, effectively shortening the warp propagation time.

3.3 Planet b Possibly Aligned with Inner Disk

The framework in Section 3.2 allows comparison of the model to the observed warp morphology. In creating Fig. 3.1, we used the observed m_p and a_p. We selected $i_p = 3.6°$, corresponding (eqn. 3.5) to a maximum vertical extent of $z_{\rm warp} = 11$ AU at $a_{\rm warp} = 85$ AU (Heap et al. 2000 Fig. 8; Golimowski et al. 2006 Fig. 5). We plot our simulations from the perspective such that both the outer disk and the planet's orbit are perfectly edge-on, as observed, which constrains the orientation of the warp. We find that the distribution of planetesimals matches the disk shape well.

Currie et al. (2011) reported that planet b is aligned with the flat outer disk and misaligned with the inclined inner disk. Indeed, the difference between two separately measured angles, (a) the intersection of the planets orbit with the sky plane, $31.32°[30.56, 32.12]$ (Currie et al. 2011), and (b) the sky position of the outer disk, 30-31° (Kalas & Jewitt 1995) or $29.5° \pm 0.5$ (Boccaletti et al. 2009), is consistent with alignment. However, at $\sim$ 2-σ, β Pictoris b may be misaligned with the flat outer disk by $i_p = 3.6°$, and aligned with the middle of the inclined inner disk, as in our model (Fig. 3.1).

3.4 Planet b Prevents Another Planet from Creating the Warp

If, contrary to the scenario of Section 3.3, more precise measurements confirm that planet b's orbit is aligned with the flat outer disk, an undiscovered planet c would be an obvious suspect. However, the presence of planet b severely restricts the parameter

space for an additional, warp-making planet. The following loose, generous constraints on planet c must be simultaneously satisfied:

1. To have escaped radial velocity detection by Galland et al. (2006), planet c must satisfy

$$\frac{m_c}{m_{\rm Jupiter}} < 9\sqrt{a_c/1{\rm AU}}$$

.

2. Planets b and c must be sufficiently separated for stability, obeying

$$\frac{\Delta a}{a} > 2.4(\mu_b + \mu_c)^{1/3}$$

where μ is the planet-to-star mass-ratio (Gladman 1993). Even if planets b and c underwent scattering, it is unlikely that their unstable configuration would last long enough to create the warp.

3. Planet c must create the observed disk morphology – an inclined inner disk from 40-90 AU – without exciting planet b's inclination. We generously allow any parameters for planet c that produce a forced inclination $i_{\rm forced} < 2^\circ$ for planet b and $3^\circ < i_{\rm forced} < 8^\circ$ for the inner disk. We calculate the forced inclinations using multi-planet secular theory (Murray & Dermott 2000, Section 7.4).

4. Given the system age of 8-20 Myr (Zuckerman et al. 2001), planet c must have a mass and semi-major axis small enough so that the evolution time of the warp at 85 AU is slower than 1 Myr (but faster than 20 Myr). If the observed dust grains have $\beta > 0$ (Section 3.2.2), the evolution time must satisfy this constraint at 85 AU $(1 - 2\beta)$, a more restrictive lower limit. The lower limit is generous, allowing for the possibility that planet c became inclined very recently.

5. A secular resonance should not disrupt the flat outer disk (90-200 AU); we calculate the locations of secular resonances using multi-planet secular theory.

We explore the parameter space of planet c's semi-major axis, mass, and inclination. For each combination, we evaluate the equations for the five criteria above in a two-planet system containing planets c, and b, with its nominal $m_b = 9 m_{\rm Jupiter}$, $a_b = 9.5$ AU, and $i_b = 0$. In Fig. 3.3, we shade the (a_c, m_c) regions for which no possible inclination of planet c can satisfy the constraints. Other choices for m_b and a_b, within observational errors, yield qualitatively similar results. Constraint 3 is most restrictive: the planet must have high enough mass to excite the warp, but low enough mass not to excite i_b; it must be far enough out that the warp can extend to 85 AU, but close enough to incline the inner disk at 40 AU. Constraint 4 considers the time dependence: the warp must reach 85 AU in the system age. The secular oscillation frequency at 85 AU depends on the mass and semi-major axis of both planets b and c – but not on their inclinations. Planet b, even on a non-inclined orbit, makes a large contribution to this frequency, leaving little room for a contribution from planet c.

Therefore we can rule out that an undiscovered planet c causes the warp, because it cannot do so in the presence of planet b. Additional planets may be present in the system, but are unlikely to be predominantly responsible for the warp.

3.5 Planet b's Inclination May Have Damped

We demonstrated that planet b's current orbit is consistent with producing the warp only at the extremes of the uncertainties (Section 3.3) and that planet b's presence

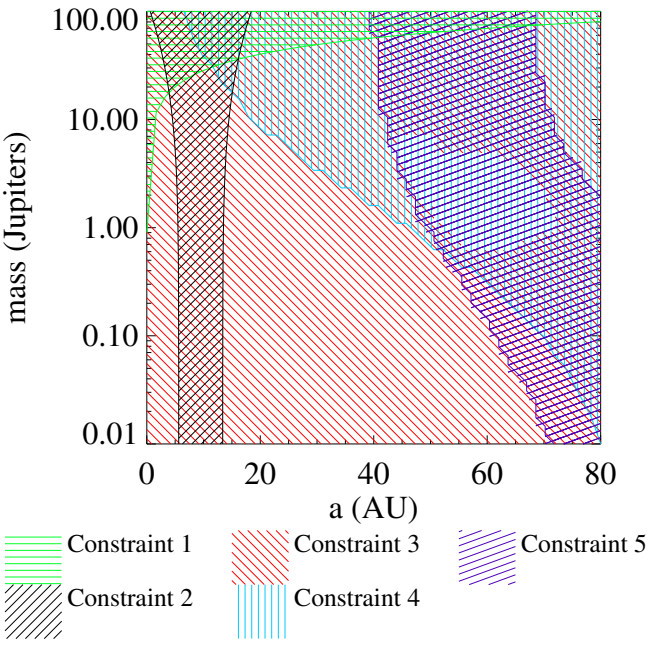

Figure 3.3.—: Constraints on a_c and m_c. The region shaded horizontal-striped green violates Constraint 1 (lack of RV detection), upward-slanted black violates Constraint 2 (stability), downward-slanted red violates Constraint 3 (produces disk morphology without exciting planet b), vertical-striped blue violates Constraint 4 (timescale consistency), and shallow-slant purple violates Constraint 5 (secular resonances in the outer disk). See text for details.

inhibits another planet from creating the warp (Section 3.4). If follow-up observations confirm the nominal orbit of β Pictoris b and position angle of the flat outer disk, we are left uncomfortably with a planet misaligned with the warp it produced. However, we need not regard that conclusion with such discomfort. A sculpted planetesimal disk can record the history of a planet's orbit, revealing a dynamical past we would never guess from the planet's current orbit. For example, Neptune has a nearly circular orbit today but may have have sculpted the Kuiper Belt, our solar system's remnant planetesimal disk, during a period of high eccentricity, which was subsequently damped by dynamical friction (see Levison et al. 2008, and references therein). Embedded in a planetesimal disk, β Pictoris b would experience damping of its inclination, though the extent and timescale depend on disk properties.

3.5.1 Consistency with Disk Morphology

First we demonstrate that the disk morphology can be consistent with the damping of β Pictoris b's orbital inclination. The planetesimals, with initial forced inclinations of i_p, begin to oscillate about the forced plane and, as we showed in Dawson & Murray-Clay (2012), effectively freeze at the inclination values they reach after one damping timescale of the planet's inclination. Therefore, the warp freezes at the distance it reaches when the planet's inclination damps. Because their forced inclinations are damped, the planetesimals have a maximum $i = i_p$ instead of $2i_p$, requiring β Pictoris b to have an initial $i_p \sim 7°$. Fig. 3.4, left panel shows an example: the disk morphology still matches the observations even though the inclined inner disk is not aligned with the planet's orbit.

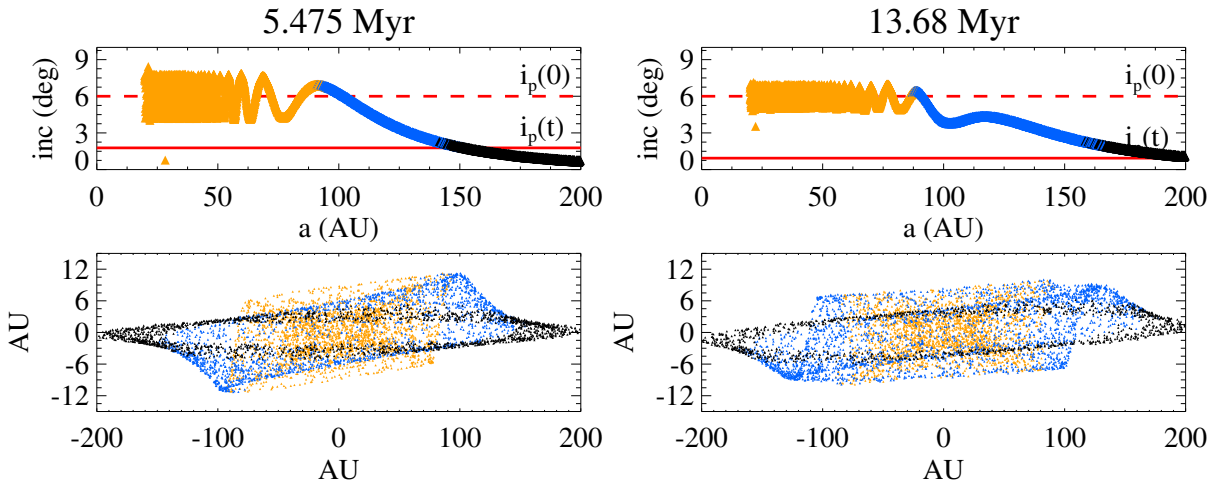

Figure 3.4.—: Snapshots at two times (left and right) from an N-body simulation of a planet ($m_p = 12 m_{\rm Jupiter}$; $a_p = 13.5$ AU; initial $i_p = 6°$) sculpting an initially flat planetesimal disk. We imposed damping of the planet's inclination of the form $\frac{\dot{i}}{i} = 2\pi/(4$ Myr), following Appendix A of Wolff et al. (2012). Top: Planetesimal inclinations vs. semi-major axis. The red dashed and solid lines are the planet's initial and current inclination, respectively. Bottom: Projected positions of the planetesimals. See Fig. 3.1 for color coding.

However, if the disk evolves for too long after the planet's inclination damps, the planetesimal nodes randomize and the morphology becomes boxy (right panel of Fig. 3.4). The distinction between a consistent and an excessively boxy morphology is qualitative and may require sophisticated modeling of the observed scattered light. However, it is clear that no more than a partial precession period at 85 AU can have passed since the planet's inclination damped. Since the system is young, this requirement does not demand implausible fine-tuning.

3.5.2 Damping Conditions

We consider the feasibility of damping planet b's orbital inclination. We expect that planet b started in the outer disk's plane, was perturbed, and is returning to its original plane. Possible perturbations include a second planet scattered inward (e.g. Jurić & Tremaine 2008), or resonant-induced inclinations in the disk near the planet (e.g. Thommes & Lissauer 2003).

Ejection of a scattered planet could alter the total angular momentum, requiring a disk with mass comparable to planet b to keep the forced plane, to which planet b damps, low (e.g. an unusually long-lived gaseous proto-planetary disk – Hillenbrand et al. 1993 – or a particularly massive planetesimal belt). We confirmed that fast precession of planet b caused by a massive disk, since the precession occurs about a misaligned axis, would not prevent the excitation of the warp. On longer timescales, the damping medium must allow planet b to remain inclined for almost the system's age. High-mass planets whose inclinations bring them several scale-heights out of the disk fail to open a gap, and thus gas interaction damps them after only ~ 100 orbits (Marzari & Nelson 2009). A more

moderate inclination ($i \lesssim 10^\circ$) for planet b, allowing it to maintain a clean gap, would lead to satisfactorily-inefficient damping (Bitsch & Kley 2011), perhaps on a 10 Myr timescale.

However, a modest disk mass may suffice. During planet-planet scattering, the total angular momentum is conserved, producing an average forced-plane still aligned with the flat outer disk. Planetesimals contributing to dynamical friction follow the forced plane, with each planetesimal attempting to damp the planet to the planetesimal's own plane. Even if planet b dominates the forced plane in its immediate vicinity, distant planetesimals, within a factor of several of the planet's semi-major axis, could damp the planet's orbit to their flat forced plane (i.e. the plane of the outer disk). (However, planet b would need to dominate the forced plane from 40 - 90 AU to excite the inclined inner disk.) Following Ford & Chiang (2007), Section 2.3, a surface density as low as 3 lunar masses within 40 AU could damp i_p from 10° over 4 million years if the disk remains thin. Collisional dissipation could keep the disk thin (Goldreich et al. 2004, eqn. 33, 50) if

$$\frac{s}{1\text{cm}} < \frac{< i_{\text{disk}} >}{2^\circ} \frac{m_{\text{disk}}}{5 m_{\text{Earth}}} \tag{3.6}$$

where s is a typical planetesimal radius. Since the collisional dissipation rate is $\propto \sigma \propto a^{-1}$, where σ is the disk surface density, collisional dissipation could keep the disk thin near planet b while allowing excitation from 40-90 AU, where the warp is created.

Clearly further study is required to find evolutionary scenarios that produce the inclination damping used in Fig. 3.4. These details are independent of this section's main message: a transient planetary orbit could establish a warp in a disk, to be observed at present, even if that planetary orbit has since changed.

3.6 Conclusion

We explored three scenarios for the apparent misalignment between the warped inner disk of β Pictoris and the orbit of the directly imaged planet b. In the first, most plausible scenario (Section 3.3), planet b's orbit is consistent with producing the warp, at the extremes of the uncertainties. We argued that the alignment depends not only on the planet's orbit but on the (separately measured) position angle of the outer disk. Therefore both of these quantities must be measured more precisely and, if possible, simultaneously from the same images.

In the second, most obvious scenario (Section 3.4), another planet warps the disk. However, we demonstrated that planet b inhibits another planet from producing the warp. Other planets may exist in the system, creating other disk features, but they cannot be responsible for the warp.

If the first scenario is ruled out by more precise observations, we are left with the third scenario (Section 3.5): planet b created the warp and then had its inclination damped. Detailed modeling of scenarios that allow for the damping of planet b's inclination will be necessary. Confirmation of the damping scenario, especially if observers discover more systems with planets misaligned with the warp they produced, could shed light on disk properties that are important for planet formation but difficult to measure directly.

Chapter 4

Radial Velocity Planets De-aliased: A New, Short Period for Super-Earth 55 Cnc e.

R. I. Dawson & D. C. Fabrycky *The Astronomical Journal*, Vol. 722, id. 937, 2010

Abstract

Radial velocity measurements of stellar reflex motion have revealed many extrasolar planets, but gaps in the observations produce aliases, spurious frequencies that are frequently confused with the planets' orbital frequencies. In the case of Gl 581 d, the distinction between an alias and the true frequency was the distinction between a frozen, dead planet and a planet possibly hospitable to life (Udry et al. 2007; Mayor et al. 2009). To improve the characterization of planetary systems, we describe how aliases originate

and present a new approach for distinguishing between orbital frequencies and their aliases. Our approach harnesses features in the spectral window function to compare the amplitude and phase of predicted aliases with peaks present in the data. We apply it to confirm prior alias distinctions for the planets GJ 876 d and HD 75898 b. We find that the true periods of Gl 581 d and HD 73526 b/c remain ambiguous. We revise the periods of HD 156668 b and 55 Cnc e, which were afflicted by daily aliases. For HD 156668 b, the correct period is 1.2699 days and minimum mass is $(3.1 \pm 0.4)\ M_{\oplus}$. For 55 Cnc e, the correct period is 0.7365 days – the shortest of any known planet – and minimum mass is $(8.3 \pm 0.3)\ M_{\oplus}$. This revision produces a significantly improved 5-planet Keplerian fit for 55 Cnc, and a self-consistent dynamical fit describes the data just as well. As radial velocity techniques push to ever-smaller planets, often found in systems of multiple planets, distinguishing true periods from aliases will become increasingly important.

4.1 Introduction

In the past two decades, over 400 extrasolar planets have been discovered, including more than 300 detected by radial velocity measurements. The entire architecture of a planetary system is encoded in the wobbles of its host star. In frequency space, the star's radial velocity variations are decomposed into the frequencies associated with each planet's gravitational interactions. One obstacle in correctly attributing these frequencies to planets are the spurious alias frequencies in the periodogram of the star's radial velocity measurements, caused by the discrete time sampling of the observations. Convolved with the orbital frequencies of alien worlds are Earth's own rotational and orbital frequencies, which dictate when the host star is visible at night, and – for many

data sets – the synodic lunar frequency, which impacts the allocation of telescope time.

Distinguishing aliases from physical frequencies is a common problem, yet making the correct distinction is crucial for characterizing extrasolar planets. For example, Udry et al. (2007) announced a super-Earth orbiting the M star Gl 581 with period 83 days, beyond the cold edge of the habitable zone. After more than doubling the number of observations, they determined that the planet's period was actually 67 days, well within the habitable zone, and that the 83 day period was an alias (Mayor et al. 2009). The distinction between an alias and physical frequency was the distinction between a frozen, dead planet and a planet possibly hospitable to life. For reasons we will describe below, planets with periods of one to several months – in or near the habitable zone of M stars – will typically have aliases with periods within about 30 days of their own orbital period. As more planets are discovered orbiting M stars, astronomers will be struggling to distinguish which of two close frequencies, one of which places the planet in the habitable zone, corresponds to a planet's orbital frequency. In general, planets with periods between a few months and a few years often have confusing aliases caused by convolution with Earth's orbital period, while planets with periods near a day, such as the super-Earth GJ 876 d (Rivera et al. 2005), have confusing aliases caused by convolution with Earth's rotational period. Automatic de-aliasing algorithms, such as CLEAN (Roberts et al. 1987), have been applied to particularly complicated radial velocity periodograms with some success (Queloz et al. 2009), yet, while they are good for cleaning up a periodogram, they should not be relied on for distinguishing between an alias and a physical frequency. Aliases also pose a challenge for observing variable stars and period-searching algorithms have been designed to not fall prey to them (see for example Plavchan et al. 2008; Reegen 2007, 2011).

Therefore, to enhance detection and characterization of planets, we have developed an approach to identify aliases by harnessing features of the "spectral window function," the Fourier transform of the observation times. Consider the star's motion as a signal that passes through a system, the time sampling window. Because of noise and loss of information, we can never perfectly reconstruct the signal. But we know everything there is to know about the system: for a sinusoid of a given amplitude, frequency, and phase, peaks in the window function cause aliases with calculable amplitudes and phases (Deeming 1975, 1976). The several time sampling frequencies – sidereal year, sidereal day, solar day, and synodic month – complicate the radial velocity periodogram yet allow us to break the degeneracy between alias and physical frequency that would exist for evenly-sampled data.

In the following section, we describe the origin and characteristics of aliases, supply the details of our approach for confirming that a particular frequency is not an alias, and clarify previous misconceptions about aliases. In the third section, we apply our approach to confirm periods for the planets GJ 876 d and HD 75898 b. We find that the orbital period for Gl 581 d and for the planets of HD 73526 cannot be definitively determined due to noise. We discover that the reported orbital period for HD 156668 b, 4.6455 days, is an alias of the true period, 1.2699 days. Finally, we analyze the 5-planet system 55 Cnc. We find that the period of 2.817 days reported in the literature for planet e (McArthur et al. 2004; Fischer et al. 2008) is actually a daily alias of its true period of 0.737 days. We conclude by summarizing the approach we have developed, considering the implications of a new period for 55 Cnc e, and suggesting observational strategies for mitigating aliases.

4.2 Method

The existence of a planet orbiting a star is frequently inferred from a signature peak in the periodogram of radial velocity measurements of the star. However, the periodogram often contains alias frequencies, the result of discrete sampling times, that, at first glance, cannot be distinguished from the true periodicities. Many astronomers have struggled to determine which periodogram peaks are physical frequencies and which are aliases, often resorting to methods that are unnecessarily computationally intensive, not definitive, reflect a misunderstanding of aliases, or all of the above. In the first subsection, we will describe the origin of aliases for evenly and unevenly sampled data. In the second subsection, we will explain the cause of the daily aliases, prominent for many Doppler datasets. In the third section, we will present a field guide for identifying aliases. In the fourth subsection, we will describe the method we have developed. In the fifth subsection, we will discuss the effects of orbital eccentricity. In the sixth subsection, we will discuss common misconceptions about aliases that lead to misidentification.

4.2.1 The Origin of Aliases for Evenly and Unevenly Sampled Data

Aliases are the result of discretely sampling a continuous signal. The resulting discretely-sampled signal is the product of the continuous signal and the sampling function, the latter being a "Dirac comb": a series of delta functions. The periodogram of the discretely-sampled signal is a convolution of periodogram of the continuous signal and the periodogram of the sampling function (the spectral window function). Consider

first the simplified case of an infinite set of evenly-spaced data points, $g_1[n]$, the result of sampling a continuous sine wave $s_1(t)$ of frequency f at sampling frequency f_s. Here we follow McClellan et al. (1999):

$$\begin{aligned} s_1(t) &= \sin(2\pi f t), \\ g_1[n] &= s(n/f_s) = \sin(2\pi f n/f_s), \end{aligned}$$

where n is an integer. However, under this sampling, the signal is indistinguishable from the sine wave $s_2(t)$ of frequency $(f + mf_s)$:

$$\begin{aligned} s_2(t) &= \sin(2\pi(f + mf_s)t), \\ g_2[n] &= \sin(2\pi(f + mf_s)n/f_s) = \sin(2\pi f n/f_s), \end{aligned}$$

where m is an integer. In the frequency domain, both g_1 and g_2 will have peaks not only at f, but also at $f + mf_s$.

Moreover, neither has a periodogram distinguishable from a sampled sinusoid of frequency $(-f + mf_s)$:

$$g_3[n] = \sin(2\pi(-f + mf_s)n/f_s) = \sin(2\pi f n/f_s + \pi).$$

That is to say, g_1 and g_2 will also have peaks at $-f + mf_s$, although the phase of those peaks will be advanced by $^1/_2$ cycle. For evenly sampled data, unless the only physically possible frequencies fall in a single Nyquist interval $f_s/2$, the frequency cannot be unambiguously determined.

Fig. 4.1 shows the spectral window function of an evenly sampled time series of f_s = 1 day^{-1}. Peaks in the spectral window function occur at mf_s, where m is an integer.

The spectral window function is given by equation 8 in Roberts et al. (1987):

$$W(\nu) = \frac{1}{N}\sum_{r=1}^{N} e^{-2\pi i \nu t_r}, \tag{4.1}$$

where N is the number of data points, and t_r is the time of the rth data point. It is evident that when $\nu = \pm m f_s$, $e^{\mp 2\pi i m f_s t_r} = e^{\mp 2\pi i m n} = 1$ and $W(\nu) = 1$. It's also evident from this equation that when $\nu = 0$, $W(\nu) = 1$. Note that $W(-\nu) = W^*(\nu)$.

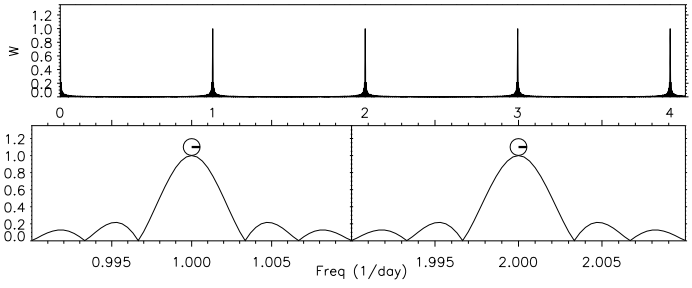

Figure 4.1.—: Spectral window of data evenly sampled in time, with a sampling frequency $f_s = 1$ day^{-1}, and 300 samples.

The top panel of Fig. 4.2 shows the periodogram[1] of a sinusoid of period 1.94 days sampled every 1 day for 300 days. For a sinusoidal signal, the resulting periodogram is a convolution of the spectral window function $W(\nu)$ with the peak corresponding to period 1.94 days. The bottom panel shows the periodogram of a sinusoid of period 2.06 days, an alias of 1.94 days, with the same even sampling. The two periodograms are indistinguishable. The aliases of the 1.94 day period occur at $f = 1/1.94 + m f_s$. For $f_s = 1$ and $m = -1$, the alias is $1/1.94 - 1 = 1/2.06$.

[1]For this and all other periodograms in this paper, at each frequency we (1) let the mean of the data float, and (2) weighted each data point with the inverse of the square of the reported error bar. See Cumming et al. 1999 and Zechmeister & Kürster 2009.

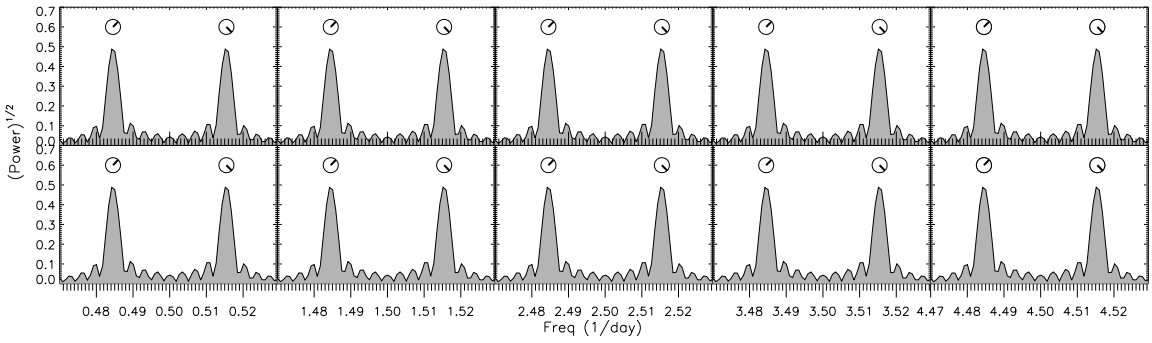

Figure 4.2.—: Periodogram of sinusoids sampled evenly in time. Top: Period 1.94 day. Bottom: Period 2.06 day. They are indistinguishable.

For a randomly selected frequency ν each $e^{-2\pi i\nu t_r}$ will add incoherently. However, if there are gaps in the data of a certain frequency ν, only certain phases occur and the complex exponentials will add in a partially coherent manner. The spectral window functions of stellar reflex motion measurements contain peaks at 1 sidereal year, 1 sidereal day, 1 solar day, and sometimes 1 synodic month. These periodicities are caused by observations being limited to only a particular portion of each of these periods. Observations are limited to a particular portion of the sidereal year and sidereal day because the star is only visible at night from the location of the telescope during particular parts of the sidereal year and day. At some telescopes, spectroscopic observations of the stars are relegated to "bright time," the portion of the synodic month when the moon is near full, because "dark time" is reserved for observing faint objects. In the next section, we will focus on the daily aliases due to both the solar day and the sidereal day.

Uneven sampling also dictates that the phase of $\exp(2\pi i f_s t_r)$ will span a width. Eyer & Bartholdi (1999) demonstrate that for unevenly sampled data, there is effectively

no Nyquist frequency. Because gaps in the data and uneven spacing sample a non-zero width in phase, the height of peaks in the window function will never be exactly 1. For a noiseless data set, the physical frequency will almost always be a higher peak in the periodogram than any alias. (The only exception is if positive and negative aliases add coherently.) For noisy data, the noise between two candidate peaks is correlated, but it may constructively interfere with the alias and destructively interfere with the true frequency, resulting in the alias peak being taller. Depending the phase of noise, it can also alter the phase of the true frequency and aliases through vector addition.

4.2.2 Daily Aliases

For most Doppler datasets, the largest peaks in the window function — corresponding to the largest aliases — are those at n day^{-1}, where n is an integer. We refer to these peaks as the daily aliases, as they result from the sampling an Earth-bound observer is able to do at nighttime from a single site.

Let us construct an example dataset, to illustrate their origin. Suppose the sampling is confined to when the Sun is down and the target star is up. In particular, suppose the samples are taken nearly daily, midway between when the star rises and the Sun rises, or midway between when the Sun sets and the star sets, depending on the time of the year. This sampling would lead to spacings between the solar day (24h 0m 0s) and the sidereal day (23h 56m 4s). Therefore, in our example dataset, let us take datapoints spaced by 23h 57m 30s, although due to telescope scheduling and weather, only a fraction of the nights (randomly chosen) are actually observed. Such a sequence is repeated in intervals of 365 days for 5 years, resulting in a total of 97 observation times. In Fig. 4.3 we

illustrate this idealized dataset. It is constructed to obey the boundaries set by the Sun and the star, which are also plotted. The actual times from real datasets are compared, to show that this sampling, though idealized, reproduces the main daily and yearly structure of a real dataset.

Figure 4.3.—: Times of observation of an idealized dataset and two real datasets, folded to illustrate the origin of daily aliases. The axes show, quantitatively, the time of the year and the time of the day. The solid lines are labeled and correspond to the time each day that either the Sun rises or sets (at a constant time-of-day in this idealized example) or the star rises or sets (which varies according to the time of the year). The dashed lines are when the star reaches 54 degrees from the zenith, within which a favorable observation can be made. The idealized dataset is described in the text. The HARPS data for Gl 581 are from Mayor et al. (2009), and we took $t = JD - 2,452,970.92$ for convenience. The Keck and Lick data for 55 Cnc are from Fischer et al. (2008), and we took $t = JD - 2,447,370.15$. Figure courtesy of Daniel Fabrycky.

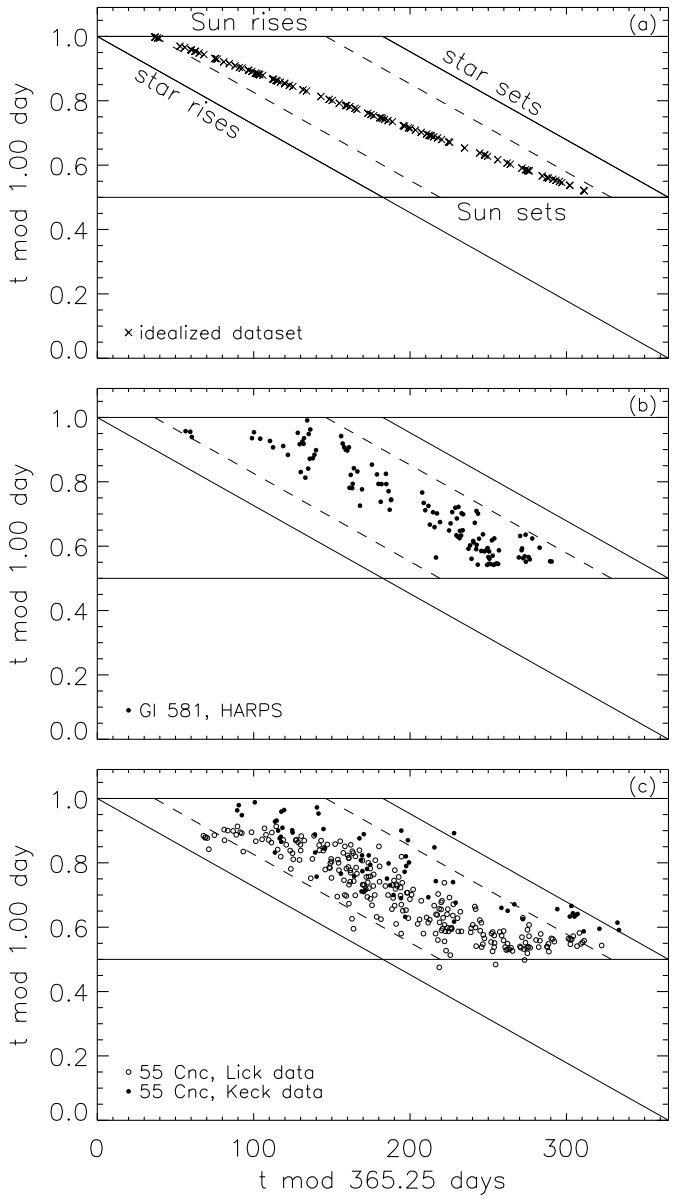

Figure 4.3.—: Continued

The window function for this idealized dataset is shown in Fig. 4.4. There are peaks at frequencies of n day^{-1} + m yr^{-1}. In particular, there is a doublet at $\nu = 1.0000$ day^{-1} and $\nu = 1.0027$ day^{-1}, with the latter peak being larger.

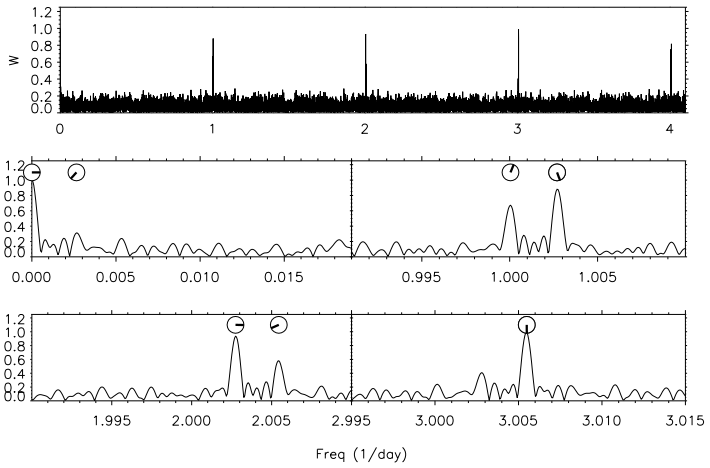

Figure 4.4.—: Spectral window function of data with gaps. The sampling is from the "idealized dataset" of panel (a) in Fig. 4.3.

How does this structure arise? We see from Fig. 4.3 that for $\nu = 1.0000$ day^{-1}, the idealized observations only sample the second half of phase. Therefore the window function as defined by equation (4.1) will have contributions only from phases π to 2π, so the complex exponential will add up coherently to a large peak. This phase coherence explains the daily aliases not just at 1 day^{-1}, but everywhere a peak occurs. For instance, consider at what times data are taken relative to the frequency of the sidereal day, $\nu = 1.0027$ day^{-1}. In Fig. 4.3, this frequency is related to the diagonal line labeled "star rises." The idealized dataset consists only of observation times between 0.1 days and 0.4 days after the star rises (above that diagonal line). Therefore the observations cover only 30% of the phase of the sidereal sampling frequency, which again results in a large peak in the window function. Here, even a smaller fraction of the total phase is covered,

so the sampling results in even more coherent summation of complex exponentials, which is why the window function peak at $\nu = 1.0027$ day^{-1} is larger than at $\nu = 1.0000$ day^{-1} (Fig. 4.4). Another way to see this is to note that the line formed by the idealized data in Fig. 4.3, panel a, has a slope more closely matching the sidereal day (the diagonal lines related to the star) than the solar day (the horizontal lines related to the Sun). Finally, we note that no peaks in the window function appear between the solar and sidereal frequencies because folding the data at those frequencies samples phases throughout 0 to 2π.

Having understood the origin of the daily aliases in the window function, including doublets, we are prepared to recognize and correctly interpret such structure when it results in periodograms.

To that end, we used this idealized dataset to sample a sinusoid of period 1.94 days or 2.06 days, and in Fig. 4.5 show their periodograms. In this example, we have taken the two periods close to those which Rivera et al. (2005) needed to decide between for GJ 876 d. Here, then, we have identified a simple way to decide between them: the slightly taller peak is expected to be the true one (because there is no noise), and the alias will consist of a doublet with spacing 0.0027 day^{-1}. We analyze the Rivera et al. (2005) dataset in subsection 4.3.1.

4.2.3 A Field Guide to Aliases

An alias is a convolution in frequency space of a physical frequency with the window function. Fig. 4.6 and Fig. 4.7 display some examples of yearly and daily aliases respectively and the window function features that cause them. We have chosen

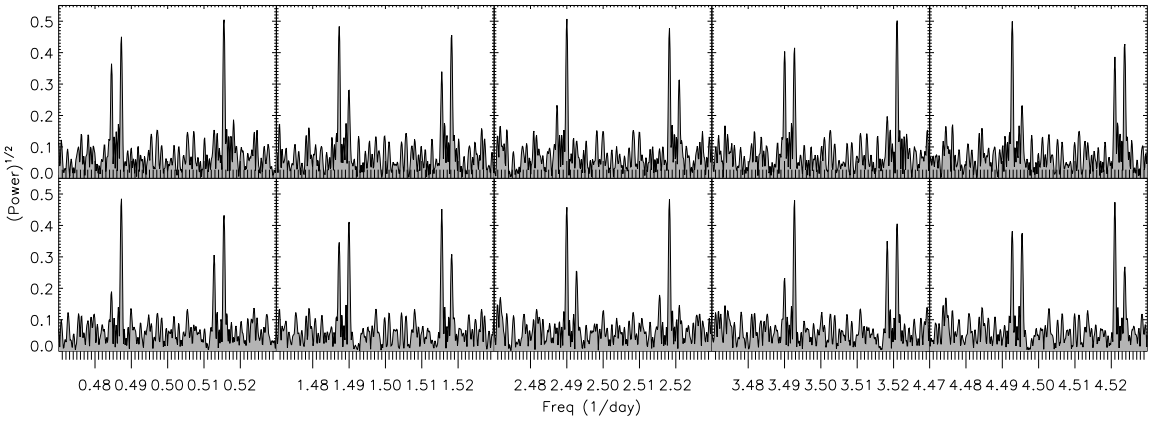

Figure 4.5.—: Top: Periodogram of sinusoid of period 1.94 day (frequency 0.515 day^{-1}) with the idealized time sampling from Fig. 4.3. Bottom: Period 2.06 day (frequency 0.485 day^{-1}). With this time sampling, the periods are distinguishable by the imprinting of the window function features from Fig. 4.4 at $f \pm f_s$ where f is the frequency of the sinusoid and f_s of the window function feature.

especially clean examples; ambiguous cases will be addressed throughout the next section.

4.2.4 Details of Our Method

We recommend the following treatment for a radial velocity dataset or residuals of an established fit (we will refer to both these categories as "data") that appear to exhibit periodic variation. As we emphasized above, the phases of peaks are helpful for determining what is the true frequency. For example, consider a set of data with peaks in the spectral window function at 1 year (0.0027 day^{-1}), 1 solar day (1 day^{-1}), and 1 sidereal day (1.0027 day^{-1}). Consider a true frequency $f_1 > 1.0027$, which will have aliases at at $f_2 = f_1 - 1$ and $f_3 = f_1 - 1.0027$. We may wonder if the peak

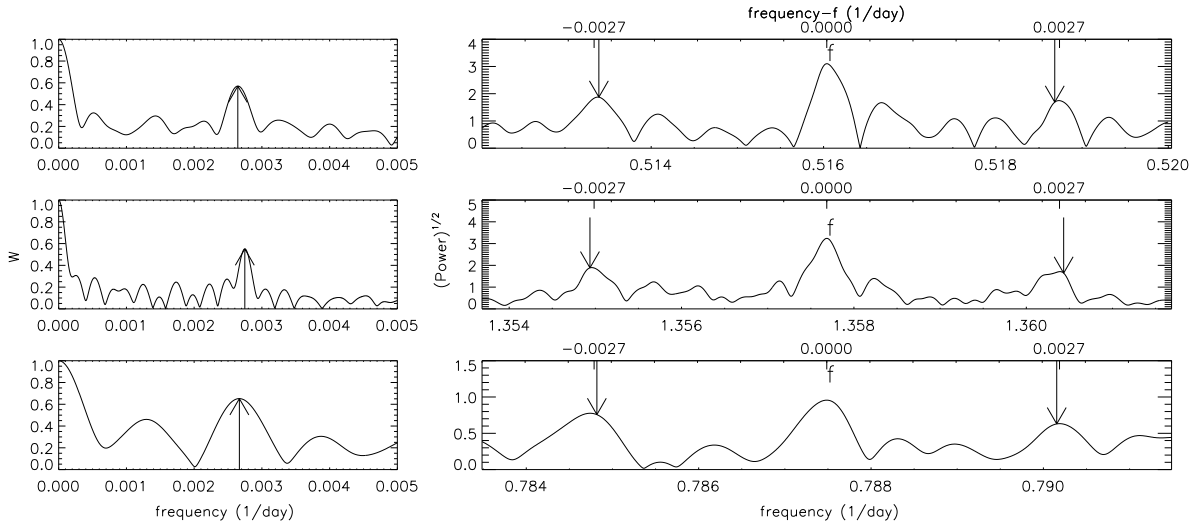

Figure 4.6.—: Illustrative examples of yearly aliases taken from GJ 876 (top), 55 Cnc (middle), and HD 156668 (bottom). The window function is plotted on the left and the periodogram of the data near the candidate frequency on the right. The arrow in the left plots indicates the peak in the window function near 1/yr and the arrows in the right plots indicate the predicted location of the yearly aliases caused by this window function feature.

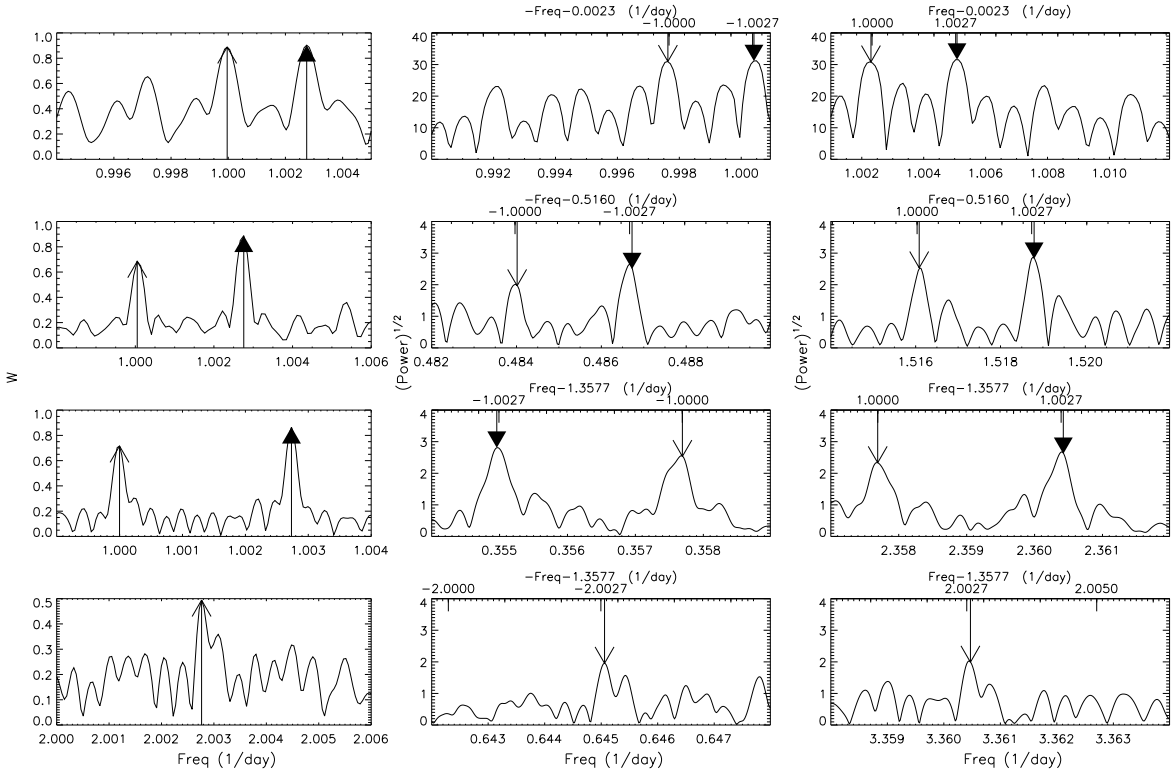

Figure 4.7.—: Illustrative examples of yearly aliases taken from HD 75898 (top), GJ 876 (second row), 55 Cnc Fischer et al. data set (third row), and 55 Cnc combined data set (bottom row). The window function near a major feature is plotted in the left column and sections of the periodogram of the data in the middle and right columns. Arrows in the left column indicate the peaks in the window function near sidereal and solar days and the arrows in the middle and right plots indicate the predicted locations of the corresponding aliases. Note that each peak in the window function results in two features in the data periodogram.

at f_2 is the true frequency, with an alias at $f_s - 0.0027 = f_3$. However, because of the phases of the peaks in the window function, the phase of the peak f_3 is different than the phase we would expect if it were an alias of f_2. Because the phase of a peak can be key in determining the true frequency, we strongly recommend plotting the phase of selected peaks. We use a symbol we call a "dial" (e.g., Fig. 4.9) where the phase angle is the counterclockwise angular position from the x-axis. The phase angle is $\tan^{-1}(\text{Imaginary}(W(\nu))/\text{Real}(W(\nu)))$ for the window function peaks and likewise $\tan^{-1}(C(f)/B(f))$ for the periodogram peaks, where B and C are the real and imaginary coefficients of the periodogram for frequency f.

Our method is composed of the following steps:

1. Plot the spectral window function (eq. 4.1), attaching dials to any large peaks. Peaks will most likely occur at or near f=0, 1/yr, 1/(solar day), 1/(1 sidereal day), and, if the observations were taken during a particular part of the lunar cycle, f = 1/month, 1/month ± 1/yr. Spectral window functions of artificial data sets are plotted in Fig. 4.1 and 4.4 and real data sets in Fig. 4.8, 4.10, 4.12, 4.13, 4.15, 4.17, 4.19 and 4.21.

2. Plot the periodogram.

3. Consider first the possibility that the largest peak is the true frequency; measure its frequency, phase, and amplitude. Attach dials to peaks we would expect are aliases, according to the peaks in the window function. If the peak in the radial velocity periodogram occurs at f and peaks in the window function occur at f_s, we expect aliases at $f \pm f_s$. (If $f_s > f$, we will still see a peak at $f - f_s$. Flipping it across 0 frequency gives the phase the opposite sign: a complex conjugation.)

Generate a sinusoid with the same frequency, phase, and amplitude as the peak in radial velocity periodogram and plot its periodogram, attaching dials in the same location. Compare the amplitude and phases of peaks. Are the major aliases for f present in the data with the predicted phase and amplitude?

4. Now consider that the largest alias(es) of what we considered the true frequency might actually be the true frequency. Repeat step 3.

5. If the periodogram of the data is well-matched by the periodogram of one and only one candidate sinusoid, then the true frequency has been determined. As Lomb (1976) said, "If there is a satisfactory match between an observed spectrum and a noise-free spectrum of period P, then P is the true period." However, if several candidate sinusoids match peaks equally well or poorly, then the data are not sufficient to distinguish the true period.

4.2.5 Treating the Orbital Eccentricity

Many extra-solar planets have elliptical orbits. The signal of the eccentricity is contained in harmonics of the orbital frequency; the first harmonic has an amplitude eK, where e is the eccentricity and K is the amplitude of the sine wave at the planet's orbital frequency (Anglada-Escudé et al. 2010). Thus for moderate eccentricities, the same analysis can be applied to the first harmonic of the orbital frequency. Except in rare unfortunate cases (such as HD 73526, treated below in section 4.3.3), the period and its aliases will be well-separated in frequency space from the eccentricity harmonic and its aliases. In section 4.3.2, we distinguish a peak in the periodogram of HD 75898 b as an alias that the Robinson et al. (2007) proposed could be an alias, eccentricity harmonic,

or additional planet.

For certain datasets, orbital eccentricity may help distinguish between a true orbital period and an alias. Consider a planet with moderate eccentricity e whose host star is observed with near evenly-spaced sampling as f_s. Even if the noise is low relative to K, it may be difficult to distinguish between the true orbital frequency f and an alias $f + f_s$. However, since the planet's orbit is eccentric, we will also observe a peak of amplitude eK at $2f$ but no such peak at $2(f + f_s)$.

In summary, orbital eccentricity contributes to the periodogram in a well-defined way and, except in rare unfortunate cases that can be easily identified, will not confuse the distinction between the true orbital period and an alias.

4.2.6 Common Misconceptions

Many problems with aliases are the result of unwarranted assumptions. We describe some common misconceptions about aliases and how they cause confusion.

1. Assuming that the largest peak in the periodogram is the physical frequency. In fact, noise may add coherently to an alias or incoherently to the physical frequency, causing the alias to appear larger. This is what happened for Gl 581 (Udry et al. 2007; Mayor et al. 2009). In multi-planet systems, aliases from several planets could add to make the highest peak a spurious signal (Foster 1995).

2. Assuming that the frequency that yields the best Keplerian or Newtonian planet fit is the true frequency. As we saw for Gl 581 d, this is not always the case, due to noise.

3. Assuming that aliases occur at frequencies only *occur* near peaks in the spectral window function. We have seen authors plot the spectral window function below the periodogram of the data and assume that if a frequency in the data periodogram is not near a peak in the spectral window function that it is not an alias. In fact, aliases occur at $|f \pm f_s|$, where f_s is a feature in the spectral window function. Depending on the relative values of f and f_s, the alias might be anywhere in the periodogram. However, periodograms will contain peaks at the sampling frequencies if there are systemics linked with the observing pattern or if the peaks are aliases of a very low frequency signal. We emphasize the difference between these two types of signals: the former is spurious and and the latter has an extra-solar origin but wrong frequency. We also emphasize the importance of employing the spectral window function to identify all major aliases, not just aliases or other spurious frequencies that occur at the sampling frequencies.

4. Assuming that any frequency above 1 is an alias. As we mentioned above, there is effectively no Nyquist frequency for unevenly sampled data. Many authors cut off their periodograms at 1 day^{-1}, potentially missing out on or misinterpreting planets with orbital periods less than a day. We know such planets exist because they have been detected by transits. Moreover, because long period planets will have aliases near 1 day, a planet with orbital periods near 1 day is vulnerable to being discarded as an alias (Kane 2007).

5. Assuming that aliases are so pernicious that one can never identify the correct period and should thus just pick the most sensible period. In fact, our method allows one to determine either a correct period or that noise prevents the identification of the correct period. In the latter case, further observations should

allow for a definitive determination in the future. It is unwise to judge a priori which period is the most "sensible" period; as mentioned above, planets have been found with periods less than a day.

6. Assuming that if an alias frequency is used in a Keplerian or Newtonian planet fit, a peak corresponding to the true frequency will appear in residuals. This would only happen if the peak at the alias frequency is much smaller than the peak at the true frequency, relative to the noise.

7. Assuming that if a frequency is an alias, it will appear in a periodogram of the data scrambled. Aliases are not caused solely by the spacing observations; they are convolution of the spectral window function with the periodogram of the data. Scrambling the data removes the true frequency and thus also removes the alias.

8. Assuming that if you "fold" (i.e., phase) the data with a candidate period, a coherent pattern will emerge only if the candidate period is the physical period. In fact, a large alias, by its very definition, will also produce a coherent pattern.

Another method we have seen applied to distinguish between two frequencies, one of which is an alias, is to generate thousands of mock data sets for each frequency by combining a sinusoid with simulated noise and then determine how often the alias is mistaken for the true frequency. This method indeed reveals the probability that the period is falsely determined, but a proper understanding of the window function leads to a less computationally intensive method, which we have advocated.

We reemphasize the peaks in the spectral window functions combined with the true frequencies are what cause aliases. Even if a peak in the periodogram is linked to

another peak by close to an integer frequency, if that integer frequency is not a peak in the spectral window function, then the peaks are not aliases of one another and might represent two distinct planets. Rather than simply noting the possibility that an integer frequency might link the peaks, the window function reveals it quantitatively.

4.3 Application to Extrasolar Planetary Systems

In the following section, we investigate instances of aliases and ambiguous periods in the literature.

4.3.1 GJ 876 d

In this section, we apply the approach described above to planetary system GJ 876. Extensive radial velocity observations spanning almost eight years have revealed three planets orbiting this M-star. A Jupiter-mass planet b was discovered in 1998 (Marcy et al. 1998), and an interior Jupiter-mass planet c in a 2:1 resonance with b was discovered three years later (Marcy et al. 2001). After several years of continued observations, Rivera et al. (2005) discovered an additional 7.5 earth mass planet d with an orbital period of 1.94 days. This discovery was independently confirmed by Correia et al. (2010) with new HARPS data. The periodogram of the residuals to the nominal two-planet, $i = 90°$, coplanar fit exhibits strong power at frequency 0.52 day^{-1} but also at $f = 0.49$ day^{-1} ($P = 2.05$ day) and $f = 1.52$ day^{-1} ($P = 0.66$ day) (Fig. 4.9, top panel). Rivera et al. (2005) performed a series of tests and argued based on the results that the peak at 2.05 days is an alias of the true period at 1.94 days. Our method is able to definitively

confirm the results of their tests, that the physical period is indeed 1.94 days.

The spectral window function and the periodogram of GJ 876 (actually, of the residuals from a dynamical fit to planets b and c) are shown in Fig. 4.8 and 4.9, respectively. Major peaks in the window function occur at 1 sidereal year, 1 sidereal day, and 1 solar day. The very same features are seen in the example periodogram described in section 4.2.2. The main peak is tallest [2]. The alias has a doublet structure.

Compared to our example idealized data set of Fig. 4.3, 4.4, and 4.5, the yearly aliases are more pronounced in the data, because the observing season is shorter than in our idealized dataset. This causes peaks on either side of the true peak (spaced by 1 $\mathrm{yr}^{-1} = 0.0027\ \mathrm{days}^{-1}$) which are symmetric in height. Thus we confirm the selection of $P = 1.94$ days as the correct period of GJ 876 d (Rivera et al. 2005), and thus we demonstrate that a signal beyond the traditional Nyquist frequency can be robustly detected with unevenly sampled data.

4.3.2 HD 75898 b

Robinson et al. (2007) discovered a Jupiter-mass planet orbiting HD 75898 b. They noticed two peaks in the periodogram, a large one near 400 days and a smaller one near 200 days. They presented three possibilities for the peak near 200 days: an alias of the 400 day period, an eccentricity harmonic (which we would indeed expect to appear near $P/2 = 200$ days), or a second planet. Applying our method, we confirm that the true period is 400 days, not 200 days; and the peak at 200 days is indeed an alias, not

[2]We point this out for identification purposes but in a given data set, because of noise, the true frequency will not necessarily be taller than the alias.

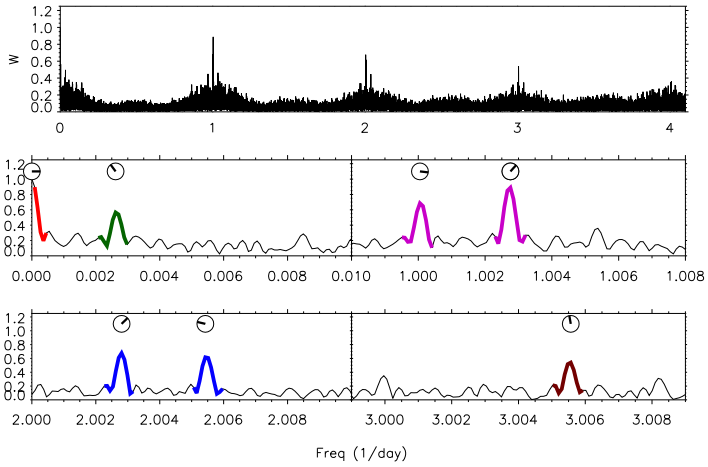

Figure 4.8.—: Spectral window function of RV Measurements of GJ 876 (Rivera et al. 2005). Major features of the spectral window function are colored: red (at 0 day^{-1}), green (yearly feature), fuschia (daily features), blue (two day^{-1}), and brown (three day^{-1}). The corresponding aliases these features cause for several candidate frequencies are indicated by these colors in Fig. 4.9.

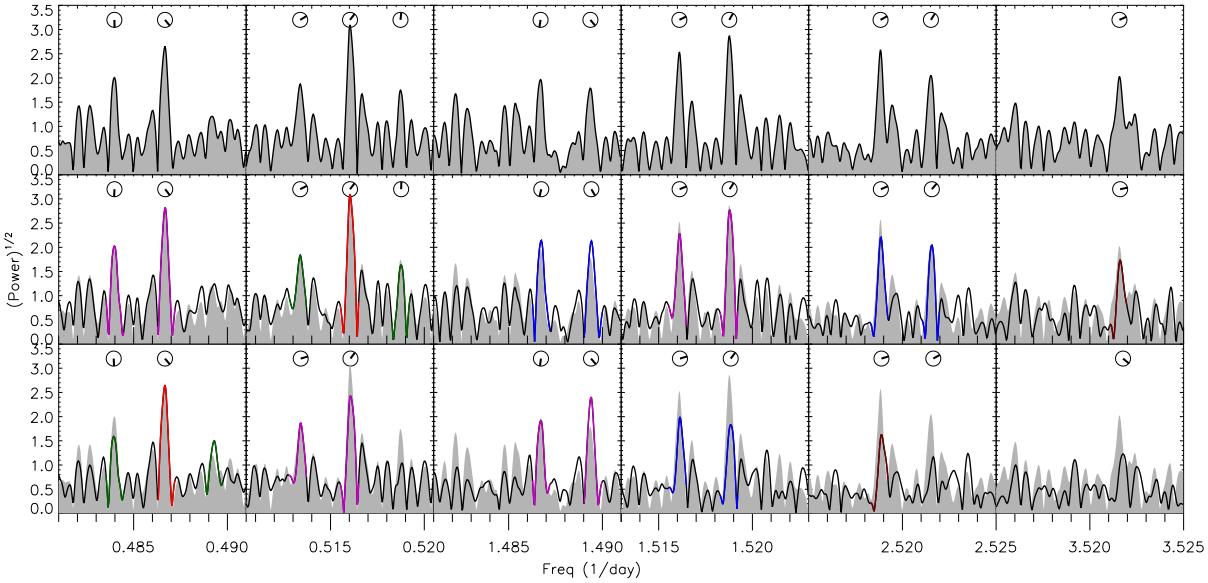

Figure 4.9.—: Periodograms of GJ 876. The top row is the periodogram of the data. The second and third rows show the periodograms of sinusoids sampled at the times of the real data sets as solid lines; they also repeat the periodogram of the data as a gray background, for comparison. Dials above the peaks show the phase at each peak. Colors correspond to the feature in the window function that creates the particular alias (see Fig. 4.8), with red being the candidate frequency, the green sidebands yearly aliases, and the fuschia, blue, and brown peaks daily, two day^{-1}, and three day^{-1} aliases respectively. The second row is the periodogram of an injected sinusoid of period 1.94 days (frequency 0.516 day^{-1}). The third row is the periodogram of an injected sinusoid of period 2.05 days (frequency 0.487 day^{-1}). The sinusoid of period 1.94 days matches the heights and phases of the peaks much better, both for the yearly aliases on either side of the main peak in column 2 and the daily aliases in the other columns. The two candidate frequencies have different types of aliases at different locations, allowing us to break the degeneracy.

an eccentricity harmonic or second planet. The spectral window function is plotted in Fig. 4.10; the peak that occurs at 1 yr^{-1} is the cause of the 200 day alias. In Fig. 4.11, the periodogram shows that a 400 day period (row 2) produces exactly the aliases we expect, including the alias at 200 days. Although an eccentricity harmonic would fall at the same place as this alias, for this system we can rule out a significant eccentricity harmonic because the peak has the exact phase and amplitude that result from it being an alias of the 400 day planet; any significant eccentricity harmonic would change the phase and/or amplitude of this peak. These plots also confirm that the true period is 400 days, not 200 days (row 3).

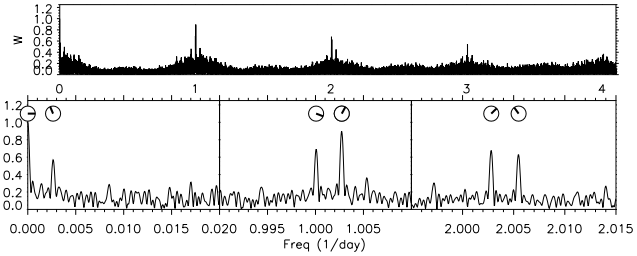

Figure 4.10.—: Spectral window function of RV Measurements of HD 75898. These features, convolved with a planet's orbital frequency, cause the aliases evident in the periodogram in Fig. 4.11.

4.3.3 HD 73526

Tinney et al. (2003) reported a planet orbiting the G-type star HD 73526 with orbital period 190.5 days. A later Bayesian analysis by Gregory (2005) revealed three possible periods for the planet: 190.4 days and (its yearly aliases) 127.88 days and 376.2 days. Gregory (2005) concluded that the periods 127.88 days and 376.2 days were more probable. After follow-up observations, Tinney et al. (2006) reported the system actually

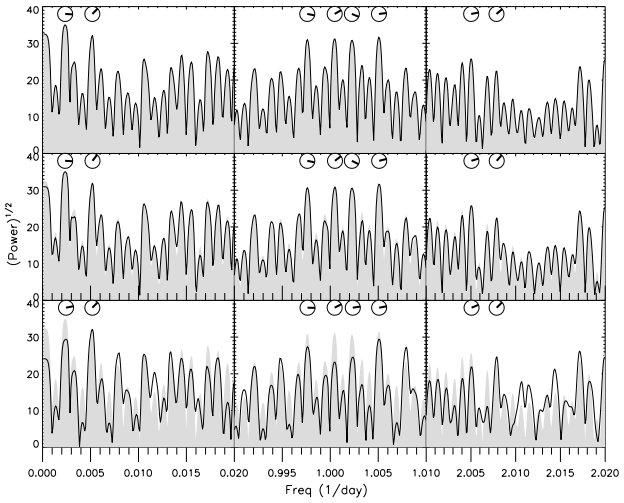

Figure 4.11.—: Periodograms of HD 75898. Dials above the peaks denote their phase. Row 1 shows the data. The other rows show sinusoids sampled at the times of the real data sets (solid line and dial), as well as the data again for reference (in gray). In Row 2 the solid line shows, for these time samplings, the periodogram of a sinusoid of frequency 0.00236 day^{-1}. For Row 3, it is for 0.00519 day^{-1}. We confirm that the peak at 0.00519 day^{-1} is an alias, not a second planet or eccentricity harmonic. In Rows 2 and 3, each peak results from the convolution of the sinusoidal frequency with the features in the spectral window function in Fig. 4.10.

contained two planets, with orbital periods 187.5 and 376.9 days, locked in a 2:1 resonance. The Keplerian fit using these two periods is an excellent match to the data, with $(\chi^2_\nu)^{1/2} = 1.09$, but the dynamical fit for the system is substantially worse, with $(\chi^2_\nu)^{1/2} = 1.57$. This implies that, though these periodicities may be strongly present in the system, the physical model of two planets orbiting with this period may need modification. Further complicating the interpretation of the system's periodicities is the degeneracy between the outer planet's eccentricity and the inner planet's mass – or even its very existence (Anglada-Escudé et al. 2010). The window function for this system and a periodogram is plotted in Fig. 4.12. The Keplerian fit has eccentricities of 0.4 for both planets, essentially tuning the phase of the power at 187.5 days (the first eccentricity harmonic of 376.9 days) to account for both a possible planet there and aliasing from 376.9 days; and introducing power at 93.8 days (the first eccentricity harmonic of 187.5 days and also a yearly alias of 127 days). However the eccentricities for the dynamical fit (Tinney et al. 2006) are substantially lower, implying that high eccentricities would cause dynamical interactions inconsistent with the data. It is possible that the periods 127.88 days and 376.2 days are incorrect but that by introducing a large eccentricity harmonic, the combination of orbital periods, eccentricity harmonics, and aliases match the periodicities of the data, which may be the result of different physical orbital frequencies. This system is complicated because of the degeneracy in frequency between resonant planets, eccentricity, and aliases. We recommend further observations and modeling of this system to confirm the orbital periods.

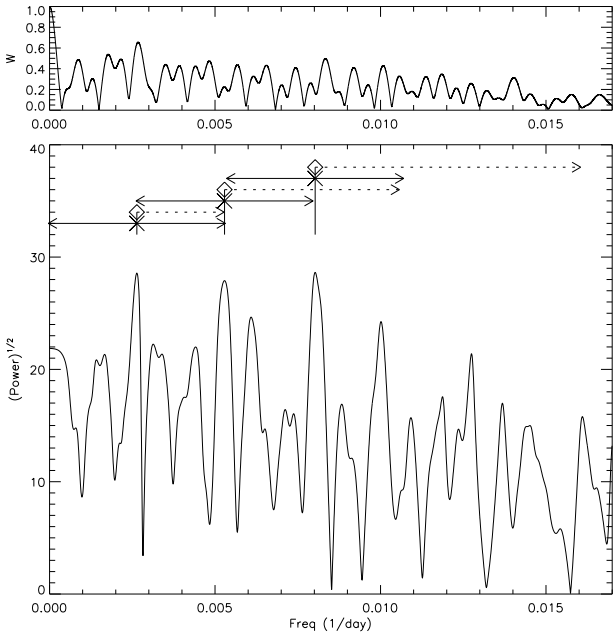

Figure 4.12.—: Top Panel: Spectral window function of RV measurements of HD 73526. Bottom Panel: Periodogram of RV measurements of HD 73526. The solid arrows indicate the locations of a peak's yearly aliases and the dashed line the location of the eccentricity harmonic.

4.3.4 Gl 581 d

HARPS measurements have revealed four planets orbiting the M dwarf Gl 581: a $\sim 2M_{\oplus}$ planet e (Mayor et al. 2009), Neptune-mass planet b (Bonfils et al. 2005), and super-Earth planets c and d (Udry et al. 2007). Planet d was originally reported to have a period of 83 days, beyond the cold edge of the habitable zone. After further observations, the HARPS team announced that the true period of planet d is 67 days, placing it within the habitable zone, and that the original 83 day period was a one year alias of the true 67 day period. In Fig. 4.13, we plot the spectral window function of Mayor et al. (2009)'s new data set. Prominent peaks are evident at 1 year, 1 sidereal day, and 1 solar day. A periodogram of the data, with planets b and c subtracted (subtracting planet e made no significant difference) and sinusoids of several candidate frequencies are plotted in Fig. 4.14. In the original data set, the highest peak in the periodogram was at 0.0122 day^{-1} (corresponding to a period of 83 days). In the new data set, the highest peak is at 0.9877 day^{-1}. The second highest peak is at 0.0150 day^{-1} (67 days), the period reported by Mayor et al. (2009). The 0.0122 day^{-1} peak and 0.0150 day^{-1} are linked by a feature in the window function at 1 sidereal year. Yet neither produces an alias that corresponds to the other frequency with a phase and amplitude that match the data (first column of rows 2 and 3). The highest peak, 0.9877 day^{-1}, is linked to the peaks at 0.0122 day^{-1} and 0.0150 days^{-1} by the window function peaks at 1 solar day and 1 sidereal day respectively; it better matches the phase and amplitude at these frequencies (row 4, column 1). This dataset has sampling which is too regular (Fig. 4.3b), which resulted in pernicious daily aliases. However, there are discrepancies between the phase and amplitude of the aliases predicted by all three candidate frequencies. For example, at 1.99 days (column 4), the larger alias predicted for 0.9877 day^{-1} (linked by the large

1 sidereal day alias) is consistent in amplitude with the data while the other frequencies (linked by the smaller window function feature at 2 days) predict aliases that are too small; however, the phase for the 0.9877 day^{-1} alias is a bit off. Although none of the frequencies is fully consistent, we slightly prefer 0.9877 day^{-1}, followed by 0.0150 day^{-1} and 0.0122 day^{-1}. However, using the previous data set from Udry et al. (2007), we favor (in order): 0.0122 day^{-1}, 0.0150 day^{-1}, and 0.9877 day^{-1}. We also fit a four-planet Keplerian model to both datasets. In the Udry et al. (2007) dataset, a frequency of 0.0122 day^{-1} for planet d gave the best fit, while in the Mayor et al. (2009) dataset, a period of 0.9877 day^{-1} gave the best fit. However, a model with orbital frequency 0.0122 day^{-1} where e_d is allowed to float gives a significantly better fit than one with orbital frequency 0.9877 day^{-1} where e_d is fixed at zero (which would likely be attained by tidal dissipation). Because the period of planet d remains ambiguous, we recommend that future observations take place with the star at a greater air mass – instead of only when the star is crossing the meridian – in order to reduce the amplitude of the aliases and allow us to definitively distinguish between these three candidate periods.

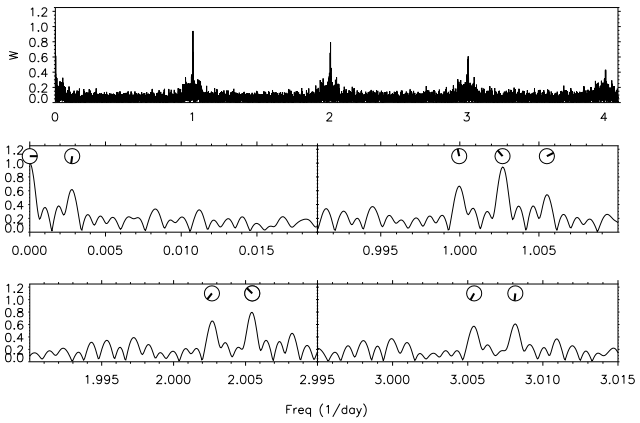

Figure 4.13.—: Spectral window function of Gl 581. These features, convolved with a planet's orbital frequency, cause the aliases evident in the periodogram in Fig. 4.14.

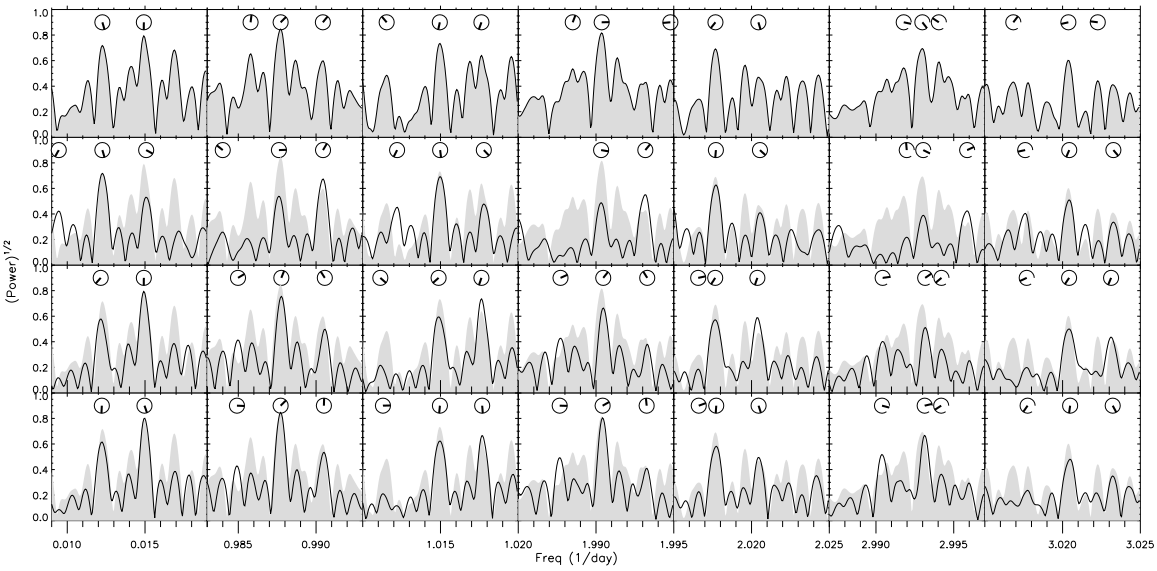

Figure 4.14.—: Periodograms of Gl 581 for planet d (planets b and c subtracted have been removed from the data set and planet e has been ignored; we obtain consistent results if we also remove planet e). Dials above the peaks denote their phase. Row 1 shows the data. The other rows show sinusoids sampled at the times of the real data sets (solid line and dial), as well as the data again for reference (in gray). In Row 2 the solid line shows, for these time samplings, the periodogram of a sinusoid of frequency 0.0122 day^{-1}. For Row 3, it is for 0.0150 day^{-1}. For Row 4, 0.9877 day^{-1}. In Rows 2-4, each peak results from the convolution of the sinusoidal frequency with the features in the spectral window function in Fig. 4.13. Note that the phases and amplitudes of 0.0122 day^{-1} and 0.0150 day^{-1} are not consistent with the aliases we would expect. The period remains ambiguous, but we favor 0.9877 day^{-1} based on this data set.

4.3.5 HD 156668 b

Howard et al. (2011) reported a 4 $M_\oplus$ planet orbiting HD 156668 b with period 4.6455 days (a frequency of 0.2153 day^{-1}). However, they considered that the correct period might be 1.2699 days (a frequency of 0.7875 day^{-1}), and our analysis confirms that as the correct period, as follows. The window function for this system is plotted in Fig. 4.15 and periodograms of the data and sinusoids at two candidate frequencies in Fig. 4.16. Note that large peaks in the window function occur at 1 sidereal and 1 synodic day while smaller peaks occur near 2 days (Fig. 4.15). For a true frequency of 0.2153 day^{-1} (second row), we would expect two pairs of large peaks due to sidereal and solar aliases (second row, second and third column) and a smaller pair of peaks for the $\sim$2 day^{-1} aliases (second row, fourth column). On the other hand, for a true frequency of 0.7875 day^{-1} (third row), we would expect two pairs of large peaks due to sidereal and solar aliases (third row, first and fourth column) and a smaller pair of peaks for the $\sim$ 2 day^{-1} aliases (third row, third column). The phase and amplitude of these aliases predicted for 0.7875 day^{-1} (row 3) are thus more consistent with the data (row 1). Therefore we conclude that the planet's true period is 1.2699 days and that the peak at period 4.6455 days identified by Howard et al. (2011) is an alias. The Keplerian orbital elements are reported in Table 4.1, along with the predicted transit window. The eccentricity was held to zero, as expected from tidal dissipation, following Howard et al. (2011). Howard et al. (2011) "filtered" the data by simultaneously fitting a two-planet model and a linear trend. They state that the "second planet" is a form of high-pass filter, not necessarily an actual planet. We do not fit a linear trend or additional planets in our reported fit and do not subtract them out in Fig. 4.16. However, we have confirmed that our results hold if we do.

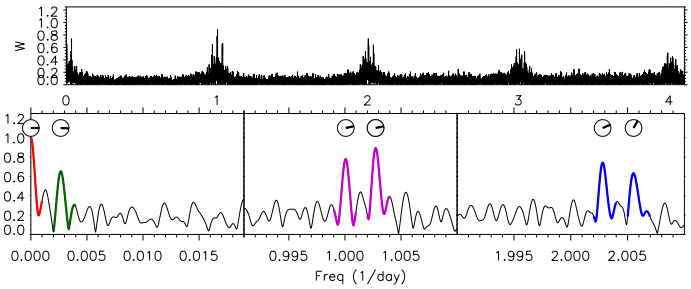

Figure 4.15.—: Spectral window function of RV measurements of HD 156668. Major features of the spectral window function are colored: red (at 0 day^{-1}), green (yearly feature), fuschia (daily features), and blue (two day^{-1}). The corresponding aliases these features cause for several candidate frequencies are indicated by these colors in 4.16.

Table 4.1. New parameters for HD 156668,$e_{\rm b} = 0$.[a]

	K ms^{-1}	$M \sin i$ M$_{Earth}$	P days	a AU	e	ω deg	λ deg	V ms^{-1}
b	2.2(3)	3.1(4)	1.26984(7)	0.0211(2)	0.000(0)	0.(0)	136.(19)	
								−0.4(2)

[a]The following gravitational constants were used: $GM_{\odot}$ = 0.0002959122082856, ratio of the sun to Earth = 332945.51. The mass of the star was assumed to be 0.77 solar masses. Formal errors from the Levenberg-Marquardt algorithm are given in parentheses, referring to the final digit(s).

Note. — Data are the Keck data presented by Howard et al. (2011). $T_{\rm epoch}$ is set to the first data point (JD 2453478.97768). These parameters predict a transit epoch of $T_{\rm tr}$[JD] = 2453478.82(7) + E × 1.26984(7).

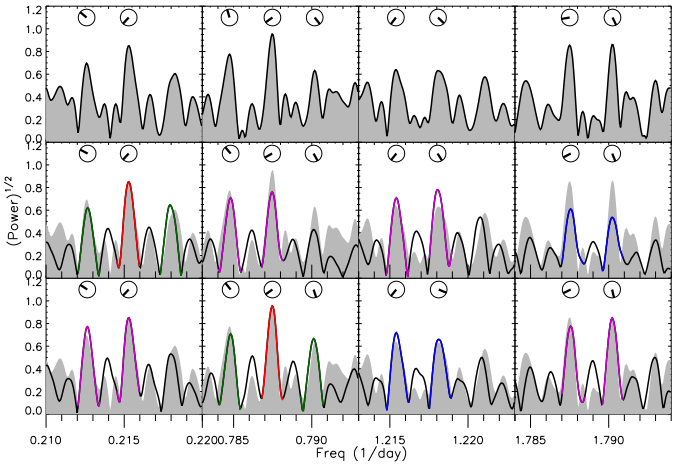

Figure 4.16.—: Periodograms of HD 156668. Row 1 shows the data. The other rows show sinusoids sampled at the times of the real data sets (solid line and dial), as well as the data again for reference (in gray). Colors correspond to the feature in the window function that creates the particular alias (see Fig. 4.15), with red being the candidate frequency, the green sidebands yearly aliases, and the fuschia and blue peaks daily and two day^{-1} aliases respectively. In Row 2 the solid line shows, for these time samplings, the periodogram of a sinusoid of frequency 0.215 day^{-1}. For Row 3, it is for 0.787 day^{-1}, our favored value. The two candidate frequencies have different types of aliases at different locations, allowing us to break the degeneracy.

4.3.6 55 Cnc

With five discovered planets (Fischer et al. 2008), more than any other extrasolar planetary system, 55 Cnc is a rich environment for study. The first planet was discovered by Butler et al. (1997): this planet b has an orbital period of 14.65 days. Five more years of observations revealed two additional planets (Marcy et al. 2002): planet c, with orbital period 44 days, and planet d, with orbital period 5000 days. Measurements from the Hobby-Eberly Telescope (McArthur et al. 2004) (HET) revealed, on their own and combined with the Lick measurements by Marcy et al. (2002) and ELODIE measurements by Naef et al. (2004), the presence of planet e, with a reported orbital period of 2.8 days. In 2005, in a poster presentation (Wisdom 2005) and an informally circulated paper [3], Wisdom (hereby referred to as W05) reanalyzed the combined HET, Lick, and ELODIE measurements, found evidence for a 260 day period planet, and questioned whether the reported 2.8 day signal might be an alias of planet c. Finally, Fischer et al. (2008) confirmed the 2.8 day planet e and reported a 260 day planet f based on a decade of Lick and Keck measurements. They also noted a peak at 460 days and considered whether this peak was an alias of the 260 day planet.

Because the literature has considered whether they might be aliases and because their periods are in the range where aliases can be the most confusing, planet e and planet f warrant additional consideration. We confirmed by our analysis that the period of f is correct. In the following subsection, we apply our method to planet e and find that the 2.8 day period is actually an alias, not of planet c but of a true period of 0.74

[3]Available electronically at

http://groups.csail.mit.edu/mac/users/wisdom/planet.ps

days: planet e still exists but its period is actually 0.7 days, not 2.8 days.

A New Period for 55 Cnc e

First, let us look at the discovery data for 55 Cnc e. We plot the window function for the data collected by McArthur et al. (2004) using HET in Fig. 4.17. The data spans only 190 days and therefore contains no yearly gaps. Therefore, no peak in the window function occurs at yr^{-1}, and there is no splitting of the daily alias into solar and sidereal days. We also note that this daily alias has quite a strong value of ~ 0.8. The consequence of that can be seen in Fig. 4.18, the periodogram using only the HET data. The top panels are the periodogram of the data themselves. The peaks at 0.356 day^{-1} and 1.358 day^{-1} are of similar size. In the middle panels, we sample a noiseless sinusoid with a period, amplitude, and phase matching that of the peak at 0.356 day^{-1}. An alias results at 1.358 day^{-1} at approximately the right height and phase, so McArthur et al. (2004) may have dismissed the latter as an alias, although they did not mention it explicitly. However, reversing the argument, if we had a noiseless sinusoid with the period, amplitude, and phase of the peak at 1.358 day^{-1} (bottom panels), then its alias nearly matches the peak at 0.356 day^{-1}, within the noise. This is to say, the data of McArthur et al. (2004) cannot distinguish between the two possible periods.

W05 presented two arguments for why the 2.8 day signal might be an alias. First he noticed that the 2.8 day period is linked to the 44 day period of planet c by a period of 3 days ($\frac{1}{2.8} \approx \frac{1}{3} + \frac{1}{44}$), but noted that there is no reason we would expect an alias to be caused by a 3 day period. In Fig. 4.17, 4.19, and 4.21 we demonstrate that there is no peak in the spectral window function at $\frac{1}{3}$ day^{-1} for any of the data sets. Therefore, the

2.8 day signal cannot be an alias of the 44 day signal.

Second, W05 noticed that in the HET data, one peak occurs at 2.808 day, while in the combined data set a pair of peaks occurs at 2.7957 days and 2.8175 day, a splitting of 1 year. In fact, this is just the doublet structure described in section 4.2.2. The combined set spans multiple years, which creates the yr^{-1} spacing in the doublet structure of the daily alias, as shown in Fig. 4.19. Therefore we would actually expect to see this doublet structure in the combined data set but only a single peak at the daily aliases in the HET data set.

So Wisdom was right to suspect that the 2.8 day signal is an alias. It is not an alias of the 44 day planet c but of a planet with true period 0.7 days; the alias is a daily alias (1/2.8 days = 1/0.74 days - 1/days).

With the combined data set, and with new data that has come out with higher precision from Lick and Keck (Fischer et al. 2008), we can confirm with high confidence that the 0.74 day period is the correct one. The window functions of these datasets are shown in Fig. 4.19 and 4.21. In Fig. 4.20 and 4.22 we show the resulting periodograms, after subtracting the signal of planets b, c, and d with a best-fitting Keplerian model. In both datasets, the true peak at 1.358 day^{-1} is very much higher and the other peaks at various frequencies are fully consistent with being an alias of it. For instance, in both datasets, doublet structure at the reported frequency shows that it is actually a daily alias. These peaks are identified for various candidate periods in Tables 4.2 and 4.4 for the combined data set and 4.3 and 4.5 for the Fischer et al. (2008) data set. We also performed the same analysis on the combined data set of all four instruments and obtained consistent results. The results are also unambiguous when only the Keck data

are used.

With this new period for planet e, we fit a 5-planet Keplerian model to the Keck and Lick data of Fischer et al. (2008), via the Levenberg-Marquardt algorithm implemented in IDL by Markwardt (2009). Following Fischer et al. (2008), jitter values of 1.5 m/s and 3.0 m/s were adopted for Keck and Lick data, respectively, such that the errors became $\sigma_i^2 = \sigma_{\rm quoted,i}^2 + \sigma_{\rm jitter,i}^2$. The resulting model fits the data much better than previous results, with the same number of free parameters. Compare Table 4.6 and Table 4.7. The rms is reduced from 6.45 $\rm ms^{-1}$ to 5.91 $\rm ms^{-1}$ (10%) and the $(\chi^2_\nu)^{1/2}$ is reduced from 1.666 to 1.411 (15%). We conclude that we have determined the correct period of 55 Cnc e.

We use an epoch chosen as the weighted average of the observation times. The weighting was $1/\sigma_i^2$; this weighting minimizes the correlation between the parameters P and λ for each planet. We have confirmed that the rms and $(\chi^2_\nu)^{1/2}$ we achieve using a weighted epoch, as opposed to using the first data point as the epoch, is identical in the Keplerian case.

With such a small period, we would expect planet e to circularize via tidal dissipation. Of course, in the presence of perturbations of the other planets, this expectation will not be completely fulfilled. Nevertheless, we also repeated the fit with the eccentricity of planet e fixed at zero (Table 4.8).

Fitting a self-consistent Newtonian 5-planet model, Fischer et al. (2008) obtained a $(\chi^2_\nu)^{1/2}$ of 2.012 and rms of 7.712 $\rm ms^{-1}$, significantly worse than their best Keplerian five-planet model. We performed our own self-consistent Newtonian 5-planet fit using the modified Wisdom-Holman symplectic integrator (Wisdom & Holman 1991) in SWIFT (Levison & Duncan 1994). Using our newly defined epoch, we obtain $(\chi^2_\nu)^{1/2}$ for both

candidate periods of planet e that are statistically indistinguishable from their Keplerian equivalents (Table 4.9 and Table 4.10). We speculate that the new epoch starts the Levenberg-Marquardt fit closer to the global minimum and strongly recommend choosing the epoch as the weighted average of the observation times, as we have done, instead of the first observation. We have only begun to explore the dynamics of this system and future work adjusting the line of sight inclination of the system and relative inclinations of the planets may result in improved fits and better characterization of the dynamics of this system.

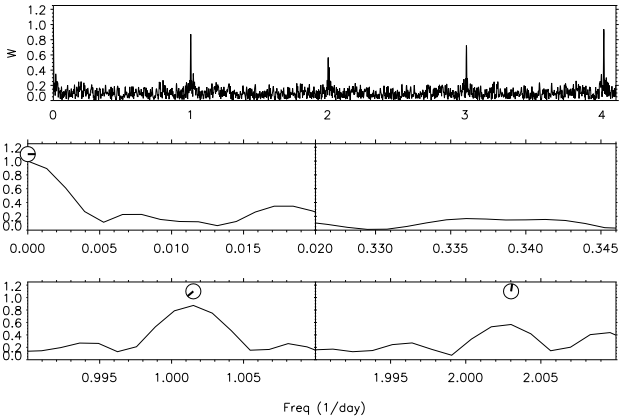

Figure 4.17.—: Spectral window function of 55 Cnc for HET data set (McArthur et al. 2004). These features, convolved with a planet's orbital frequency, cause the aliases evident in the periodogram in Fig. 4.18.

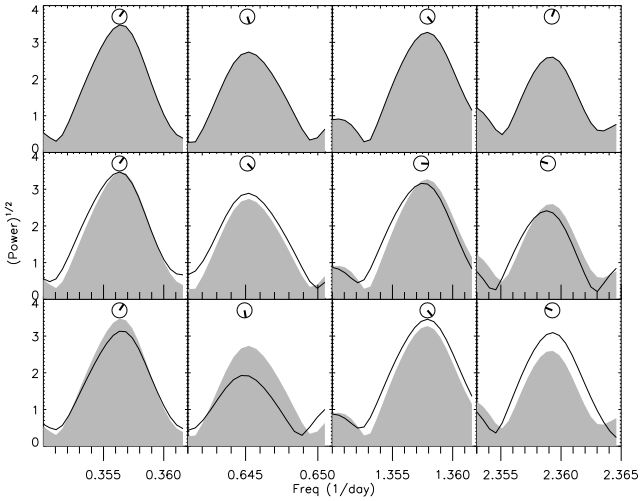

Figure 4.18.—: Periodograms of 55 Cnc for planet e only, using only the data from HET (McArthur et al. 2004). The top row is the periodogram of the data themselves. The other rows show the periodograms of sinusoids sampled at the times of the real data sets as solid lines; they also repeat the periodogram of the data as a gray background, for comparison. Dials above the peaks show the phase at each peak. The second row has a sinusoid of the reported frequency. The third row has a sinusoid of the new frequency. In Rows 2 and 3, each peak results from the convolution of the sinusoidal frequency with the features in the spectral window function in Fig. 4.17. In this data set, due to noise, neither noiseless candidate frequency matches the data. Note the large phase discrepancies between the reported frequency and the data. Based on this data set alone, the planet's orbital period cannot be unambiguously determined.

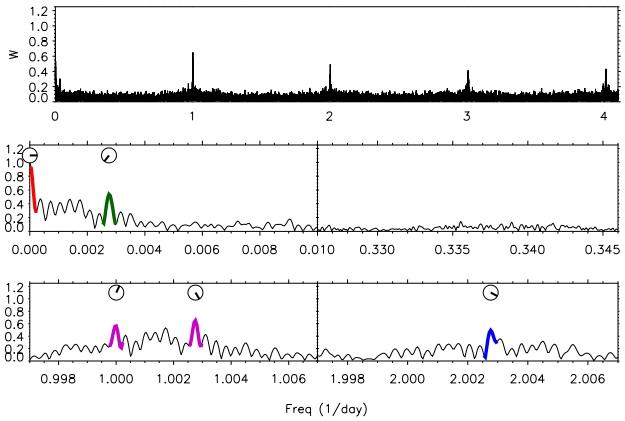

Figure 4.19.—: Spectral window function of 55 Cnc for HET data set combined with ELODIE (Naef et al. 2004) and Lick (Marcy et al. 2002). Major features of the spectral window function are colored: red (at 0 day^{-1}), green (yearly feature), fuschia (daily features), and blue (two day^{-1}). The corresponding aliases these features cause for several candidate frequencies are indicated by these colors in 4.20.

Table 4.2. 55 Cnc Combined Data Set: expectations from the window function.

Candidate	Window Function Feature							
frequency, f	0.0028-f	0.0028+f	1.0000-f	1.0027-f	1.0000+f	1.0027+f	2.0028-f	2.0028+f
0.3550	0.3522	0.3578	0.6450	0.6477	**1.3550**	1.3577	–	–
0.3577	0.3549	**0.3605**	0.6423	0.6450	1.3577	**1.3604**	–	2.3604
1.3577	**1.3549**	**1.3605**	**0.3550**	**0.3577**	**2.3577**	**2.3604**	–	–

Note. — Along the top row are peaks in the window function at frequencies f_s (Fig. 4.19). Each row refers to a candidate frequency f; rows 1-3 in this table match to rows 2-4 in Fig. 4.20, respectively. The cells are frequency values $|f \pm f_s|$ expected for peaks in the periodogram. If the predicted alias is consistent with a peak in the data in both amplitude and phase, the cell is bolded. A non-emphasized cell indicates a large discrepancy in amplitude or phase. For dashed cells, no comparison was done. Units are day^{-1}. The frequency of $f = 1.3577$ day^{-1} is overwhelmingly the best match to the data.

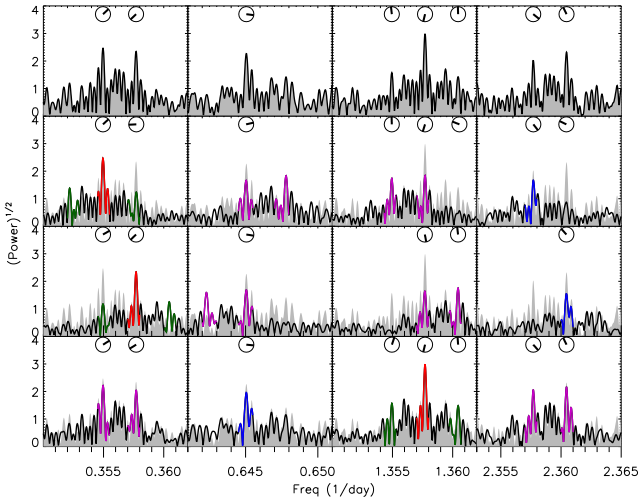

Figure 4.20.—: Periodogram of 55 Cnc for planet e only. Dials above the peaks denote their phase. Colors correspond to the feature in the window function that creates the particular alias (see Fig. 4.19), with red being the candidate frequency, the green sidebands yearly aliases, and the fuschia and blue peaks daily and two day^{-1} aliases respectively. The top row shows the data (HET+ELODIE+Lick). In Row 2 the solid lines show, for these time samplings, the periodogram of a sinusoid of frequency 0.3550 day^{-1}. For Row 3, it is for 0.3577 day^{-1}. For Row 4, it is for 1.3577 day^{-1}, our now-favored value. The three candidate frequencies have different types of aliases at different locations, allowing us to break the degeneracy.

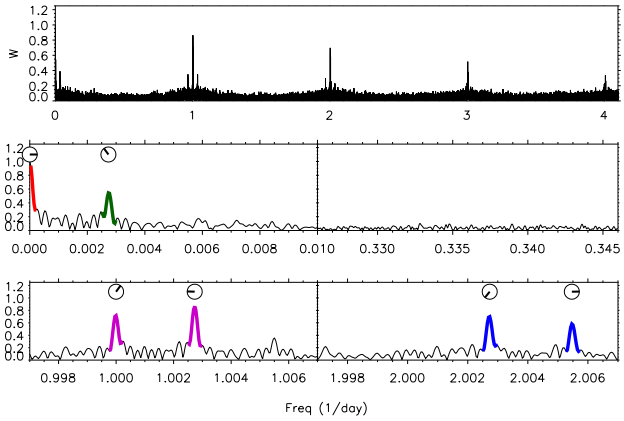

Figure 4.21.—: Spectral Window Functions of 55 Cnc for combined Lick and Keck data set (Fischer et al. 2008). Major features of the spectral window function are colored: red (at 0 day^{-1}), green (yearly feature), fuschia (daily features), and blue (two day^{-1}). The corresponding aliases these features cause for several candidate frequencies are indicated by these colors in 4.22.

Table 4.3. 55 Cnc Fischer et al. (2008) Data Set: expectations from the window function.

Candidate	Window Function Feature									
frequency, f	0.0028-f	0.0028+f	1.0000-f	1.0027-f	1.0000+f	1.0027+f	2.0027-f	2.0055-f	2.0027+f	2.0055+f
0.3550	**0.3522**	0.3578	**0.6450**	0.6477	**1.3550**	1.3577	–	–	**2.3577**	2.3605
0.3577	0.3549	**0.3605**	**0.6423**	**0.6450**	1.3577	**1.3604**	–	–	2.3604	**2.3632**
1.3577	**1.3542**	**1.3605**	**0.3550**	**0.3577**	**2.3577**	**2.3604**	**0. 6450**	**0.6478**	–	–

Note. — The format is the same as Table 4.2. Features in the window function are from Fig. 4.21. The candidate frequencies in rows 1-3 in this table match to rows 2-4 in Fig. 4.22, respectively.

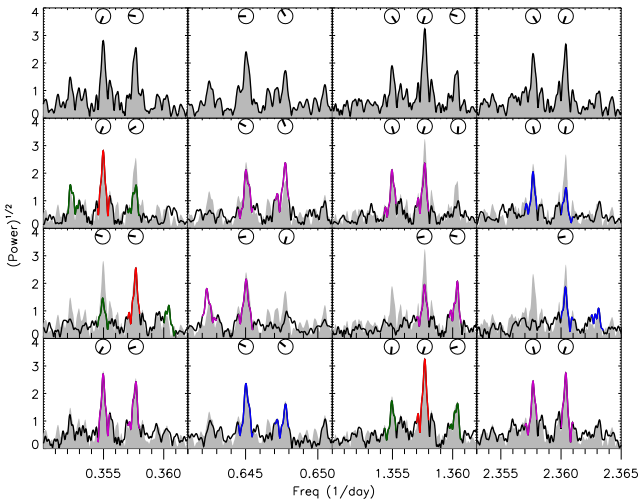

Figure 4.22.—: Periodogram of 55 Cnc for planet e only. Dials above the peaks denote their phase. Colors correspond to the feature in the window function that creates the particular alias (see Fig. 4.21), with red being the candidate frequency, the green sidebands yearly aliases, and the fuschia and blue peaks daily and two day^{-1} aliases respectively. Row 1 shows the data (Lick+Keck). In Row 2 the solid lines show, for these time samplings, the periodogram of a sinusoid of frequency 0.3550 day^{-1}. For Row 3, it is for 0.3577 day^{-1}. For Row 4, it is for 1.3577 day^{-1}, our now-favored value. The three candidate frequencies have different types of aliases at different locations, allowing us to break the degeneracy.

Table 4.4. 55 Cnc Combined Data Set: features in the data periodogram.

Candidate	Major Data Feature					
frequency, f	0.3550	0.3577	0.6450	1.3577	2.3577	2.3604
0.3550	**f**	f + 0.0028	**1.0000-f**	**1.0027+f**	**2.0027+f**	
0.3577	f-0.0028	**f**	**1.0027-f**	1.0000+f		2.0027+f
1.3577	**f-1.0027**	**f -1 .0000**	**2.0027-f**	**f**	**1.0000+f**	**1.0027+f**

Note. — The top row indicates a major peak seen in the data *near the frequencies where aliases are predicted.* Each row refers to a candidate frequency; rows 1-3 in this table match to rows 2-4 in Fig. 4.19, respectively. If, based on examining the plots, the frequency creates an alias that matches that peak in the data in both amplitude and phase, the cell is bolded. A non-emphasized cell indicates a large discrepancy in amplitude or phase. A blank cell indicates that the candidate frequency does not cause an alias at that frequency. Units are day^{-1}. This table shows that a frequency of 1.3577 day^{-1} is best able to account for the peaks in the data.

Table 4.5. 55 Cnc Fischer et al. (2008) Data Set: features in the data periodogram.

Candidate	Major Data Feature						
frequency, f	0.3550	0.3577	0.6450	0.6478	1.3577	2.3577	2.3604
0.3550	**f**	f + 0.0028	**1.0000-f**	1.0027-f	**1.0027+f**	**2.0027+f**	2.0054+f
0.3577	f-0.0028	**f**	**1.0027-f**		1.0000+f		2.0027+f
1.3577	**f-1.0027**	**f -1 .0000**	**2.0027-f**	**2.0054-f**	**f**	**1.0000+f**	**1.0027+f**

Note. — The format is the same as Table 4.4. Candidate frequencies in rows 1-3 in this table match to rows 5-8 in Fig. 4.21, respectively.

Table 4.6. 55 Cnc Keplerian radial velocity fit, $P_e = 2.8$ days.[a]

	K ms^{-1}	$M \sin i$ M_{Jup}	P days	a AU	e	ω deg	λ deg	V_L ms^{-1}	V_K ms^{-1}	χ^2	N	$(\chi^2_\nu)^{1/2}$
e	5.2(2)	0.0346(16)	2.81705(5)	0.0382(3)	0.066(48)	238.(41)	86(14)					
b	71.3(3)	0.824(3)	14.65164(11)	0.1148(8)	0.014(4)	135.(15)	327.4(10)					
c	10.0(2)	0.167(4)	44.349(7)	0.2402(17)	0.09(3)	66.(17)	312(7)					
f	5.3(3)	0.148(9)	259.7(5)	0.780(6)	0.40(5)	182.(9)	308(14)					
d	46.9(4)	3.84(4)	5191.(53)	5.76(6)	0.015(9)	223.(33)	201(4)					
								6.8(6)	5.9(7)	813.2	27	1.666

[a]The following gravitational constants were used: $GM_\odot = 0.0002959122082856$, ratio of the sun to Jupiter = 1047.35. The mass of the star was assumed to be 0.94 solar masses. Formal errors from the Levenberg-Marquardt algorithm are given in parentheses, referring to the final digit(s). Masses and semi-major axes are in Jacobian coordinates, as recommended by Lee & Peale (2003).

Note. — Data are the Lick and Keck data presented by Fischer et al. (2008). T_{epoch} is set to the weighted mean of the observation times (JD 2453094.762), which should minimize the correlation in the errors between P and λ for each planet.

Table 4.7. 55 Cnc Keplerian radial velocity fit, $P_e = 0.74$ days.[a]

	K ms^{-1}	$M \sin i$ M_{Jup}	P days	a AU	e	ω deg	λ deg	V_L ms^{-1}	V_K ms^{-1}	χ^2	N	$(\chi^2_\nu)^{1/2}$
e	6.2(2)	0.0261(10)	0.736539(3)	0.01564(11)	0.17(4)	177.(13)	126(2)					
b	71.4(3)	0.826(3)	14.65160(11)	0.1148(8)	0.014(4)	146.(15)	139.7(2)					
c	10.2(2)	0.171(4)	44.342(7)	0.2402(17)	0.05(3)	95.(28)	90.(2)					
f	5.1(3)	0.150(8)	259.8(5)	0.781(6)	0.25(6)	180.(12)	36(4)					
d	46.6(4)	3.83(4)	5205.(54)	5.77(6)	0.024(10)	192.(16)	222.7(8)					
								6.7(5)	6.5(6)	583.1	27	1.411

Note. — Data are the Lick and Keck data presented by Fischer et al. (2008). T_{epoch} is set to the weighted mean of the observation times (JD 2453094.762), which should minimize the correlation in the errors between P and λ for each planet. For planet e, these parameters predict a transit epoch of $T_{\mathrm{tr}}[\mathrm{JD}] = 2453094.728(10) + \mathrm{E} \times 0.736539(3)$.

Table 4.8. 55 Cnc Keplerian radial velocity fit, $P_{\rm e} = 0.74$ days,$e_{\rm e} = 0$.[a]

	K $\rm ms^{-1}$	$M \sin i$ $\rm M_{Jup}$	P days	a AU	e	ω deg	λ deg	V_L $\rm ms^{-1}$	V_K $\rm ms^{-1}$	χ^2	N	$(\chi^2_\nu)^{1/2}$
e	6.1(2)	0.0258(10)	0.736540(3)	0.01564(11)	0.000(0)	0.(0)	126(2)					
b	71.4(3)	0.825(3)	14.65158(11)	0.1148(8)	0.012(4)	147.(17)	139.7(2)					
c	10.3(2)	0.172(4)	44.341(7)	0.2402(17)	0.06(3)	99.(23)	90.5(15)					
f	5.0(3)	0.150(8)	260.0(5)	0.781(6)	0.13(6)	180.(21)	37(3)					
d	46.7(4)	3.83(4)	5214.(54)	5.77(6)	0.029(10)	189.(14)	222.6(8)					
								6.8(5)	6.3(6)	598.1	27	1.429

Note. — Data are the Lick and Keck data presented by Fischer et al. (2008). $T_{\rm epoch}$[JD] = 2453094.762 Because tidal dissipation has most likely nearly circularized planet the orbit or planet e, here $e_{\rm e}$ is held at zero. For planet e, these parameters predict a transit epoch of $T_{\rm tr}$[JD] = 2453094.688(4) + E × 0.736540(3).

Table 4.9. 55 Cnc dynamical radial velocity fit, $P_e = 2.8$ days.[a]

	K $\rm ms^{-1}$	$M \sin i$ $\rm M_{Jup}$	P days	a AU	e	ω deg	λ deg	V_L $\rm ms^{-1}$	V_K $\rm ms^{-1}$	χ^2	N	$(\chi^2_\nu)^{1/2}$
e	5.1(2)	0.0339(16)	2.81703(17)	0.0382(3)	0.09(5)	178(4)	118(4)					
b	71.4(3)	0.825(3)	14.6507(4)	0.1148(8)	0.011(3)	143(19)	139.7(4)					
c	10.1(2)	0.169(4)	44.375(10)	0.2403(17)	0.02(2)	359.9(3)	88(2)					
f	5.8(3)	0.158(8))	259.8(4)	0.781(6)	0.42(4)	178(3)	33.(3)					
d	47.1(6)	3.84(4)	5165.(43)	5.74(4)	0.012(6)	279(22)	224.0(6)					
								6.3(5)	5.9(6)	830.1	27	1.683

Note. — Data are the Lick and Keck data presented by Fischer et al. (2008). $T_{\rm epoch}$ is set to the weighted mean of the observation times (JD 2453094.762), which should minimize the correlation in the errors between P and λ for each planet. Masses and semi-major axes are in Jacobian coordinates, as recommended by Lee & Peale (2003).

Table 4.10. 55 Cnc dynamical radial velocity fit, $P_e = 0.74$ days.[a]

	K ms^{-1}	$M \sin i$ M_{Jup}	P days	a AU	e	ω deg	λ deg	V_L ms^{-1}	V_K ms^{-1}	χ^2	N	$(\chi^2_\nu)^{1/2}$
e	6.2(2)	0.0260(10)	0.736537(13)	0.01560(11)	0.17(4)	181(2)	125.(6)					
b	71.4(3)	0.825(3)	14.6507(4)	0.1148(8)	0.010(3)	139(17)	139.6(3)					
c	10.2(2)	0.171(4)	44.364(7)	0.2403(17)	0.005(3)	252.(41)	90.(2)					
f	5.4(3)	0.155(8)	259.8(5)	0.781(6)	0.30(5)	180.(10))	35.(3)					
d	46.8(6)	3.82(4)	5169.(53)	5.74(4)	0.014(9)	186(8)	223.2(7)					
								6.3(5)	6.3(6)	591.7	27	1.421

Note. — Data are the Lick and Keck data presented by Fischer et al. (2008). T_{epoch} is set to the weighted mean of the observation times (JD 2453094.762), which should minimize the correlation in the errors between P and λ for each planet.

4.4 Discussion

4.4.1 Summary of Approach

Aliases result from a convolution between a true physical frequency and the spectral window function, which is created by gaps in the data set due to observational constraints. Our method harnesses features in the window function to distinguish aliases from true frequencies. For a given frequency f and window function peak f_s, aliases will occur at $|f \pm f_s|$, where f_s is a feature in the window function. In the ranges where we expect major aliases to occur, we compare the phase and amplitude of aliases predicted by a sinusoid of the candidate frequency sampled to the data, with other known planets subtracted off beforehand. We judge whether the "pattern" of the predicted aliases matches the data: for example, yearly aliases appear as sidebands of the candidate frequency while daily aliases often appear as a doublet caused by the sidereal and solar day. If all the aliases match in amplitude, phase, and pattern, we can be confident that we have found the true orbital period. If there are discrepancies and the aliases of none of the candidate frequencies match the data, we know that noise prevents us from definitively determining the true period and that follow-up observations are necessary. Misunderstandings about aliases have previously led to incorrect identification of planet's orbital periods, a key parameter in defining the planet's properties, as well as the dynamical behavior of the planets in the system. We have corrected common misconceptions, including that aliases always appear near the frequency of peaks in the window function, that any frequency above 1 cycle/day is necessarily an alias, and that aliases will appear if the data are scrambled or if the true frequency is subtracted out.

4.4.2 Summary of Results

For two systems, we confirmed previous distinctions between alias and true frequency. The period of GJ 876 d is indeed 1.94 days, not 2.05 days. The period of HD 75898 b is indeed 400 days and the periodogram peak at 200 days is indeed an alias, not a second planet or eccentricity harmonic, the alternative explanations proposed by Robinson et al. (2007).

For two other systems, we determined that the data are too noisy to allow us to definitely distinguish between alias or true frequency. According to our analysis, it remains unclear whether the period of Gl 581 d is 67 days or 83 days; even a period of 1 day cannot be ruled out. It also remains unclear whether HD 73526 contains two planets with orbital periods 187.5 and 376.9 days, locked in a 2:1 resonance, or whether one of the periods is actually 127 days. Further observations of these systems are required, preferably at times that reduce the aliasing.

For a final pair of systems, we determined the reported orbital period was incorrect, due to mistaking a daily alias for the true frequency. According to our analysis, the orbital period of HD 156668 b is actually 1.2699 days, not 4.6455 days. The orbital period 55 Cnc e is 0.7365 days, not 2.817 days. The standard, general-purpose software *SigSpec* mentioned in the introduction (Reegen 2007, 2011) agrees with our orbital period distinctions (we used the parameters: depth=2, par = 0.2 and par = 0.5, and a frequency upper limit of 2 day$-$1).

4.4.3 Implications for 55 Cnc e

What are the implications of an updated period for the innermost planet of 55 Cnc?

First, it dramatically lowers the effective noise when determining the parameters of the planetary system. Fischer et al. (2008) reported independent Keplerian fits with rms of 6.74 m/s, and a self-consistent dynamical fit with rms of 7.712 m/s. Our Keplerian fit achieves rms of 5.91 m/s, and our self-consistent coplanar dynamical fit achieves rms of 5.96 m/s. By adjusting the inclination of the system relative to our line-of-sight and the planets' mutual inclinations, an even better self-consistent might be possible. Therefore perturbations might be directly detected via a lower rms when interactions among the planets are included, and the architecture of the system further constrained. We have just begun exploring this avenue.

Second, 55 Cnc e itself can now be searched for transits at the new period, with high a priori probability of $\sim 25\%$. Given the period and phase of the radial-velocity signal, we report predicted transit epochs in Tables 4.7 and 4.8. The predictions differ because the latter assumes zero eccentricity, and the formally significant value of $e_{\rm e}$ matters. Nevertheless, folding the systematic uncertainty related to eccentricity into the predicted transit time, we still can predict transit times good to $\sigma_T \simeq 1$ hour in 2010. This search can be accomplished simply by folding the photometric data reported by Fischer et al. (2008) at the new ephemeris. Gregory Henry (priv. comm.) has made such a search, finds no positive signal, and constrains putative transits in the period range $0.7 - 0.8$ days to a depth < 0.7 mmag, or $> 2.6\ R_\oplus$. Earth-composition models of super-Earths predict a radius $\sim 1.9\ R_\oplus$ (Valencia et al. 2006), so a search at higher precision is certainly worthwhile.

Third, even apart from a transit, this super-Earth must be very hot, as it is very close-in to a solar-type star. Following Léger et al. (2009), we find that the substellar point could be up to 2750 K, if the insolation is absorbed then reradiated locally. We would naively expect that the enormous radiation this planet takes in would evaporate any atmosphere (e.g., Jackson et al. 2010). Moreover, the host star is also very bright as seen from Earth. Therefore it might be useful to look for its phase curve with Spitzer, to detect or rule out an atmosphere (Seager & Deming 2009). Another attractive possibility is probing a magma ocean, which may exist because of the irradiation (Gelman et al. 2009; Gaidos et al. 2010), but this may require transit measurements.

Fourth, the presence of the other 4 planets surely injects a non-zero eccentricity into this tidally-dissipating planet. Its expected value remains to be calculated, but will likely be on the order of 10^{-4}. This forced eccentricity could stimulate considerable geologic activity — it might be a "super-Io" (Barnes et al. 2010).

4.4.4 Observational Strategies for Mitigating Aliases

Can aliases be prevented or mitigated by the choice of observation times? Constraints on when the star is visible at night necessarily result in gaps in the data that cause aliases. However, we encourage observers to engage in "window carpentry" (Scargle 1982) by observing the star during the greatest span of the sidereal and solar day possible, not just when the star transits the meridian. Unfortunately, observing stars as they rise and set poses a challenge for observers, who minimize slew time[4] and thus maximize the

[4]If the slew time exceeds the read-out time, fewer observations may be gathered per night. However, the wise spacing of observation times can more than make up for this through disambiguation of alias

number of stars observed per night by observing at the meridian for the majority of the night. This observing strategy (Fig. 4.3b) results in strong daily and yearly aliases (ex. Fig. 4.13). Another strategy is to start in the west and gradually move east over the course of the night (Fig. 4.3c), observing as much of the sky as possible. This strategy reduces yearly aliases but sidereal daily aliases remain strong (ex. Fig. 4.15 and 4.21). To reduce sidereal daily aliases, we recommend the following procedure. Start the telescope somewhere west of the meridian (randomized from night to night) and move east to cover half the sky over the course of half the night. Then make one large slew to the place the telescope started and re-observe the same portion of the sky. Some stars will gain the advantage of being observed twice in one night. Moreover, when the data are folded at the mean sampling period, they still show some variety in phase of observation, which is needed to reduce window function peaks and de-alias candidate periods. However, another consideration is that at higher air mass, both the extinction is greater and the seeing is worse. The increased atmospheric attenuation means a longer integration time is required, reducing the number of stars that can be observed, while the seeing increases the measurement errors. For a particular set of stars, observers can work out a slew pattern that will maximize the number of stars observed while minimizing aliasing. Saunders et al. (2006) present a clever method for determining the optimal sampling when period searching using satellite telescopes or a longitude-distributed network that can observe continuously. Unfortunately this strategy is impractical to implement using a single telescope on the ground. Ford (2008) presents useful adaptive scheduling algorithms for observing multiple targets that can be parametrized to reduce aliasing.

---

frequencies using fewer data points.

We suggest taking advantage of any unusual time windows: for example, the rare granted dark time or time at the beginning or end of another observer's night. Observers focusing on a large group of stars can determine which star would most benefit from this unusual time by calculating the window function with the new observation times added or, in the case of a planet with two candidate periods, determining for which system the observation times would best distinguish between two candidate orbits. We also suggest that it would be beneficial to observe stars using telescopes in two or more locations at different latitude and longitudes (ex. Fig. 4.19).

At the stage of data analysis, we encourage the use of our method to distinguish true frequencies from aliases, crucial for the correct characterization of the planet. As astronomers push to observing lower mass planets and modeling planets near the noise limit, they cannot assume that the highest peak in the periodogram – or even the best Keplerian fit – corresponds to the true orbital period. Only by harnessing features in the window function to compare the amplitude, phase, and pattern of an assortment of predicted aliases to the data can we distinguish the planet's true orbital frequency – or determine that more observations are needed.

4.4.5 Conclusion

Knowing a planet's correct orbital period is essential for accurately characterizing it. By Kepler's law, the planet's distance from the star increases as its orbital period increases. Therefore the planet's orbital period sets its temperature: too hot, too cold, or just right for life. The planet's inferred mass, as calculated from the radial velocity amplitude, increases as the period decreases – a closer planet needs less mass to exert a given force

on the star – so a difference in orbital period may be the difference between an Earth analog and a super-Earth. In the case of multi-planet systems, the spacing of the planets determines their mutual interactions: therefore a difference in orbital period may be the difference between a precariously placed planet and one locked deep in a stabilizing resonance. The signal of a planet's eccentricity is contained in the harmonics of the planet's orbital period: therefore a difference in orbital period may be the difference between a planet that formed in situ and a planet violently scattered, a calm planet that has long been tidally circularized or a planet erupting with volcanoes due to tidal dissipation. But periods that correspond to totally different worlds are only subtly distinguishable in the radial velocity signal. Such are the machinations of aliases.

Through our method, astronomers can confirm a planet's orbital period or determine that noise prevents a definitive distinction. In the latter case, follow-up observations taken according to the suggestions above should eventually allow the true period to be determined. Ironically, Earth's own rotational and orbital period make it challenging to uncover the orbital period of other worlds, particularly Earth analogs. But by better understanding of digital signal processing, we can mitigate the deleterious effects of the inevitable sunrise and starset.

Chapter 5

The Photoeccentric Effect and Proto-hot Jupiters. I. Measuring Photometric Eccentricities of Individual Transiting Planets

R. I. Dawson & J. A. Johnson *The Astronomical Journal*, Vol. 756, id. 122, 2012

Abstract

Exoplanet orbital eccentricities offer valuable clues about the history of planetary systems. Eccentric, Jupiter-sized planets are particularly interesting: they may link the "cold" Jupiters beyond the ice line to close-in hot Jupiters, which are unlikely to

have formed in situ. To date, eccentricities of individual transiting planets primarily come from radial velocity measurements. *Kepler* has discovered hundreds of transiting Jupiters spanning a range of periods, but the faintness of the host stars precludes radial velocity follow-up of most. Here we demonstrate a Bayesian method of measuring an individual planet's eccentricity solely from its transit light curve using prior knowledge of its host star's density. We show that eccentric Jupiters are readily identified by their short ingress/egress/total transit durations – part of the "photoeccentric" light curve signature of a planet's eccentricity — even with long-cadence *Kepler* photometry and loosely-constrained stellar parameters. A Markov Chain Monte Carlo exploration of parameter posteriors naturally marginalizes over the periapse angle and automatically accounts for the transit probability. To demonstrate, we use three published transit light curves of HD 17156 b to measure an eccentricity of $e = 0.71^{+0.16}_{-0.09}$, in good agreement with the discovery value $e = 0.67 \pm 0.08$ based on 33 radial-velocity measurements. We present two additional tests using actual *Kepler* data. In each case the technique proves to be a viable method of measuring exoplanet eccentricities and their confidence intervals. Finally, we argue that this method is the most efficient, effective means of identifying the extremely eccentric, proto hot Jupiters predicted by Socrates et al. (2012).

5.1 Introduction

Many exoplanets have highly eccentric orbits, a trend that has been interpreted as a signature of the dynamical processes that shape the architectures of planetary systems (e.g. Jurić & Tremaine 2008; Ford & Rasio 2008; Nagasawa & Ida 2011). *Giant* planets on eccentric orbits are of particular interest because they may be relics of the same

processes that created the enigmatic class of planets known as hot Jupiters: planets on very short period (P $<$ 10 days) orbits that, unlike smaller planets (e.g. Hansen & Murray 2012), could not have formed in situ. Hot Jupiters may have smoothly migrated inward through the disk from which they formed (e.g. Goldreich & Tremaine 1980; Ward 1997; Alibert et al. 2005; Ida & Lin 2008; Bromley & Kenyon 2011). Alternatively, the typical hot Jupiter may have been perturbed by another body onto an eccentric orbit (see Naoz et al. 2012), with a star-skirting periapse that became the parking spot for the planet as its orbit circularized through tidal dissipation, initiated by one of several perturbation mechanisms (e.g. Wu & Murray 2003; Ford & Rasio 2006; Wu & Lithwick 2011).

Socrates et al. (2012b) (hereafter S12) refer to this process as "high eccentricity migration" (HEM). If HEM were responsible for hot Jupiters, at any given time we would observe hot Jupiters that have undergone full tidal circularization, failed hot Jupiters that have tidal timescales too long to circularize over the star's lifetime, and proto hot Jupiters that are caught in the process of tidal circularization. S12 predicted that the *Kepler* Mission should detect several "super-eccentric" proto hot Jupiters with eccentricities in excess of 0.9. This prediction was tested by Dong et al. (2013) on a sample of eclipsing binaries in the *Kepler* field: in an incomplete search, they found 14 long-period, highly eccentric binaries and expect to eventually find a total of 100.

As a test of planetary architecture theories, we are devoting a series papers to measuring the individual eccentricities of the *Kepler* Jupiters to either identify or rule out the super-eccentric proto hot Jupiters predicted by S12. In this first paper, we describe and demonstrate our technique for measuring individual eccentricities from transit light curves. Measuring the eccentricity of a Jupiter-sized planet is also key to

understanding its tidal history (e.g. Jackson et al. 2008a; Hansen 2010) and tidal heating (e.g. Mardling 2007; Jackson et al. 2008b), climate variations (e.g. Kataria et al. 2011), and the effect of the variation in insolation on the habitability (e.g. Spiegel et al. 2010; Dressing et al. 2010) of possible orbiting rocky exomoons detectable by *Kepler* (e.g. Kipping et al. 2009).

To date, the measurements of eccentricities of individual transiting planets have been made through radial velocity follow-up, except when the planet exhibits transit timing variations (e.g. Nesvorný et al. 2012). However, a *transit light curve* is significantly affected by a planet's eccentricity, particularly if the photometry is of high quality: we refer to the signature of a planet's eccentricity as the "photoeccentric" effect. One aspect is the asymmetry between ingress and egress shapes (Burke et al. 2007; Kipping 2008). The eccentricity also affects the timing, duration, and existence of secondary eclipses (Kane & von Braun 2009; Dong et al. 2013). The most detectable aspect of the photoeccentric effect in *Kepler* photometry for long-period, planet-sized companions is the transit event's duration at a given orbital period P, which is the focus of this work.

Depending on the orientation of the planet's argument of periapse (ω), the planet moves faster or slower during its transit than if it were on a circular orbit with the same orbital period (Barnes 2007, Burke 2008, Ford et al. 2008, hereafter FQV08; Moorhead et al. 2011). If the transit ingress and egress durations can be constrained, the duration aspect of the photoeccentric effect can be distinguished from the effect of the planet's impact parameter (b), because although $b > 0$ shortens the full transit duration (T_{23}, during which the full disk of the planet is inside the disk of the star, i.e. from second to third contact), it lengthens the ingress/egress duration. Therefore, with prior knowledge or assumptions of the stellar parameters, combined with measurements from the light

curve of the planet's period and size ($R_P/R_\star$), one can identify highly eccentric planets as those moving at speeds inconsistent with a circular orbit as they pass in front of their stars (see also §3 of Barnes 2007, §3.1 of FQV08).

Barnes (2007) presented the first comprehensive description of the effects of orbital eccentricity on a transit light curve, including that a short transit duration corresponds to a minimum eccentricity, contingent on the measurement of b and of the host star's density. Burke (2008) discussed the effect of orbital eccentricity on transit detection and on the inferred distribution of planetary eccentricities. FQV08 laid out the framework for using photometry to measure both the distribution of exoplanet eccentricities and, for high signal-to-noise transits of stars with known parameters, the eccentricities of individual planets. They derived expressions linking the orbital eccentricity to the transit duration and presented predicted posterior distributions of eccentricity and ω for a given ratio of: 1) the measured total transit duration (i.e. from first to fourth contact, including ingress and egress) T_{14} to 2) the T_{14} expected for a planet on a circular orbit with the same b, stellar density $\rho_\star$, and P. Then they showed how the distribution of planetary transit durations reveals the underlying eccentricity distribution. FQV08 focused on the possibility of measuring the eccentricity distribution of terrestrial planets, which has implications for habitability. Here we will show that the technique they describe for measuring *individual* planet eccentricities is particularly well-suited for Jupiter-sized planets.

The work of FQV08 was the basis for several recent analyses of high-precision light curves from the *Kepler* mission that have revealed information about the eccentricity distribution of extra-solar planets and the eccentricities of planets in multi-transiting systems. By comparing the distribution of observed transit durations to the distribution

derived from model populations of eccentric planets, Moorhead et al. (2011) ruled out extreme eccentricity distributions. They also identified individual planets with transit durations too long to be consistent with a circular orbit; these planets are either on eccentric orbits (transiting near apoapse) or orbit host stars whose stellar radii are significantly underestimated.

Kane et al. (2012) used the distribution of transit durations to determine that the eccentricity distribution of *Kepler* planets matches that of planets detected by the RV method and to discover a trend that small planets have less eccentric orbits. In contrast, Plavchan et al. (2012) found that the distribution of eccentricities inferred from the transit durations is not in agreement with the eccentricity distribution of the RV sample; they suggested that the difference may be due to errors in the stellar parameters. Finally, Kipping et al. (2012) presented a method that they refer to as *Multibody Asterodensity Profiling* to constrain eccentricities of planets in systems in which multiple planets transit. They noted that one can also apply the technique to single transiting planets, but discouraged doing so, except for planets whose host star densities have been tightly constrained (e.g. by asteroseismology). FQV08 recommend measuring eccentricities photometrically only for planets with "well-measured stellar properties" but also point out the weak dependence of eccentricity on stellar density.

In this work we apply the idea first proposed by FQV08 to real data and demonstrate that we can measure the eccentricity of an individual transiting planet from its transit light curve. We show that this technique is particularly well-suited for our goal of identifying highly eccentric, giant planets. In Section 5.2, we show that even a loose prior on the stellar density allows for a strong constraint on the planet's orbital eccentricity. In Section 5.3, we argue that Markov Chain Monte Carlo (MCMC) exploration of the

parameter posteriors naturally marginalizes over the periapse angle and automatically accounts for the transit probability. We include both a mathematical and practical framework for transforming the data and prior information into an eccentricity posterior. In Section 5.4, we measure the eccentricity of HD 17156 b from ground-based transit light curves alone, finding good agreement with the nominal value from RV measurements. We also measure the eccentricity of a transit signal injected into both short and long cadence *Kepler* data and of *Kepler* Object of Interest (KOI) 686.01 from long-cadence, publicly-available *Kepler* data, finding an eccentricity of $e = 0.62^{+0.18}_{-0.14}$. In Section 5.5, we present our program of "distilling" highly eccentric Jupiters from the KOI sample and we conclude (Section 5.6) with prospects for further applications of the photoeccentric effect.

5.2 Precise Eccentricities from Loose Constraints on Stellar Density

To first order, a transiting planet's eccentricity and its host star's density depend degenerately on transit light curve observables. Kipping et al. (2012) harnessed the power of multiple planets transiting the same host star to break this degeneracy (see also Ragozzine & Holman 2010). Yet, as FQV08 first pointed out, although the transit observables depend on the stellar density, this dependence is weak (the ratio of the planet's semi-major axis to the stellar radius $a/R_\star \propto \rho_\star^{1/3}$). Thus a loose prior on the stellar density should allow for a strong constraint on the eccentricity.

In the limit of a constant star-planet distance during transit and a non-grazing

transit (such that the transit is approximately centered at conjunction), Kipping (2010b) derived the following expression (Kipping 2010b Equations 30 and 31) for T_{14}, the duration from first to fourth contact (i.e. the total transit duration including ingress and egress), and for T_{23}, the duration from first to third contact (i.e. the full transit duration during which the full disk of the planet is inside the disk of the star):

$$T_{14/23} = \frac{P}{\pi}\frac{(1-e^2)^{3/2}}{(1+e\sin\omega)^2}\arcsin\left[\frac{\sqrt{(1+/-\delta^{1/2})^2 - (a/R_\star)^2(\frac{1-e^2}{1+e\sin\omega})^2\cos^2 i}}{(a/R_\star)\frac{1-e^2}{1+e\sin\omega}\sin i}\right] \tag{5.1}$$

where P is the orbital period; e is the eccentricity; ω is the argument of periapse; $R_\star$ is the stellar radius; $\delta = (R_p/R_\star)^2$ is the fractional transit depth with R_p the planetary radius; a is the semi-major axis; and i is the inclination. By combining T_{14} and T_{23}, we can rewrite Equation (5.1) as

$$\sin^2(\frac{\pi}{P}\frac{[1+e\sin\omega]^2}{(1-e^2)^{3/2}}T_{14}) - \sin^2(\frac{\pi}{P}\frac{[1+e\sin\omega]^2}{(1-e^2)^{3/2}}T_{23}) = \frac{4\delta^{1/2}(1+e\sin\omega)^2}{\sin^2 i\ (a/R_\star)^2(1-e^2)^2} \tag{5.2}$$

Using the small angle approximation, which is also used by Kipping (2010b), allows us to group the transit light curve observables on the right-hand side:

$$\frac{a}{R_\star}g(e,\omega)\sin i = \frac{2\delta^{1/4}P}{\pi\sqrt{T_{14}^2 - T_{23}^2}} \tag{5.3}$$

where

$$g(e,\omega) = \frac{1+e\sin\omega}{\sqrt{1-e^2}} \tag{5.4}$$

The g notation is inspired by Kipping (2010b) and Kipping et al. (2012)'s variable Ψ, for which $\Psi = g^3$. Dynamically, g is the ratio of the planet's velocity during transit (approximated as being constant throughout the transit) to the speed expected of a planet with the same period but $e = 0$. Note that ω is the angle of the periapse from the sky plane, such that $\omega = 90^\circ$ corresponds to a transit at periapse and $\omega = -90^\circ$ to a transit at apoapse. For a given P and δ, T_{14} and T_{23} are shortest (longest) and g largest

(smallest) when the planet transits at periapse (apoapse). Moreover, if we approximate $\sin i = 1$, we can rewrite Equation (5.3) as:

$$\frac{a}{R_\star} g(e, \omega) = \frac{2\delta^{1/4} P}{\pi \sqrt{T_{14}^2 - T_{23}^2}} \tag{5.5}$$

Finally, using Kepler's third law and assuming that the planet mass is much less than the stellar mass ($M_p \ll M_\star$), the transit observables can be expressed in terms of the stellar density $\rho_\star$:

$$\rho_\star(e, \omega) = g(e, \omega)^{-3} \rho_{\rm circ} \tag{5.6}$$

where

$$\rho_{\rm circ} = \rho_\star(e = 0) = \left[\frac{2\delta^{1/4}}{\sqrt{T_{14}^2 - T_{23}^2}} \right]^3 \left(\frac{3P}{G\pi^2} \right) \tag{5.7}$$

Although Equation 5.6 was derived under several stated approximations, the relationships among $\rho_\star$, e, and ω are key to understanding how and to what extent we can constrain a transiting planet's eccentricity using a full light curve model. Because $g(e, \omega)$ is raised to such a large power, a small range of $g(e, \omega)$ corresponds to a large range in the ratio $\rho_\star / \rho_{\rm circ}$, i.e. the ratio of the true stellar density to the density measured from fitting a circular transit light curve model. For instance, the assumed value of $\rho_\star$ would need to be in error by two orders of magnitude to produce the same effect as a planet with $e = 0.9$ and $\omega = 90°$. Thus the $\rho_{\rm circ}$ derived from the transit light curve strongly constrains g, even with a weak prior on $\rho_\star$, because $g \propto \rho_\star^{1/3}$.

5.2.1 Constraints on $\rho_{\rm circ}$ from the Light Curve: Common Concerns

One might worry that long-cadence data, such as the 30-minute binning of most *Kepler* light curves, cannot resolve the ingress and egress times sufficiently to constrain $a/R_\star$, or

equivalently $\rho_{\rm circ}$. In other words, one might worry that $a/R_\star$ is completely degenerate with b, and hence that the denominator of Equation (5.5) is unconstrained. This is often the case for small planets. However, Jupiter-sized planets have high signal-to-noise transits and longer ingress and egress durations (due to the large size of the planet). See Section 2.1 of FQV08 for an analysis of how the precision of *Kepler* data affects constraints on the total, ingress, and egress durations.

Furthermore, even if the ingress is unresolved or poorly resolved, it is often impossible for the impact parameter b to account for the short duration of a highly eccentric, Jupiter-sized planet's non-grazing transit. The maximum non-grazing impact parameter is $1 - R_P/R_\star \lesssim 0.9$ for a Jupiter around a Sun-like star. Imagine that an eccentric planet transits at zero impact parameter (i.e. travels across $2R_p + 2R_\star$) at speed g. If we instead assume that planet is transiting at its circular speed $g = 1$ across the short chord of length $(2\sqrt{(R_\star + R_p)^2 - (b_{\rm large\ enough} R_\star)^2})$, the required impact parameter would be:

$$b_{\rm large\ enough} \approx (1 + \delta^{1/2})\sqrt{1 - 1/g^2} \tag{5.8}$$

For $g = 2.38$ (corresponding to $e = 0.7, \omega = 90^\circ$) and $\delta^{1/2} = R_p/R_\star = 0.1$, b would need to be ≈ 0.998, which would be inconsistent with a non-grazing transit. In contrast, a planet with $R_p/R_\star = 0.01$ would have $b_{\rm large\ enough} \approx 0.917$, consistent with the $b < 0.99$ necessary for a non-grazing transit. We note this effect simply to highlight a constraint that arises naturally when fitting a Mandel & Agol (2002) transit model to a light curve.

Additionally, with a properly binned model (as discussed in Kipping 2010a, who advocates resampling the data times, computing a model light curve, and then smoothing to match the data cadence), multiple transits allow for constraints on the ingress and

egress, even if they are poorly resolved in a single transit. We demonstrate eccentricity measurements using long-cadence data in Section 5.4.2.

Another concern regards the degeneracy of $a/R_\star$ and b with the limb-darkening parameters. Limb darkening causes the shape of the transit to be rounded instead of flat, potentially causing confusion between the full transit and the ingress/egress. However, in practice we find that it makes little difference whether we freely vary the limb darkening parameters or impose a normal prior based on the stellar parameters (e.g. the coefficients computed for the *Kepler* bandpass by Sing 2010). FQV08 also find that limb darkening does not have a significant effect on the other parameters, as demonstrated through tests on simulated light curves (see FQV08 Section 2.1 and FQV08 Figure 5).

Finally, one might worry about dilution by light from a nearby or background star blended with the target star (see Johnson et al. 2011b for a *Kepler* example). Dilution would cause $R_p/R_\star$ to appear too small. Consider the impact that dilution would have on the derived parameters of an eccentric planet transiting near periapse. The ingress and egress durations would be longer than expected, and the inferred maximum impact parameter to avoid a grazing orbit (i.e. $1 - R_p/R_\star$) would be too large. Both of these effects would caused the planet's orbit to appear *less* eccentric (or, equivalently, for $\rho_{\rm circ}$ to appear smaller; see Kipping & Tinetti 2010 for a formal derivation of the effect of blending on the measurement of $a/R_\star$). Therefore, dilution would not cause us to overestimate a planet's eccentricity, if the transit duration is shorter that circular. Moreover, because $\rho_{\rm circ}$ depends only weakly on the transit depth (Equation 5.7), the effect of blending on the eccentricity measurement is small. We quantify this effect through an example in the next subsection.

Furthermore, if we were to mistakenly attribute an apparently overly-long transit caused by blending to a planet transiting near apoapse, the resulting false eccentricity would be quite small. Imagine that the planet is on a circular orbit, but that the blend causes us to measure $\rho_{\rm circ} = (1-f)\rho_\star$, where $0 < f \ll 1$. The inferred g would be $g = [\rho_{\rm circ}/\rho_\star]^{1/3} \approx 1 - f/3$, very close to the true $g = 1$ of the circular orbit.

5.2.2 Constraints on Eccentricity

From Equation 5.6, it might appear that e and ω are inextricably degenerate for a single transiting planet. Certainly, if $\rho_{\rm circ}$ is consistent with $\rho_\star$, any eccentricity is consistent with the transit observables. However, a nominal value of $\rho_\star$ smaller than $\rho_{\rm circ}$ translates to a *minimum eccentricity* $e_{\rm min}$, the value obtained by assuming the planet transits at periapse ($\omega = 90°$; see also Barnes 2007, Section 3; Kane et al. 2012, Section 4). Conversely, a value of $\rho_\star$ larger than $\rho_{\rm circ}$ corresponds to an $e_{\rm min}$ obtained by assuming the planet transits at apoapse ($\omega = -90°$). Therefore, we can easily identify planets with large eccentricities. A full MCMC exploration provides a confidence interval that shrinks as $e \to 1$, as we discuss in detail in Section 5.3. For example, consider a planet with an eccentricity of 0.9 that transits at semilatus rectum ($\omega = 0$). Based on the transit light curve observables, we would deduce that it has an eccentricity of at least $e_{\rm min} = 0.68$. A planet transiting at semilatus rectum with $e = 0.98$ would have a deduced $e_{\rm min} = 0.92$. Above the sharp lower limit $e_{\rm min}$, the eccentricity posterior probability falls off gradually, as we discuss in Section 5.3. Note that the $e_{\rm min}$ we have defined here, which assumes we can distinguish between b and $\rho_{\rm circ}$ (i.e. via some constraint on ingress/egress time), is a stronger limit than the minimum eccentricity from the constraint that the transit be

non-grazing (which we discussed in Section 5.2.1).

Returning to the issue of contamination by blending (discussed in Section 5.2.1), consider a transit with $g = 2.5$ and thus $e_{\rm min} = 0.724$. If the transit depth were diluted by a factor[1] of 0.9 by an undetected second star in the photometric aperture, we would measure $g = 0.9^{1/4}2.5 = 2.435$ and infer nearly the same minimum eccentricity of $e_{\rm min} = 0.711$. Finally, imagine that some of the constraint on g measured from the light curve came from the non-grazing shape of the transit, implying an impact parameter greater than $1 - R_p/R_\star$. If the $R_p/R_\star$ measured from the diluted transit curve were 0.1, the inferred maximum impact parameter would be 0.9. If the true $R_p/R_\star$ is 5% larger, then the maximum impact parameter should be 0.895. This translates into a negligible effect on the constraint on g.

In Figure 5.1, we plot $\rho_{\rm circ}$ as a function of ω. Centered at $\omega = 90^\circ$ is a broad range of ω for which $\rho_{\rm circ}$ would be quite high. For example, for $e = 0.9$, $\rho_{\rm circ}$ would be erroneously high by a factor of 10-100 for $-3^\circ < \omega < 183^\circ$, over half the possible orientations. Moreover, although the periapses of eccentric planets are intrinsically randomly oriented throughout the galaxy, based on geometry eccentric planets with $\omega \approx 90^\circ$ are more likely to transit. For example, from a population of planets with $e = 0.9\,(0.95, 0.99)$ and a given orbital separation, we would be able to observe 19 (39,photo199) times as many transiting at periapse as at apoapse.

Another happy coincidence is that the true stellar density is unlikely to be *higher* than the *Kepler* Input Catalog (KIC, Batalha et al. 2010) value by a factor of 10.

[1]This is a worst-case scenario because in fact we could easily detect a companion causing such a large dilution.

The opposite situation is common; a star identified as being on the main sequence may actually be a low-density subgiant or giant (e.g. Mann et al. 2012; Dressing & Charbonneau 2013). Conversely, there are not many stars with the density of lead. Even when precise measurements of the stellar density are unavailable, our basic knowledge of stellar structure and evolution often allows for constraints on the eccentricity. If there exists a population of highly-eccentric Jupiter-sized planets, many of them will be identifiable from the light curve alone, i.e. we would deduce a large $e_{\rm min}$.

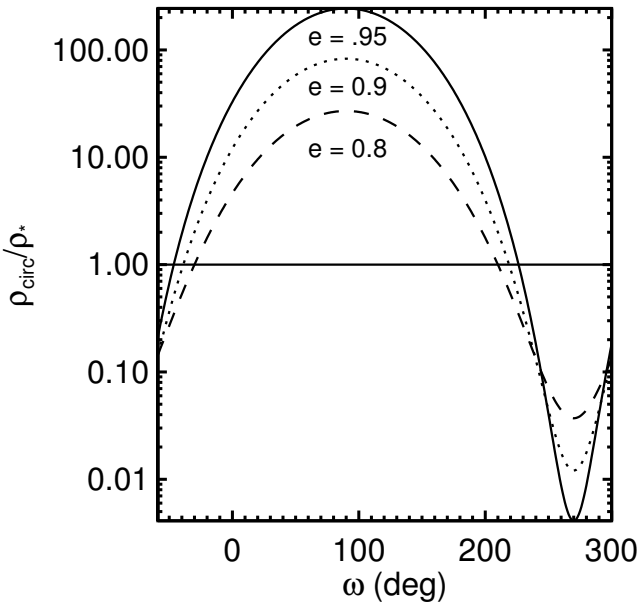

Figure 5.1.—: The ratio of the circular density to the nominal stellar density, $\rho_{\rm circ}/\rho_\star$, required for a circular model to account for the transit observables of an eccentric planet. The ratio is plotted as a function of the planet's argument of periapse. The solid (dotted, dashed) line corresponds to a planet with an eccentricity of 0.95 (0.9, 0.8). For a large range of periapse angles, one would infer a density much larger than the nominal value if one modeled the eccentric planet's orbit as circular.

5.3 Generating an Eccentricity Posterior Probability Distribution

Through an MCMC exploration—in our case implemented in the Transit Analysis Package software (TAP, Gazak et al. 2012)–we can not only determine $e_{\min}$ but impose even tighter constraints on a planet's eccentricity. For example, in Section 5.2 we stated that a candidate whose circular density is consistent with the nominal value could have any eccentricity (i.e. for any value of eccentricity, there is an ω that satisfies $g(e, \omega) = 1$). However, for $g \sim 1$, the eccentricity posterior marginalized over ω will be dominated by low eccentricity values, even with a flat prior on the eccentricity. For example, if $e = 0$, any value of ω will satisfy $g = 1$, whereas only a small range of ω allow for $g = 1$ and $e > 0.9$. Thus, because we expect planetary periapses to be distributed isotropically in the galaxy, a deduced $g = 1$ is most likely to truly correspond to a planet with a low eccentricity. By the same argument, the eccentricity posterior corresponding to a measured $g \neq 1$ will peak just above $e_{\min}$.

Of course, the transit probability also affects the eccentricity posterior distribution (Burke 2008): an eccentric orbit with a periapse pointed towards us ($\omega = 90°$) is geometrically more likely to transit than a circular orbit or an eccentric orbit whose apoapse is pointed towards us. We will discuss how an MCMC exploration automatically accounts for the transit probability later in this section.

5.3.1 Monte Carlo Simulation of Expected Eccentricity and ω Posteriors

To calibrate our expectations for the output of a more sophisticated MCMC parameter exploration, we first perform a Monte Carlo simulation to generate predicted posterior distributions of e vs. ω via the following steps:

1. We begin by generating a uniform grid of e and ω, equivalent to assuming a uniform prior on each of these parameters.

2. Then we calculate $g(e, \omega)$ (Equation 5.4) for each point (e, ω) on the grid.

3. We compute

$$\text{prob}_{\text{ng}} = \frac{R_\star}{a}(1 - R_p/R_\star)\frac{1 + e\sin\omega}{1 - e^2}, \tag{5.9}$$

   where prob_{ng} is the probability of a non-grazing transit, for each point (e, ω) (Winn 2010, Equation 9). We generate a uniform random number between 0 and 1 and discard the point if the random number is greater than the transit probability.

4. We calculate the periapse distance $\frac{a}{R_\star}(1 - e)$ for each grid point and drop the point if the planet's periapse would be inside the star (effectively imposing a physically-motivated maximum eccentricity, which is most constraining for small $a/R_\star$).

5. We downsample to a subset of grid points that follows a normal distribution centered on g, with a width of $\sigma_g/g = 0.1$, corresponding to a 30% uncertainty in the stellar density. To do this, we calculate the probability

$$\text{prob}_g = \frac{1}{\sigma_g\sqrt{2\pi}}\exp\left(-\frac{[g(e,\omega) - g]^2}{2\sigma_g^2}\right) \tag{5.10}$$

and discard the point (e, ω) if a uniform random number is greater than prob_g.

We plot the resulting posterior e vs. ω distributions in Figure 5.2 for two $a/R_\star$, one large and one small, and $R_p = 0.1$. The banana shape of the posterior results from the correlation between e and ω (i.e. Equation 5.4).

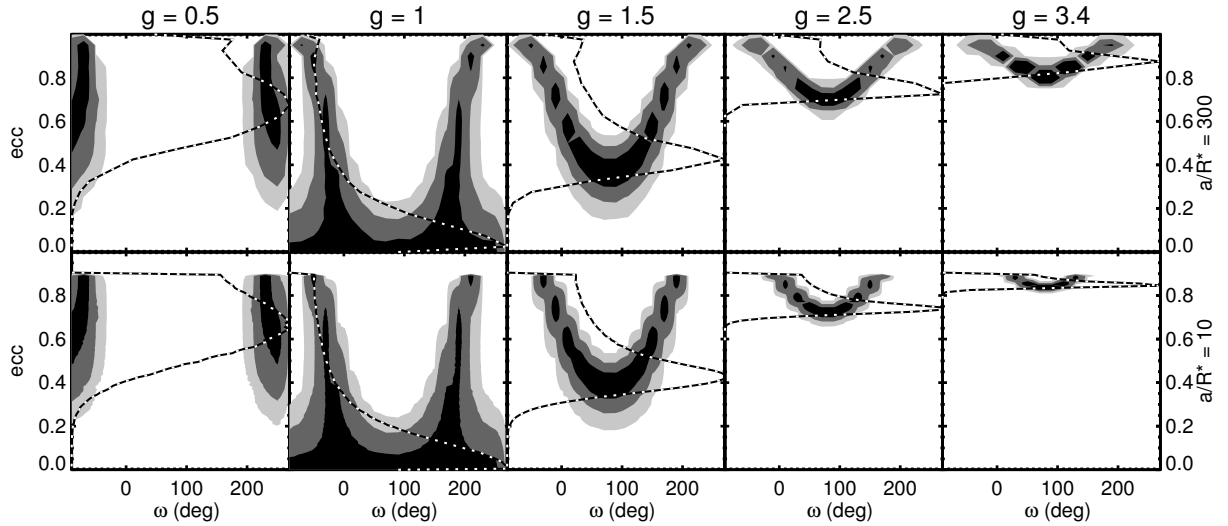

Figure 5.2.—: Contoured eccentricity vs. ω posteriors from Monte Carlo simulations for representative values of g. The points follow a normal distribution centered at the indicated value of g (columns) with a width of 10%, corresponding to a 30% uncertainty in $\rho_\star$. We show the posteriors for two values of $a/R_\star$ (rows). The black (gray, light gray) contours represent the $\{68.3, 95, 99\}$% probability density levels (i.e. 68% of the posterior is contained within the black contour). Over-plotted as a black-and-white dotted line are histograms illustrating the eccentricity posterior probability distribution marginalized over ω.

The posteriors reveal that, rather than being inextricably entwined with ω, the eccentricities deduced from g are well constrained. A ρ_{circ} consistent with the nominal value ($g = 1$ with $\rho_\star$ constrained to within 30%) is more likely to correspond to a

small e (e.g. the probability that $e < 0.32$ is 68.3% for $a/R_\star = 10$ and that $e < 0.35$ is 68.3% for $a/R_\star = 300$), while circular densities inconsistent with the normal values (g significantly different from unity) have a well-defined minimum e, above which the eccentricity posterior falls off gently. For example, for $g = 2.5$ and $a/R_\star = 300$, the probability that $e > 0.69$ is 99%. Furthermore, the eccentricity is likely to be close to this minimum eccentricity because the range of possible ω narrows as $e \to 1$. For $g = 2.5$ and $a/R_\star = 300$, the probability that $0.69 < e < 0.89$ is 95%.

Next we explore how the uncertainty in $\rho_\star$ affects the eccentricity posterior, quantifying how "loose" this prior constraint can be. In Figure 5.3, we plot eccentricity contours using a/R* = 30 for g = 1 (i.e. consistent with circular; bottom) and g = 2.5 (top) for five values of $\sigma_{\rho_\star}/\rho_\star$ assuming a normal distribution and that $\sigma_g/g = \frac{1}{3}\sigma_{\rho_\star}/\rho_\star$. For g = 2.5, the measured eccentricity is always e = 0.79; it has an uncertainty of $^{+0.12}_{-0.06}$ for $\sigma_{\rho_\star}/\rho_\star = 0.01$ and $^{+0.12}_{-0.07}$ for $\sigma_{\rho_\star}/\rho_\star = 0.5$. Thus the eccentricity remains tightly constrained even for large uncertainties in the stellar density. For $g = 1$, the measured eccentricity depends more strongly on the uncertainty: $e = 0.03^{+0.34}_{-0.03}$ for $\sigma_{\rho_\star}/\rho_\star = 0.01$ and $e = 0.24^{+0.41}_{-0.18}$ for $\sigma_{\rho_\star}/\rho_\star = 0.5$. Thus for full, ingress, and egress durations consistent with circular, a tighter constraint on the stellar density allows for a stronger upper limit on the eccentricity. However, even for a very poorly constrained $\rho_\star$, the posterior reveals that the eccentricity is most likely to be small.

5.3.2 A Bayesian Framework for Generating Posteriors

In the Monte Carlo simulation in the previous subsection, we used random numbers to select grid points in (e, ω) that were consistent with the light curve parameters, the prior

knowledge of the stellar density, and the transit probability. An MCMC fitting routine naturally generates such a posterior in eccentricity and ω according to the following Bayesian framework.

Let the model light curve be parametrized by e, ω, $\rho_\star$, and X, where X represents the additional light curve parameters (i.e. orbital period, cos(inclination), radius ratio, mid transit-time, limb darkening parameters, and noise parameters). Let D represent the light curve data. We wish to determine the probability of various e and ω conditioned on the data, or $\text{prob}(e, \omega, \rho_\star, X|D)$.

According to Bayes' theorem:

$$\text{prob}(e, \omega, \rho_\star, X|D) \propto \text{prob}(D|e, \omega, \rho_\star, X)\text{prob}(e, \omega, \rho_\star, X) \tag{5.11}$$

where the final term represents prior knowledge.

We assume a uniform prior on all the parameters except $\rho_\star$, for which we impose a prior based on the stellar parameters and their uncertainties. Therefore, we can rewrite the equation as:

$$\text{prob}(e, \omega, \rho_\star, X|D) \propto \text{prob}(D|e, \omega, \rho_\star, X)\text{prob}(\rho_\star) \tag{5.12}$$

Next we marginalize over X and $\rho_\star$ to obtain

$$\text{prob}(e, \omega|D) \propto \int\int \text{prob}(D|e, \omega, \rho_\star, X)\text{prob}(\rho_\star) dX d\rho_\star \tag{5.13}$$

the two-dimensional joint posterior distribution for eccentricity and ω. The first term under the integral is the likelihood of the data given e, ω, $\rho_\star$ and X. Thus a uniform prior on both these quantities naturally accounts for the transit probability because

prob$(D|e, \omega, \rho_\star, X)$ *is* the transit probability; for certain values of e and ω, the observed transit D is more likely to occur. Combinations of parameters that produce no transits are poor models, resulting in a low likelihood of the data. Evaluation of the likelihood prob$(D|e, \omega, \rho_\star, X)$ is part of how we obtain the parameter posteriors through an MCMC exploration, the details of which we describe in the next subsection.

Finally, we can marginalize over ω to obtain

$$\text{prob}(e|D) \propto \int\int\int \text{prob}(D|e, \omega, \rho_\star, X)\text{prob}(\rho_\star)dX d\rho_\star d\omega \tag{5.14}$$

Thus, although stellar density, eccentricity, and ω depend degenerately on light curve properties (Equation 5.6), a Bayesian approach to parameter space exploration translates a loose prior on the stellar density, prob$(\rho_\star)$, and uniform priors on the intrinsic planetary values of eccentricity and ω, into a tight constraint on the planet's eccentricity.

5.3.3 Obtaining the Eccentricity Posterior through an MCMC Sampling Method

When performing light curve fits with eccentric orbital models, it is essential to use an MCMC sampling method, or some other algorithm for which the time spent in each region of parameter space is proportional to the probability. We refer the reader to Bowler et al. (2010) (Section 3) for a helpful description of the MCMC method. The MCMC method can be used to minimize the χ^2 (in the limit of uniform priors and Gaussian noise) or to maximize whatever likelihood function is most appropriate given one's prior knowledge. In our case, we impose a normal prior on $\rho_\star$ and account for red

noise using a wavelet-based model by Carter & Winn 2009. Obtaining the eccentricity posterior through an MCMC sampling method offers several advantages:

1. It naturally allows for marginalization over all values of ω. For example, in the case of a circular density near the nominal value ($g \sim 1$), the chain will naturally spend more time at low eccentricities, for which a large range of ω provide a good fit, than at high eccentricities, for which only a narrow range of ω provide a good fit.

2. It reveals and comprehensively explores complicated parameter posteriors. In particular, some of the distributions in Figure 5.2 and 5.3 have banana shapes, which often cause conventional chi-squared minimization algorithms to remain stuck in the region of parameter space where they began. In contrast, an MCMC exploration will eventually fully sample the posterior distribution. (See Chib & Greenberg 1995, for a pedagogical proof of this theorem.) Because of the "banana-shaped" e vs. ω posterior for high eccentricities (Figure 5.2 and 5.3), conventional MCMC algorithms, like TAP, require many iterations to converge and fully explore parameter space. In our case, we test for convergence by plotting e and ω each as a function of chain link and assess if the exploration appears random. We also check to ensure that the ω posterior is symmetric about $\omega = 90°$. Asymmetry indicates that the chains have not yet converged. We note that the variables $e\cos\omega$ and $e\sin\omega$ also have a banana-shaped posterior. When feasible, we recommend implementing an affine-invariant code such as `emcee` that more efficiently explores banana-shaped posteriors (e.g. Foreman-Mackey et al. 2012). In Section 5.3.3, we describe how to speed up the fit convergence by using g instead of e as a variable while maintaining a uniform prior in e and ω.

3. It allows us to easily impose priors on certain parameters, such as the stellar density. If desired, one can impose a prior on the eccentricity. In Section 5.4, we perform an additional fit for each dataset using a Jeffrey's[2] prior on the eccentricity, which is appropriate if we wish to avoid assumptions about the magnitude of the eccentricity. Here we implement the prior through regularization (i.e. as an extra term in the jump probability).

4. It automatically accounts for the transit probability, because jumps to regions of parameter space that do not produce a transit are rejected. To address what may be a misconception, we emphasize that it is unnecessary — and actually a double penalty — to impose transit probability priors on the eccentricity or periapse.

5. It provides uncertainties that are more reliable than the estimates based on a simple covariance matrix (as obtained from traditional least-squares minimization) because there is no assumption that the uncertainties are normally distributed. The uncertainties fully account for complicated parameter posteriors and correlations. Therefore we can be confident in the constraints on $\rho_{\rm circ}$ even when the ingress and egress are not well-resolved.

We caution that although this Bayesian framework is appropriate for obtaining the posteriors of a single planet, selection effects must be carefully considered when making

[2]We use a true Jeffrey's prior prob$(e) \propto 1/e$, which we have not normalized because we only consider the ratio of probabilities when assessing a jump in an MCMC chain. For the fits in Section 4, for which $e_{\rm min}$ is well above 0, this prior is sufficient. However, if $e = 0$ is a possibility (i.e. for g near 1), the reader may wish to use a modified Jeffrey's prior, prob$(e) \propto 1/(e + e_0)$, where e_0 is the noise level. We recommend estimating an upper limit on g from the uncertainty in $\rho_{\rm circ}$ and $\rho_\star$ and solving Equation (5.4) for e_0 using $\omega = 90°$.

inferences about a population.

Using g as a Variable for Faster Convergence

Using g (Equation 5.4) instead of e as a variable in the transit fit model avoids the MCMC having to explore a banana-shaped posterior. The g variable allows for faster convergence and prevents the chain from getting stuck. In order to preserve a uniform prior in e and ω, we must impose a prior on g by adding an additional term to the likelihood function. Following the Appendix of Burke et al. (2007), the transformation from a uniform prior in e to a prior in g is:

$$\begin{aligned} \text{prob}(g)dg &= \text{prob}(e)\frac{\partial e}{\partial g}dg \\ \text{prob}(g) &= \text{prob}(e)\frac{\partial e}{\partial g} = \frac{\sin^2\omega\left(\sin^2\omega - 1\right) + g^2\left(1 + \sin^2\omega\right) \pm 2g\sin\omega\sqrt{\sin^2\omega - 1 + g^2}}{\sqrt{\sin^2\omega - 1 + g^2}\left(g^2 + \sin^2\omega\right)^2} \end{aligned} \tag{5.15}$$

where we have assumed $\text{prob}(e) = 1$ and for which the $+$ corresponds to $g > 1$ and the $-$ to $g < 1$. .

Therefore, we add the following term to the log likelihood:

$$\Delta\mathcal{L} = \ln\left[\frac{\sin^2\omega\left(\sin^2\omega - 1\right) + g^2\left(1 + \sin^2\omega\right) \pm 2g\sin\omega\sqrt{\sin^2\omega - 1 + g^2}}{\sqrt{\sin^2\omega - 1 + g^2}\left(g^2 + \sin^2\omega\right)^2}\right] \tag{5.16}$$

We demonstrate the use of this variable in Section 5.4. We note that in our light curve fits, we use g only to explore parameter space, transforming the variable to e in order compute the Keplerian orbit, with no approximations, for the Mandel & Agol (2002) light curve model.

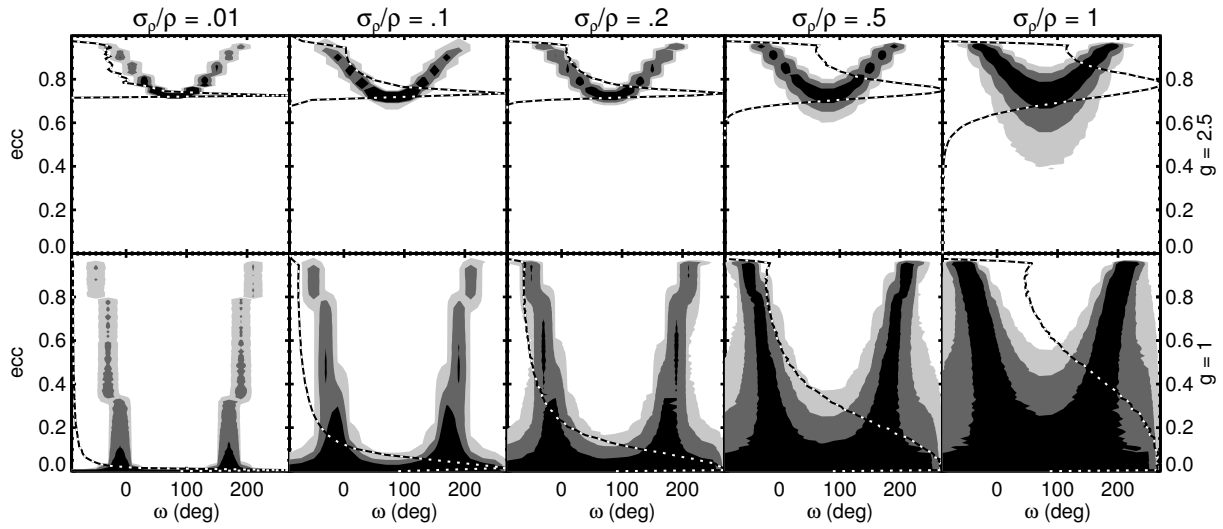

Figure 5.3.—: Contoured eccentricity vs. ω posteriors from Monte Carlo simulations for representative values of g (rows; the points follow a normal distribution centered g) and uncertainty in $\rho_\star$ (columns), all for $a/R_\star = 30$. The black (gray, light gray) contours represent the [68.3,95,99]% probability density levels. Over-plotted as a black-and-white dotted line are histograms illustrating the eccentricity posterior probability distribution marginalized over ω.

5.3.4 Obtaining the Eccentricity Posterior from the Circular-Fit Posterior

The Monte Carlo exploration in Section 5.3.1 was meant to give us a handle on what the eccentricity and ω posterior should look like and how they are affected by uncertainty in $\rho_\star$. However, one could use a more formal version of this exploration to obtain posteriors of eccentricity and ω directly from the posteriors derived from circular fits to the light curve, an approach that was adopted by Kipping et al. (2012). One could maximize the following likelihood for the parameters $\rho_\star$, e, and ω:

$$\mathcal{L} = -\frac{1}{2}\frac{\left[g(e,\omega)^3\rho_\star - \rho_{\rm circ}\right]^2}{\sigma^2_{\rho_{\rm circ}}} - \frac{1}{2}\frac{\left[\rho_\star - \rho_{\star,\rm measured}\right]^2}{\sigma^2_{\rho_{\star,\rm measured}}} + \ln\left(\text{prob}_{\rm ng}\right) \tag{5.17}$$

The first term in the likelihood function demands agreement with the $\rho_{\rm circ}$ derived from the circular fit to the light curve. If the $\rho_{\rm circ}$ posterior is not normal, one could replace this term with the log of the probability of $g(e,\omega)^3\rho_\star$ given the $\rho_{\rm circ}$ posterior. Note that $g(e,\omega)$ can either be computed from the approximation in Equation (5.4) or by solving and integrating Kepler's equation to obtain the mean ratio of the transiting planet's velocity to its Keplerian velocity over the course of the transit. The second term is the prior on $\rho_\star$ from the stellar parameters independently measured from spectroscopy (or asteroseismology). The final term is the probability of a non-grazing transit (Equation 5.9). If one uses the variable g instead e, one should add Equation (5.16) to the likelihood. We warn that this likelihood function drops constants, so although it can be used to generate parameter posteriors, it should not be used to compute the Bayesian evidence quantity.

In the next section, we demonstrate that this approach yields the same eccentricity and ω posteriors as directly fitting for the eccentricity from the light curve.

5.4 Demonstration: Measuring the Eccentricities of Transiting Jupiters

To demonstrate that the duration aspect of the photoeccentric effect allows for precise and accurate measurements of a transiting planet's eccentricity from the light curve alone, we apply the method described in Section 5.3 to several test cases. In Section 5.4.1 we measure the eccentricity of a transiting planet that has a known eccentricity from RV measurements. In Section 5.4.2 we inject a transit into short and long cadence *Kepler* data and compare the resulting e and ω posteriors. In Section 5.4.3, we measure the eccentricity of a *Kepler* candidate that has only long-cadence data available.

5.4.1 HD 17156 b: a Planet with a Large Eccentricity Measured from RVs

HD 17156 b was discovered by the Next 2000 Stars (N2K) Doppler survey (Fischer et al. 2005, 2007). Fischer et al. (2007) reported that the planet has a large orbital eccentricity of $e = 0.67 \pm 0.08$. We identified this planet and the relevant references using `exoplanets.org` (Wright et al. 2011). Barbieri et al. (2007) reported several partial transits observed by small-telescope observers throughout the Northern Hemisphere, and Barbieri et al. (2009) and Winn et al. (2009d) observed full transits using high-precision,

ground-based photometry. Here we demonstrate that the planet's eccentricity could have been measured from the transit light curve data alone.

We simultaneously fit three light curves (Figure 5.4), one from Barbieri et al. (2009) and two from Winn et al. (2009d) using TAP (Gazak et al. 2012), which employs an MCMC technique to generate a posterior for each parameter of the Mandel and Agol (2002) transit model. Time-correlated, "red" noise is accounted for using the Carter & Winn (2009) wavelet-based likelihood function. To achieve the 2^N (where N is an integer) data points required by the wavelet-based likelihood function without excessive zero-padding, we trimmed the first Winn et al. (2009d) light curve from 523 data points to 512 data points by removing the last 11 data points in the time series. Initially, we fixed the candidate's eccentricity at 0 and fit for $\rho_{\rm circ}$ with no prior imposed, to see how much it differs from the well-measured value of $\rho_\star$. Then we refitted the transit light curves with a normal prior imposed on the stellar density, this time allowing the eccentricity to vary. In both cases, we treated the limb darkening coefficients following the literature: we fixed the coefficients for the Barbieri et al. (2009) light curve and left the coefficients free for the Winn et al. (2009d) light curves. Following Winn et al. (2009d), we also included linear extinction free parameters for the two Winn et al. (2009d) light curves. (The published Barbieri et al. 2009 light curve was already pre-corrected for extinction.)

Figure 5.5 shows posterior distributions from a circular fit (top row) and an eccentric fit (bottom row) with a prior imposed on the stellar density from Gilliland et al. (2011). In Figure 5.6, we compare the posteriors generated from a) the eccentric fit to the light curve using g as a parameter (with a prior imposed to maintain a uniform eccentricity prior; Equation (5.16) to posteriors generated using: b) a Jeffrey's prior

on the eccentricity, c) e instead of g as a free parameter (to demonstrate that they are equivalent), and d) the likelihood-maximization method described in Section 3.4, using the posterior of $\rho_{\rm circ}$ from the circular fit. The four sets of posteriors closely resemble one another. The computation times were about 1 day for the circular fit, about 1 day for the eccentric fit using g as a parameter, several days for the eccentric fit using e as a parameter, and thirty minutes for the likelihood maximization method of Section 3.4. Note that the final method requires the best-fitting parameters resulting from a circular fit to the light curve, including accurate parameter posteriors. We therefore caution against using the parameters listed in the *Kepler* public data releases for this purpose because those values are the result of a least-squares fit and make the assumption of normally distributed parameter uncertainties. However, if one has already precomputed circular fits using an MCMC algorithm that incorporates red noise and limb darkening—as we have done for all of the Jupiter-sized KOIs (Section 5.5)—the final method (Section 5.3.4) is advantageous because of the decreased computation time.

Based on the circular fit alone, we would infer $g(e_{\rm min}, \pi/2) = 2.0$, corresponding to a minimum eccentricity of $e_{\rm min} = 0.61$. From the eccentric fit, we obtain a value of $e = 0.71^{+0.16}_{-0.09}$ using a uniform prior on the eccentricity and $e = 0.69^{+0.16}_{-0.09}$ using a Jeffrey's prior. Therefore, we could have deduced the eccentricity determined from 33 RV measurements — $e = 0.67 \pm 0.08$ (Fischer et al. 2007) — from these three transit light curves alone.

The host star has a particularly well-constrained density from asteroseismology (Gilliland et al. 2011). We artificially enlarge the error bars on the stellar density from 1% to 20% and repeat the fitting procedure, obtaining an eccentricity of $e = 0.70^{+0.14}_{-0.09}$. We also repeat the fitting procedure with a density derived from the

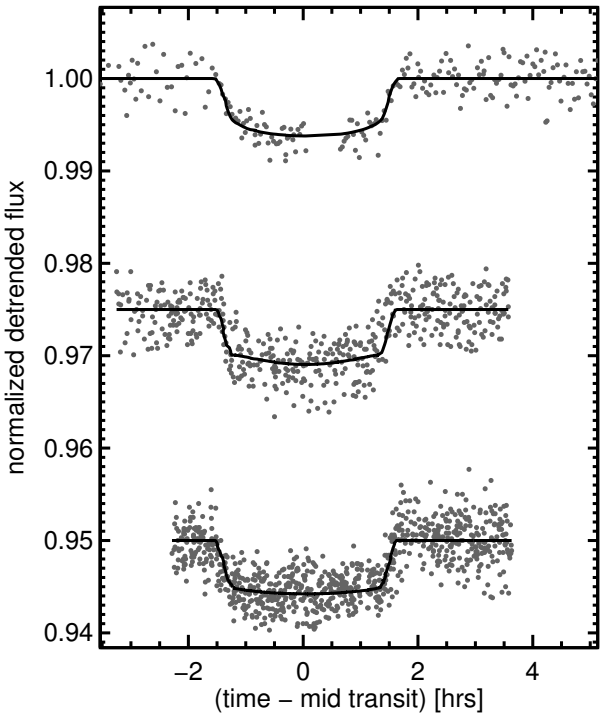

Figure 5.4.—: Light curves of HD 17156 from Barbieri et al. (2009) (top) and Winn et al. (2009d) (middle, bottom). A set of eccentric model light curves drawn from the posterior are plotted as solid lines.

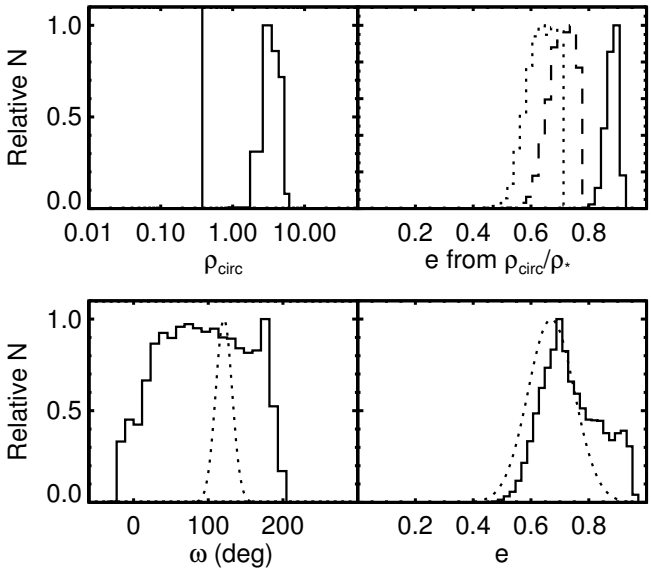

Figure 5.5.—: Posterior distributions of e and ω for the HD 17156 transiting system, with eccentricity fixed at 0 (row 1) and free to vary (row 2). Row 1: Left: $\rho_\star$ derived from circular fit. The solid line marks the nominal value. Right: Posterior distribution for eccentricity solving Equation (5.5) for $\omega = 0$ (solid line), $\omega = 45°$ (dashed line), and $\omega = 90°$ (dotted line). Row 2: Left: Posterior distribution for ω from eccentric fit (i.e. a fit to the light curve in which the eccentricity is a free parameter; solid). Gaussian illustrating posterior from Fischer et al. (2007) RV fit (dotted line). Right: Same for eccentricity posterior.

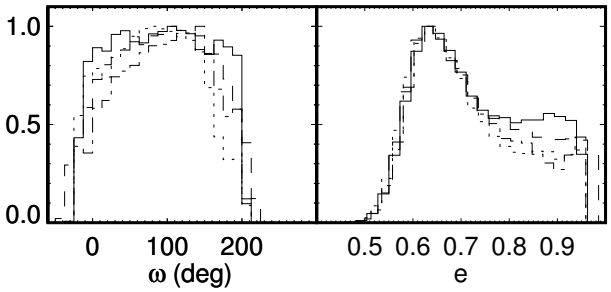

Figure 5.6.—: Left: Posterior distribution for ω for a fit to the light curve using g as a free parameter with a uniform prior on the eccentricity (sold line) and Jeffrey's prior (dotted line). Posterior distribution using e instead of ω as a free parameter (dot-dashed line). Posterior distribution using method described in Section 5.3.4 (dashed line). Right: Same as left, for eccentricity posterior.

stellar parameters $M_\star$ and $R_\star$ determined by Winn et al. (2009d) from isocrone fitting. This "pre-asteroseismology" density has an uncertainty of 10% and, moreover, is about 5% larger than the value measured by Gilliland et al. (2011). We obtain an eccentricity of $e = 0.70^{+0.16}_{-0.11}$. In Figure 5.7 and 5.8, we plot the resulting posterior distributions, which are very similar. Therefore, even with uncertainties and systematics in the stellar density, we can measure a transiting planet's eccentricity to high precision and accuracy.

5.4.2 Short vs. Long Cadence *Kepler* Data

Kipping (2010a) explored in detail the effects of long integration times and binning on transit light curve measurements, with a particular focus on long-cadence *Kepler* data. He demonstrated that by binning a finely-sampled model to match the cadence of the data, as TAP has implemented, one can fit accurate (though less precise than from short cadence data) light curve parameters. Using short and long cadence *Kepler* data of a

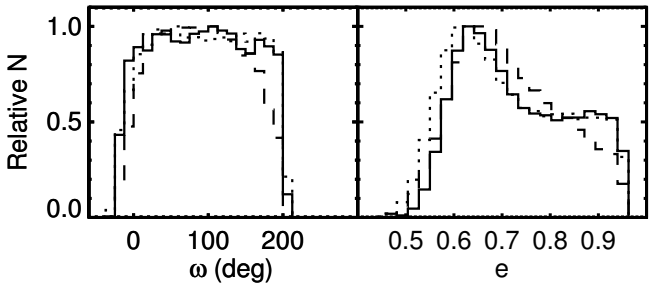

Figure 5.7.—: Posterior distributions of e and ω for the HD 17156 transiting system, with three different priors on the stellar density: the density measured by Gilliland et al. (2011) (solid); the density measured by Gilliland et al. (2011) with uncertainties enlarged to $\sigma_{\rho_\star}/\rho_\star = 0.2$, (dashed) and the density based on the stellar parameters from Winn et al. (2009d) (dotted).

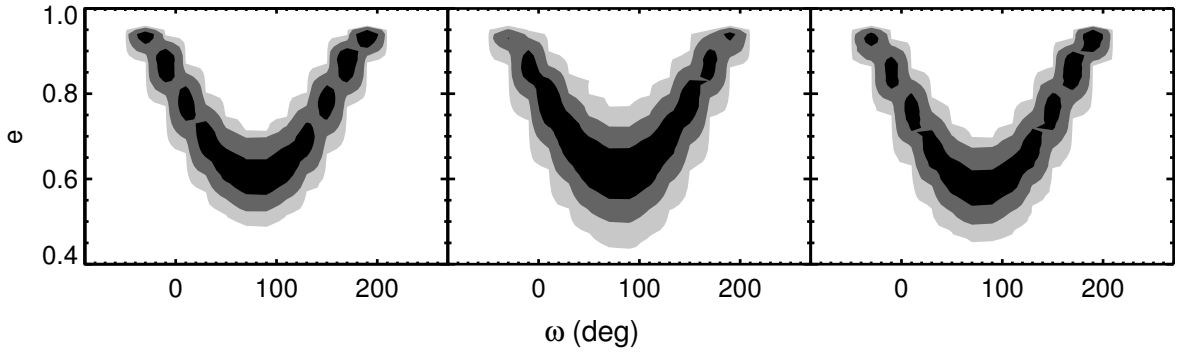

Figure 5.8.—: Eccentricity vs. ω posterior distributions for HD 17156 b based on fits using a prior on the stellar density from Gilliland et al. (2011) (left); Gilliland et al. (2011) with error bars enlarged to 20% (middle); and Winn et al. (2009d) (left).

planet with known parameters (TrES-2-b), he validated this approach.

Here we explore, through a test scenario of an eccentric planet injected into short and long *Kepler* data, whether this approach holds (as one would expect) for fitting an eccentric orbit and what value short-cadence data adds to the constraint on eccentricity. We chose parameters for the planet typical of an eccentric Jupiter and main-sequence host star: $P = 60$ days, $i = 89.5°$, $R_p/R_\star = 0.1$, $e = 0.8$, $\omega = 90°$, $M_\star = R_\star = 1$, and limb darkening parameters $\mu_1 = \mu_2 = 0.3$. We considered the situation in which long cadence data is available for Q0-Q6 but short-cadence is available only for one quarter (or may be in the future). We retrieved Q0-Q6 data from the Multimission Archive at the Space Telescope Science Institute (MAST) for *Kepler* target star KIC 2306756, selected because it has both long and short cadence data. Then we applied the TAP MCMC fitting routine to fit a) one short-cadence transit (fixing the period at 60 days) that took place in a single segment of short-cadence data and b) all seven long-cadence transits.

As in Section 5.4.1, we performed one set of fits fixing the orbit as circular and another set with g and ω as free parameters, imposing a prior on the stellar density corresponding to a 20% uncertainty in the stellar density and a prior on g from a uniform prior in e and ω (Equation 5.16). In both cases, we allowed the limb darkening to be a free parameter. We plot the resulting posterior distributions of eccentricity and ω in Figure 5.9. From the circular fits, the constraint on $\rho_{\rm circ}$ is somewhat stronger from the short cadence data ($26.3^{+1.0}_{-1.6}\ \rho_\odot$) than from the long cadence data ($25.9^{+1.0}_{-2.7}\ \rho_\odot$), as Kipping (2010a) found. From the short cadence data, we measure an eccentricity of $e = 0.85^{+0.08}_{-0.05}$ with a uniform prior on the eccentricity and $e = 0.85^{+0.07}_{-0.05}$ with a Jeffrey's prior. From the long cadence data, we measure an eccentricity of $e = 0.84^{+0.08}_{-0.05}$ with a

uniform prior on the eccentricity and $e = 0.84^{+0.07}_{-0.04}$ with a Jeffrey's prior. Therefore, the long cadence data is sufficient to obtain a precise eccentricity measurement. In this case, the 20% uncertainty in the stellar density dominated over the constraint from the transit light curve on $\rho_{\rm circ}$; however, for very well-constrained stellar properties, we would expect the greater precision of the short cadence data to allow for a tighter constraint on the eccentricity (see Figure 5.3).

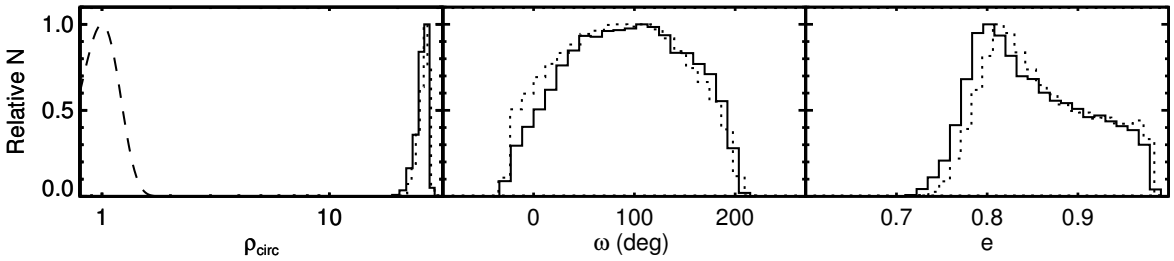

Figure 5.9.—: Posterior distributions of e and ω for an injected, artificial transit, with eccentricity fixed at 0 (panel 1) and free to vary (panel 2-3). The sold curves are from a fit to seven light curves from the long-cadence data and the dotted to a single light curve from the short cadence data. Left: $\rho_\star$ derived from circular fit. The dashed curve represents the nominal value and its uncertainty. Middle: Posterior distribution for ω from eccentric fit (solid line). Right: Eccentricity posterior.

5.4.3 KOI 686.01, a Moderately Eccentric, Jupiter-sized *Kepler* Candidate

KOI 686.01 was identified by Borucki et al. (2011) and Batalha et al. (2013) as a 11.1 $R_{\rm Earth}$ candidate that transits its host star every 52.5135651 days. We retrieved the Q0-Q6 data from MAST and detrended the light curve using `AutoKep` (Gazak et al. 2012). We plot the light curves in Figure 5.10.

We obtained a spectrum of KOI 686 using the HIgh Resolution Echelle Spectrometer (HIRES) on the Keck I Telescope (Vogt et al. 1994). The spectrum was obtained with the red cross-disperser and 0.″86 slit using the standard setup of the California Planet Survey (CPS), but with the iodine cell out of the light path. The extracted spectrum has a median signal-to-noise ratio of 40 at 5500 $\AA$, and a resolution $\lambda/\Delta\lambda \approx 55,000$. To estimate the stellar temperature, surface gravity, and metallicity, we use the `SpecMatch` code, which searches through the CPS's vast library of stellar spectra for stars with *Spectroscopy Made Easy* (SME; Valenti & Piskunov 1996; Valenti & Fischer 2005) parameters and finds the best matches. The final values are the weighted mean of the 10 best matches. We then interpolate these stellar parameters onto the Padova stellar evolution tracks to obtain a stellar mass and radius. We checked these values using the empirical relationships of Torres et al. (2010). We find $\rho_\star = 1.02^{+0.45}_{-0.29}\ \rho_\odot$ (the other stellar parameters for this KOI and parameters for other KOI will be published as part of another work, Johnson et al. 2012, in prep).

We then fit circular and eccentric orbits to the transit light curve, as described above, binning the model light curves to match the 30-minute cadence of the data. We impose a normal prior on the limb-darkening coefficients based on the values from Sing (2010). Figure 5.11 shows posterior distributions from a circular fit (top row) and an eccentric fit (bottom row) with a prior imposed on the stellar density. We measure the eccentricity to be $e = 0.62^{+0.18}_{-0.14}$.

We caution that this candidate has not yet been validated; Morton & Johnson (2011b) estimate a false-positive probability of 8%. If the candidate is a false positive, its orbit (and other properties, such as its radius) is likely to be different from that inferred. However, we note that if the candidate is a background binary or hierarchical

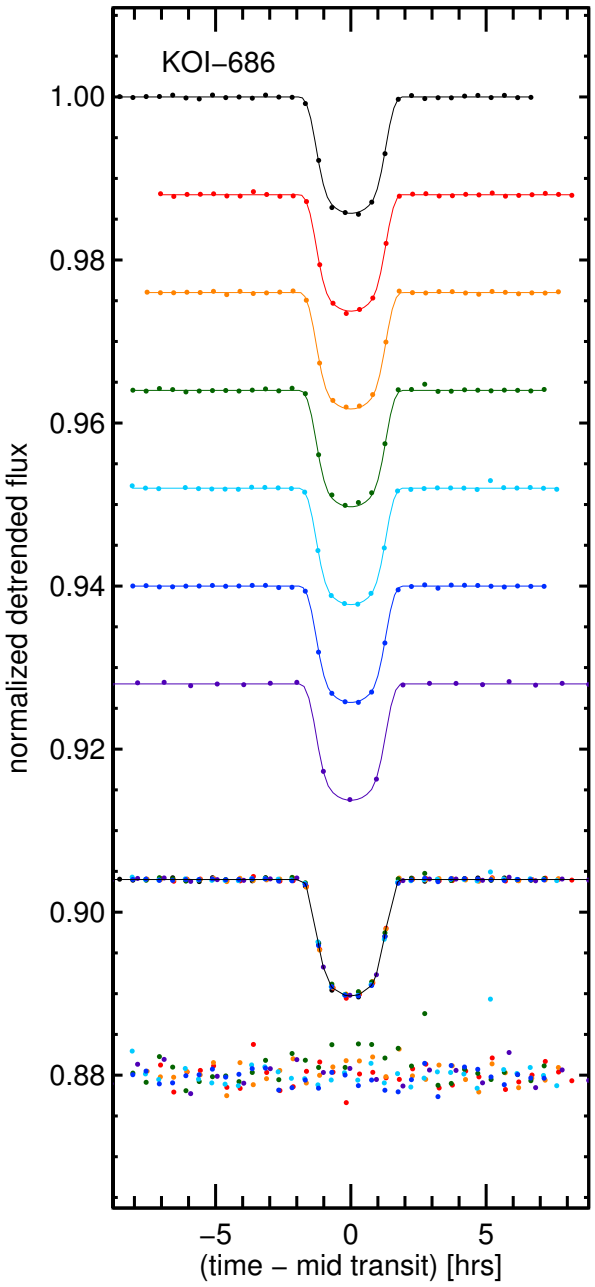

Figure 5.10.—: Light curves of KOI 686. A set of eccentric model light curves drawn from the posterior are plotted as solid lines. The second-from-bottom curve is a compilation of all the light curves. The bottom points are the residuals multiplied by 10.

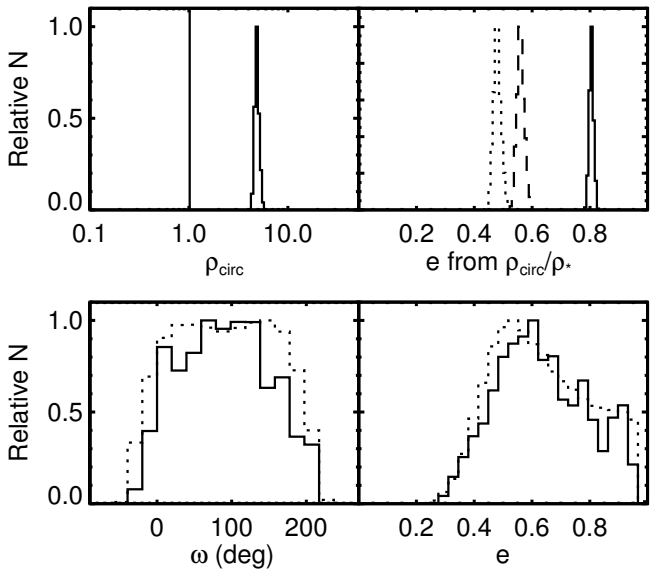

Figure 5.11.—: Posterior distributions for KOI 686.01 with eccentricity fixed at 0 (row 1) and free to vary (row 2). Row 1: Left: $\rho_\star$ derived from circular fit. The solid line marks the nominal value. Right: Posterior distribution for eccentricity solving Equation (5.5) for $\omega = 0$ (solid line), $\omega = 45°$ (dashed line), and $\omega = 90°$ (dotted line). Row 2: Left: Posterior distribution for ω from eccentric fit (solid). Posterior distribution using method from Section 5.3.4 (dotted). Right: Same as left, for eccentricity posterior.

triple and is actually larger than a planet, the inferred eccentricity would actually be higher (i.e. if the candidate is actually larger, it must be moving through its ingress and egress even faster), unless KOI 686 is not the primary and the primary has a higher density than KOI 686. Another possibility, if the candidate is false positive, is that the assumption of $M_p \ll M_\star$ may no longer hold and $\rho_\circ$ (Equation 5.6) should be compared to $\rho_\star + \rho_{\rm companion}$ rather than $\rho_s tar$ to obtain g. However, even if $\rho_{\rm companion} \sim \rho_\star$, the error in g would be only $(\frac{1}{2})^3 = 12.5\%$.

Santerne et al. (2012) recently found a false positive rate of 35% for Jupiter-sized candidates, comprised of brown dwarfs, undiluted eclipsing binaries, and diluted eclipsing binaries. In the case of diluted eclipsing binaries, the blend effects that we discussed in Section 5.2 could be larger than we considered. However, Morton (2012) notes that most of the false positives that Santerne et al. (2012) discovered through radial-velocity follow-up already exhibited V-shapes or faint secondary eclipses in their light curves. In the search for highly eccentric Jupiters, we recommend a careful inspection of the transit light curve for false-positive signatures and, when possible, a single spectroscopic observation and adaptive-optics imaging to rule out false-positive scenarios.

If the planetary nature of this object is confirmed, it will be one of a number of Jupiter-sized planets with orbital periods of 10-100 days and moderate eccentricities, but the first in the *Kepler* sample with a photometrically-measured eccentricity. Many previously known, moderately-eccentric planets have orbits inside the snow line; their eccentricities are thought to be signatures of the dynamical process(es) that displaced them from their region of formation.

5.5 A plan for Distilling Highly-Eccentric Jupiters from the *Kepler* Sample

To test the HEM hypothesis (S12), we are "distilling" highly-eccentric, Jupiter-sized planets — proto hot Jupiters — from the sample of announced *Kepler* candidates using the publicly released *Kepler* light curves (Borucki et al. 2011; Batalha et al. 2013). To identify planets that must be highly eccentric, we are refitting the *Kepler* light curves of all the Jupiter-sized candidates using the TAP. Initially, we fix the candidate's eccentricity at 0. We identify candidates whose posteriors for $\rho_{\rm circ}$ are wildly different than the nominal value $\rho_\star$ from the KIC. From this subset of objects, we obtain spectra of the host stars. We refine the stellar parameters using `SpecMatch`, interpolate them onto the Padova stellar evolution tracks to obtain a stellar mass and radius, and check the inferred $M_\star$ and $R_\star$ using the empirical relationships of Torres et al. (2010). We validate the candidate using the method outlined in Morton (2012). Finally, we refit the transit light curves with a prior imposed on the stellar density, this time allowing the eccentricity to vary. This process will allow to us easily identify the most unambiguous highly-eccentric hot Jupiters.

5.6 Discussion

Measuring a transiting planet's orbital eccentricity was once solely the province of radial-velocity observations. Short-period planets were discovered by transits and followed-up with RVs, which sometimes revealed a sizable eccentricity (e.g. HAT-P-2b, Bakos et al. 2007; CoRoT-10b, Bonomo et al. 2010). Long-period planets—which, based

on the RV distribution, are more commonly eccentric—were discovered by radial-velocity measurements and, on lucky occasions, found to transit (e.g. HD 17156 b, Fischer et al. 2007, the planet discussed in Section 5.4.1, as well as HD 806066 b, Naef et al. 2001). But now, from its huge, relatively unbiased target sample size of 150,000 stars, *Kepler* has discovered a number of long-period, transiting candidates. Among these are likely to be a substantial number of eccentric planets (S12), which have enhanced transit probabilities (Kane et al. 2012). Moorhead et al. (2011); Kane et al. (2012) and Plavchan et al. (2012) have characterized the eccentricity distributions of these candidates based on *Kepler* photometry. Kipping et al. (2012) are employing MAP to measure the eccentricities of planets in systems in which multiple planets transits. Here we have demonstrated that it is also possible to constrain an individual planet's eccentricity from a set of high signal-to-noise transits using a Bayesian formalism that employs relatively loosely-constrained priors on the stellar density. The technique we have presented can be applied to any transit light curve, as we did in Section 5.4.1, for HD 17156 b using ground-based photometry. Comparing this technique to Kipping et al. (2012)'s MAP, MAP is more model independent – requiring no knowledge at all of the stellar density – but our technique is applicable to single transiting planets, as Jupiter-sized *Kepler* candidates tend to be (e.g. Latham et al. 2011). We are the process of fitting the orbits of all Jupiter-sized *Kepler* candidates, which will lead to the following prospects:

1. For candidates with host stars too faint for RV follow-up (65% of candidates in Borucki et al. 2011 are fainter than *Kepler* magnitude 14), our technique will provide an estimate of the planet's eccentricity. We may also be able to deduce the presence of companions from transit timing variations, thereby allowing us to search for "smoking gun" perturbers that may be responsible for the inner planet's

orbital configuration. In a companion paper (Dawson et al. 2012), we present the validation and characterization of a KOI with a high, photometrically-measured eccentricity and transit timing variations.

2. For candidates bright enough for follow-up RV measurements, the eccentricity and ω posteriors from photometric fits allow us to make just a few optimally timed radial velocity measurements to pinpoint the planet's eccentricity, the mass and host-star density, instead of needing to devote precious telescope time to sampling the full orbital period. The tight constraints on eccentricity from photometry alone can be combined with radial-velocity measurements to constrain the candidate's orbit—either by fitting both datasets simultaneously or by using the posteriors from the photometry as priors for fitting a model to the RVs. To maximize the information gain, the prior on the stellar density should remain in place. This serves as an additional motivation for measuring the spectroscopic properties of candidate host stars in the *Kepler* field.

3. We can also measure the spin-orbit angles of the candidates orbiting the brightest stars with Rossiter-McLaughlin measurements. Then we can compare the distribution of spin-orbit angles of those planets we have identified as eccentric with the distribution of those we have constrained to be most likely circular.

4. S12 argue that HEM mechanisms for producing hot Jupiters should also produce a population of highly eccentric ($e > 0.9$) proto hot Jupiters and predict that we should find 3-5 in the *Kepler* sample. Moreover, *Kepler*'s continuous coverage may offer the best prospect for detecting highly eccentric planets, against which RV surveys are biased (Johnson et al. 2006; O'Toole et al. 2009). In Section 5.5,

we described our process for distilling highly-eccentric Jupiters from the *Kepler* sample.

The *Kepler* sample has already revealed a wealth of information about the dynamics and architectures of planetary systems (e.g. Lissauer et al. 2011; Fabrycky et al. 2012a) but primarily for closely-packed systems of low mass, multiple-transiting planets. Measuring the eccentricities of individual, Jupiter-sized planets in the *Kepler* will allow us to investigate a different regime: planetary systems made up of massive planets that potentially underwent violent, mutual gravitational interactions followed by tidal interactions with the host star.

Chapter 6

The Photoeccentric Effect and Proto-hot Jupiters. II. KOI-1474.01, a Candidate Eccentric Planet Perturbed by an Unseen Companion

R. I. Dawson, J. A. Johnson, T. D. Morton, J. R. Crepp, D. C. Fabrycky, R. A. Murray-Clay, & A. W. Howard *The Astronomical Journal*, Vol. 761, id. 163, 2012

Abstract

The exoplanets known as hot Jupiters—Jupiter-sized planets with periods less than 10 days—likely are relics of dynamical processes that shape all planetary system

architectures. Socrates et al. (2012) argued that high eccentricity migration (HEM) mechanisms proposed for situating these close-in planets should produce an observable population of highly eccentric proto-hot Jupiters that have not yet tidally circularized. HEM should also create failed-hot Jupiters, with periapses just beyond the influence of fast circularization. Using the technique we previously presented for measuring eccentricities from photometry (the "photoeccentric effect"), we are distilling a collection of eccentric proto- and failed-hot Jupiters from the *Kepler* Objects of Interest (KOI). Here we present the first, KOI-1474.01, which has a long orbital period (69.7340 days) and a large eccentricity $e = 0.81^{+0.10}_{-0.07}$, skirting the proto-hot Jupiter boundary. Combining *Kepler* photometry, ground-based spectroscopy, and stellar evolution models, we characterize host KOI-1474 as a rapidly-rotating F-star. Statistical arguments reveal that the transiting candidate has a low false-positive probability of 3.1%. KOI-1474.01 also exhibits transit timing variations of order an hour. We explore characteristics of the third-body perturber, which is possibly the "smoking-gun" cause of KOI-1474.01's large eccentricity. Using the host-star's rotation period, radius, and projected rotational velocity, we find KOI-1474.01's orbit is marginally consistent with aligned with the stellar spin axis, although a reanalysis is warranted with future additional data. Finally, we discuss how the number and existence of proto-hot Jupiters will not only demonstrate that hot Jupiters migrate via HEM, but also shed light on the typical timescale for the mechanism.

6.1 Introduction

The start of the exoplanet era brought with it the discovery of an exotic new class of planets: Jupiter-sized bodies with short-period orbits ($P \lesssim 10$ days), commonly known as hot Jupiters (Mayor & Queloz 1995; Marcy et al. 1997). Most theories require formation of Jupiter-sized planets at or beyond the so-called "snow line," located at roughly a few AU,[1] and debate the mechanisms through which they "migrated" inward to achieve such small semimajor axes. The leading theories fall into two categories: smooth migration through the proto planetary disk (e.g. Goldreich & Tremaine 1980; Ward 1997; Alibert et al. 2005; Ida & Lin 2008; Bromley & Kenyon 2011), or what Socrates et al. (2012b) (hereafter S12) term high eccentricity migration (HEM), in which the planet is perturbed by another body onto an inclined and eccentric orbit that subsequently circularizes through tidal dissipation (e.g. Wu & Murray 2003; Ford & Rasio 2006; Fabrycky & Tremaine 2007a; Naoz et al. 2011; Wu & Lithwick 2011)

From the present-day orbits of exoplanets we can potentially distinguish between mechanisms proposed to shape the architectures of planetary systems during the early period of dynamical upheaval. In this spirit, Morton & Johnson (2011b) used the distribution of stellar obliquities to estimate the fraction of hot Jupiters on misaligned orbits and to distinguish between two specific migration mechanisms (see also Fabrycky & Winn 2009; Triaud et al. 2010; Winn et al. 2010); Naoz et al. (2012) recently applied a similar technique to estimate the relative contributions of two different mechanisms. However, deducing dynamical histories from the *eccentricity* distribution of exoplanets

[1]Kenyon & Bromley (2008) and Kennedy & Kenyon (2008) explore in detail the location of the ice line for different stellar and disk parameters.

poses a challenge because most hot Jupiters have already undergone tidal circularization and "cold" Jupiters at larger orbital distances may have formed in situ. Furthermore, type-II (gap-opening) migration may either excite or damp a planet's eccentricity through resonance torques (Goldreich & Sari 2003; Sari & Goldreich 2004). Finally, Guillochon et al. (2011) find evidence that some hot Jupiters may have undergone disk migration either prior to or following scattering. In the latter case, disk migration may have damped their eccentricities. The eccentricity distribution is potentially shaped by a combination of HEM, tidal circularization, and planet-disk interactions.

Motivated by the HEM mechanisms proposed by Wu & Murray (2003) and others, S12 proposed an observational test for HEM. As an alternative to modeling the *distribution* of eccentricities, they suggested that we look for the *individual* highly eccentric, long-period progenitors of hot Jupiters caught of the act of tidal circularization. S12 identified HD 80606 b as one such progenitor, which was originally discovered by radial velocity (RV) measurements of its host star's reflex motion (Naef et al. 2001) and later found to transit along an orbit that is misaligned with respect to its host star's spin axis (Moutou et al. 2009; Winn et al. 2009c). From statistical arguments S12 predicted that if HEM produces the majority of hot Jupiters, the *Kepler* Mission should detect several "super-eccentric" Jupiters with orbital periods less than 93 days and eccentricities in excess of 0.9. A couple of these planets should be proto-hot Jupiters, with post-circularization semimajor axes in the region where all hot Jupiters have circularized (i.e. $P < 5$ days). Several more eccentric planets should have final periods above 5 days, in the region where not all hot Jupiters have circularized; these planets may be "failed-hot Jupiters" that will never circularize over their host stars' lifetimes. A failed-hot Jupiter may have either halted at its post-HEM location due to

the tidal circularization timescale exceeding the age of the system, or undergone some tidal circularization but subsequently stalled after a perturber in the system raised its periapse. S12's prediction is supported by the existence of super-eccentric eclipsing binaries in the *Kepler* sample, which are also thought to have been created by HEM mechanisms (Dong et al. 2013).

To test the HEM hypothesis we are "distilling" eccentric, Jupiter-sized planets from the sample of announced *Kepler* candidates using the publicly released *Kepler* light curves (Bromley & Kenyon 2011; Batalha et al. 2013). We described the distillation process and our technique for measuring eccentricities from transit light curves based on the "photoeccentric effect" in Dawson & Johnson (2012), hereafter Paper I. In summary, eccentric Jupiters are readily identified by their short ingress/egress/total transit durations (Barnes 2007; Ford & Rasio 2008; Burke 2008; Plavchan et al. 2012; Kane et al. 2012). A Markov-Chain Monte Carlo (MCMC) exploration of the posterior distributions of the transit parameters, together with a loose prior imposed on the stellar density, naturally accounts for the eccentricity-dependent transit probability and marginalizes over the periapse angle, yielding a tight measurement of a large orbital eccentricity (Paper I).

Here we present the first eccentric, Jupiter-sized candidate from the *Kepler* sample: *Kepler* Object of Interest (KOI) number 1474.01. We find that this eccentric candidate also has large transit-timing variations (TTVs). In fact, the TTVs are so large that they were likely missed by the automatic TTV-detection algorithms, as they were not listed in a recent cataloging of TTV candidates (Ford et al. 2012; Steffen et al. 2012b). Ballard et al. (2011) recently deduced the presence and planetary nature of the non-transiting Kepler-19c from the TTVs it caused in the transiting planet Kepler-19b, demonstrating

the viability of detecting non-transiting planets through TTVs. More recently, Nesvorný et al. (2012) characterized a Saturn-mass non-transiting planet using this technique. Thus the TTVs of 1474.01 may place constraints on the nature of an additional, unseen companion, thereby elucidating the dynamical history of the system.

In Section 6.2, we present the light curve of KOI-1474.01. In Section 6.3, we characterize the host-star KOI-1474 using *Kepler* photometry, ground-based spectroscopy, and stellar evolution models. In Section 6.4, we estimate the candidate's false positive probability (FPP) to be 3.1%. In Section 6.5, we measure KOI-1474.01's large eccentricity, investigate its TTVs and the perturbing third body that causes them, and measure the projected alignment of the transiting planet's orbit with the host star's spin axis. In Section 6.6, we place KOI-1474.01 in the context of known hot Jupiters, proto-hot Jupiters, and failed-hot Jupiters, and explore whether KOI-1474.01 is a failed-hot Jupiter that will retain its current orbit or a proto-hot Jupiter that will eventually circularize at a distance close to the host star. We conclude in Section 6.7 by discussing the implications for planetary system formation models and suggesting directions for future follow up of highly eccentric planets in the *Kepler* sample.

Figure 6.1.—: Detrended light curves, color-coded by transit epoch, spaced with arbitrary vertical offsets. The top eight light curves are phased based on a constant, linear ephemeris (Table 6.2, column 3), revealing the large TTVs. Each light curve is labeled 'C' with its best-fit mid-transit time (Table 6.2, column 3). In the second-from-the-bottom compilation, each light curve is shifted to have an individual best-fitting mid-transit time at t=0. The bottom points are the residuals multiplied by 10. Solid lines: best-fitting eccentric model (Table 6.2, column 3).

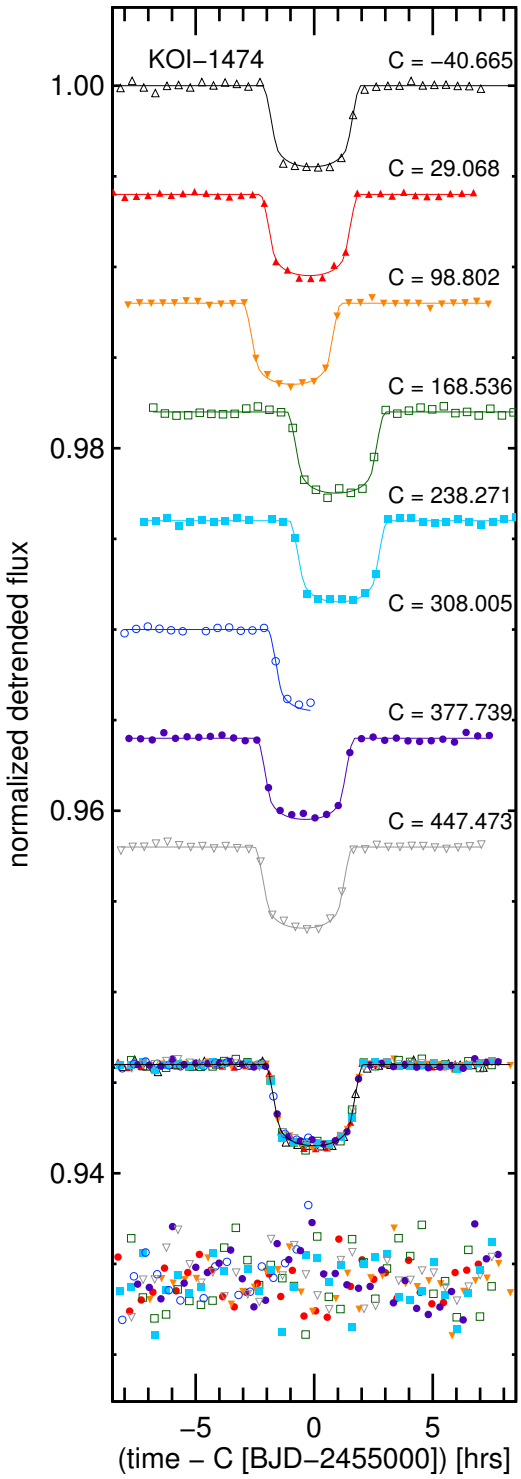

Figure 6.1.—: Continued

6.2 KOI-1474.01: an Interesting Object of Interest

KOI-1474.01 was identified by Borucki et al. (2011) as an 11.3 $R_\oplus$ candidate that transits its 1.23 $M_\odot$, 6498 K host star every 69.74538 days (Batalha et al. 2010). With a *Kepler* bandpass magnitude $K_P = 13.005$, the star is one of the brighter candidates in the *Kepler* sample, making it amenable to follow up by Doppler spectroscopy. We retrieved the Q0-Q6 data from the Multimission Archive at the Space Telescope Science Institute (MAST) and detrended the light curve using `AutoKep` (Gazak et al. 2012). We identified eight transits (Figure 6.1), which together reveal three notable properties:

1. When folded at a constant period, the transits are not coincident in phase. Indeed, some fall early or late by a noticeable fraction of a transit duration.

2. The transit durations are short for a planet with such a long orbital period (the total transit duration, from first to last contact, is T_{14}=2.92 hours, or 0.17% of the 69.74538 day orbital period). Yet instead of the V shape characteristic of a large impact parameter, the transit light curves feature short ingresses and egresses—corresponding to a planet moving at 3 times the circular Keplerian velocity [based on the *Kepler* Input Catalog (KIC) stellar parameters]—and a nearly flat bottom, implying that either the planet has a large eccentricity or orbits a very dense star (see Paper I). The candidate's reported $a/R_\star = 129.0525 \pm 0.0014$ (Borucki et al. 2011) corresponds to a stellar density of $6\rho_\odot$, which is inconsistent with main-sequence stellar evolution for all stars but late M-dwarfs. This implausibly high density derived from a circular orbital fit to the light curve implies that the planet has an eccentric orbit and is transiting near periapse (e.g. Figure 1 of Paper I).

3. The in-transit data feature structures that may be caused by star spot crossings (e.g. the bump in the purple, solid circle light curve marked C=377.739 in Figure 6.1). The ratio of scatter inside of transits to that outside of transits is about 1.2. If the star exhibits photometric variability due to the rotation of its spot pattern, we may be able to measure the stellar rotation period and combine it with other stellar parameters to constrain the line-of-sight component of the system's spin-orbit configuration (e.g. Sanchis-Ojeda et al. 2011; Nutzman et al. 2011; Désert et al. 2011). If the star's surface temperature were greater than or equal to the KIC estimate of 6498 K (Batalha et al. 2010), we might expect the star to lack a convective envelope (Pinsonneault et al. 2001) and star spots. Therefore the star may be significantly cooler than this estimate.[2]

The light curve implies that the transiting candidate KOI-1474.01 may be an eccentric planet experiencing perturbations from an unseen companion and with a measurable spin-orbit alignment, an ideal testbed for theories of planetary migration. However, in order to validate and characterize the candidate, first we must pin down the stellar properties and assess the probability that the apparent planetary signal is a false positive.

[2]However, Hirano et al. (2012) recently found photometric variability due to star spots for several hot stars, including KOI-1464, which has a surface temperature of 6578 ± 70 K, so the signatures of star spots we notice are not necessarily inconsistent with KOI-1474's KIC temperature.

6.3 Host KOI-1474, a Rapidly-rotating F Star

The stellar properties of KOI-1474 are essential for validating and characterizing the transiting candidate, but the parameters in the KIC are based on broadband photometry and may be systematically in error, as noted by Brown et al. (2011b). Here we use a combination of spectroscopy (Section 6.3.1), photometry (Section 6.3.2), and stellar evolution models (Section 6.3.3) to characterize host star KOI-1474.

6.3.1 Stellar Temperature, Metallicity, and Surface Gravity from Spectroscopy

John Johnson obtained two high signal-to-noise, high resolution spectra for KOI-1474 using the HIgh Resolution Echelle Spectrometer (HIRES) on the Keck I Telescope (Vogt et al. 1994). The spectra were observed using the standard setup of the California Planet Survey, with the red cross disperser and the $0\farcs86$ C2 decker, but with the iodine cell out of the light path (Johnson et al. 2012). The first observation was made with an exposure time of 270 seconds, resulting in a signal-to-noise ratio (SNR) of ≈ 45 at 6000 $\AA$; the second exposure was 1200 seconds long, resulting in a SNR ≈ 90.

As described in Paper I, John Johnson used `SpecMatch` to compare the two spectra to the California Planet Survey's vast library of spectra for stars with parameters from *Spectroscopy Made Easy* (SME; Valenti & Piskunov 1996; Valenti & Fischer 2005). The closest-matching spectrum is that of HD 3861. In order to match KOI-1474 to this relatively slowly rotating F dwarf, John Johnson rotationally broadened the spectrum of HD 3861. The total line broadening for KOI-1474, $v_{\rm rot} \sin i_s = 13.6 \pm 0.5$

km/s, is a combination of the HIRES instrumental profile, rotational broadening, and broadening due to turbulence (macroturbulence being the dominant term, rather than microturbulence: Valenti & Fischer 2005). John Johnson assumed that KOI-1474 has the same macroturbulent broadening and instrumental profile as HD 3861. Then he applied additional rotational broadening to HD 3861 using MORPH (Johnson et al. 2006) to match the spectra of KOI-1474 using the rotational broadening kernel described by Gray (2008). The $v_{\rm rot} \sin i_s$ for KOI-1474 is

$$v_{\rm rot} \sin i_s = \sqrt{(v_{\rm rot} \sin i_s)^2_{\rm HD3861} + (v_{\rm rot} \sin i_s)^2_{\rm broad}}$$

where $(v_{\rm rot} \sin i_s)_{\rm HD3861} = 2.67$ km/s is the known $v_{\rm rot} \sin i_s$ of HD 3861 (Valenti & Fischer 2005) and $(v_{\rm rot} \sin i_s)_{\rm broad} = 13.3$ km/s is the additional rotational broadening applied to the HD 3861 spectrum to match the lines of KOI-1474. See Albrecht et al. (2011), Section 3.1 for a discussion and demonstration of this technique for measuring $v_{\rm rot} \sin i_s$.

Next, from a weighted average of the properties of HD 3861 and the other best match spectra, John Johnson measured an effective temperature $T_{\rm eff} = 6240 \pm 100$ K, surface gravity $\log g = 4.16 \pm 0.20$, and iron abundance [Fe/H] $= 0.09 \pm 0.15$. These measured values are consistent with the KIC estimates of $T_{\rm eff} = 6498 \pm 200$ K and $\log g = 4.08 \pm 0.4$ (with uncertainties estimated by Brown et al. 2011b) but are more accurate and precise because they come from high-resolution spectroscopy rather than broadband photometry. Based on the revised, cooler value for its effective temperature, KOI-1474 may indeed have a convective envelope and thus the structures in the transit light curves (Figure 6.1) could be due to spots. Therefore spot-induced photometric variability may allow us to measure the stellar rotation period $P_{\rm rot}$ (Section 6.3.2), which we can combine with other stellar parameters to infer the transiting candidate's

projected spin-orbit alignment (Section 6.5.2).

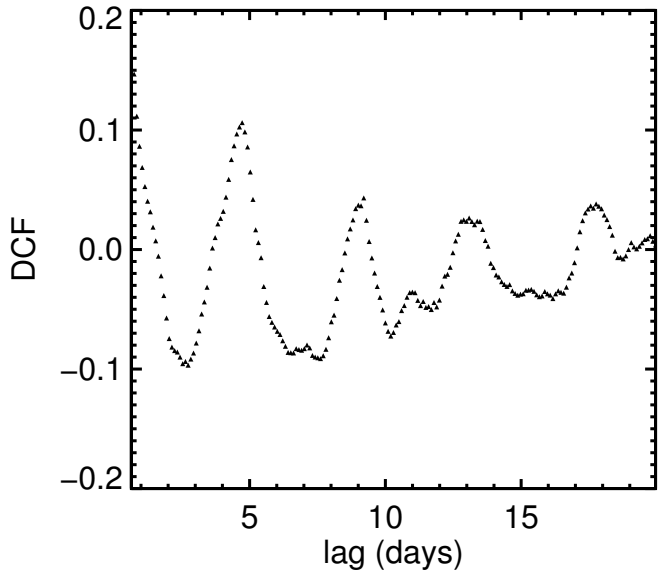

Figure 6.2.—: Discrete-correlation-function (DCF, Edelson and Krolik 1988) for the long-cadence *Kepler* Q0-Q6 KOI-1474 photometric, dataset as a function of time lag. The peak at 4.6 ± 0.4 days corresponds to the stellar rotation period.

6.3.2 Stellar Rotation Period from Photometry

KOI-1474 appears to exhibit rotational photometric variability due to star spots, which cause the star to appear brighter (dimmer) as the less (more) spotted hemisphere rotates into view. We see what may be an effect of these spots in the purple, solid circle light curve marked C=377.739 in Figure 6.1: a bump during transit consistent with a planet crossing a star spot. A periodogram (not shown) of the entire photometric dataset (Q0-Q6) exhibits a prominent cluster of peaks near 5 days. However, a periodogram is not the best tool to measure stellar rotation periods because: a) the photometric variability is non-sinusoidal, and b) the spot pattern is not expected to remain coherent

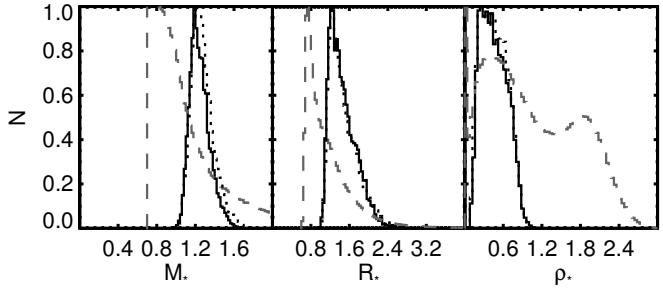

Figure 6.3.—: Posteriors (solid) of stellar radius (panel 1), mass (panel 2), and density (panel 3) in solar units. The posteriors obtained from the prior alone (dashed gray) and from the data alone (dotted) are plotted in each panel, demonstrating that our data provide stronger constraints on the stellar parameters than do our priors.

over the entire 508-day dataset and thus the phase and amplitude of the best-fit sinusoid change over the data's timespan.

To obtain an optimal measurement of the stellar rotation period, we compute the discrete-correlation-function (DCF, Equation 2 of Edelson & Krolik 1988), which was recently used to measure the rotation period of Corot-7 (Queloz et al. 2009) and Kepler-30 (Fabrycky et al. 2012b). First we detrended the data with the `PyKE` routine[3] using co-trending vectors. Welsh (1999) found that it is crucial to remove long-term trends from the time series before applying the DCF or biases may result. Then we computed the DCF using the Institut für Astronomie und Astrophysik Tübingen DCF routine,[4] an IDL implementation of the DCF described in Edelson & Krolik (1988). The possible range for the DCF is -1 to 1; the amplitude is normalized such that DCF = 1 indicates perfect correlation. We plot the DCF (computed with a lag range of 0.1 days

[3]Available at *Kepler* Guest Observer Home: http://keplergo.arc.nasa.gov

[4]Available at http://astro.uni-tuebingen.de/software/idl/aitlib/index.shtml

to 20 days and with 200 frequencies) as a function of time lag in Figure 6.2. The DCF is highest in the region lag < 0.2 days (i.e. lags that are small but greater than 0, for which the DCF =1 by definition), indicating that most of the photometric variability occurs on short timescales, most likely due to a combination of high-frequency stellar variability and instrumental noise. However, we also see lower amplitude but pronounced peaks at longer periods.

The DCF exhibits the variations we expect due to star spots. Imagine observing the star at time t; the hemisphere in view has either more or fewer spots than the unseen hemisphere. At time $t + P_{\rm rot}/2$, the other hemisphere has fully rotated into view, so the flux at t and $t + P_{\rm rot}/2$ are negatively correlated. Therefore, we interpret the negative DCF near 2 days as corresponding to half the stellar rotation period. At time $t + P_{\rm rot}$, we see the same hemisphere as at time t; therefore, we interpret the strong positive correlation at lag 4.6 ± 0.4 days as the stellar rotation period, for which uncertainty range corresponds to the width at half-maximum. The amplitude DCF = 0.1 indicates a 10% correlation between points separated in time by $P_{\rm rot}$. The other hemisphere rotates fully into view again at $t + 3P_{\rm rot}/2$, corresponding to the negative DCF at lag 7 days; at lag $2P_{\rm rot} = 9$ days, the DCF is positive again. This pattern continues, and the amplitude would remain constant if the spot pattern were constant. However, the spot pattern is changing over time, so the amplitude of the correlation "envelope" decreases with time lag.[5] The measured rotation period of 4.6 days is consistent with the distribution measured for F, G, K stars by Reiners & Schmitt (2003); they find that the distribution

[5]Unfortunately, the decrease in the correlation amplitude with lag implies that we are unlikely to be able to measure the stellar obliquity using the method of Sanchis-Ojeda et al. (2011) and Nutzman et al. (2011). The spot cycle is likely shorter than the interval between subsequent transits.

of projected rotation periods (i.e. the rotation periods measured from $v_{\rm rot} \sin i_s$ assuming $i_s = 90^\circ$) peaks at 5 days.

6.3.3 Stellar Density from Evolution Models

The candidate's orbital eccentricity, the ultimate quantity of interest, depends weakly on the host star's density (see Paper I and references therein). Thus it is important to have an accurate, if not precise, estimate of the host star's density and, importantly, a conservative estimate of the uncertainty. For this task we use the finely-sampled YREC stellar evolution models computed by Takeda et al. (2007), sampled evenly in intervals of 0.02 dex, 0.02 $M_\odot$, and 0.02 Gyr for metallicity [Fe/H], stellar mass $M_\star$ and age $\tau_\star$ respectively. The model parameters are stellar age $\tau_\star$, mass $M_\star$, and fractional metallicity Z, and we wish to match the effective temperature $T_{\rm eff}$, surface gravity $\log g$, and [Fe/H] measured spectroscopically in Section 6.3.3, along with their 68.2% confidence ranges denoted by their "one-sigma errors" $\{\sigma_{T_{\rm eff}}, \sigma_{\log g}, \sigma_{\rm [Fe/H]}\}$, respectively. In what follows, the subscript "spec" refers to the spectroscopically measured quantity, while quantities with no subscript are the model parameters.

Applying Bayes' theorem, the model posterior probability distribution is

$$\begin{aligned} &{\rm prob}(M_\star, \tau_\star, Z | T_{\rm eff,spec}, [{\rm Fe/H}]_{\rm spec}, \log g_{\rm spec}, I) \propto \\ &{\rm prob}(T_{\rm eff,spec}, [{\rm Fe/H}]_{\rm spec}, \log g_{\rm spec} | M_\star, \tau_\star, Z, I) {\rm prob}(M_\star, \tau_\star, Z | I) \end{aligned} \tag{6.1}$$

where I represents additional information available to us based on prior knowledge of the Galactic stellar population.

The first term on the right hand side (RHS) is the likelihood, which we compute by

comparing the effective temperature, surface gravity, and metallicity generated by the model to the values we measured from spectroscopy:

$$\begin{aligned} &\mathrm{prob}(T_{\mathrm{eff,spec}}[\mathrm{Fe/H}]_{\mathrm{spec}}, \log g_{\mathrm{spec}} | M_\star, \tau_\star, Z, I) \\ &\propto \exp\left(-\frac{\chi^2_{T_{\mathrm{eff}}}}{2}\right) \exp\left(-\frac{\chi^2_{[\mathrm{Fe/H}]}}{2}\right) \exp\left(-\frac{\chi^2_{\log g}}{2}\right) \end{aligned} \tag{6.2}$$

where

$$\begin{aligned} \chi^2_{T_{\mathrm{eff}}} &= \frac{\left[T(M_\star, \tau_\star, Z) - T_{\mathrm{eff,spec}}\right]^2}{\sigma^2_{\mathrm{Teff,spec}}} \\ \chi^2_{[\mathrm{Fe/H}]} &= \frac{\left[[\mathrm{Fe/H}](M_\star, \tau_\star, Z) - [\mathrm{Fe/H}]_{,\mathrm{spec}}\right]^2}{\sigma^2_{[\mathrm{Fe/H}],\mathrm{spec}}} \\ \chi_{\log g} &= \frac{\left[\log g(M_\star, \tau_\star, Z) - \log g_{\mathrm{spec}}\right]^2}{\sigma^2_{\log \mathrm{g,spec}}} \end{aligned} \tag{6.3}$$

The second term on the RHS of Equation (6.1), $\mathrm{prob}(M_\star, \tau_\star, Z|I)$, is the prior information known about the model parameters. Here we make use of some additional information I—the galactic latitude and longitude of the Kepler field and the measured apparent Kepler magnitude of KOI-1474—to infer the relative probability of observing different types of stars. A number of factors go into this probability, including the present-day stellar mass function, the volume distribution and ages of stars along our line of sight to the Kepler field, and the Malmquist bias. Fortunately, the TRILEGAL code (TRIdimensional modeL of thE GALaxy; Girardi et al. 2005) synthesizes a large body of observational, empirical, and theoretical studies to produce a model population of stars in the Kepler field that are consistent with KOI-1474's apparent Kepler magnitude $K_P = 13.005 \pm 0.030$ (Batalha et al. 2010) and Galactic coordinates. From this model population, we use a Gaussian kernel density estimator to compute a three-dimensional density function for the prior $\mathrm{prob}(M_\star, \tau_\star, Z|I)$.

Each combination of Takeda et al. (2007) model parameters — $(M_\star, \tau_\star, Z)$ — has a corresponding $R_\star$ and $L_\star$, and we calculate the corresponding stellar density $\rho_\star = \frac{M_\star}{M_\odot} (\frac{R_\odot}{R_\star})^3 \rho_\odot$. We compute the star's absolute Kepler bandpass magnitude $K_{P,\mathrm{absolute}}$ through the follow steps: we transform $L_\star$ into a V magnitude using a bolometric correction, transform V into the absolute Sloan magnitude g, and compute the distance modulus using the difference between the absolute g magnitude and the apparent g magnitude from the KIC (Batalha et al. 2010). Then we apply the distance modulus to the apparent K_P to obtain $K_{P,\mathrm{absolute}}$. Thus we can transform the model posterior $\mathrm{prob}(M_\star, \tau_\star, Z | T_{\mathrm{eff,spec}}, [\mathrm{Fe/H}]_{\mathrm{spec}}, \log g_{\mathrm{spec}}, I)$ into posteriors for the stellar stellar properties $M_\star$, $\tau_\star$, $R_\star$, $\rho_\star$, $L_\star$, and $K_{P,\mathrm{absolute}}$ (Table 6.1, column 3). In Figure 6.3 we plot the resulting posteriors for $M_\star$, $R_\star$, and $\rho_\star$. We also plot the same distributions obtained from the data alone and from the priors[6] alone; evidently most of the constraint comes from the data (i.e. the spectroscopic quantities).

[6]The $M_\star$ prior probability appears truncated below $M_\star = 0.78$ in Figure 6.3 because we only compute Takeda et al. (2007) models above this value. However, the likelihood completely rules out stars with $M_\star < 1 M_\odot$.

Table 6.1. Stellar Parameters for KOI 1474

Parameter	Value[a]	
	Measured	Derived from model
Right ascension, RA (hour,J2000)	19.694530	
Declination, Dec (degree,J2000)	51.184800	
Projected rotation speed, $v_{\rm rot} \sin i_s$ [km s^{-1}]	13.6±0.5	
Stellar effective temperature, $T_{\rm eff}$ [K]	6240±100	6230±100
Iron abundance, [Fe/H]	0.09 ±0.15	$0.00\ ^{+0.16}_{-0.12}$
Surface gravity, $\log(g[{\rm cms}^{-2}]$	4.16±0.20	$4.23^{+0.13}_{-0.16}$
Limb darkening coefficient, μ_1 [b]		0.320 ± 0.015
Limb darkening coefficient, μ_2 [b]		0.304 ± 0.007
Main sequence age, $\tau_\star$ [Gyr] [c]		$2.8^{+1.3}_{-1.2}$
Stellar mass, $M_\star$ $[M_\odot]$ [c]		$1.22^{+0.12}_{-0.08}$
Stellar radius, $R_\star$ $[R_\odot]$		$1.40^{+0.37}_{-0.21}$
Stellar density, $\rho_\star$ $[\rho_\odot]$		$0.44^{+0.26}_{-0.20}$
Stellar luminosity, $L_\star$ $[L_\odot]$		$2.7^{+1.6}_{-0.8}$
Apparent Kepler-band magnitude, K_P	13.005 ± 0.030	
Absolute Kepler-band magnitude, $K_{P,\rm absolute}$		$3.6^{+0.4}_{-0.5}$
Distance (kpc)		$0.78^{+0.23}_{-0.13}$
Rotation period, $P_{\rm rot}$ [days]	4.6 ± 0.4	
Rotation speed, $v_{\rm rot}$[km s^{-1}]		$14.7^{+2.6}_{-1.0}$
Sine of stellar spin axis inclination angle, $\sin i_s$		$0.93^{+0.06}_{-0.14}$
Stellar spin axis inclination angle, i_s[degree]		69^{+14}_{-17}
Deviation of stellar spin axis from edge-on, $\lvert 90 - i_s$ [degree]		21^{+17}_{-14}

Table 6.1—Continued

Parameter	Value[a]

[a]The uncertainties represent the 68.3% confidence interval of the posterior distribution.

[b]Sing 2010

[c]A prior was imposed on this parameter.

Table 6.2. Planet Parameters for KOI 1474.01

Parameter	Value[a]	
	Circular fit	Eccentric fit
Average orbital period, P [days][b]	69.7339±0.0016	69.7340±0.0015
Average mid transit epoch, T_c [days] [BJD-2455000]	238.273±0.011	238.273±0.010
Mid transit epoch of transit 1, T_1 [days] [BJD-2455000]	-40.6701±0.0008	-40.6702±0.0009
T_2 [days] [BJD-2455000]	29.0600±0.0006	29.0600±0.0007
T_3 [days] [BJD-2455000]	98.7647±0.0006	98.7647±0.0007
T_4 [days] [BJD-2455000]	168.5752±0.0006	168.5752±0.0007
T_5 [days] [BJD-2455000]	238.3146±0.0005	238.3146±0.0007
T_6 [days] [BJD-2455000]	308.0092±0.0008	308.0092±0.0009
T_7 [days] [BJD-2455000]	377.7250±0.0006	377.7250±0.0007
T_8 [days] [BJD-2455000]	447.4555±0.0006	447.4555±0.0007
Planet-to-star radius ratio, $R_p/R_\star$	$0.0618\ ^{+0.0007}_{-0.0003}$	$0.0617\ ^{+0.0006}_{-0.0004}$
Stellar density, $\rho_\star$	$9.2\ ^{+0.4}_{-1.6}$	$0.36^{+0.30}_{-0.10}$
Orbital inclination, i [degree]	$89.93\ ^{+0.05}_{-0.08}$	$89.2\ ^{+0.4}_{-1.3}$
Limb darkening coefficient, μ_1[c]	$0.314^{+0.018}_{-0.012}$	$0.311^{+0.016}_{-0.012}$
Limb darkening coefficient, μ_2[c]	$0.302\ ^{+0.006}_{-0.008}$	$0.304^{+0.005}_{-0.009}$
Impact parameter, b	$0.18^{+0.21}_{-0.12}$	$0.14^{+0.25}_{-0.09}$
Planetary radius, R_p [$R_\oplus$]		$9.5^{+2.4}_{-1.4}$
Normalized red noise, σ_r	$0.00005^{+0.00007}_{-0.00003}$	$0.00007^{+0.00005}_{-0.00005}$
Normalized white noise, σ_w	$0.000131^{+0.000010}_{-0.000004}$	$0.000134^{+0.000007}_{-0.000007}$
Eccentricity, e		$0.81^{+0.10}_{-0.07}$
Orbital period after tidal circularization, $P_{\rm final}$		14^{+6}_{-10}

Table 6.2—Continued

Parameter	Value[a]
Line-of-sight spin-orbit angle, $\|i - i_s\|$ [degree]	$21.^{+17}_{-14}$

[a]The uncertainties represent the 68.3% confidence interval of the posterior distribution.

[b]P and T_c are determined from a linear fit to the transit times. The uncertainty in T_c is the median absolute deviation of the transit times from this ephemeris; the uncertainty P is this quantity divided by the number of orbits between the first and last observed transits.

[c]A prior was imposed on this parameter.

The derived density for KOI-1474, $0.44^{+0.26}_{-0.20}\rho_{\odot}$, has an uncertainty range encompassing the KIC value of 0.26 $\rho_{\odot}$ (Batalha et al. 2010). The star is significantly less dense than the value of $6\rho_{\odot}$ derived from $a/R_{\star}$ in the table of candidates (Borucki et al. 2011; Batalha et al. 2013) . Therefore, planet candidate KOI-1474.01 is likely to have a large eccentricity, which we will measure in §6.5. Fortunately, as shown as Paper I, even the loose constraint on the stellar density derived here will result in a precise measurement of the candidate's large orbital eccentricity.

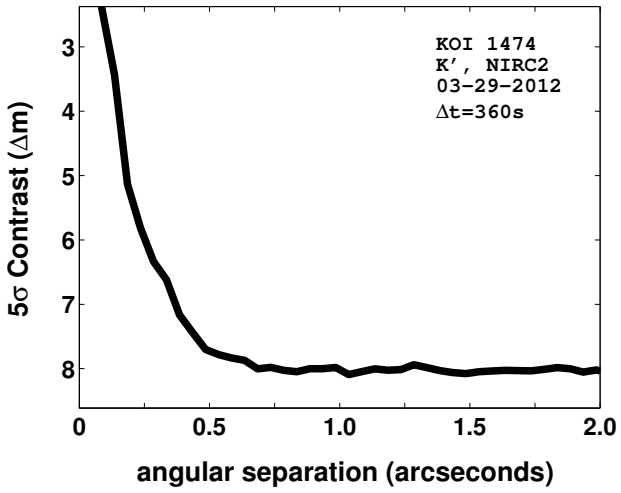

Figure 6.4.—: Sensitivity to off-axis sources in the immediate vicinity of KOI-1474 using adaptive optics imaging observations with NIRC2 at Keck in the K'-band ($\lambda_c = 2.12\mu m$). Figure courtesy of Justin Crepp.

6.4 False Positive Probability

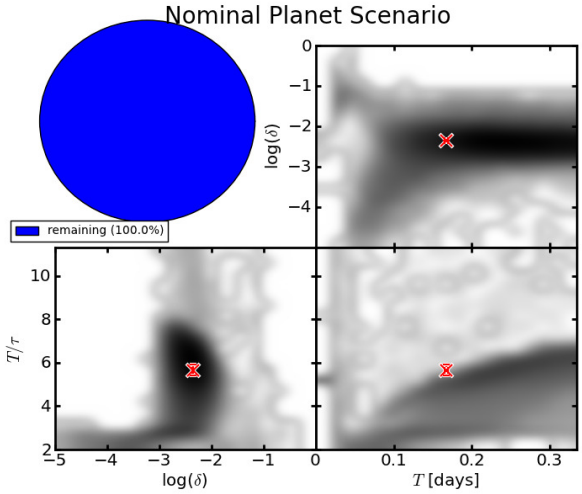

Figure 6.5.—: Three-dimensional probability distribution for the trapezoidal shape parameters (depth δ, duration T, and "slope" T/τ) for the nominal planet scenario. The distributions are generated by simulating a statistically representative population (see Morton 2012, Section 3.1) for the scenario and fitting the shape parameters to each simulated instance. Each population begins with 100,000 simulated instances, and only instances that pass all available observational constraints are included in these distributions. In this case, no additional observational constraints are available so the 100% of the distribution remains. The transit's shape parameters δ, T, and T/τ are marked on each plot with an "X" denoting the the median of an MCMC fit. Figure courtesy of Timothy Morton.

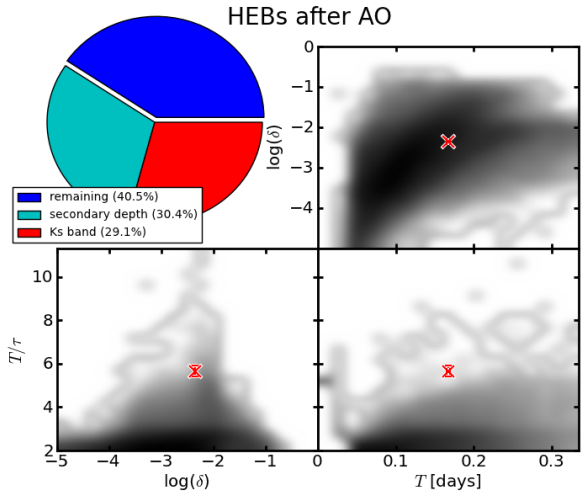

Figure 6.6.—: Same as Figure 6.5 for the HEB scenario. In this case, the upper-limit of 200 ppm we place on the secondary eclipse depth eliminates 30.4% of the distribution and limits from the Ks-band adaptive optics image eliminate 29.1% of the distribution, leaving 40.5% remaining. Figure courtesy of Timothy Morton.

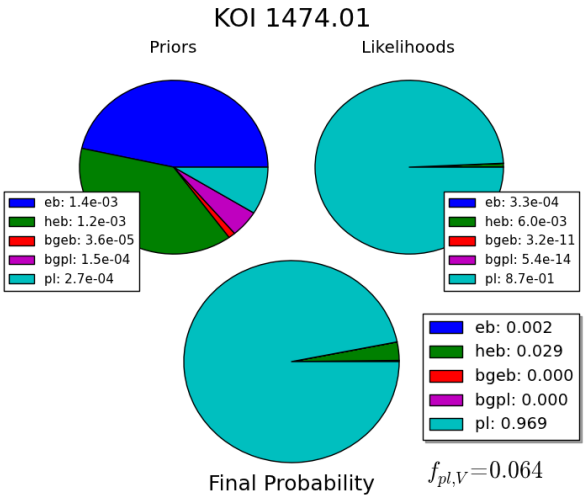

Figure 6.7.—: Prior (top left), likelihood (top right), and final (bottom) probabilities for four false positive scenarios — an undiluted eclipsing binary ("eb"), hierarchical eclipsing binary ("heb"), background eclipsing binary ("bgeb"), and background planet ("bgpl"). The priors and likelihoods are computed following Morton (2012). Each final probability is the product of the scenario's prior and likelihood, normalized so that the total probabilities sum to 1. The quantity $f_{\rm pl,V}$ indicates the specific occurrence rate for planets of this size that we would need to assume in order for the FPP to be less than 0.5%. Since this rate, $f_{\rm pl,V} = 6.4\%$, is higher than our assumed $f_{\rm pl} = 0.01$, we do not consider the candidate validated. Figure courtesy of Timothy Morton.

Although a transiting planet may cause the photometric signal observed in light curves (Figure 6.1), any of several scenarios involving stellar eclipsing binaries might cause a similar signal. This is the well-known problem of astrophysical false positives for transit surveys (e.g. Brown 2003; Torres et al. 2011). Traditionally transiting planets have been confirmed through detection of their radial velocity (RV) signals. However, the *Kepler* mission has necessitated a different paradigm: one of *probabilistic validation*. If the false positive probability (FPP) of a given transit signal can be shown to be sufficiently low (e.g. $\ll 1\%$), then the planet can be considered *validated*, even if not dynamically confirmed. Timothy Morton attempted to validate KOI-1474.01 but found a 3.1% probability that the signal is due to an astrophysical false positive.

At first glance, the short duration of KOI-1474.01's transit (Section 6.2) causes particular concern: the signal could be a transit or eclipse of an object orbiting a smaller, blended star, which would make the duration more in line with that expected for a circular orbit. In order to calculate the FPP for KOI-1474.01, Timothy Forton followed the procedure outlined in Morton (2012), which incorporates simulations of realistic populations of false positive scenarios, the KIC colors, the measured spectroscopic stellar properties, and a descriptive, trapezoidal fit to the photometric data.

To place constraints on blending by searching for nearby sources, Justin Crepp obtained adaptive optics images of KOI-1474 on March 29, 2012 using NIRC2 (PI: Keith Matthews) at the 10m Keck II telescopes. KOI-1474 is sufficiently bright to serve as its own natural guide star ($K_P = 13.005$) and therefore does not require the use of a laser to correct for wavefront errors introduced by the Earth's atmosphere. His observations consist of 18 dithered images (10 coadds per frame, 2 seconds per coadd) taken in the K' filter ($\lambda_c = 2.12\mu$m). He used NIRC2's narrow camera mode, which has a platescale of

10 mas / pix, to provide fine spatial sampling of the stellar point-spread function.

Raw frames were processed by cleaning hot pixels, flat-fielding, subtracting background noise from the sky and instrument optics, and coadding the results. No off-axis sources were noticed in individual frames or the final processed image. Figure 6.4 shows the contrast levels achieved from Justin Crepp's observations. His diffraction-limited images rule out the presence of contaminants down to $\Delta K' = 5$ mag and $\Delta K' = 8$ mag fainter than the primary star for separations beyond 0.2" and 0.7" respectively.

Timothy Morton plots the probability distributions for the nominal planet scenario in Figure 6.5, as well as for the most likely alternative to a transiting planet: an hierarchical eclipsing binary (HEB) (Figure 6.6), in which KOI-1474 has a wide binary companion of comparable brightness (within a few magnitudes) that is being eclipsed by a small tertiary companion. The probability of the HEB scenario is 2.3%. In Figure 6.7, Timothy Morton summarizes the prior, likelihood, and total probability of the nominal transiting planet scenario compared to that of several false positive scenarios. The FPP is:

$$\mathrm{FPP} = \frac{L_{FP}}{L_{FP} + \frac{f_P}{0.01} L_{TP}} = \frac{(0.002 + 0.029 + 0.000 + 0.000)}{(0.002 + 0.029 + 0.000 + 0.000) + \frac{0.01}{0.01} 0.969} = 0.031 \qquad (6.4)$$

where L_{FP} is the sum of the probabilities of the false-positive scenarios, L_{TP} is the probability of the nominal planet scenario, and f_P is the assumed specific occurrence rate[7] for planets between 5.7 and 11.3 $R_\oplus$. Although this FPP is low, we do not consider it sufficiently low to validate the planet. In the analysis following in the remainder of the

[7]The assumed 1% occurrence rate is motivated by the debiased 1% occurrence rate for hot Jupiters in

paper, we assume that KOI-1474.01 is a planet and refer to it as "planet," but in fact it remains a candidate planet. John Johnson is conducting a radial-velocity follow-up campaign of this target to confirm this candidate by measuring its mass.

6.5 The Highly Eccentric Orbit of KOI-1474.01

In Section 6.3, we revised the stellar properties of KOI-1474 and found that the star's density indicates that the (validated) planet's orbit is highly eccentric. To quantify the eccentricity, we now model the light curves (Figure 6.1) with the Transit Analysis Package software (TAP, Gazak et al. 2012) to obtain the posterior distribution for the eccentricity and other transit parameters (Section 6.5.1), using the technique described in Paper I. In Section 6.5.2, we place constraints on the spin-orbit alignment based on stellar properties measured in Section 6.3.3. In Section 6.5.3, we assess the observed TTVs and explore the nature of the third-body perturber.

6.5.1 Fitting Orbital Parameters to the Light Curve

Here we measure KOI-1474.01's orbital parameters, including eccentricity, from the transit light curves (Figure 6.1). We use TAP to fit a Mandel & Agol (2002) light curve model, employing the wavelet likelihood function of Carter & Winn (2009). We replace the parameter $a/R_\star$ with $\rho_\star$ (Winn 2010, Equation 30) in the limit that $(M_\star + M_p)/(\frac{4}{3}\pi R_\star)^3 \rightarrow \rho_\star$, but transform $\rho_\star$ into $a/R_\star$ to compute the light curve model.

the RV sample (Wright et al. 2012). In order to produce a FPP of than 0.5%, f_p would have be greater than 6.4%. See Morton (2012) for a discussion of specific planet occurrence rates.

Using the spectroscopic stellar parameters measured in Section 6.3.1 (Table 6.1, column 2), we calculate the limb darkening coefficients μ_1 and μ_2 and their uncertainties with the table and interpolation routine provided by Sing (2010). In all the orbital fits discussed here, we impose normal priors on μ_1 and μ_2 (Table 6.1), which are well-measured for the Kepler bandpass. We also verified that uniform priors on the limb darkening yield consistent results (with slightly larger uncertainties) for all the orbital fits we perform. The other light curve parameters we fit for are the mid-transit time of each light curve T, the planet-to-stellar radius ratio $R_p/R_\star$, the fractional white noise σ_w, the red noise σ_r, the inclination i, and the argument of periapse ω, with uniform priors on each of these quantities.

Finally, to speed up the fit convergence, we explore parameter space using the parameter g instead of the planet's orbital eccentricity e. The parameter g corresponds approximately to the ratio of the observed transit speed to the speed expected of a planet with the same period but $e = 0$:

$$g(e, \omega) = \frac{1 + e \sin \omega}{\sqrt{1 - e^2}} = \left(\frac{\rho_\star}{\rho_{\rm circ}} \right)^{1/3} \tag{6.5}$$

We impose a prior on g to maintain a uniform eccentricity prior (see Section 3.3.1 of Paper I for further details):

$$\text{prob}(g) = \frac{\sin^2 \omega \left(\sin^2 \omega - 1 \right) + g^2 \left(1 + \sin^2 \omega \right) \pm 2g \sin \omega \sqrt{\sin^2 \omega - 1 + g^2}}{\sqrt{\sin^2 \omega - 1 + g^2} \left(g^2 + \sin^2 \omega \right)^2} \tag{6.6}$$

for which the + corresponds to $g > 1$ and the $-$ to $g < 1$. We transform g into e to compute the light curve model.

First we fit a circular orbit (Table 6.2, column 2), fixing $e = 0$ and leaving free $\rho_\star$, to which we refer as $\rho_{\rm circ}$. We find that: 1) although we only have long-cadence data for KOI-1474 (Figure 6.1), $\rho_{\rm circ}$ and the impact parameter b are separately well-constrained (see also Section 4.2 of Paper I for a discussion of long-cadence data), and 2)the $\rho_\star$ posterior computed from stellar properties in Section 6.3.3 ($\rho_\star = 0.44^{+0.26}_{-0.20}\rho_\odot$) falls far outside the transit light curve posterior distribution for $\rho_{\rm circ}$ ($\rho_\star = 9.2^{+0.4}_{-1.6}\rho_\odot$, Figure 6.8, top left panel), where the uncertainties indicate the 68.3% confidence interval. Thus a circular fit is inconsistent with our prior knowledge of the stellar parameters.

Because the eccentricity depends only weakly on the assumed stellar density, the eccentricity measurement we are about to perform is relatively robust to errors in the assumed stellar density. When $\rho_\star > \rho_{\rm circ}$, the transiting planet has a minimum eccentricity obtained by setting $\omega = \pi/2$ in Equation (6.5) (i.e. the planet transits at periapse). Imagine that $\rho_\star$ were biased or in error. The fractional change in $e_{\rm min}$ would be:

$$\frac{\Delta e_{\rm min}}{e_{\rm min}} = \frac{4}{3\left[\left(\frac{\rho_\star}{\rho_{\rm circ}}\right)^{2/3} - \left(\frac{\rho_\star}{\rho_{\rm circ}}\right)^{-2/3}\right]} \frac{\Delta(\frac{\rho_\star}{\rho_{\rm circ}})}{(\frac{\rho_\star}{\rho_{\rm circ}})} \tag{6.7}$$

The ratio $\frac{\rho_\star}{\rho_{\rm circ}} = \frac{9.2}{0.44} = 21$, corresponding to $e_{\rm min} = 0.77$ and $\frac{\Delta e_{\rm min}}{e_{\rm min}} = 0.18\frac{\Delta(\frac{\rho_\star}{\rho_{\rm circ}})}{(\frac{\rho_\star}{\rho_{\rm circ}})}$. So if the stellar density were biased upward by 10%, the minimum eccentricity would be biased upward by only 1.8%. See Section 3.1 and Section 4.1 Paper I for a detailed exploration of how the stellar density's assumed probability distribution affects the eccentricity measurement.

Next we fit the light curve allowing the planet to have an eccentric orbit (Table 6.2, column 3) and using the stellar density posterior from Section 6.3.3 as the stellar density prior for the light curve fit. As argued in Paper I (Section 3), an MCMC exploration —

as implemented in TAP — naturally accounts for the transit probability and marginalizes over the uncertainties in other parameters. Even though e and ω are degenerate for a given g (Equation 6.5), there is a lower limit on e, and the posterior falls off gradually, as $e \to 1$ and the range of possible ω satisfying Equation 6.5 narrows. The posterior distributions for e and ω are plotted in Figure 6.8. We measure $e = 0.81^{+0.10}_{-0.07}$. For comparison, if we had set the stellar density prior to be uniform between $0.1\rho_\odot - 0.2\rho_\odot$ ($0.6\rho_\odot - 1.2\rho_\odot$), we would measure $e = 0.90^{+0.03}_{-0.03}$ ($e = 0.73^{+0.15}_{-0.09}$).

By conservation of angular momentum, this planet would attain a final period $P_{\rm final}(1-e^2)^{3/2} = 14^{+9}_{-10}$ days if it were to undergo full tidal circularization. In Section 6.6, we will discuss whether the planet is best classified as a proto-hot Jupiter — likely to circularize over the star's lifetime and achieve a short-period orbit — or a failed-hot Jupiter, just outside the reach of fast tidal circularization.

6.5.2 Constraints on Spin-orbit Alignment

Whatever process perturbed KOI-1474.01 onto an eccentric orbit may have also tilted the planet's orbit from the plane in which it formed. With a temperature of 6240 ± 100 K (Section 6.3.1), KOI-1474 sits right on the 6250 K boundary between hot stars with high obliquities and cool stars with well-aligned planets (Winn et al. 2010). However, if 1) cool stars have low obliquities because their hot Jupiters have realigned the star's outer convective layer, as proposed by Winn et al. (2010), and 2) KOI-1474.01 is a failed-hot Jupiter, with a tidal dissipation rate too low to experience significant circularization over KOI-1474's lifetime, then KOI-1474.01 may have also not yet realigned KOI-1474's outer layer. Ultimately we will wish to determine ψ, the total misalignment between the orbit

normal and the host star spin axis, from three measured projected angles (Fabrycky & Winn 2009; Schlaufman 2010): i, the inclination between the planet's orbit and the observer's line of sight; the sky-projected spin-orbit angle λ; and i_s, the inclination between the stellar spin axis and the line of sight. We measured i from the transit light curve in Section 6.5.1 (Table 6.2). The sky-projected spin-orbit angle λ could one day be measured via the Rossiter-McLaughlin (RM) effect (McLaughlin 1924; Rossiter 1924; Queloz et al. 2000), the change in the observed radial velocity as a transiting planet blocks portions of the star rotating toward or away from the observer. The effect has a maximum amplitude of about 50 m/s (Winn 2010, Equation 40) However, because KOI-1474.01's transits can occur early or late by over an hour, RM measurements of KOI-1474.01 will remain challenging until the TTV pattern "turns over" in future Kepler observations, allowing us to predict future transits to much higher precision (Section 6.5.3). We can measure the third projected angle, i_s, from $(v_{\rm rot} \sin i_s)_{\rm spec}$ (Section 6.3.1) and the posteriors of $P_{\rm rot}$ (Section 6.3.2) and $R_\star$ (Section 6.3.3), an approach that was recently applied by Hirano et al. (2012) to fifteen KOI systems. KOI-1474's rotational velocity is $v_{\rm rot} = \frac{2\pi R_\star}{P_{\rm rot}}$ and we have measured the projected rotational velocity $(v_{\rm rot} \sin i_s)_{\rm spec}$. Therefore we can find the angle of that projection, i_s. According to Bayes theorem:

$$\text{prob}\left(P_{\rm rot}, R_\star, i_s | (v_{\rm rot} \sin i_s)_{\rm spec}\right) = \text{prob}\left((v_{\rm rot} \sin i_s)_{\rm spec} | P_{\rm rot}, R_\star, i_s\right) \text{prob}\left(P_{\rm rot}, R_\star, i_s\right). \tag{6.8}$$

The prior, $\text{prob}\left(P_{\rm rot}, R_\star, i_s\right)$, is the product

$$\text{prob}\left(P_{\rm rot}, R_\star, i_s\right) = \text{prob}(P_{\rm rot})\text{prob}(R_\star)\text{prob}(i_s)$$

where $\text{prob}(P_{\rm rot})$ is a normal distribution with mean 4.6 m/s and standard deviation 0.4 m/s (Section 6.3.2) and $\text{prob}(R_\star)$ is the posterior from Section 6.3.3. Assuming stellar

spin axes are randomly oriented throughout the Galaxy, the distribution of $\cos i_s$ is uniform and thus $\text{prob}(i_s) = \frac{1}{2}\sin i_s$.

Next, we integrate Equation 6.8 over $P_{\rm rot}$ and $R_\star$ to obtain the stellar inclination i_s conditioned on our measured projected rotational velocity $v_{\rm rot}\sin i_s$.

$$\text{prob}\left(i_s|(v_{\rm rot}\sin i_s)_{\rm spec}\right) = \int\int \text{prob}\left((v_{\rm rot}\sin i_s)_{\rm spec}|P_{\rm rot}, R_\star, i_s\right)\text{prob}\left(P_{\rm rot}, R_\star, i_s\right) dP_{\rm rot} dR_\star \tag{6.9}$$

As a practical implementation of Equation (6.9) we randomly draw $P_{\rm rot}$ and $R_\star$ from the distributions calculated in Section 6.3.2 and Section 6.3.3 respectively and i_s from a uniform distribution of $\cos i$ between 0 and 1. Drawing from these respective distributions is equivalent to creating a grid in these parameters and subsequently downsampling according to the prior probabilitities. Then we compute the likelihood

$$\begin{aligned}&\text{prob}\left((v_{\rm rot}\sin i_s)_{\rm spec}|P_{\rm rot}, R_\star, i_s\right)\\ &= \exp\left[-\left(\frac{2\pi R_\star}{P_{\rm rot}}\sin i_s - (v_{\rm rot}\sin i_s)_{\rm spec}\right)^2 \Big/ \left(2\sigma^2_{(v_{\rm rot}\sin i_s)_{\rm spec}}\right)\right]\end{aligned} \tag{6.10}$$

where $(v_{\rm rot}\sin i_s)_{\rm spec}$ =13.6 m/s and $\sigma_{(v_{\rm rot}\sin i_s)_{\rm spec}}$ = 0.5 m/s (Section 6.3.1). Then we select a uniform random number between 0 and 1; if the uniform random number is less than $\text{prob}\left((v_{\rm rot}\sin i_s)_{\rm spec}|P_{\rm rot}, R_\star, i_s\right)$ (Equation 6.10), we include the model $(P_{\rm rot}, R_\star, i_s)$ in the posterior. We repeat drawing $(P_{\rm rot}, R_\star, i_s)$ models until we have thousands of models that comprise the posterior.

We measure a projected angle for the stellar spin axis $i_s = 69^{+14}_{-17}$ degrees. Combining the posterior of i_s with the posterior of the planet's inclination i (Section 6.5.1),we obtain $|i - i_s| = 21^{+17}_{-14}$, for which the total uncertainty is dominated by the uncertainty in the stellar radius. We list these angles in Table 6.2, and plot the posterior for the line-of-sight spin-orbit angle $|i - i_s|$ in Figure 6.8 (top right panel). Our posterior distribution is

consistent (within 2 σ) with close alignment, yet allows misaligned configurations as well. We also caution that differential rotation may cause systematic errors in the measured alignment, depending on the latitude of the spots (see Hirano et al. 2012, Section 5.3 for a detailed discussion). Furthermore, the line-of-sight spin-orbit angle $|i - i_s|$ offers no constraint on whether the planet's orbit is prograde or retrograde. However, two types of future follow-up observations will allow us to better constrain the planet's orbit in three dimensions. First, additional constraints on the planet's orbit through radial-velocity measurements will in turn constrain the stellar radius, providing a more precise measurement of $|i - i_s|$. To this end we are currently conducting a Doppler follow-up program at Keck with HIRES. Second, from the measurement of the sky-projected spin-orbit angle λ via the RM effect, the total spin-orbit angle ψ can be computed by combining λ with a refined line-of-sight measurement $|i - i_s|$.

6.5.3 Transit Timing Variations

The light curves in Figure 6.1 reveal large variations in the mid-transit times of KOI-1474.01, which may be caused by perturbations from another planet or sub-stellar companion. If KOI-1474.01 underwent HEM, this perturber may have been responsible. Table 6.2 displays the mid-transit times from the orbital fits performed in Section 6.5.1. There the best-fitting linear ephemeris is also given, from which the times deviate significantly. In Figure 6.9, we plot an observed minus calculated (O-C) diagram of the observed transit time minus the transit time calculated from a constant orbital period. The scale and sharpness of the features in Figure 6.9 suggest a nearby giant planet or brown dwarf perturber. We assume this perturber is on an exterior orbit,

as KOI-1474.01's eccentric orbit leaves little dynamical room interior to itself. John Johnson undertaking a radial-velocity follow-up campaign (Johnson et al. 2013, in prep) that may allow us to rule out an interior, Jupiter-mass companion.

The "jump" in the O-C diagram likely corresponds to the periapse passage of an eccentric companion (Borkovits et al. 2003, 2004; Agol et al. 2005; Borkovits et al. 2011). Throughout its orbit, this perturbing companion creates a tidal force on the orbit of the transiting planet. If the companion's orbit is exterior to and within the plane of the transiting planet's, the tidal force increases the inner planet's orbital period or, equivalently, decreases the effective mass of the central star (see Section 4 of Agol et al. 2005 for a detailed derivation). The tidal force varies with the distance between the perturber and star and is strongest when the perturber is at periapse. Therefore, as the perturber approaches periapse, the transiting planet's orbital period lengthens, causing later and later transit arrival times, corresponding to the discontinuity seen in Figure 6.9. The period of the TTV cycle corresponds to the perturbing planet's orbital period. The amplitude is set by the change in the tidal force (a combination of the perturbing planet's mass and periapse distance, which is a function of the eccentricity and orbital period). The sharpness of the O-C depends on the perturber's eccentricity — whether the perturbation is the flyby of a companion on a highly eccentric orbit or the gradual approach of a moderately eccentric companion. The transiting planet's orbital eccentricity also subtly affects the shape of the O-C diagram, as explored in detail by Borkovits et al. (2011). Our Figure 6.9 has a similar appearance to the TTVs produced by Borkovits et al. (2011)'s analytical and numerical models of eccentric, hierarchal systems.

Currently we do not have a long enough TTV baseline to uniquely model the

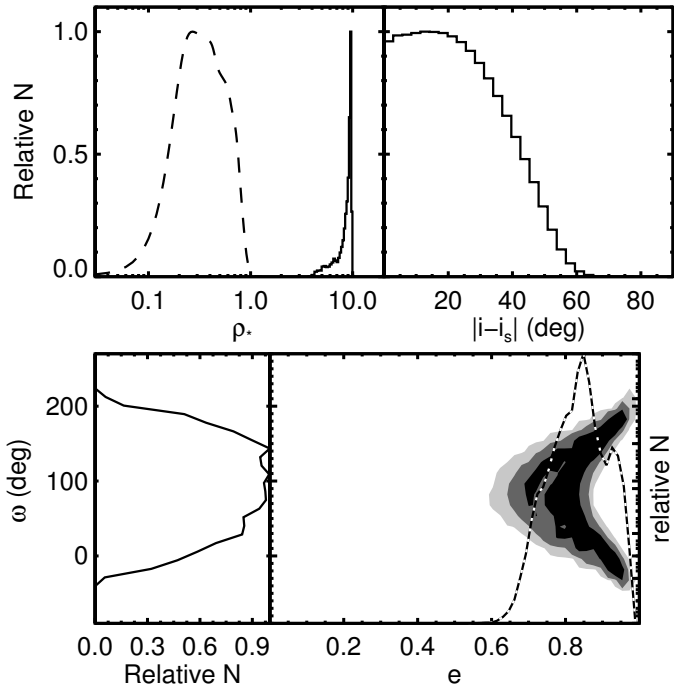

Figure 6.8.—: Top left: $\rho_{\rm circ}$ obtained from circular fit to the transit light curve (solid) and posterior for $\rho_\star$ from Section 6.3.3 (dashed); since the host star is not highly dense (i.e. the two posteriors do not overlap), the planet's orbit must be highly eccentric. Top right: Posterior for projected spin-orbit alignment from an eccentric fit to transit light curve, imposing a prior on $\rho_\star$. Bottom left: Posterior distribution ω from an eccentric fit to transit light curve, imposing a prior on $\rho_\star$. Bottom right: Joint posterior for ω vs. e. The black (gray, light gray) contours represent the $\{68.3, 95, 99\}\%$ probability density levels (i.e. 68% of the posterior is contained within the black contour) Over-plotted as a black-and-white dotted line is a histogram of the eccentricity posterior probability distribution marginalized over ω.

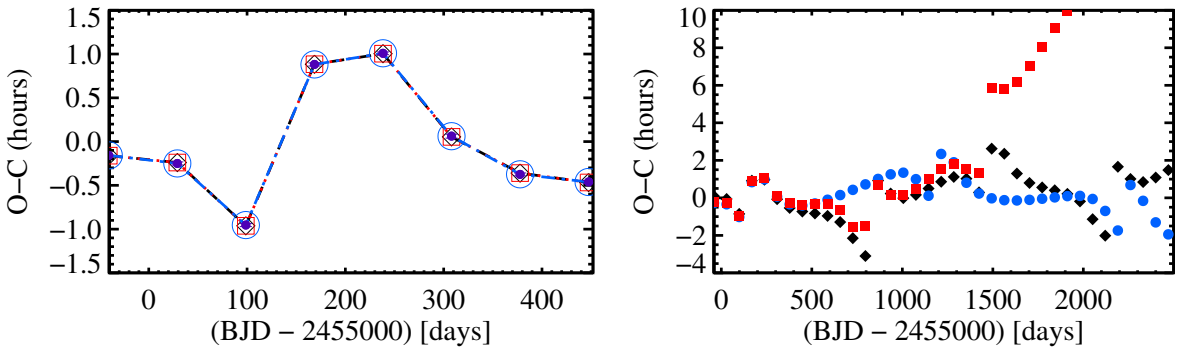

Figure 6.9.—: Left: Observed mid transit times (purple dots) of the eight transits of 1474.01 with subtracted best fit linear ephemeris from the Section 6.5.1 transit light curve model (Table 6.2, column 3). TTV predictions from the first (solid black, open diamonds), second (red, open squares), and third (blue, open circles) dynamical model in Table 6.3. All three models match the data well. Right: Same models as left plotted over longer timespan; the models differ in their predictions for future O-C variations. Models courtesy of Daniel Fabrycky.

perturbing companion, as Nesvorný et al. (2012) achieved for the system KOI-857. Since "jumps" in the O-C diagram correspond to the perturber's periapse passage and we have only seen one such jump, apparently the current TTVs cover less than one orbit of the outer companion. Therefore we cannot well constrain the outer body's orbital period. The TTV amplitude – set by the tidal force on the transiter's orbit – is well constrained but depends on the perturber's mass, orbital period, and eccentricity; therefore we expect to find degeneracy among these quantities. Furthermore, the tidal force on the transiter's orbit depends on the mutual inclinations of the bodies. The tide due to a polar position for the perturber would *decrease* the transiter's orbital period; averaging over the bodies' positions, a very inclined perturber could be more massive and yet produce a comparable amplitude perturbation.

Daniel Fabrycky explored a subset of all possible parameters for the perturbing planet. With only eight transit times (Table 6.2), he had a great amount of freedom in the fits, but it is still of interest whether or not a physical model of a perturber can fit these data.[8] Thus he proceeded with direct 3-body fits to the data. He did not expect the TTVs to be sensitive to the mass of the transiting planet or the host star (Borkovits et al. 2011; Nesvorný et al. 2012) so he fixed $M_{.01} = 1 M_{\rm Jup}$ and $M_\star = 1.22 M_\odot$. He fixed the eccentricity and argument of periapse of KOI-1474.01 to various values consistent with the light curve, then fit for the period P_2, the conjunction epoch $T_{0,2}$, $e_2 \cos\omega_2$, $e_2 \sin\omega_2$, and the mass M_2 of the perturbing body (denoted "2"). The fits are performed

[8]For example, Nesvorný et al. (2012) demonstrated that, as expected, they could not find a physically plausible model when they scrambled their TTVs. Failure to find an orbital model that reproduces the observed TTVs would cast suspicion on our interpretation that they are the signature of an unseen companion.

via a Levenberg-Marquardt algorithm driving a numerical integration that solves for transit times (Fabrycky 2010).

Initially Daniel Fabrycky considered coplanar, edge-on orbits. This configuration is consistent with the transiting planet, and although no transit of the perturbing body has been observed, it may transit in future data or may be within a few degrees of edge-on, which would make little difference to the TTVs. He first allowed all 5 parameters of the outer planet to float freely, finding the best fits at each value. He performed two fits (Table 6.3, rows 1-4), one with KOI-1474.01 transiting at periapse and another with it transiting at semilatus rectum. Both fits are acceptable, so he found that he cannot currently use TTVs to distinguish these possibilities. In Figure 6.9, we plot the O-C variations generated by Daniel Fabrycky's two models. In both cases, the perturber is a giant planet on a moderately eccentric orbit with a roughly Martian orbital period. He repeated both these fits with a fixed mass of $100 M_{\rm Jup}$ for KOI-1474.01 and found, as expected, that the solutions were similar, with only a slightly larger ($\sim 20\%$) best-fit mass for the perturber.

Next he performed a fit for which the transiting planet and the perturbing body have a 124° mutual inclination, a possible outcome of the secular chaos HEM mechanism (Naoz et al. 2011). As discussed above, non-coplanar orbits allow for a more massive perturbing companion. This fit (Table 6.3, row 5-6), featuring a 24.3 $M_{\rm Jup}$ brown dwarf companion with a one-thousand day orbital period and moderate eccentricity, is an excellent match to the observed TTVs and is plotted in Figure 6.9. In contrast to the coplanar fits, this model predicts deviations not only in the central transit times but in the duration of the transits (e.g. Miralda-Escudé 2002; Nesvorný et al. 2012), due to a secular variation in the transiting planet's duration. However, the small transit duration

Table 6.3. Parameter values for TTV fits, courtesy of Daniel Fabrycky. Fixed in all fits are $M_\star = 1.22 M_\odot$, $M_{.01} = 1 M_{\rm Jup}$, $i_{.01} = 90°$, and $\Omega_{.01} = 0°$. Orbital elements are Jacobian elements (the outer body's orbit referred to the center-of-mass of the star and the planet) defined at dynamical epoch BJD 2455200. Table and fits courtesy of Daniel Fabrycky.

$P_{.01}$ [days]	$T_{.01}$[BJD-2455000] [days]	e_{01}	$\omega_{.01}$	P_2 [days]	T_2[BJD-2455000] [days]	$e_2 \cos\omega_2$	$e_2 \sin\omega_2$	M_2 ($M_{\rm Jup}$)	i_2	Ω_2	χ^2
69.709474	238.271516	0.74	90°	660.7	496.0	-0.0092	-0.1824	6.66	90°	0°	4.65
±0.001696	±0.002734	fixed	fixed	±21.0	±7.2	±0.0105	±0.0192	±0.34	fixed	fixed	
69.721695	238.150714	0.90	180°	643.8	304.81	0.148	-0.0496	5.82	90°	0°	2.62
±0.002548	±0.004422	fixed	fixed	±50.6	±2.31	± 0.059	±0.0103	±0.98	fixed	fixed	
69.749706	238.303853	0.74	90°	1038.0	841.9	-0.0681	-0.3567	24.28	60°	130°	0.01
±0.000499	±0.000672	fixed	fixed	±38.5	±21.3	±0.0078	±0.0148	±0.41	fixed	fixed	

variations predicted by this model would not be significantly detected in the current data and, depending on the impact parameter, may or may not be detectable in by the *Kepler* extended mission. Comparing the goodness of this fit to the two coplanar ones, Daniel Fabrycky saw the he could neither distinguish the orbital plane of the third body, nor limit its mass to the planetary regime.

In all three cases, we see in the integrations that, as expected, the "jumps" in the TTVs correspond to the companion's periapse passage. In the right panel of Figure 6.9, we plot the TTVs[9] into the future. Additional transits in the Q7-Q12 data scheduled for future public release and through the *Kepler* extended mission may allow us to distinguish among them, as well as the many other possible models among which we cannot distinguish currently. We have used the Bulirsch Stoer integrator in `Mercury` (Chambers 1999) to confirm that all three fits described here are dynamically stable over 10 Myr, with no planet-planet scattering occuring during this interval. The fits do not rule out past planet-planet scattering: in the context of HEM, the bodies could have undergone scattering in the past and subsequently stabilized as KOI-1474.01's orbit shrank through tidal dissipation. We note that the transiting planet's eccentricity undergoes secular variations and, in the case of the first two fits, the current e_{01} is not the maximum and thus the planet experiences enhanced tidal dissipation during other parts of the secular cycle. We discuss this behavior further in the next section, in which we consider whether KOI-1474.01 is a failed- or proto-hot Jupiter. We defer exhaustive exploration of the parameter space of the three body model until more data are available,

[9]In plotting these extended models, we have slightly adjusted the linear ephemeris of the transiting planet to remain consistent with the data while keeping future O-C variations centered at 0. Otherwise the predicted differences between the three different models appear misleadingly large.

including additional transit times that extend the baseline to cover the perturber's subsequent periapse passage and complementary constraints on the perturber's mass, period, and eccentricity from planned radial-velocity measurements. However, the possibilities illustrated here show that pinning down the perturber's mass and orbit will likely reveal clues about the past mechanism of HEM and the future fate of KOI-1474.01.

6.6 KOI-1474.01: a Proto- or Failed-hot Jupiter?

KOI-1474.01 is a highly eccentric, Jupiter-sized planet being perturbed by an unseen companion, the "smoking gun" that may have been responsible for KOI-1474.01's HEM. The transiting planet might be either a proto-hot Jupiter that will achieve a short period, low eccentricity orbit via tidal dissipation over its host star's lifetime or a failed-hot Jupiter, too far from its star to experience significant tidal dissipation. If the planet is a failed-hot Jupiter, it is destined to spend the remainder of its host star's lifetime in the "period valley" (Jones et al. 2003; Udry et al. 2003; Wittenmyer et al. 2010), between the region where it formed (beyond 1 AU) and the hot Jupiter region (P $<$ 10 days $\approx$ 0.091 AU).

S12 predicted the discovery of super-eccentric hot Jupiter progenitors among the *Kepler* candidates based on the following argument. A Jupiter kicked to a small periapse via one of several proposed HEM mechanisms will enter the proto-hot Jupiter stage. Assuming that a steady flux of hot Jupiters are being spawned throughout the Galaxy, there must exist a steady-state stream of highly eccentric planets on their way to becoming the population of hot Jupiters thus far observed. The tidally-decaying Jupiters follow tracks of constant angular momentum: $P_{\rm final} = P(1-e^2)^{3/2}$, where P and e are

the values corresponding to any time during the circularization process.

To predict the number of highly-eccentric proto-hot Jupiters that *Kepler* will discover, S12 used the Exoplanet Orbit Database (EOD) sample of planets with $M_p \sin i > 0.25 M_{\rm Jup}$ and $P_{\rm final} < 10$ days (Wright et al. 2011, `http://www.exoplanets.org`). The $P_{\rm final}$ cut-off is motivated by the excess of currently known Jupiter-mass planets on circular orbits with $P < 10$ days. They computed the fraction of Jupiters in the ranges $3 < P_{\rm final} < 5$ days and $5 < P_{\rm final} < 10$ days that are moderately eccentric ($0.2 < e < 0.6$). Next they multiplied these fractions by the total number of Jupiter-sized ($\rm R > 8 R_\oplus$) *Kepler* candidates in these two $P_{\rm final}$ ranges, yielding the predicted number of moderately eccentric *Kepler* Jupiters. Finally, they use the Hut (1981) tidal equations to compute the relative number of highly eccentric to moderately eccentric Jupiters at a given $P_{\rm final}$ and predict 5-7 super eccentric Jupiters in the *Kepler* sample with $e > 0.9$ and $P < 93$ days.

Because of the uncertainty in KOI-1474.01's eccentricity, we cannot definitively say whether it is one of the super-eccentric Jupiters predicted by S12. From our orbital fits in Section 6.5.1, we derive a $P_{\rm final}$ posterior distribution of which 42% have $P_{\rm final} < 10$ days and 19% have $P_{\rm final} < 5$ days. Therefore, the evidence only slightly favors the interpretation that KOI-1474.01 is a failed-hot Jupiter with a $P_{\rm final} > 10$ days. Follow-up, high-precision radial velocity measurements may allow us to constrain KOI-1474.01's eccentricity even more tightly and confirm or rule out $e > 0.9$ and $P_{\rm final} < 10$ days. Furthermore, the perturbing companion may cause secular variations in KOI-1474.01's eccentricity (Section 6.5.3), boosting the tidal circularization rate during intervals of higher eccentricity; additional constraints on the perturber's identity may one day allow us to explore this effect.

In Figure 6.10, we display KOI-1474.01 (gray circle) in the context of the current sample of Jupiter-sized and Jupiter-mass planets. We plot the quantity $(1 - e^2)$ vs. a to allow us to overlay tracks of constant angular momentum while visually distinguishing high vs. low eccentricities. An $a_{\rm final}$ track is the path through phase space that a particular Jupiter follows during its tidal evolution; a Jupiter's current $a_{\rm final}$ defines its angular momentum and remains constant as the Jupiter undergoes tidal circularization. The solid, black lines represent tracks of angular momentum corresponding to $a_{\rm final} = 0.057, 0.091$ AU, i.e. $P_{\rm final} = 5, 10$ days around Sun-like stars. Any Jupiter along an $a_{\rm final}$ track will stay on that track, reaching $a = a_{\rm final}$ as its $e \to 0$. The other symbols represent planets with $M_p \sin i > 0.25 M_{\rm Jup}$, $0.7 M_\odot < M_\star < 1.3 M_\odot$, and measured eccentricities from the EOD (Wright et al. 2011). The median of KOI-1474.01's eccentricity posterior places the planet in the period valley from $0.1 < a < 1$ AU, along with about a dozen other eccentric Jupiters. At one-sigma, KOI-1474.01 may be within (i.e. to the left of) the $a_{\rm final} < 0.057$ AU track (i.e. will end up at a semi-major axis less than 0.057 AU if it fully circularizes), like the poster-planet of high eccentricity, HD 80606 b (red square).

However, KOI-1474.01's ultimate fate is determined not only by $P_{\rm final}$ but by its tidal circularization rate; even if the planet has $P_{\rm final} < 10$ days, it will not become a hot Jupiter unless it can circularize over its host star's lifetime. A hot Jupiter's tidal circularization rate depends on a combination of orbital properties and physical planetary and stellar properties. Following Eggleton et al. (1998) and Hansen (2010) — and neglecting the effects of the planet's spin and tides raised on the star — a

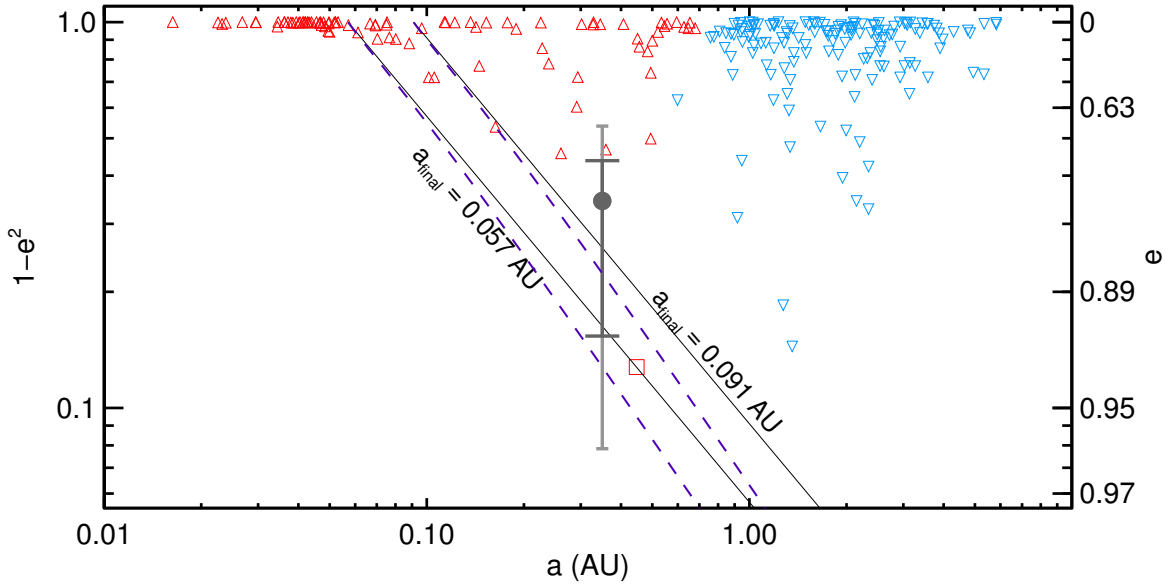

Figure 6.10.—: Distribution $(1-e^2)$ vs. semimajor axis for known exoplanets from the EOD with $0.7M_{\odot} < M_{\star} < 1.3M_{\odot}$, measured eccentricities, $M_p \sin i > 0.25M_{\rm Jup}$, and with apoapses beyond 0.9 AU (blue, downward triangles) or within 0.9 AU (red, upward triangles) (Wright et al. 2011, `http://www.exoplanets.org`). The gray circle marks KOI-1474.01, with the asymmetric gray error bars representing the 1-sigma (dark gray), 2-sigma (light gray) confidence interval of KOI-1474.01's eccentricity. HD 80606 b is denoted with a red square symbol. The solid black lines are tracks of constant angular momentum corresponding to $a_{\rm final} = 0.057$, 0.091AU; each indicates a track that a *single* Jupiter follows through phase space as it undergoes tidal circularization and maintains a constant angular momentum. As it fully circularizes ($e \rightarrow 0$), a Jupiter ends up at the top of the track at $1-e^2 = 1$. The purple, dashed lines represent constant tidal circularization rates corresponding to $a_{\rm circ} = 0.057$, 0.091AU (Equation 6.13). A group of Jupiters that lie along a particular purple $a_{\rm circ}$ line is undergoing tidal circularization at the same rate.

tidally-circularizing planet's eccentricity e-folding time is:

$$\frac{e}{\dot{e}} = -\frac{a^8(1-e^2)^{13/2}M_p}{63M_\star^2 R_p^{10} f_e \sigma_P} \tag{6.11}$$

where σ_P is the planet's internal dissipation constant and

$$f_e = \frac{1 + \frac{45}{14}e^2 + 8e^4 + \frac{685}{224}e^6 + \frac{255}{448}e^8 + \frac{25}{1792}e^{10}}{1 + 3e^2 + \frac{3}{8}e^4} \simeq 1 + 2.63e^3 \tag{6.12}$$

Note that the tidal circularization timescale $e/\dot{e}$ depends steeply on the planet's semimajor axis and eccentricity, but only weakly on physical stellar and planetary parameters[10]. Therefore we might expect to see a signature of tidal circularization in our $1-e^2$ vs. a plot even neglecting the difference in physical properties among the planets plotted.

First imagine if all the planets underwent HEM at once and have tidally evolved for time t. A certain curve in $(1-e^2)$ vs. a space, $a_{\rm circ}(a, 1-e^2)$, represents the circularization time (Equation 6.11) equal to t. We would expect this curve to envelope the still-eccentric Jupiter population, because all planets to the left of the curve (i.e. with $1-e^2$ less than the curve for a given semi-major axis) would have already undergone an e-folding's worth of circularization. The semi-major axis $a = a_{\rm circ}$ would be the edge of the circular population we call "hot Jupiters," planets for which t was a sufficient

[10]The other parameter raised to a large power is R_p^{10}. Most objects with $M > 0.25M_{\rm Jup}$ — from Jupiters to brown dwarfs — have $R_p \approx R_{\rm Jup}$; the R_p^{10} term varies by a factor of 60 from 1 Jupiter radius to 1.5 Jupiter radius. However, in practice we find if that we normalize a by $(R_p/R_{\rm Jup})^{5/4}$ for planets with known radii, Figure 6.10 does not change significantly. The circularization rate's strong dependence on a dominates, because a undergoes large fractional changes throughout the hot Jupiter region, with a change in semimajor axis of 0.02 AU corresponding to an order of magnitude change in the tidal circularization timescale.

amount of time to circularize. In reality, proto-hot Jupiters are being continuously spawned as new stars are born and as Jupiters undergo HEM. However, because of the steep a tidal dependence – with the tidal circularization timescale changing by an order of magnitude roughly every 0.02 AU in the hot Jupiter region — we still expect to see an $a_{\rm circ}$ boundary, corresponding to a circularization time equal to a typical stellar lifetime. To the left of this this $a_{\rm circ}$ boundary would be only true proto-hot Jupiters, caught in the act of tidal circularization. With a detailed accounting for observational bias and the relatively weak effects of the planets' different physical properties, one could predict the relative number of proto-hot Jupiters on each $a_{\rm circ}$ curve (e.g. Hansen 2010).

Solving Equation (6.11) for $(1-e^2)$, we can combine all the constants — including the timescale $e/\dot{e}$ — into $a_{\rm circ}$ and rewrite:

$$(1-e^2)f_e^{-2/13} = \left(\frac{a_{\rm circ}}{a}\right)^{16/13} \tag{6.13}$$

where $a_{\rm circ}$ represents the distance within which circular hot Jupiters have arrived via tidal dissipation. For small eccentricities, the factor of f_e is negligible. For large eccentricities, we can solve Equation (6.13) numerically for $(1-e^2)$. We plot $a_{\rm circ}$ curves – along which all Jupiters have a similar tidal circularization rate – in Figure 6.10 as purple dashed lines. We emphasize that although the black $a_{\rm final}$ lines and purple, dashed $a_{\rm circ}$ lines Figure 6.10 are close together, their physical interpretation is different: the quantity $a_{\rm circ}$ represents a proxy for the tidal circularization rate, whereas $a_{\rm final}$ is a track that an individual Jupiter follows as it undergoes tidal circularization obeying conservation of angular momentum. If the tidal evolution according to Eggleton et al. (1998) that yielded Equation 6.13 is a good approximation, then $a_{\rm circ}$ may be the best quantity to consider for the cut-off between proto- and failed-hot Jupiter.

Since we see a pile-up of circular hot Jupiters and no Jupiters with $1 - e^2 < 0.9$ to the left of the purple dashed line $a_{\rm circ} < 0.057$ AU (P = 5 days around a Sun-like star), this may represent the timescale at which circularization happens over a fraction of a stellar lifetime. Under this interpretation, HD 80606 b's identity as a proto-hot Jupiter is not certain: it lies between $a_{\rm circ} = 0.057$ AU and $a_{\rm circ} = 0.091$ AU, along with several other eccentric Jupiters that have yet to circularize. Using the internal dissipation constant $\sigma_P = 3.4 \times 10^{-7}(5.9 \times 10^{-54}){\rm g}^{-1}{\rm cm}^{-2}$ derived by Hansen (2010), the cut-off is even stricter: a Jupiter-like planet around a Sun-like star would only undergo an e-folding's worth of circularization over 10 Gyr if it had $a_{\rm circ} < 0.034$ AU. However, we note that Hansen (2010) derived the tidal dissipation constant under the assumption that proto-hot Jupiters, upon beginning their tidal circularization, have eccentricities drawn from a normal distribution with a mean $e = 0.2$ and standard deviation of 0.25. If the starting eccentricities are larger — as assumed by S12 for proto-hot Jupiters — a larger dissipation constant may be necessary to match the observed hot Jupiter sample. In order for a 10 Gyr e-folding time to correspond to $a_{\rm circ} = 0.057$ AU, the dissipation constant would need to be larger by a factor of 60.

The two-sigma upper limit on KOI-1474's eccentricity places the planet within $a_{\rm circ} < 0.057$ AU, but the two-sigma lower limit places it well beyond this boundary. The host star's age $\tau_\star$ is currently poorly constrained (Section 6.3.3), and we do not know how recently the planet underwent HEM. However, if the assumptions behind the discussion above are correct, the steep dependence of the tidal circularization rate on a and e means that most Jupiters within $a_{\rm circ} < 0.057$ AU would have circularization timescales $\ll \tau_\star$ and most Jupiters beyond $a_{\rm circ} > 0.057$ would have circularization timescales $\gg \tau_\star$. Thus the planet's fate is not sensitively dependent on either the star's age or when the planet

underwent HEM; the more important quantity to pinpoint is e.

Finally, we note that the expected number of proto-hot Jupiters depends on the timescale for the S12 assumption of steady production. Consider the following two possibilities for the dominant HEM mechanism:

- HEM typically occurs on a short timescale compared to the stellar lifetime (for example, immediately as the gas disk has dissipated). Since we cannot detect planets via the transit or radial-velocity method around very young stars due to their enhanced activity, we would miss most proto-hot Jupiters, except for those in the small sliver of parameter space for which tidal circularization timescale is of order one stellar lifetime.

- HEM typically occurs on a timescale comparable to the stellar lifetime. In this case, we would expect to see proto-hot Jupiters at every $a_{\rm circ}$, with the relative number of eccentric Jupiters (accounting for observational biases) set by the tidal circularization timescale corresponding to that $a_{\rm circ}$.

The timescale of HEM depends on which HEM mechanism is at play and on the typical initial architectures of planetary systems (e.g. for the planet-planet scattering mechanism, how tightly packed the initial configuration is). Therefore, the discovery of definitive proto-hot Jupiters would not only reveal that HEM occurs but also constrain the details of the dominant HEM mechanism. If the highly eccentric planets we find are clustered at a single $a_{\rm circ}$ — which would correspond to a tidal circularization timescale of order the stellar lifetime — then we would conclude that HEM usually occurs early in a planetary system's history. But if highly eccentric planets are found at a range of $a_{\rm circ}$

— including $a_{\rm circ}$ within (i.e. to the left of) which most planets have circularized — then we would conclude that HEM typically occurs throughout a planetary system's history.

6.7 Discussion and Future Directions

We have identified KOI-1474.01 as a highly eccentric, Jupiter-sized planet using a combination of a detailed analysis of the light curve shape and the statistical validation procedure of Morton (2012). This makes KOI-1474.01 the second planet or planet candidate with an eccentricity measured solely via the duration aspect of the "photoeccentric effect," joining KOI-686.01 whose eccentricity we measured in Paper I. We measured one component of the angle between the stellar spin axis and the planet's orbit, finding that the degree of misalignment is not currently well-constrained. Based on the variations in KOI-1474.01's transit times, we explored the identity of a perturbing companion; we found the TTVs to be consistent with perturbations from a massive, eccentric outer companion but could not uniquely constrain the perturber's mass, period, eccentricity, and mutual inclination with the currently available data. However, the main reason the perturber's parameters are poorly constrained is that we have only witnessed perturber periapse passage; we are likely to witness another periapse passage over the timespan of the *Kepler* mission, potentially allowing us to distinguish between possible perturbers, including a coplanar giant planet vs. a brown dwarf with a large mutual inclination.

Because of the uncertainty in KOI-1474.01's measured orbital eccentricity and possible secular variations in that eccentricity due to the perturbing companion, it is not yet clear whether KOI-1474.01 is a proto-hot Jupiter — with a periapse close enough to

its star that the planet will undergo full tidal circularization over the star's lifetime — or a failed-hot Jupiter, just outside the reach of fast tidal circularization. However, either way, the planet's discovery adds to the growing evidence that HEM mechanisms play a major role in shaping the architecture of planetary systems. The broad eccentricity distribution of extrasolar planets (Jurić & Tremaine 2008), the sculpting of debris disks by planets on inclined and eccentric orbits (e.g. Mouillet et al. 1997; Thommes et al. 1999; Augereau et al. 2001; Quillen 2006; Levison et al. 2008; Chiang et al. 2009; Dawson et al. 2011; Dawson & Murray-Clay 2012), the population of free-floating planets (Sumi et al. 2011), and the large mutual inclinations measured in the Upsilon Andromeda system (McArthur et al. 2010) all point to a dynamically violent youth for planetary systems. But the strongest evidence for HEM comes from hot Jupiters themselves — their existence and, in many cases, misaligned or retrograde orbits (e.g. Winn et al. 2009a; Johnson et al. 2011a; Triaud 2011).

As a proto- or failed-hot Jupiter, KOI-1474.01 plays the crucial role of linking hot Jupiters, which are intrinsically rare, to other planetary systems. Even though they make up only a small percentage of the planet population (Howard et al. 2010; Youdin 2011; Howard et al. 2012b; Mayor et al. 2011; Wright et al. 2012) we focus attention on hot Jupiters because, like meteorites discovered in Antarctica, they are known to come from somewhere else, bringing with them vital information about the past. In contrast, we do not know whether planets at greater orbital distances or of smaller sizes underwent migration, or if they formed in situ (e.g. Veras et al. 2009; Hansen & Murray 2012). Moreover, the HEM mechanisms for producing hot Jupiters — including planet-planet scattering (Nagasawa & Ida 2011), the Kozai mechanism (Wu & Murray 2003; Fabrycky & Tremaine 2007a; Naoz et al. 2011), dynamical relaxation (Jurić & Tremaine 2008),

and secular chaos (Wu & Lithwick 2011) — make specific predictions for the inclination distributions of hot Jupiters, which can be probed via the Rossiter-McLaughlin effect. The existence of proto- and failed-hot Jupiters will allow us to argue that the mechanisms for producing hot Jupiters are, more generally, the mechanisms that sculpt many types of planetary systems, particularly those with giant planets within 1 AU.

The KOI-1474 system—an inner proto- or failed-hot Jupiter with a massive, long-period companion—may be the prototype of systems of hot Jupiters with distant, massive, outer companions, including as HAT-P-13 (Bakos et al. 2009), HAT-P-17 (Howard et al. 2012a; a hot Saturn), and Qatar-2 (Bryan et al. 2012). Bryan et al. (2012) present a compilation of the eight other hot Jupiters with known outer companions. HD 163607 (Giguere et al. 2012) resembles KOI-1474.01 in that it harbors both an eccentric inner planet (e = 0.73, P = 75.29 days) and an outer companion (in this case, a massive outer planet); however, inner planet HD 163607 b is very likely a failed-hot Jupiter, as it has $P_{\rm final} = 24$ days. The expanding baseline for radial-velocity measurements may reveal additional, long-period outer companions of other hot Jupiters, proto-hot Jupiters, and failed-hot Jupiters (Wright et al. 2009). These additional companions may have been the culprits responsible for the HEM of their inner brethren. Moreover, although Steffen et al. (2012a) examined the transit timing variations of *Kepler* hot Jupiters and found no evidence for *nearby* massive planets, the extended *Kepler* Mission will allow for the detection of distant companions, should they exist, through TTVs.

Through radial-velocity follow up with Keck/HIRES we will measure the mass of KOI-1474.01, tighten the measurement of its high eccentricity, place additional constraints on the outer companion, and potentially discover additional bodies in the

system. Assuming a Jupiter-like composition to estimate a mass for KOI-1474.01 of $M_p \approx M_{\rm Jup}$, host star KOI-1474 would have an radial velocity semiamplitude of ~ 70 m s^{-1}, feasible for detection using Keck/HIRES. We will then combine the RV-measured eccentricity with the transit light curves to more tightly constrain the stellar parameters, yielding a better constraint on the planet's line-of-sight spin-orbit angle $|i - i_s|$, which is currently ambiguous due to uncertainty in the stellar radius. It may even be possible to detect the Rossiter-McLaughlin effect, which has a maximum amplitude of ≈ 50 m/s (Winn 2010, eqn. 40). Although RV measurements of such a faint star ($K_P = 13.005$) pose a challenge, Johnson et al. (2012) have demonstrated the feasibility of following up faint *Kepler* targets with their measurements of KOI-254, a much fainter, redder star ($K_P = 15.979$).

KOI-1474.01 contributes to the growing sample of proto- and failed-hot Jupiters. From an estimate of the unbiased number of proto-hot Jupiters, we can determine whether HEM accounts for all the hot Jupiters observed, or whether another mechanism, such as smooth disk migration, must deliver some fraction of hot Jupiters. (See Morton & Johnson 2011a for the statistical methodology necessary for such a measurement.) Transiting failed-hot Jupiters orbiting cool stars will be valuable targets for testing the obliquity hypothesis of Winn et al. (2010) that hot Jupiters realign cool stars: we would expect failed-hot Jupiters - which have long tidal friction timescales — to be misaligned around both hot and cool stars.

Designed to search for Earth twins in the habitable zones of Sun-like stars, *Kepler* is revealing a wealth of information about the origin of the most unhabitable planets of all: hot Jupiters. *Kepler's* precise photometry, combined with a loose prior on the stellar density, allow us to measure the eccentricities of transiting planets from light curves

alone and to search for the highly eccentric proto- and failed-hot Jupiters we would expect from HEM but not from smooth disk migration (S12). If our basic understanding of HEM and tidal circularization is correct, KOI-1474.01 is the first of a collection of highly eccentric planets that will be discovered by *Kepler* .

Chapter 7

A Paucity of Proto-hot Jupiters on Supereccentric Orbits,

R. I. Dawson, J. A. Johnson, & R. A. Murray-Clay submitted to *The Astronomical Journal*, arXiv:1211.0554

Abstract

Gas giant planets orbiting within 0.1 AU of their host stars, unlikely to have formed in situ, are evidence for planetary migration. It is debated whether the typical hot Jupiter smoothly migrated inward from its formation location through the proto-planetary disk or was perturbed by another body onto a highly eccentric orbit, which tidal dissipation subsequently shrank and circularized during close stellar passages. Socrates and collaborators predicted that the latter class of model should produce a population of super-eccentric proto-hot Jupiters readily observable by *Kepler*. We find a paucity

of such planets in the *Kepler* sample, inconsistent with the theoretical prediction with 95.8% confidence. Observational effects are unlikely to explain this discrepancy. We find that the fraction of hot Jupiters with orbital period $P > 3$ days produced by the stellar binary Kozai mechanism does not exceed (at two-sigma) 33%. Our results may indicate that disk migration is the dominant channel for producing hot Jupiters with $P > 3$ days. Alternatively, the typical hot Jupiter may have been perturbed to a high eccentricity by interactions with a planetary rather than stellar companion and began tidal circularization much interior to the ice line after multiple scatterings. A final alternative is that tidal circularization occurs much more rapidly early in the tidal circularization process at high eccentricities than later in the process at low eccentricities, contrary to current tidal theories.

7.1 Introduction

Roughly 1% of Sun-like stars host hot Jupiters, giant planets with small semi-major axes (Mayor et al. 2011; Howard et al. 2012b; Wright et al. 2012). Unlikely to have formed in situ, hot Jupiters are evidence for the prevalence of planetary migration, which may take place via interactions with the proto-planetary disk (e.g. Goldreich & Tremaine 1980; Ward 1997; Alibert et al. 2005; Ida & Lin 2008; Bromley & Kenyon 2011), or other bodies in the system. One or more companions can create a hot Jupiter by perturbing a cold Jupiter onto an eccentric orbit, which tidal forces shrink and circularize during close passages to the star. Proposed mechanisms for this "high eccentricity migration" (HEM) include Kozai oscillations induced by a distant stellar binary companion (e.g. Wu & Murray 2003; Fabrycky & Tremaine 2007a; Naoz et al. 2012) or by another planet

in the system (Naoz et al. 2011; Lithwick & Naoz 2011), planet-planet scattering (e.g. Rasio & Ford 1996; Ford & Rasio 2006; Chatterjee et al. 2008; Ford & Rasio 2008; Jurić & Tremaine 2008; Matsumura et al. 2010; Nagasawa & Ida 2011; Beaugé & Nesvorný 2012; Boley et al. 2012), and secular chaos (Wu & Lithwick 2011).

One way to distinguish whether disk migration or HEM is dominant in setting the architecture of systems of giant planets is to search for additional populations of giant planets that may also result from HEM, including 1) failed hot Jupiters, which are stuck at high eccentricities but with periapses too large to undergo significant tidal circularization over the star's lifetime, 2) Jupiters on short-period, moderately-eccentric orbits, nearing the end of their HEM journey, and 3) proto-hot Jupiters on super-eccentric orbits in the process of HEM. Recently, Socrates et al. (2012b) (S12 hereafter) suggested that, if HEM is the dominant channel for producing hot Jupiters, we should readily detect a number of super-eccentric Jupiters in the act of migrating inward. Moreover, they showed that the number of super-eccentric Jupiters can be estimated from the number of moderately-eccentric Jupiters that have similar angular momentum, based on their relative circularization rates. Based on the number of moderately-eccentric, short-period Jupiters found by other planet hunting programs (tabulated in the Exoplanet Orbit Database, EOD, by Wright et al. 2011), S12 predicted that the *Kepler* Mission should discover 5-7 proto-hot Jupiters with eccentricities $e > 0.9$ and noted that these planets should in fact already be present in the Borucki et al. (2011) candidate collection.

The S12 prediction requires a steady production rate of hot Jupiters throughout the Galaxy, as well as several conventional assumptions, including conservation of the hot Jupiter's angular momentum, tidal circularization under the constant time lag approximation, and the beginning of HEM at or beyond the ice line. This prediction is a

useful, quantitative test for discerning the origin of hot Jupiters. Confirmation of their prediction would reveal that hot Jupiters are produced by interactions with companions, not a disk, while a paucity of proto-hot Jupiters in the *Kepler* sample would inform us that HEM is not the dominant channel, or that some aspect of our current understanding of HEM is incorrect.

Motivated by the S12 prediction, we have been using what we term the "photoeccentric effect" to measure individual eccentricities of Jupiter-sized planets from their transit light curves (Dawson & Johnson 2012, DJ12 hereafter). Dawson et al. (2012) (D12 hereafter) identified KOI-1474.01 as a transiting planet candidate with a long orbital period (69.7 days), a large eccentricity ($e = 0.81 \pm 0.10$), and transit timing variations caused by a massive outer companion. However, uncertainty in the candidate's eccentricity made it ambiguous whether KOI-1474.01 is one of the proto-hot Jupiters predicted by S12 or, alternatively, a failed-hot Jupiter beyond the reach of tidal circularization over its host star's lifetime.

Here we examine the entire sample of *Kepler* Jupiters to assess whether the planets expected from HEM are present. We find with 95.8% confidence that the putative highly-eccentric progenitors of hot Jupiters are partly or entirely missing from the *Kepler* sample. In Section 7.2, we summarize the S12 prediction and assumptions. In Section 7.3, we update the S12 prediction, accounting for Poisson counting uncertainties and incompleteness, and translate it into a prediction for transit light curve observables. In Section 7.4, we compare the prediction of Section 7.3 to the light curve properties of candidates in the *Kepler* sample and conclude that there is a paucity of proto-hot Jupiters. We consider observational causes, finding that they are unlikely to explain the discrepancy between theory and observations. In Section 7.5, we place an upper-limit on

the fraction of hot Jupiters created by stellar binaries, consider the contribution of disk migration to the hot Jupiter population, and present Monte Carlo predictions for other dynamical scenarios, finding that the paucity of proto-hot Jupiters can be compatible with HEM. We conclude (Section 7.6) by outlining the theoretical and observational pathways necessary to distinguish the dominant channel for hot Jupiter creation.

7.2 Predictions and Assumptions by Socrates and Collaborators

S12 predicted that the *Kepler* mission should discover a number of super-eccentric, hot Jupiter progenitors in the process of high eccentricity migration (HEM). Previously (DJ12), we showed that super-eccentric planets should be easily identifiable from their transit light curves and thus precise radial-velocity (RV) follow-up is not necessary. This is fortunate as most *Kepler* stars are too faint to be amenable to precise RV observations. To predict the number of super-eccentric Jupiters, S12 considered a population of proto-hot Jupiters undergoing tidal circularization along a "track" of constant angular momentum. Using an eccentricity-dependent tidal circularization rate (described below), they computed the number ratio of super-eccentric to moderately-eccentric proto-hot Jupiters along the track. In Section 7.2.1, we follow S12 to derive a formula for the expected number of super-eccentric proto-hot Jupiters. In Section 7.2.2, we summarize the assumptions on which the S12 prediction depends and how these assumptions affect the expected number of proto-hot Jupiters.

7.2.1 Number of Super-eccentric Jupiters Along an Angular Momentum Track

To predict the number of super-eccentric proto-hot Jupiters, S12 assumed a steady production of hot Jupiters and assessed the relative amount of time spent in the early, high-eccentricity phase by a proto-hot Jupiter undergoing tidal circularization, compared to the time spent at moderate eccentricities later in the process. They assumed that the planet's specific orbital angular momentum h is conserved in HEM and thus the planet follows a "track" defined by a constant $a_{\rm final}$, the semi-major axis the planet reaches once its orbit has fully circularized. For a planet with mass M_p orbiting a star of $M_\star$:

$$a_{\rm final} = h^2/[G(M_\star + M_p)] = a(1-e^2) \tag{7.1}$$

where G is the universal gravitational constant, a the instantaneous semi-major axis, and e the instantaneous eccentricity. The angular momentum can also be defined in terms of the final orbital period $P_{\rm final}$:

$$P_{\rm final} = (2\pi a_{\rm final}^2)/h = P(1-e^2)^{3/2} \tag{7.2}$$

where P is the instantaneous orbital period.

The number of super-eccentric Jupiters ($\overline{N}_{\rm sup}$) along a track of constant angular momentum is related to the number of moderately-eccentric Jupiters ($\overline{N}_{\rm mod}$) by:

$$\overline{N}_{\rm sup} = \overline{N}_{\rm mod} r(e_{\rm max}) \tag{7.3}$$

where the variable $e_{\rm max} = \left[1 - (P_{\rm final}/P_{\rm max})^{2/3}\right]^{1/2}$ is set by maximum observable orbital period $P_{\rm max}$ and $r(e_{\rm max})$ is the ratio of time spent at super-eccentricities ($0.9 < e < e_{\rm max}$)

to moderate eccentricities ($0.2 < e < 0.6$). We place bars over $N_{\rm sup}$ and $N_{\rm mod}$ to indicate that these are mean numbers. The observationally counted numbers are sampled from Poisson distributions defined by these means. The ratio is

$$r(e_{\rm max}) = \frac{\int_{0.9}^{e_{\rm max}} |\dot{e}|^{-1} de}{\int_{0.2}^{0.6} |\dot{e}|^{-1} de}, \tag{7.4}$$

For example, for $P_{\rm max} = 1.5$ years and $P_{\rm final} = 5$ days, $e_{\rm max} = 0.978$. The eccentricity damping rate $\dot{e}$ due to tides raised on the planet under the constant tidal time lag approximation (Eggleton et al. 1998, Hansen 2010, S12, Socrates & Katz 2012; Socrates et al. 2012a), assuming the planet's spin is pseudo-synchronous, is:

$$\frac{\dot{e}}{e} = -\frac{(1-e^2)^{3/2} f_e}{C_{\rm phys} a_{\rm final}^8} \tag{7.5}$$

where f_e, a function of e of order unity, and $C_{\rm phys}$, a constant based on $M_\star$, M_p, and the planet's radius R_p, are defined in Table 7.1.

Table 7.1. Table of tidal quantities

Quantity	Definition
σ_p	global planetary
	tidal dissipation constant (Hansen 2010)
f_e	$\left(7+\frac{45}{2}e^2+56e^4+\frac{685}{32}e^6+\frac{255}{64}e^8+\frac{25}{256}e^{10}\right)$
	$/\left[4(1+3e^2+3/8e^4)\right]$
	$\approx 7(1+2.63e^3)/4$
$C_{\rm phys}$	$M_p/\left[M_\star(M_p+M_\star)R_p^{10}\sigma_P\right]$

Most Jupiters in the *Kepler* sample lack measured eccentricities, and therefore $\overline{N}_{\rm mod}$ of the *Kepler* sample is unknown. Following S12, we make use of the sample of planets detected by non-*Kepler* surveys, which we denote with subcript 0 (Figure 7.1, compiled from the EOD, Wright et al. 2012, queried on April 10th, 2013). To estimate $\overline{N}_{\rm mod}$ along a track in the *Kepler* sample, we use the ratio of $\overline{N}_{\rm mod,0}$ to the number in another class of calibration object. This other class needs to be countable in the *Kepler* sample. Ideally, this class would along a $P_{\rm final}$ track. However, because the eccentricities of the *Kepler* planets are unknown, instead the class we use is planets with orbital period $P = P_{\rm final}$, of which there are $\overline{N}_{P=P{\rm final},0}$ in the calibration sample. If we assume this ratio $\overline{N}_{\rm mod,0}/\overline{N}_{P=P{\rm final},0}$ is the same for calibration sample as for the *Kepler* sample, then we can compute the expected $\overline{N}_{\rm mod}$ for the *Kepler* sample:

$$\overline{N}_{\rm mod} = \frac{\overline{N}_{\rm mod,0}}{\overline{N}_{P=P{\rm final},0}} \overline{N}_{P=P{\rm final}} \tag{7.6}$$

Based on Equation (7.3)[1] S12 predicted 5-7 super-eccentric proto-hot Jupiters in the Borucki et al. (2011) sample. We will recompute this prediction in Section 7.3, incorporating the latest survey samples, Poisson uncertainties, and incompleteness.

[1]S12 used $N_{P=P{\rm final}}$ for the *Kepler* sample but, for the calibration sample, they used the total number of planets observed along the $P_{\rm final}$ track. However, we wish to treat both samples the same and thus use the same type of quantity for both: $N_{P=P{\rm final}}$ for the *Kepler* sample and $N_{P=P{\rm final},0}$ for the calibration sample. Another difference between our sample and S12 is that we combine non-*Kepler* planets detected by transit surveys and those detected radial-velocity surveys in order to enhance our sample size. The non-*Kepler* transit surveys are not particularly better suited than the radial-velocity surveys for a comparison to the *Kepler* stars, except for the transit probability. However, as noted by S12, the transit probability is constant along an angular momentum track, so the ratio of planets along different portions of the tracks is not affected.

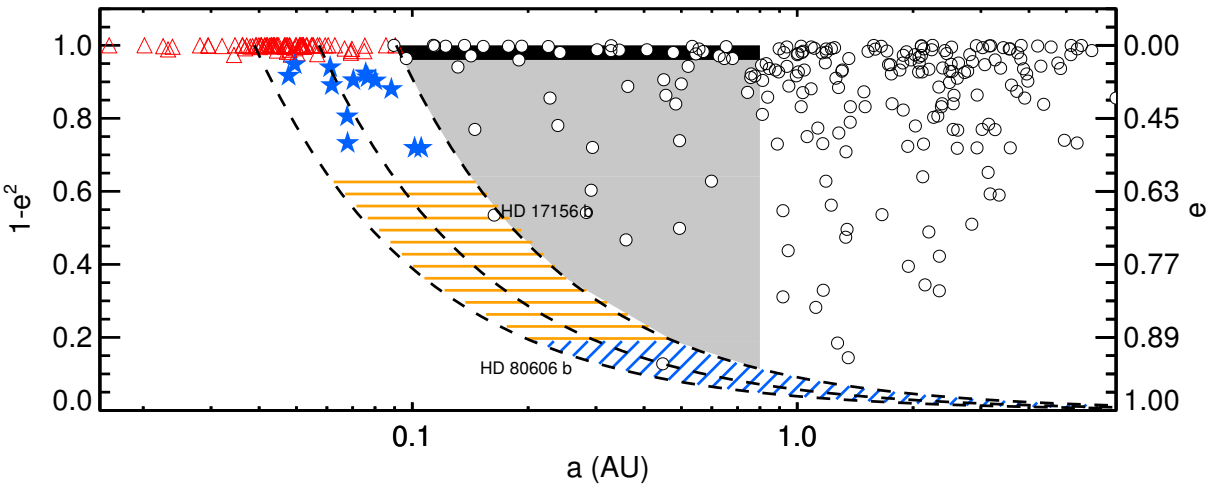

Figure 7.1.—: Giant planets detected by non-*Kepler* surveys from the EOD (Wright et al. 2012; queried on April 12th, 2013). All are Jupiter-mass ($M_p > 0.25 M_{\rm Jup}$ or $8 R_\oplus < 22 R_\oplus$) planets orbiting stars with $4500 < T_{\rm eff} < 6500$ K, $\log g > 4$. The dashed lines represent tracks of $P_{\rm final} = 3, 5, 10$ days. The shaded and patterned regions correspond to Figure 7.6. Within the $3 < P_{\rm final} < 10$ days angular momentum tracks are hot Jupiters (red triangles), moderately-eccentric Jupiters with $0.2 < e < 0.6$ (blue stars), Jupiters with $0.6 < e < 0.9$ (orange horizontal striped region), and super-eccentric Jupiters (blue, diagional-striped region), The RV-discovered planet HD 17156 b lies in the orange, horizontal striped region, and the RV-discovered planet HD 80606 b lies in the blue, diagonal-striped region. Period valley: grey region denotes Jupiters with $P_{\rm final} > 10$ days but interior to the ice line, and the black region houses circular Jupiters interior to the ice line but exterior to hot Jupiters.

7.2.2 Summary of Assumptions Forming the Basis for the S12 Prediction

Here we summarize both stated and unstated assumptions of S12 and infer how violations would affect the expected number of super-eccentric proto-hot Jupiters in the *Kepler* sample. Certain assumptions, if violated, may result in fewer than expected super-eccentric Jupiters. We discuss these assumptions in detail in Section 7.5: hot Jupiters of orbital periods up to 10 days have migrated via tidal circularization (Section 7.5.1); a proto-hot-Jupiter typically begins its HEM journey at or beyond the ice line, after which it experiences no perturbations that permanently change its angular momentum (Sections 7.5.2 and 7.5.3); a steady "current" of proto-hot Jupiters is being produced around the sample of observable stars (Section 7.5.4); and the ratio used in Equation (7.6) is the same for the *Kepler* and calibration samples (Section 7.5.4).

In Section 7.9, we describe additional assumptions, which we do not expect to affect our results. S12 assumed that the planet's radius does not change, an assumption which, if violated, would not result in fewer super-eccentric Jupiters. S12 made several assumptions that we do not expect to be violated: angular momentum is not exchanged between the star and planet or between the planet's spin and orbit, moderately-eccentric Jupiters in the calibration sample truly have $e > 0.2$, and the *Kepler* false positive rate is low.

Finally, S12 assumed that tidal evolution (for tides raised on the planet; see Section 7.9 regarding tides raised on the star) occurs according to the constant tidal time lag approximation (Hut 1981; Eggleton et al. 1998; Socrates & Katz 2012; Socrates et al. 2012a). This assumption controls the ratio $r(e_{\max})$ (Equation 7.4) of

high-eccentricity proto-hot Jupiters to moderate-eccentricity hot Jupiters along a given angular momentum track. The constant tidal time lag approximation is conventional but may be violated: if the dissipation rate were larger for highly-eccentric Jupiters along a given angular momentum track than for moderately-eccentric Jupiters, we would expect fewer super-eccentric proto-hot Jupiters than predicted or vice versa.

Dynamic tides, in which dissipation occurs through surface gravity waves (e.g. Zahn 1975), may be important in a proto-hot Jupiter's tidal evolution. Beaugé & Nesvorný (2012) argue that dynamic tides act at high eccentricities and equilibrium tides at low eccentricities; they added an empirical correction factor to the constant time-lag model so that, at large eccentricities, it matches the numerical results of the dynamical tide model computed by Ivanov & Papaloizou (2011). The empirical correction factor is proportional to 10^{200qe^2}, where q is the periapse distance (Beaugé & Nesvorný 2012). Along a given angular momentum track, $q = a_{\rm final}/(1+e)$, so the tidal dissipation timescale [proportional to $10^{200a_{\rm final}e^2/(1+e)}$] is longer for larger eccentricities. If this correction factor applies, the contribution of dynamical tides would *increase* the expected number of super-eccentric proto-hot Jupiters.

The effect of tides on orbital evolution remains uncertain and is a topic of ongoing research. It remains unclear whether the true typical tidal evolution would result in more or in fewer super-eccentric Jupiters. Our results should be revisited as this subfield continues to advance.

7.3 Updated Prediction for Number of Super-eccentric Proto-hot Jupiters and Transit Light Curve Observables

In Section 7.3.1, we derive the expected number of identifiable *Kepler* super-eccentric proto-hot Jupiters, following S12 but using updated survey samples. We refine the S12 prediction by quantifying its uncertainty and incorporating incompleteness due to the limited timespan of the data. In Section 7.3.2, we describe how to confirm or rule out the existence of super-eccentric proto-hot Jupiters using *Kepler* photometry alone by recasting the prediction in terms of light curve observables.

7.3.1 Expected Number of Proto-hot Jupiters with $e > 0.9$ in the *Kepler* Sample

In Section 7.2.1, we followed S12 to derive an equation for the expected number of super-eccentric proto-hot Jupiters for a given $P_{\rm final}$ (Equation 7.3) based on $\overline{N}_{\rm mod,0}$, $\overline{N}_{P=P{\rm final},0}$, and $\overline{N}_{P=P{\rm final}}$. However, to estimate posteriors for these means from the counted numbers, we must account for incompleteness and Poisson uncertainty.

The prediction by S12 was for an ideal Kepler sample complete out to orbital periods of 2 years (Subo Dong, private communication, 2012). In contrast, the *Kepler* Mission nominally only lasts for 3 years (though fortunately, due to its great success, the mission was recently extended to 7 years). To derive the expected number of super-eccentric proto-hot Jupiters in a sample of a limited timespan $t_{\rm sur}$ we must account

for incompleteness. If $N_{\rm trans,min}$ transits are the minimum number of transits required for the *Kepler* transit pipeline to detect the proto-hot Jupiter, the completeness (with respect to this effect alone) $C_{\rm comp}$ ranges from 100% at orbital periods $\leq t_{\rm sur}/N_{\rm trans,min}$ to 0% at orbital periods of $t_{\rm sur}/(N_{\rm trans,min}-1)$. We update Equation (7.4) to account for incompleteness:

$$r(e_{\rm max}) = \frac{\int_{0.9}^{e_{\rm max}} C_{\rm comp}(e)|\dot{e}|^{-1}de}{\int_{0.2}^{0.6}|\dot{e}|^{-1}de} \tag{7.7}$$

where the completeness $C_{\rm comp}$(e) is

$$C_{\rm comp}(e) = \begin{cases} 1 \quad , \; e < e(t_{\rm sur}/N_{\rm trans,min}) \\ 1+(1-e^2)^{3/2}(t_{\rm sur}/P_{\rm final}) - N_{\rm trans,min} \quad , e(\frac{t_{\rm sur}}{N_{\rm trans,min}}) < e < e[\frac{t_{\rm sur}}{(N_{\rm trans,min}-1)}], \end{cases} \tag{7.8}$$

and $e[t_{\rm sur}/N_{\rm trans,min}] = \left[1-(N_{\rm trans,min}P_{\rm final}/t_{\rm sur})^{2/3}\right]^{1/2}$,
and $e[t_{\rm sur}/(N_{\rm trans,min}-1)] = \left(1-[(N_{\rm trans,min}-1)P_{\rm final}/t_{\rm sur}]^{2/3}\right)^{1/2}$.

Although calculations are often made under the assumption that the *Kepler* candidate list (Borucki et al. 2011; Batalha et al. 2013; Burke et al. 2013) is complete for Jupiter-sized planets exhibiting two transits in the timespan under consideration (e.g. Fressin et al. 2013), we make a more conservative assumption about the completeness here. The *Kepler* pipeline is set up to only detect objects that transit three times during the quarters over which the pipeline was run and all candidates (Borucki et al. 2011; Batalha et al. 2013; Burke et al. 2013) transiting only 1-2 times were detected by eye (Christopher Burke and Jason Rowe, private communication, 2013). There exists no estimate for the by-eye completeness. The latest candidates list (Burke et al. 2013) is only complete for Jupiter-sized planets that transit three times within Q1-Q8 ($t_{\rm sur}$ = 2

years). The threshold-crossing events table (TCE) is complete for Jupiter-sized planets that transit three times within Q1-Q12 ($t_{\rm sur} = 3$ years), but those objects have been not been vetted as candidates. As described in Section 7.8, we use the TCE table to expand our sample so that it is complete for Jupiter-sized planets that transit three times in Q1-Q12, finding three additional candidates. Then we employ Equation 7.8 using $t_{\rm sur} = 3$ years and $N_{\rm trans,min} = 3$. We obtain $r = 0.813, 0.608, 0.370$ for $P_{\rm final} = 3, 5, 10$ days respectively. Later in this section we will update the completeness further to account for noise and missing data.

Next we describe the selection cuts we make to count $N_{\rm mod,0}$ (blue stars, Figure 7.1), $N_{P=P{\rm final},0}$ (open symbols, Figure 7.1), and $N_{P=P{\rm final}}$. Because the stellar parameters from the *Kepler* Input Catalog (KIC) are not reliable for stars outside the temperature range $4500 < T_{\rm eff} < 6500$ K (Brown et al. 2011b) we only include stars within this temperature range in both the *Kepler* and calibration samples. We impose an aggressive cut of stellar surface gravity $\log g > 4$ to exclude giant stars, because their KIC parameters are unreliable (we include stars with $\log g$ below 4 but are consistent with $\log g = 4$ within two sigma). We select planets with $8R_\oplus < R_p < 22R_\oplus$. From the Burke et al. (2013) *Kepler* sample, we remove three known false positives (KOI-425.01, Santerne et al. 2012 and see also Madhusudhan et al. 2012; KOI-208.01 and KOI-895.01, Demory & Seager 2011). Since it is not possible to detect planets along *exactly* the same angular momentum track, we follow S12 and consider two $P_{\rm final}$ intervals: $2.8 < P_{\rm final} < 5$ (Interval 1)[2] and $5 < P_{\rm final} < 10$ (Interval 2). The transit probability does not change very much throughout each interval. We tabulate the counted numbers and their sources

[2]We use a lower limit of 2.8 days because 2.8 days is the $P_{\rm final}$ below which we do not see any moderately eccentric Jupiters in the non-*Kepler* surveys.

in Table 7.2.

Each number of counted planets (Table 7.2) is drawn from a Poisson distribution with an unknown mean. We wish to compute the expected number of super-eccentric proto-hot Jupiters using not the counted numbers but rather using estimated posteriors for the mean numbers, incorporating uncertainty. See Section 7.7 for a description of our approach. We use a Jeffrey's prior. Note that in the calibration sample, we exclude planets whose eccentricities are poorly constrained. For planets with $e = 0$ in the EOD, we refer to the literature or fit the data ourselves and only include planets listed with $e = 0$ that are constrained to have $e < 0.2$.

There are two additional effects on the completeness that we now consider. First, transits may fall during gaps in the data or missing quarters. To incorporate this effect, we numerically integrate Equation 7.4, inserting an extra factor $C_{\rm comp,sampled}$ into the integrand, where $C_{\rm comp,sampled}$ is the fraction of phases for which we would observe three or more transits during Q1-Q12. We estimate $C_{\rm comp,sampled}$ using the observation times through Q12 for the 43 hot Jupiters hosts with $2.8 < P < 10$ days in our sample (Table 7.2). In using the hot Jupiter hosts, we assume that their observational cadence is representative of that of proto-hot Jupiter hosts. The factor $C_{\rm comp,sampled}$ naturally incorporates $C_{\rm comp}$ (Equation 7.8). Accounting for missing data reduces r to $0.769, 0.569, 0.332$ for $P_{\rm final} = 2.8, 5, 10$ days respectively.

Second, we consider whether the transits have sufficient signal-to-noise to be detected. For the expected progenitors of a given hot Jupiter, the signal-to-noise is

Table 7.2. Counted planets

e	Interval [days]	Counted	Mean [a]	Sample[b]
$0.2 < e < 0.6$	1: 2.8-5	$N_{\mathrm{mod},0}= 7$	$\overline{N}_{\mathrm{mod},0}= 7^{+3}_{-2}$	Cal
	2: 5-10	$N_{\mathrm{mod},0}= 7$	$\overline{N}_{\mathrm{mod},0}= 7^{+3}_{-2}$	Cal
unspecified	1: 2.8-5	$N_{P=P\mathrm{final},0}= 69$	$\overline{N}_{P=P\mathrm{final},0}= 69^{+9}-8$	Cal
	1: 2.8-5	$N_{P=P\mathrm{final}} = 24$	$\overline{N}_{P=P\mathrm{final}}= 24 \pm 5$	Kep
	2: 5-10	$N_{P=P\mathrm{final},0}= 18$	$\overline{N}_{P=P\mathrm{final},0}= 18^{+5}_{-4}$	Cal
	2: 5-10	$N_{P=P\mathrm{final}}= 19$	$\overline{N}_{P=P\mathrm{final}}= 19^{+5}_{-4}$	Kep

[a]Median, with 68.3% confidence interval, of posterior of Poisson means, each defining a Poisson distribution from which the counted number may be sampled.

[b]Kep = *Kepler* ; Cal = calibration non-*Kepler* (Figure 7.1).

(based on Howard et al. 2012b, Equation 1):

$$\mathrm{S/N} = \frac{\delta}{\sigma_{\mathrm{CDPP}}}\sqrt{\frac{t_{\mathrm{survey}}(1-e^2)^{3/2}}{P_{\mathrm{HJ}}}}\sqrt{\frac{t_{\mathrm{HJ}}/(1+e\cos\omega)}{t_{\mathrm{CDPP}}}}$$
$$\mathrm{S/N} = \frac{\delta}{\sigma_{\mathrm{CDPP}}}\sqrt{\frac{t_{\mathrm{survey}}t_{\mathrm{HJ}}(1-e^2)^{3/2}}{P_{\mathrm{HJ}}t_{\mathrm{CDPP}}(1+e\cos\omega)}} \tag{7.9}$$

where δ is the transit depth, σ_{CDPP} is the combined differential photometric precision (CDPP), $\frac{t_{\mathrm{survey}}(1-e^2)^{3/2}}{P_{\mathrm{HJ}}}$ is the average number of transits for a hot-Jupiter progenitor with $P = P_{\mathrm{HJ}}(1-e^2)^{-3/2}$, t_{HJ} is the transit duration of the hot Jupiter's transit and $t_{\mathrm{HJ}}/(1+e\cos\omega)$ is the duration of the progenitor's transit, and t_{CDPP} is the timescale of the CDPP. For each of the 43 *Kepler* hot Jupiters hosts with $2.8 < P < 10$ days, we compute the signal-to-noise of set of randomly generated progenitors, weighted by $\dot{e}$, the completeness (Equation 7.8), and the transit probability. Note that two of the hot Jupiters have S/N of < 9 in a single transit, meaning that multiple transits are likely required to detect the planet; a progenitor at a long period with a short duration and few transits may escape detection. This approach automatically accounts for the effect of impact parameter on the transit duration by using the observed transit duration of the hot Jupiters. The resulting distribution of SNR peaks at 60, with 95% of progenitors have an SNR greater than 16. Following Fressin et al. (2013), we model the SNR-dependent completeness as a linear ramp ranging from 0 at SNR = 6 to 100% at SNR = 16. As a result, 96% of progenitors are detected. Incorporating this effect (in addition to the effect of missing data above), $r = 0.738, 0.546, 0.319$ for $P_{\mathrm{final}} = 2.8, 5, 10$ days respectively.

Finally, we allow for the possibility that some planets exhibiting just two transits in the Q1-Q8 data were detected. Of the planets that transit twice in Q1-Q8 and again before the end of Q12, five out of seven were included in the Bolmont et al.

(2013) candidates list. We recompute $C_{\rm comp,sampled}$ but allow for 5/7 probability that a planet that transits twice in Q1-Q8 but has its third transit after Q12 is detected. Combining this new $C_{\rm comp,sampled}$ with the SNR completeness, $r = 0.789, 0.563, 0.330$ for $P_{\rm final} = 2.8, 5, 10$ days respectively.

Next we derive the mean number of super-eccentric planets, $\overline{N}_{\rm sup}$. To do so we insert the posteriors from Table 7.2 into Equation (7.3), making use of Equations (7.6) and (7.7), with the r described above. We perform this procedure separately for Interval 1 and Interval 2 and use $t_{\rm sur} = 3$ year, obtaining a $\overline{N}_{\rm sup}$ posterior for each interval, which we sum to compute a total $\overline{N}_{\rm sup}$ (Figure 7.2). The total expected number is $\overline{N}_{\rm sup} = 5.2^{+2.2}_{-1.6}$. This posterior represents a distribution of Poisson means. We transform the distribution of means into a distribution of expected values by sampling $N_{\rm sup}$ from $\overline{N}_{\rm sup}$ according to Equation (7.16). Each sample requires first drawing a mean ($\overline{N}_{\rm sup}$) from the distribution of means (Figure 7.2, top row) and then drawing an observed number $N_{\rm sup}$ from the Poisson distribution with that mean. The expected observed number is $N_{\rm sup} = 5^{+3}_{-2}$, where the uncertainties represent the range falling within 1 sigma. The two-sigma range is 2-12. The change of observing 0 is 1.4%. The expected number will continue to increase as the *Kepler* sample becomes more complete to long-period Jupiter-sized planets; we will apply the framework described here to a future sample, once available.

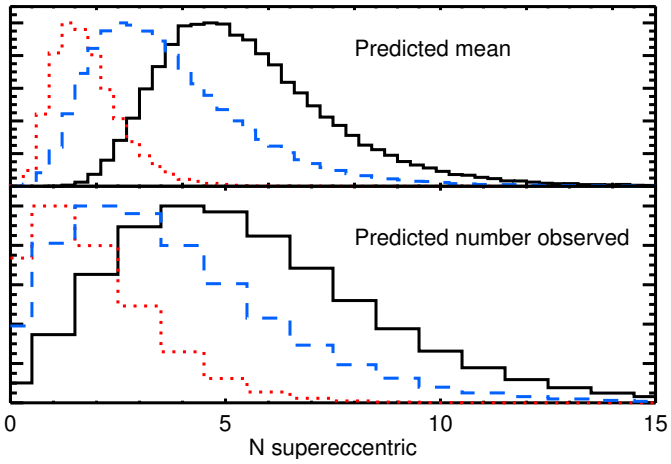

Figure 7.2.—: Top: Predicted mean number of super-eccentric Jupiters (Interval 1: red dotted, Interval 2: blue dashed, total: black solid). Bottom: Sampling from above distribution of Poisson means to create a distribution of expected number observed.

7.3.2 Prediction for Transit Light Curve Observables

We expect to be able to identify super-eccentric proto-hot Jupiters in the *Kepler* sample by fitting their transit light curves and identifying those for which the light curve model parameters are inconsistent with a circular orbit. A planet's orbital eccentricity affects its transit light curve in a number of ways (e.g. Barnes 2007; Ford et al. 2008; Kipping 2008). For long-period, highly eccentric, Jupiter-sized planets, the most detectable effect is on the transit duration. For a wide range of periapse orientations relative to our line of sight, a planet on a highly eccentric orbit transits its star moving at a much larger speed than if it were on a circular orbit with the same orbital period. For Jupiter-sized planets, one can distinguish the effects of the transit speed on the ingress, egress, and full transit duration from the effects of the transit impact parameter and/or limb-darkening, even with long-cadence *Kepler* data (DJ12).

For each planet, we fit a Mandel & Agol (2002) transit light curve model with the following parameters: the planetary-to-stellar radius ratio $R_p/R_\star$, the orbital period P, the inclination i, the scaled semi-major axis $a/R_\star$, and the quadratic limb darkening parameters μ_1 and μ_2. Assuming a circular orbit and a planetary mass much less than the stellar mass ($M_p << M_\star$), one can recast the scaled semi-major axis $a/R_\star$ (by substituting $a = \left[GM_\star \left(P/[2\pi]\right)^2\right]^{1/3}$) as the bulk stellar density, $\rho_\star = M_\star/(\frac{4}{3}\pi R_\star^3)$, which we will refer to simply as the stellar density hereafter. The stellar density measured from the light curve under the assumption of a circular orbit, $\rho_{\rm circ}$, is related to the true stellar

density, $\rho_\star$ by:

$$\rho_\star(e,\omega)g^3(e,\omega) = \rho_{\rm circ}, \tag{7.10}$$

where

$$g(e,\omega) = \frac{1 + e\sin\omega}{\sqrt{1-e^2}} \tag{7.11}$$

is approximately the ratio of the observed transit speed to the transit speed that the planet would have if it were on a circular orbit with the same orbital period (see Kipping 2010b and DJ12 for a detailed derivation). The argument of periapse ω represents the angle on the sky plane ($\omega = 90°$ for a planet transiting at periapse).

We determine $\rho_{\rm circ}$ by fixing $e = 0$, allowing the stellar density to vary as a free parameter in the light curve model. The resulting $\rho_{\rm circ}$ is determined entirely by the shape and timing of the light curve. We then compare $\rho_{\rm circ}$ to the value of $\rho_\star$ determine through other methods (i.e. stellar models fit to the temperature and surface gravity determined through colors or spectroscopy). Although g is degenerate with the host star's density (Equation 7.10), a loose (order-of-magnitude) constraint on $\rho_\star$ is sufficient for a tight constraint on the eccentricity (DJ12), measurement of which we will describe and perform in Section 7.4. For now, we use $\rho_{\rm circ}/\rho_\star$. If $\rho_{\rm circ}/\rho_\star$ is very large, then g must be large, and therefore the planet is moving more quickly during transits than a planet with orbital period P on a circular orbit. In Section 7.10, we summarize how our approach avoids problems caused by incorrect stellar parameters.

Expectations for Super-eccentric Planets

We perform a Monte Carlo simulation to predict the signature in the transit light curve observable $\rho_{\rm circ}/\rho_\star$ expected from the super-eccentric proto-hot Jupiters (Section 7.3.1).

We generate two-dimensional (2D) probability distributions in $(P, \rho_{\rm circ}/\rho_\star)$ in Figure 7.3, where P is the orbital period, as follows:

1. We begin with an assumed $P_{\rm final}$.

2. Using the completeness Equation 7.8, we generate a distribution of eccentricities $\{e_i\}$ with a normalization constant $C_{\rm norm}$ following:

$$\text{Prob(e)} = \begin{cases} 0 & e > e_{\rm max} \text{ or } e < 0.9 \\ C_{\rm norm} C_{\rm comp,sampled} |\dot{e}|^{-1} & 0.9 < e < e_{\rm max} \end{cases} \tag{7.12}$$

3. For each eccentricity, we compute the corresponding orbital period P_i and randomly select an argument of periapse ω_i. Assuming a Sun-like star, we compute the scaled semi-major axis $a_i/R_\star$.

4. We compute the transit probability:

$$\text{prob}_{\rm transit} = \frac{R_\star}{a_i} \frac{1 + e_i \sin \omega_i}{1 - e_i^2} \tag{7.13}$$

   Then we select a uniform random number between 0 and 1. If the number is less than the transit probability, we retain (e_i, ω_i) in the distribution.

5. Then we compute $\rho_{\rm circ}/\rho_\star$ using Equation (7.10).

We use the above procedure to generate four plots, corresponding to different $P_{\rm final}$ (Figure 7.3). In the fourth panel, instead of using a single $P_{\rm final}$, we draw the $P_{\rm final}$ of each trial from the observed $N_{P=P{\rm final}}$, weighting each $P_{\rm final}$ by $N_{\rm mod,0}/N_{P=P{\rm final},0}$ in the two intervals. We see that a population of super-eccentric Jupiters will manifest itself as a collection of light curves with astrophysically implausible $\rho_{\rm circ}$ of 10-1000 times the estimated values for $\rho_\star$. The super-eccentric proto-hot Jupiters will have orbital periods

that range from $P = 2.8$ days$/(1-0.9^2)^{3/2} = 34$ days to two years (this maximum period will increase with the timespan of the Mission). About 90% of the expected planets have $\rho_{\rm circ}/\rho_\star > 10$, making them easy to identify.

Proto-hot Jupiters with $0.6 < e < 0.9$

S12 focused their prediction on super-eccentric planets with $e > 0.9$. However, we also expect to find proto-hot Jupiters with less extreme eccentricities ($0.6 < e < 0.9$) along the same $P_{\rm final}$ track. We repeat the procedure in 7.3.2 for the interval $0.6 < e < 0.9$. The overall occurrence rate for this interval is 0.61 relative to $\overline{N}_{\rm mod}$. As shown in Figure 7.4, the proto-hot Jupiters in the $0.6 < e < 0.9$ range have shorter orbital periods ($6 < P < 121$ days). However, their transit durations and the inferred stellar density from a circular fit are not as strikingly anomalous as for the super-eccentric proto-hot Jupiters, making them less easy to identify. Therefore, we do not focus on these objects but discuss them further in the conclusion (Section 7.6).

7.4 Results: a Paucity of Proto-hot Jupiters

We search for the super-eccentric proto-hot Jupiters predicted by S12 and find significantly fewer than expected. We describe our search procedure and present our measurements (Section 7.4.1) and assess the significance of this null result (Section 7.4.2).

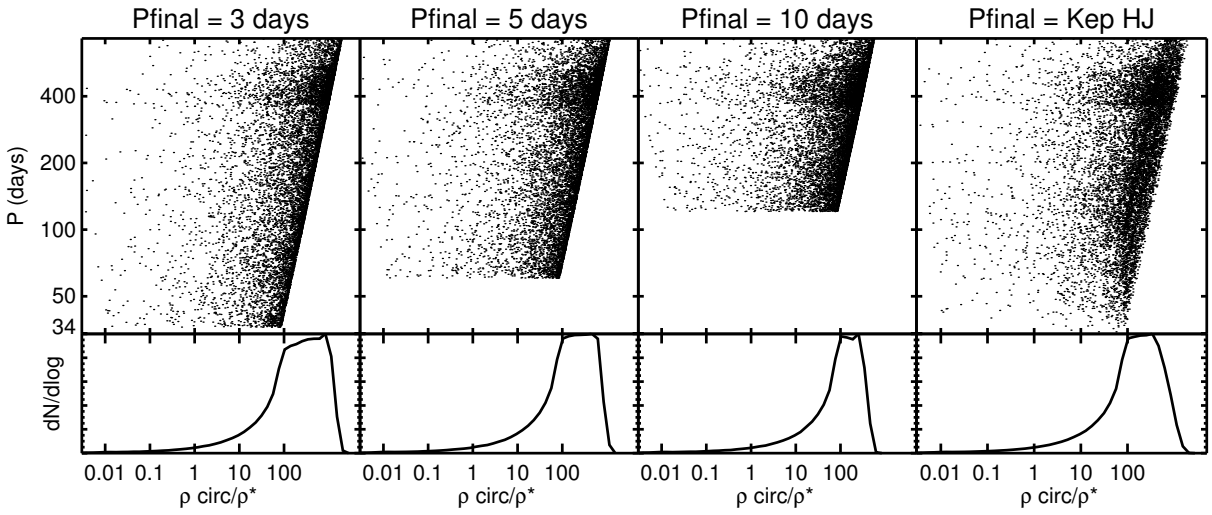

Figure 7.3.—: Top: 2D posterior, orbital period P vs. $\rho_{\rm circ}/\rho_\star$, for planets with $e > 0.9$ and $P_{\rm final} = 3, 5, 10$ days (panels 1-3) or $P_{\rm final}$ drawn from *Kepler* hot Jupiters with $3 < P < 10$ days (panel 4). Bottom: Posterior $\rho_{\rm circ}/\rho_\star$ marginalized over orbital period. Proto-hot Jupiters with $e > 0.9$ should have anomalously large $\rho_{\rm circ}$ measured from the transit light curve compared to their estimated $\rho_\star$, making them easy to identify. We expect half a dozen super-eccentric proto-hot Jupiters in the high probability density region.

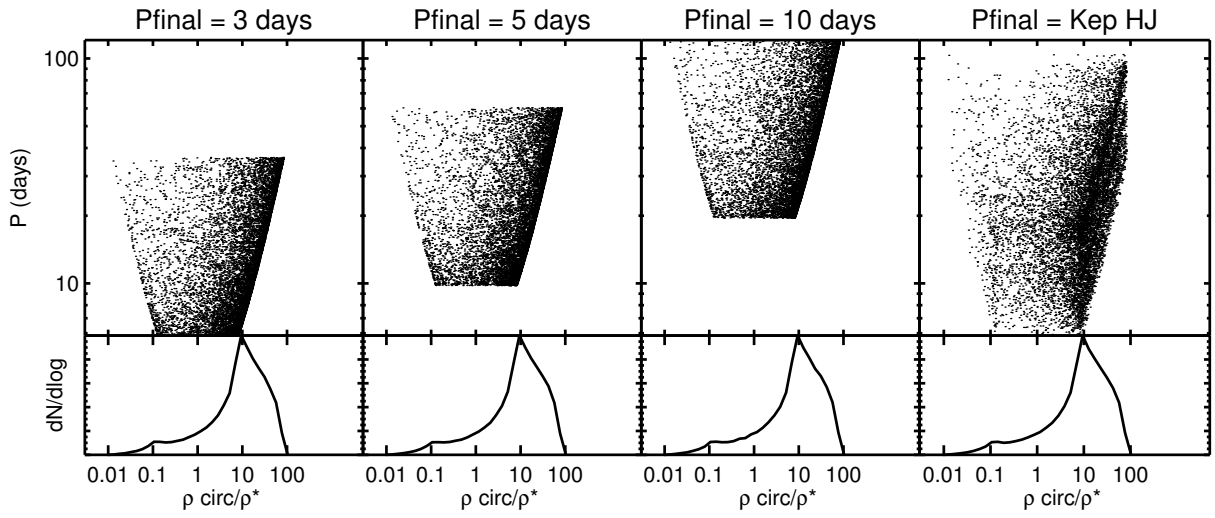

Figure 7.4.—: Top: 2D posterior for orbital period P vs. $\rho_{\rm circ}/\rho_\star$ for planets with $0.6 < e < 0.9$ and $P_{\rm final} = 3, 5, 10$ days (panels 1 - 3) or with $P_{\rm final}$ drawn from *Kepler* hot Jupiters in the interval $3 < P < 10$ days (panel 4). Bottom: Posterior $\rho_{\rm circ}/\rho_\star$ marginalized over orbital period. Proto-hot Jupiters with $0.6 < e < 0.9$ do not typically have such large $\rho_{\rm circ}/\rho_\star$ as their super-eccentric ($e > 0.9$) counterparts (Figure 7.3), making them less easy to identify.

7.4.1 Transit Light Curve Observables for Potential Proto-hot Jupiters

We begin by identifying planet candidates that conform to our selection criteria using the Burke et al. (2013) candidates list provided by NExScI, queried on April 10th, 2013. Applying the same criteria as in Section 7.3, we identify candidates with $8R_\oplus < R_p < 22R_\oplus$ and stellar parameters $4500 < T_{\rm eff} < 6500$ K and $\log g > 4$ (or, for those with $\log g < 4$, consisent with 4 within the uncertainty). We restrict the orbital periods to those between 34 days and which – based on their period and phase — at least twice in Q1-Q8 (i.e. if there should be two transits in Q1-Q8 but one is missing, we still include the planet, provided it transit again before Q14 so we can measure its period), with the lower limit corresponding to $P_{\rm final} = 2.8$ for $e = 0.9$. We are left with 42 planet candidates, including KOI-1474.01 (D12).

For each candidate, we retrieve the Q0-Q9 publicly-available data from MAST. We extract the transits using `AutoKep` (Gazak et al. 2012) and perform an MCMC fit using the Transit Analysis Package (`TAP`; Gazak et al. 2012). We fix $e = 0$ but allow all other parameters to vary, including noise parameters for the Carter & Winn (2009) wavelet likelihood function and first-order polynomial correction terms. We use short-cadence data when available. We obtain each candidate's $\rho_{\rm circ}$ posterior.

Next we follow[3] Section 3.3 of D12 to compute a $\rho_\star$ posterior for each host star using

[3]Instead of imposing a prior on the stellar mass, metallicity, and age from a TRILEGAL (TRIdimensional modeL of thE GALaxy; Girardi et al. 2005) synthetic *Kepler* field population, we assume a uniform prior on these model parameters, because a similar prior was already imposed by Batalha et al. (2010) to generate the effective temperature and surface gravity in the KIC.

the Takeda et al. (2007) stellar evolution models and the estimated effective temperature and surface gravity listed in the *Kepler* candidates Table (Batalha et al. 2013). For stars with stellar properties measured from spectroscopy, we adopt conservative uncertainties of 100 K for $T_{\rm eff}$ and 0.1 for $\log g$ (all above the uncertainties reported in Brown et al. 2011b). For stars for which the effective temperature and surface gravity were derived from the KIC colors, we adopt uncertainties of 200 K for the effective temperature (Brown et al. 2011b). For stars with updated temperatures from Pinsonneault et al. (2012), we adopt that value and its uncertainty. Based on Verner et al. (2011), we adopt an uncertainty of 0.3 for the $\log g$ of *Kepler* stars measured from the KIC colors and use the points from their Figure 2 to correct the $\log g$ for stars with $g - r < 0.65$. We describe exceptions to this procedure, as well as additional cuts that left us with 27 planet candidates, in Section 7.11.

Finally, we combine the $\rho_{\rm circ}$ and $\rho_\star$ posteriors into a posterior of $\rho_{\rm circ}/\rho_\star$ for each candidate, marginalized over all other parameters. In Figure 7.5, we plot the resulting values on top of the probability distribution for predicted super-eccentric proto-hot Jupiters (Figure 7.3, panel 4). None of the candidates fall in the high-probability area of the prediction. We indicate candidates with known companions in their system with blue bars; none can have $e > 0.9$ and $3 < P_{\rm final} < 10$ days without its orbit crossing a companion's. As expected, all[4] candidates with companions have $\rho_{\rm circ}/\rho_\star$ close to 1.

Two candidates without companions, KOI-1474.01 (D12) and KOI-211.01 both have $\rho_{\rm circ}/\rho_\star > 10$. The probability of KOI-211.01 having $e > 0.9$ and $2.8 < P_{\rm final} < 10$ days is 17%. D12 found that KOI-1474.01 has $e = 0.81^{+0.10}_{-0.07}$ and $P_{\rm final} = 14^{+6}_{-10}$ days. The

[4]KOI-433.02 has a low $\rho_{\rm circ}/\rho_\star$. We discuss it further in Section 7.11.

probability of it having $e > 0.9$ and $2.8 < P_{\rm final} < 10$ days is 12%. However, we have conducted radial-velocity measurements of KOI-1474 that rule out $e > 0.9$ (Johnson et al., in preparation). In assessing the consistency of the observations with the prediction of Section 7.3, we will fully consider the possibility that KOI-211.01 might be a super-eccentric proto-hot Jupiter.

We emphasize that it is not surprising that many of the candidates lie in the low-probability region (likely Jupiters with $e < 0.9$ or $P_{\rm final} > 10$ days, of which there may be any number). It is only surprising that we do not see half a dozen in the high-probability region.

7.4.2 Statistical Significance of Lack of Proto-hot Jupiters

None of the observed candidates lie in the high-probability-density region of Figure 7.5, so it is unlikely that the half a dozen predicted (Section 7.3.1) super-eccentric proto-hot-Jupiters are present but missed. If we were certain that none of the candidates has $e > 0.9$ and $2.8 < P_{\rm final} < 10$ days, the probability that observed number of super-eccentric proto-hot-Jupiters agrees with the prediction would simply be 1.4%. (This is the probability, computed in Section 7.3, of observing 0 super-eccentric proto-hot Jupiters given the Poisson uncertainties in the observed number of super-eccentric Jupiters and in numbers used to compute the prediction.) However, there is a small chance that there are indeed super-eccentric proto-hot-Jupiters among the sample but that they just so happen to have their periapses oriented in the narrow range of angles producing an unremarkable $\rho_{\rm circ}/\rho_\star$. Therefore we use a Monte Carlo procedure to assess the consistency of $\rho_{\rm circ}/\rho_\star$ posterior derived for each candidate with the predicted

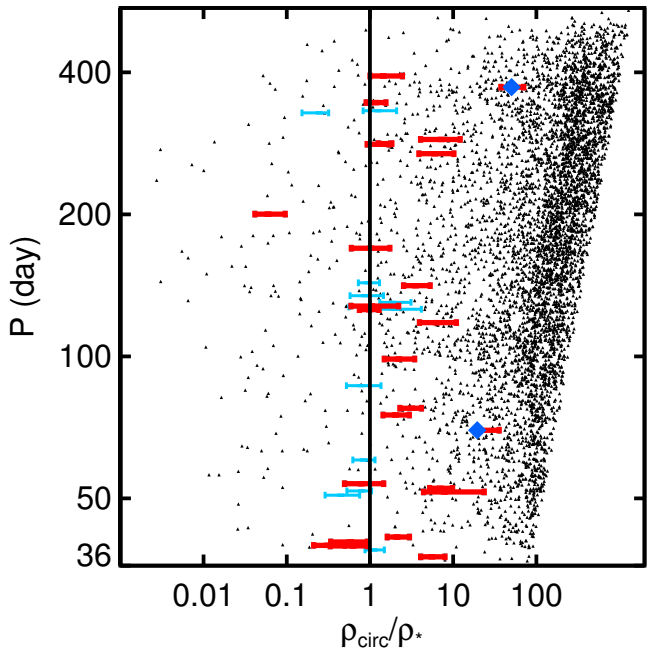

Figure 7.5.—: Expected 2D posterior for orbital period P vs. $\rho_{\rm circ}/\rho_\star$ (taken from panel 4 of Figure 7.3). The values we measured for our 31 candidates are overplotted. Thin, blue bars: candidates with companions in their systems. Thick, red bars: candidates with no known companions. We do not see the expected half a dozen candidates in the region of high-probability density. Blue diamonds: KOI-1474.01 (bottom), KOI-211.01 (top).

population of super-eccentric planets.

We first use the $\rho_{\rm circ}/\rho_\star$ posteriors to generate an eccentricity posterior for each candidate, via a MCMC exploration of a limited set of parameters: $\rho_{\rm circ}$, $\rho_\star$, e and ω (as outlined in DJ12, Section 3.4). Although we can only make a tight eccentricity measurement when the planet's eccentricity is large (DJ12), the broad eccentricity posterior for the typical candidate here is useful for this purpose: it contains very little probability at the high eccentricities corresponding to $e > 0.9, 2.8 < P_{\rm final} < 10$ days. We then perform 10^6 trials in which we randomly select an eccentricity from each candidate's eccentricity posterior. We compute $P_{\rm final}$ and count $N_{\rm sup}$ in Intervals 1 and 2. If both are greater than or equal to the respective numbers drawn from posteriors in Figure 7.2, bottom panel (red dotted and blue dashed curves), we count the trial as a success, meaning that at least as many super-eccentric Jupiters as predicted were detected. 95.8% of trials were unsuccessful. We exclude the candidates with known companions from this procedure (Figure 7.5, thin blue bars), because it so happens that none of them can have $e > 0.9$ and $2.8 < P_{\rm final} < 10$ days without crossing the orbit of another candidate in the system. We find that, with 95.8% confidence, we detected too few super-eccentric proto-hot Jupiters to be consistent with the prediction of Section 7.3. For example, 40% of trials had 0 super-eccentric proto-hot Jupiters, 78% had 1 or fewer, and 95% had 2 or fewer. From these trials, we measure a $N_{\rm sup}$ posterior with a median $N_{\rm sup} = 1 \pm 1$.

7.5 Explaining the Paucity of Proto-hot Jupiters

So far (Sections 7.1-7.4) we have been considering a scenario in which hot Jupiters begin beyond the ice line on super-eccentric orbits — caused by gravitational perturbations

from a companion (e.g. stellar binary Kozai, planetary Kozai, planet-planet scattering, secular chaos) — and subsequently undergo tidal circularization along a constant angular momentum track, reaching a final orbital period $P_{\rm final}$. This process is known as high-eccentricity migration (HEM). We schematically summarize this (black arrows) and other possible origins for hot Jupiters (white and gray arrows), as well as moderately-eccentric Jupiters with $3 < P_{\rm final} < 10$ days, in Figure 7.6. The corresponding populations from the RV-detected sample (EOD, Wright et al. 2012) are plotted in Figure 7.1. Now we relax previous assumptions about HEM (Section 7.2.2) and explore how we can account for the lack of super-eccentric proto-hot Jupiters (Section 7.4). In Sections 7.5.1 and 7.5.2, we relax the assumption that Jupiters began beyond the ice line, finding that this possibility could indeed account for the lack of super-eccentric Jupiters. In Section 7.5.3, we consider the particular case of HEM via the Kozai mechanism with a planetary perturber. In Section 7.5.4, we relax the assumption of a steady current of hot Jupiters produced by HEM but find that a lack of steady current is unlikely to account for the lack of super-eccentric proto-hot Jupiters. In Section 7.5.5, we place an upper-limit on the fraction of hot Jupiters caused by Kozai perturbations from a stellar binary companion.

Figure 7.6.—: Schematic of pathways (arrows) for creating the observed giant planet populations, which we assume formed beyond the ice line and reached semi-major axes interior to the ice line via the stellar binary Kozai mechanism, planetary Kozai mechanism, planet-planet scattering, secular chaos, or disk migration. "Track" refers to the angular momentum range under consideration, i.e. $3 < P_{\rm final} < 10$ days. The black arrows indicate the path that we have assumed throughout the paper for HEM caused either by a planetary or stellar perturber. For example, a Jupiter may be perturbed by a stellar binary companion, follow the black arrow to the region of super-eccentric Jupiters with $3 < P_{\rm final} < 10$ days (blue, diagonal stripe region), undergo tidal circularization along its angular momentum track to $e < 0.9$ (horizontal orange striped region), become a moderately-eccentric Jupiter (blue stars), and eventually achieve hot-Jupiter-hood (red triangles). The purple dashed arrows represent planetary Kozai, which (depending on the perturber) may cause the proto-hot Jupiter to undergo low-eccentricity excursions off the track (Smadar Naoz, private communication, 2012). The other color arrows indicate alternative pathways caused by secular chaos or scattering (white) or disk migration (gray), and colors and patterns of the boxes correspond to the regions of parameter space in Figure 7.1. See text for detailed discussion of the possible scenarios represented here.

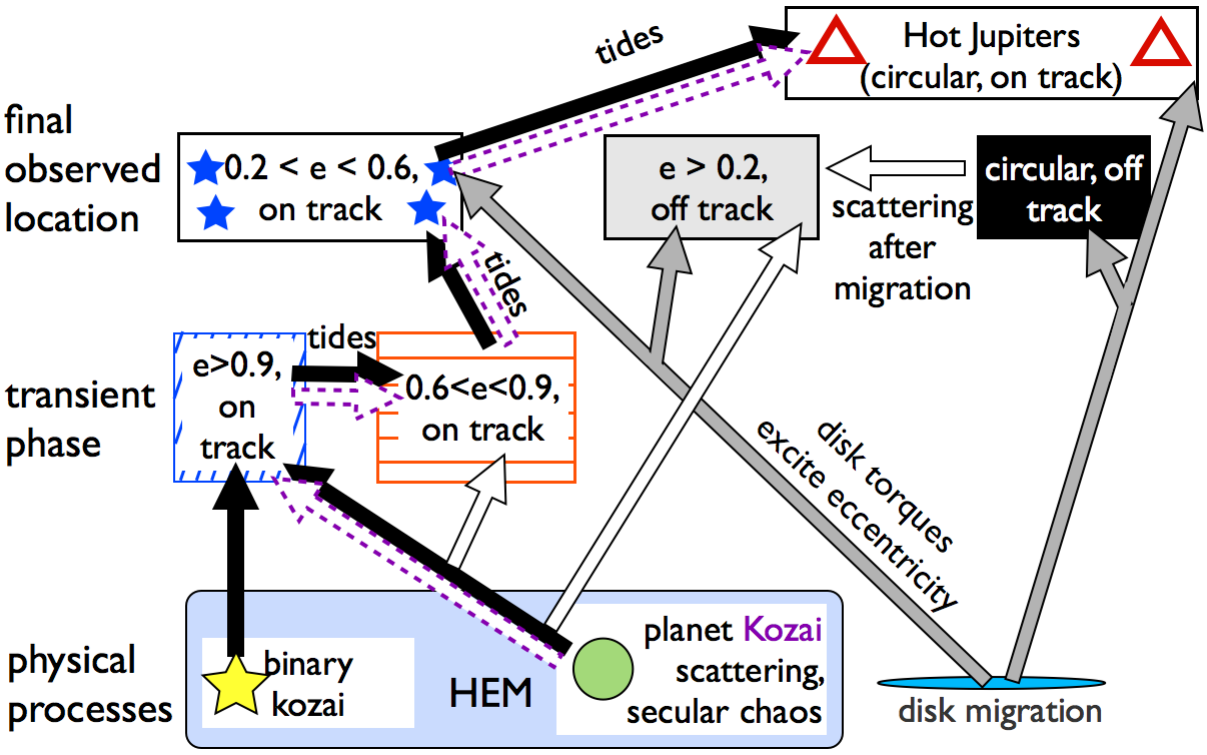

Figure 7.6.—: Continued

7.5.1 No Tidal Circularization: Hot Jupiters and Moderately-eccentric Jupiters Implanted Interior to the Ice Line

Rather than starting on highly-eccentric orbits exterior to the ice line, hot Jupiters and moderately-eccentric Jupiters may have been placed directly into the region we observe today. The moderately-eccentric Jupiters (blue stars, Figure 7.1, 7.6, 7.1) observed along the angular momentum tracks have may not have undergone tidal circularization but may have been placed there by whatever mechanism eccentric Jupiters interior to the ice line (gray region, Figures 7.6 and 7.1). This underlying population could originate from planet-planet scattering or secular chaos, or possibly from disk migration. Wu & Lithwick (2011) found that secular chaos should produce a number of moderate-to-high eccentricity "warm Jupiters" in the region from 0.1 to 1 AU. Goldreich & Sari (2003) and Sari & Goldreich (2004) argued that disk migration can potentially excite moderate eccentricities through resonance torques, but recently Dunhill et al. 2013 modeled planet-disk interactions using high-resolution three-dimensional simulations and found that disks are unlikely to excite the eccentricities of giant planets.

In Figure 7.1, the blue stars look as if they could be an extension of the distribution in the gray region. In Table 7.3, we compute the occurrence rate of giant planets in the RV-discovered sample in different regions of Figure 7.1. The occurrence rate per log semi-major axis interval of moderately-eccentric Jupiters with $2.8 < P_{\rm final} < 10$ days is less than or equal to that in the gray region ($10 < P < 250$ days). Therefore a separate mechanism for producing the blue stars apart from direct implantation may not be necessary. If non-tidal implantation was dominant, the number of moderately-eccentric Jupiters should not be used to predict the number of super-eccentric Jupiters because

the moderately-eccentric Jupiters did not tidally circularize from super-eccentric orbits.

If moderately-eccentric Jupiters with $2.8 < P_{\rm final} < 10$ days did not undergo tidal circularization, hot Jupiters themselves could be part of a continuous distribution of circular Jupiters interior to the ice line (Figure 7.6 and 7.1, black region), which must have migrated somehow. Disk migration effectively produces planets on circular orbits, but seems inconsistent with the high obliquities of hot Jupiters orbiting hot stars (Winn et al. 2010; Albrecht et al. 2012, but see also Rogers et al. 2012). However, disk migration may have produced some or all of the well-aligned hot Jupiters, if their low obliquities are not the result of tidal realignment.

If the cut-off for tidal circularization is 2.8 days, rather than 10 days, Jupiters on circular orbits with $P > 3$ days would actually be part of the so-called "period-valley," rather than the hot Jupiter pile-up. The period valley refers to the region exterior to hot Jupiters but interior to the ice line ($P < 250$ days), where giant planets are scarce. The divide between hot Jupiters and the period valley (i.e. if it is 2.8 days, 10 days or some other value) is ambiguous in the literature (e.g. Jones et al. 2003; Udry et al. 2003; Wright et al. 2009; Wittenmyer et al. 2010). The observed "edge" of hot Jupiters in ground-based transit surveys may be partially caused by a combination of the reduced geometric transit probability of long-period planets and inefficiency of ground-based transit surveys in detecting them (Gaudi et al. 2005), rather than a drop in the intrinsic occurrence rate. We note that the distribution of giant planets inferred from the *Kepler* Mission, assessed out to 50 days (Youdin 2011; Howard et al. 2012b), has no such edge. However, Wright et al. (2009) detect an edge at approximately 0.07 AU (5 days) in their RV survey, which suffers from different (but less severe) biases than transit surveys. Thus, the existence and location of the cut-off remains uncertain.

Table 7.3. Occurrence[a] of Jupiters detected by RV surveys

Period range (days)	Eccentricity	Count	Poisson range[b]	Number per $\log_{10} a$
$2.8 < P_{\rm final} < 10$	$0.2 < e < 0.6$	4	4 ± 2	11^{+6}_{-5}
$10 < P < 250$	$0.2 < e < 0.6$	18	18^{+5}_{-4}	19^{+5}_{-4}
$2.8 < P < 5$	$0 < e < 0.2$	17	17 ± 4	100^{+30}_{-20}
$2.8 < P < 10$	$0 < e < 0.2$	21	21^{+5}_{-4}	57^{+13}_{-11}
$5 < P < 10$	$0 < e < 0.2$	4	$4.2^{+2.4}_{-1.7}$	21^{+12}_{-9}
$5 < P < 250$	$0 < e < 0.2$	29	29^{+6}_{-5}	26^{+5}_{-4}
$10 < P < 250$	$0 < e < 0.2$	25	25 ± 5	27^{+6}_{-5}

[a]Numbers do not account for RV observational biases

[b]Range of Poisson means from whose distributions the count could have been drawn, computed using Jeffrey's prior. The median is higher than the counted number due to the skewed Poisson distribution shape.

Therefore the cut-off may in fact be *between* $P = 2.8$ days and $P = 10$ days. In Figure 7.1, the edge of the pile-up of circular Jupiters appears to end at around 0.057 AU (5 days), as Wright et al. (2009) found. If we separate the hot Jupiters below this cut-off, we recover a pile-up of hot Jupiters: in the region from $2.8 < P < 5$ days, we observe an excess of circular Jupiters inconsistent with the occurrence rate in the period valley by a factor of 3 (Table 7.3). If the cut-off for hot-Jupiters is truly 5 days, the prediction for super-eccentric proto-hot Jupiters should be based only on the number moderately-eccentric Jupiters with $2.8 < P_{\rm final} < 5$ days. In that case (repeating the calculations of Section 7.3.1), we expect to find only $1^{+2}{-}1$ super-eccentric proto-hot Jupiters with $e > 0.9$ and $2.8 < P_{\rm final} < 5$ days, and our confidence that we found fewer than predicted (Section 7.4.2) drops to 66%.

7.5.2 Some or All Proto-hot Jupiters May Have Bypassed the $e > 0.9$ Portion of the $P_{\rm final}$ Track

Alternatively, the typical hot Jupiter may have undergone tidal circularization but bypassed the high eccentricity phase, starting on the HEM track with $0.6 < e < 0.9$ in the region indicated by orange stripes in Figure 7.6 and 7.1 (or even in the $0.2 < e < 0.6$ region). For $P_{\rm final} < 10$ days, a Jupiter would begin the HEM track at an orbital period less than 120 days, or 0.5 AU around a Sun-like star. The Jupiter is unlikely to have formed here — the critical core mass required to accrete a massive atmosphere most likely exceeds the amount of refractory materials available (Rafikov 2006) — but may have been delivered to this region via planet-planet scattering or secular chaos. Assuming a steady-flux of proto-hot Jupiters into the orange striped region, if the

two moderately-eccentric, RV-detected[5] Jupiters (corresponding to $\overline{N}_{\rm mod} = 2.7^{+2.0}_{-1.3}$) in Figure 7.1 (blue stars) originated from the orange region, we would expect

$$\overline{N}_{\rm mod} \left(\int_{0.6}^{0.9} C_{\rm comp}(e) |\dot{e}|^{-1} de \right) / \left(\int_{0.2}^{0.6} C_{\rm comp}(e) |\dot{e}|^{-1} de \right) = 2.7^{+2.0}_{-1.3} \times 0.616 = 1.7^{+1.2}_{-0.8}$$

proto-hot Jupiters in the orange region. We indeed see one such planet, HD 17156 b (Figure 7.1).

Since we observe HD 80606 b in the blue striped region, all proto-hot Jupiters would not necessarily begin in the orange striped region. Planet-planet scattering or secular chaos may place proto-hot Jupiters in both the orange striped region and the blue striped region, with the majority in orange striped region. The proto-hot Jupiters in these two regions would be created by the same dynamical processes responsible for Jupiters with $P_{\rm final} > 10$ days (failed hot Jupiters), of which we observe more with $0.6 < e < 0.9$ than with $e > 0.9$ (though this may be partly due to observational bias). The overall picture of this scenario is that proto-hot Jupiters start the HEM track interior to the ice line with eccentricities similar to those of planets we observe in the period valley, rather than starting with $e \to 1$ beyond the ice line.

[5]In this calculation, we use the RV-detected sample. Even though transit probability is constant along an $a_{\rm final}$ track, ground-based transit survey are still strongly biased against detecting planets transiting with longer orbital periods. RV samples suffer from their own biases against long period and eccentric planets, which we do not account for here.

7.5.3 Proto-hot Jupiters Created by Planetary Kozai

Proto-hot Jupiters created by distant stellar companions likely decoupled by time they reach $P < 2$ years. However, those created by nearby planetary companions may still be coupled to their perturbers and spend much of their evolution at low e (Smadar Naoz, private communication, 2012).The possibility that a proto-hot Jupiter spends part of its time off the HEM track due to Kozai oscillations is indicated by white, purple dashed arrows in Figure 7.6. We clarify that the possibility that supereccentric proto-hot Jupiters spend time at low eccentricities does not reduce their expected number. S12 demonstrate that tidal dissipation primarily occurs during high eccentricity intervals. Regardless of how much time the Jupiter spends off its $a_{\rm final}$ track during low-eccentricity Kozai phases, it spends the same total amount of time on the $a_{\rm final}$ track undergoing tidal dissipation. Therefore Equation (7.3) predicts the total number of super-eccentric Jupiters *observed on the track*.

However, there are two ways in which the planetary Kozai could cause fewer super-eccentric proto-hot Jupiter than computed in Section 7.3. First, even the moderately-eccentric calibration proto-hot Jupiters ($N_{\rm mod,0}$ blue stars in Figure 7.1) could potentially still be coupled to a nearby planetary perturber (Smadar Naoz, private communication, 2012). We note that several of the moderately-eccentric Jupiters (HAT-P-34 b, HAT-P-31 b, and WASP-8 b) have linear trends in the RV observations (Wright et al. 2011), indicating the presence of a companion in the system; it may be the companion is sufficiently massive, inclined, and nearby to remain coupled. If the moderately-eccentric Jupiters are still undergoing Kozai oscillations, we may be observing them in the low-eccentricity portions of their cycles, and they may actually

be tidally dissipating on a track with $P_{\rm final} < 3$ days. If so, they should not have been used to compute the expected number of super-eccentric proto-hot Jupiters with $3 < P_{\rm final} < 10$ days. We clarify that even if the moderately eccentric Jupiters oscillate to high eccentricity intervals corresponding to a dissipation track with $P_{\rm final} < 3$ days, they should not be used to compute the number of super-eccentric Jupiters with $P_{\rm final} < 3$ days, because Equation (7.3) only applies to planets observed on the track.

Second, assuming that the proto-hot Jupiter and its planetary perturber formed co-planar in the disk, they likely underwent scattering to achieve the mutual inclinations necessary for Kozai. This scattering process may have delivered the proto-hot-Jupiter interior to the ice line, leading to the scenario described in Section 7.5.2, in which the proto-hot Jupiter embarks on its HEM track at $a < 0.5$ AU and $e < 0.9$. Indeed, in planetary Kozai, the proto-hot Jupiter can sometimes only reach a maximum eccentricity of only $0.6 < e < 0.9$, rather than $e \rightarrow 1$ (Smadar Naoz, private communication, 2012).

7.5.4 Alternatives to the "Steady Current" Approximation

The S12 prediction of a readily observable number of super-eccentric proto-hot Jupiters assumed a "steady current" of proto-hot Jupiter production. We only expect a steady current if: a) the rate of hot Jupiter production throughout a star's lifetime is constant (e.g. that a hot Jupiter is just as likely to be produced between 4.1-4.2 Gyr as it is during the first 100 Myr), or b) although the hot Jupiter production rate may, for example, be restricted to early in a star's lifetime, new planetary systems are being produced at a constant rate throughout the Galaxy. In the latter case, we would see proto-hot Jupiters along all $a_{\rm final}$ tracks only if the sample included stars in the stage of hot Jupiter

production. Nonetheless, even if neither is true, *we would still expect to observe proto-hot Jupiters.* However, they would restricted to the narrow range of $a_{\rm final}$ tracks for which the circularization timescale is of order a star's age, instead of being found along all $a_{\rm final}$ tracks in proportion to the circularization timescale ($e/\dot{e} \propto a_{\rm final}^8$, Equation 7.5).

Assumption (a) seems unlikely. In the HEM mechanisms proposed (Section 7.1), proto-hot Jupiters are spawned on instability timescales (planet-planet scattering, secular chaos) or the Kozai timescale, which are unlikely to always coincide with the typical stellar lifetime. More likely, the distribution of timescales is uniform (or normal) in order of magnitude and thus most proto-hot Jupiters are spawned early in their host stars' lifetimes. Indeed, Quinn et al. (2012) recently discovered hot Jupiters in the 600 Myr Beehive cluster and found that the, accounting for the cluster's enhanced metallicity, the hot Jupiter occurrence rate is consistent with that of the solar neighborhood. Regarding assumption (b), in practice we expect young stars to be rotating too rapidly to be amenable to Doppler observations and too uncommon in our stellar neighborhood to make up a representative sample of transit surveys. Therefore the steady current approximation is unlikely to hold.

Inspired by population simulations by Hansen (2010) and Hansen (2012), we simulate an extreme scenario in which every proto-hot Jupiter in the observable sample is created simultaneously (Figure 7.7, left panel). We begin with a population of Jupiters uniformly distributed in eccentricity and semi-major axis, extending to 10 AU; gray open circles had initial semi-major axes interior to 1 AU (representing the possibility that planets can begin HEM interior to the ice line, as discussed in Section 7.5.2). Then we evolve the tidal evolution equations (Equations 7.5 and the corresponding $\dot{a}/a$) until Jupiters with $P_{\rm final} < 5$ days have circularized. We overplot tracks of constant

angular momentum (dotted lines), as well as lines defined by a constant "orbital change timescale,"

$$t_{\rm move} \;=\; \left[(\dot{a}/a)^2 + (\dot{e}/e)^2\right]^{-1/2}, \tag{7.14}$$

(dashed orange lines) which match the $a_{\rm final}$ tracks at low eccentricities. Although there is no steady current, we see a "track" consisting of a) Jupiters along the same $a_{\rm final}$ track but with different starting eccentricities/semi-major axes, and b) Jupiters along close, adjacent $a_{\rm final}$ tracks (those along the slightly larger $a_{\rm final}$ track have higher eccentricities because $e/\dot{e} \propto a_{\rm final}^8$).

For comparison (Figure 7.7, right panel) we perform a simulation featuring a steady current of hot Jupiters. In this case, the proto-hot Jupiters are distributed over a range of angular momenta tracks but are most common (black diamonds) along the track where the tidal circularization time is order the total elapsed time (i.e. most of the proto-hot Jupiters began their HEM early in the lifetime of the oldest stars in the sample). The smaller $a_{\rm final}$ tracks (red squares, blue X) are more sparsely populated because these planets circularize very quickly and we just happen to be catching some. The left and right panels are not strikingly different. Particularly with a small observational sample size, we are unlikely to be able to be able to distinguish whether we are seeing a narrow range of $a_{\rm final}$ tracks due to a lack of steady current (left) or simply due to a higher relative population along the $a_{\rm final}$ track of order a stellar age (right).

However, without a steady current of hot Jupiters, the number of moderately-eccentric Jupiters in a $P_{\rm final}$ range cannot be used in Equation (7.7) to predict the number of super-eccentric Jupiters. The number of super-eccentric Jupiters would depend on the initial conditions generated by HEM mechanisms: the relative number of hot Jupiters

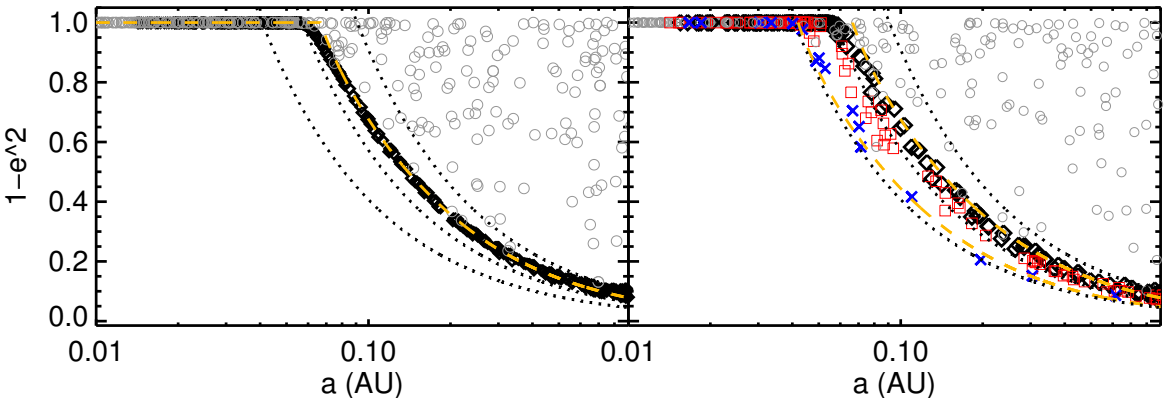

Figure 7.7.—: Monte Carlo simulation of tidal evolution of proto-hot Jupiters assuming that all the proto-hot Jupiters were created at once (left panel) or that there is a steady current (right panelu). In each simulation, proto-hot Jupiters are drawn from a distribution uniform in eccentricity and semi-major axis, extending to 10 AU. Planets that began interior to 1 AU are marked as open, gray circles. We overplot tracks of constant angular momentum (dotted lines) corresponding to $P_{\rm final} = 3, 5, 10$ days, as well as lines defined by a constant "orbital change timescale" (dashed orange lines). In the right panel, the outer orange-dashed line represents a timescale 40 times longer than the inner orange-dashed line. The red squares (blue x) were created two (thirteen) times more recently than the black diamonds.

along adjacent angular momentum tracks and beginning at different semi-major axes along the same track. However, if the initial eccentricities are roughly independent of semi-major axis, the distribution today would resemble one resulting from a steady current. The observed lack of super-eccentric proto-hot Jupiters would require very fine-tuned initial conditions, such as substantially fewer Jupiters beginning along a slightly larger angular momentum track. Therefore the paucity we found in Section 7.4 is unlikely to be fully accounted for by a lack of steady current.

Throughout this work, we have assumed that proto-hot Jupiters *can* travel along HEM tracks with circularization timescales of order a stellar lifetime. However, a nearby planetary perturber can potentially permanently remove the proto-hot Jupiter from the angular momentum track before tidal circularization decouples it. For example, in secular chaos, a planet may be perturbed to a high eccentricity, begin to circularize along a track with a timescale longer than the chaos timescale, but then be chaotically perturbed by nearby planets again. If all proto-hot Jupiters are created early in the star's lifetime and only those with extremely short tidal circularization timescales escape the perturbations of nearby planets, we would indeed see a lack of super-eccentric proto-hot Jupiters in a sample that lacks young stars. In this framework, the observed moderately-eccentric Jupiters would not have been produced by HEM but by some other mechanism, as explored in Section 7.5.1. Their survival indicates that the circularization timescale is not extremely short in $3 < P_{\rm final} < 10$ days, and therefore the argument that planets can only travel along paths with very short circularization timescales would only apply for hot Jupiters with $P < 3$ days.

Finally, a related issue is whether the ratio of moderately-eccentric Jupiters to Jupiters with $P = P_{\rm final}$ is the same in the *Kepler* and calibration samples (i.e.

$\overline{N}_{\rm mod}/\overline{N}_{P=P{\rm final}} \simeq \overline{N}_{\rm mod,0}/\overline{N}_{P=P{\rm final},0}$), as assumed in Equation (7.6). We would expect the pile-up of hot Jupiters to be greater in the older sample (i.e. the *Kepler* sample) and therefore that Equation (7.6) might over predict the number of super-eccentric Jupiters. However, we note that the overall occurrence rate of hot Jupiters in the *Kepler* sample is actually *smaller* than the in the RV-sample (Howard et al. 2012b; Wright et al. 2012), so this is unlikely to be a problem in practice.

7.5.5 Upper Limit on Stellar Kozai Contribution

If the observed moderately-eccentric proto-hot Jupiters began beyond the ice line with $e \rightarrow 1$ and underwent tidal circularization while staying on a track of constant angular momentum (black arrows, Figure 7.6), we would expect to see 7^{+5}_{-3} super-eccentric proto-hot Jupiters (Section 7.3); the lack of such planets indicates that one or more of the alternative pathways in Figure 7.6 (white, purple, and gray arrows) may dominate. These alternative pathways all originate from a planetary perturber or disk, rather than a stellar perturber. Here we place an upper limit on the fraction of hot Jupiters that followed the black arrow channel of HEM, beginning with a super eccentricity and moving along a track of constant angular momentum. Since this is the only pathway open to hot Jupiters produced by stellar binary Kozai oscillations, the upper limit is also on the fraction of hot Jupiters created by stellar binaries. We repeat the MCMC procedure in Section 7.4.2 but update Equation (7.3) with an additional parameter, $f_\star$, representing the fraction of hot Jupiters that undergo HEM from super-eccentricities (or, equivalently, the maximum fraction produced by stellar Kozai):

$$\overline{N}_{\rm sup} = f_\star r(e_{\rm max}) \overline{N}_{\rm mod}. \tag{7.15}$$

We impose a modified Jeffrey's prior on $f_\star$, so the prior is uniform between 0 and 5% and scales with $1/f_\star$ above $f_\star = 5\%$. We choose 5% because, with only 87 Jupiters in the non-*Kepler* sample, a lower rate would be within the Poisson noise. We obtain a two-sigma limit of 33% on the fractional contribution from stellar binaries. Therefore, we expect the majority of hot Jupiters were created by a planetary perturber (or a disk). We note that this result technically only applies to hot Jupiters with $P > 2.8$ days, because no super-eccentric Jupiters with $P_{\rm final} < 2.8$ days were expected. This limit is consistent with 30% contribution rate found by Naoz et al. (2012).

This limit also implies that we would need at least a 67% false positive rate to account for the discrepancy. As discussed in Appendix 7.9, such a high false positive rate is unlikely.

7.6 Conclusion

S12 predicted that if high-eccentricity migration (HEM) is the primary channel for producing hot Jupiters, the *Kepler* candidate collection should harbor a population of super-eccentric Jupiter-sized planets that are in the midst of tidal circularization. We developed and performed a procedure to use the publicly-available *Kepler* transit light curves to confirm or rule out this prediction and found a paucity of proto-hot Jupiters on super-eccentric orbits. Incorporating uncertainties due to counting statistics, uncertainties in the light curve fit parameters and in the assumed stellar parameters,

incompleteness due to the limited observational timespan and missing data, and the signal-to-noise limit, we expected to observe $N_{\rm sup} = 5^{+3}_{-2}$ (Section 7.3) but instead found only 1 ± 1 (Section 7.4). False positives are unlikely to account for the discrepancy. The lack of super-eccentric proto-hot Jupiters may indicate that the assumed constant tidal time lag approximation — which sets the ratio of super-eccentric proto-hot Jupiters to the observed, partially circularized moderately-eccentric Jupiters used to compute the prediction — is incorrect (Section 7.2.2). However, violation of this assumption could only account for the discrepancy if tidal dissipation were actually much *stronger* at high eccentricities along a given angular momentum track.

With the current sample, the statistical signifiance of our results is 95.8%. The expected number of supereccentric Jupiters will increase steeply as the mission continues and the completeness to long-period planets increases. If we continue to find a paucity of super-eccentric Jupiters, our confidence will increase, or perhaps we have been very unlucky and will find one after all. In the future, we will also utilize a pipeline targeted to finding large-period, Jupiter-sized planets and inject the transits of simulated super-eccentric Jupiters to ensure that the assumptions about completeness we have made here are correct.

In Section 7.5, we explored a number of dynamical explanations for the paucity of super-eccentric proto-hot Jupiters, relaxing the assumptions by S12 that proto-hot Jupiters begin HEM beyond the ice line and that a steady current of hot Jupiters is being produced. We found that the lack of super-eccentric planets could be explained by one of the following scenarios. First, hot Jupiters with $P > 2.8$ days may be directly implanted interior to the ice line, and only those with $P < 3$ days have undergone tidal circularization. This would be the case either if the tidal circularization timescale is

typically only less than a stellar lifetime for $P_{\rm final} < 2.8$ days or if only proto-hot Jupiters with fast circularization timescales can manage to complete their circularization without being moved by a nearby planetary perturber. Second, hot Jupiters with $P > 2.8$ days may have undergone tidal circularization but bypassed the super-eccentric phase of HEM, beginning their tidal circularization interior to 0.5 AU with $0.6 < e < 0.9$ rather than beyond the ice line with $e \rightarrow 1$. Third, the moderately-eccentric Jupiters used to calibrate the prediction may be undergoing Kozai eccentricity oscillations caused by a nearby planetary perturber and we are observing them in the low-eccentricity phase, in which they are not currently undergoing tidal dissipation. In that case, we would not expect to observe super-eccentric Jupiters currently undergoing tidal dissipation.

All these explanations point either to disk migration or to secular chaos, planet-planet scattering, or planetary Kozai (or other yet-to-be-proposed dynamical mechanism) as the dominant channel for hot-Jupiter production, rather than the stellar Kozai mechanism. In Section 7.5, we placed an upper limit of 33% on the contribution of stellar Kozai to hot Jupiters, consistent with the findings of Naoz et al. (2012). Our limit only applies to hot Jupiters with orbital periods greater than 2.8 days, as the prediction for super-eccentric Jupiters only applied to those ending their HEM journey at $2.8 < P < 10$ days.

In this paper, we explored S12's prediction for proto-hot Jupiters, but they made a similar prediction for a population super-eccentric binary stars, which they subsequently discovered (Dong et al. 2013). It would not be surprising if short-period stars were produced by the Kozai mechanism but short-period planets primarily by scattering and chaos, which can potentially deliver the planets observed interior to the ice line without the planets undergoing a super-eccentric phase. The initial conditions for stellar systems

and planetary systems may differ in that planetary systems are both theorized (e.g. Barnes & Raymond 2004) and observed (e.g. Wright et al. 2009; Lissauer et al. 2011; Mayor et al. 2011) to form packed with many planets, a condition that may often lead to scattering and secular chaos. In contrast, stellar multiples are typically hierarchical, an optimal setup for the Kozai mechanism.

The lack of super-eccentric proto-hot Jupiters is a new piece of evidence that models for making hot Jupiters must match, joining the distribution of spin orbit measurements (e.g. Fabrycky & Winn 2009; Morton & Johnson 2011a; Naoz et al. 2012). We recommend that future theoretical studies of dynamical models for forming hot Jupiters predict: the distribution of timescales for instabilities that form proto-hot Jupiters, how often the high-eccentricity phase of HEM is bypassed, the initial conditions along the HEM angular momentum tracks, and the expectations for high-eccentricity "failed" hot Jupiters that likely have periapses too distant to undergo tidal circularization, such as KOI 1474.01 (D12). For the brightest *Kepler* host stars, we recommend measuring the spin-orbit alignment of planets in the period valley, whose obliquities have presumably not been affected by tides. Such measurements could elucidate whether the planets in the period valley have a single origin or if there are two populations, which might correspond to the circular planets and the eccentric planets. Additionally, we recommend investigating whether a gas disk could flatten and circularize a period valley planet's orbit if the planet were scattered there before the gas disk dissipated.

We recommend that observers strive to better characterize the eccentricity distribution of the period valley, which we argued may be the launching point for the typical hot Jupiter's HEM journey. It would be helpful to assess if the occurrence rate of eccentric Jupiters in this region is – when extrapolated to the $3 < P_{\rm final} < 10$ days region

– sufficient to launch all the hot Jupiters interior to, rather than at or beyond, the ice line. We also recommend that observers attempt to nail down the period or semi-major axis cut-off between the hot Jupiter pile-up and the period valley. Finally, although we found that it would be more difficult to identify proto-hot Jupiters with $0.6 < e < 0.9$ using the "photoeccentric effect," it could be feasible with more accurate and precise stellar parameters. We recommend spectroscopic follow-up of KOI host stars for this purpose.

7.7 Computing the Posterior of the Mean Number of Planets Based on the Observed Number of Planets

The probability of observing $N_{\rm pl}$ from a Poisson distribution with mean $\overline{N}_{\rm pl}$ is:

$$\mathrm{prob}(N_{\rm pl}|\overline{N}_{\rm pl}) = \frac{\overline{N}_{\rm pl}^{N_{\rm pl}}}{N_{\rm pl}!}\exp[-\overline{N}_{\rm pl}] \tag{7.16}$$

We wish to determine the posterior distribution for $\overline{N}_{\rm pl}$, give the observed $N_{\rm pl}$. Applying Bayes' theorem:

$$\mathrm{prob}(\overline{N}_{\rm pl})|N_{\rm pl}) = \mathrm{prob}(N_{\rm pl}|\overline{N}_{\rm pl})\mathrm{prob}(\overline{N}_{\rm pl}) = \frac{\overline{N}_{\rm pl}^{N_{\rm pl}}}{N_{\rm pl}!}\exp[-\overline{N}_{\rm pl}]\mathrm{prob}(\overline{N}_{\rm pl}) \tag{7.17}$$

where $\mathrm{prob}(\overline{N}_{\rm pl})$ is the prior on $\overline{N}_{\rm pl}$. For a uniform prior on $\mathrm{prob}(\overline{N}_{\rm pl})$, the median of the posterior, $\mathrm{Med}(\overline{N}_{\rm pl})$ is the solution to the equation:

$$0.5 = \frac{\int_{\mathrm{Med}(\overline{N}_{\rm pl})}^{\infty}\frac{\overline{N}_{\rm pl}^{N_{\rm pl}}}{N_{\rm pl}!}\exp[-\overline{N}_{\rm pl}]\mathrm{prob}(\overline{N}_{\rm pl})d\overline{N}_{\rm pl}}{\int_{0}^{\infty}\frac{\overline{N}_{\rm pl}^{N_{\rm pl}}}{N_{\rm pl}!}\exp[-\overline{N}_{\rm pl}]\mathrm{prob}(\overline{N}_{\rm pl})d\overline{N}_{\rm pl}} \tag{7.18}$$

For a uniform prior prob($\overline{N}_{\rm pl}$) $\propto 1$,

$$0.5 = \frac{\int_{{\rm Med}(\overline{N}_{\rm pl})}^{\infty} \overline{N}_{\rm pl}^{N_{\rm pl}} \exp[-\overline{N}_{\rm pl}] d\overline{N}_{\rm pl}}{\int_{0}^{\infty} \overline{N}_{\rm pl}^{N_{\rm pl}} \exp[-\overline{N}_{\rm pl}] d\overline{N}_{\rm pl}} = \frac{\Gamma[N_{\rm pl}+1, {\rm Med}(\overline{N}_{\rm pl})]}{\Gamma[N_{\rm pl}+1]} \tag{7.19}$$

where Γ is the gamma function. For a Jeffrey's prior (appropriate when the scale of the parameter is unknown), which for a Poisson distribution is prob($\overline{N}_{\rm pl}$) $\propto (\overline{N}_{\rm pl})^{-1/2}$ (e.g. Bernardo & Smith 2000; Farr et al. 2013),

$$0.5 = \frac{\int_{{\rm Med}(\overline{N}_{\rm pl})}^{\infty} \overline{N}_{\rm pl}^{N_{\rm pl}-0.5} \exp[-\overline{N}_{\rm pl}] d\overline{N}_{\rm pl}}{\int_{0}^{\infty} \overline{N}_{\rm pl}^{N_{\rm pl}-0.5} \exp[-\overline{N}_{\rm pl}] d\overline{N}_{\rm pl}} = \frac{\Gamma[N_{\rm pl}+0.5, {\rm Med}(\overline{N}_{\rm pl})]}{\Gamma[N_{\rm pl}+0.5]} \tag{7.20}$$

The 68.3% confidence interval be calculated by equating the ratios in Equation 7.19 and 7.20 to 0.1585 and 0.8415. These posteriors have medians slightly larger than the counted numbers because of the skewed shape of a Poisson distribution at small values of the mean ($\overline{N}_{\rm pl} < 10$). It is more probable that we are observing fewer planets than the true mean number than vice versa. As an extreme example, if the mean number of planets per sample is greater than 0, there's some possibility that our sample will happen to contain 0.

7.8 New Candidates Identified from the Threshold Crossing Events (TCE) Table

We identified three new candidates from the Threshold Crossing Events, which is complete for transits with sufficient signal-to-noise and at least three transits: KIC 12735740 (orbital period 282 days), KIC 8827930 (orbital period 288 days), and KIC 9025971 (orbital period 141 days). The first two exhibited two transits in Q1-Q8 but were apparently not caught by eye. The third did not exhibit two transits, despite its

shorter orbital period, due to missing data. These new candidates were also found by Planet Hunters (Wang et al. 2013), and there were no other planets in Wang et al. (2013)'s sample of long-period giant planets that met our criteria. However, a final candidate, KIC 6805414 (orbital period 200 days), was not in the TCE table or in Wang et al. (2013) but was discovered by Huang et al. (2013) using the HAT pipeline. Of the new candidates discovered by Huang et al. (2013)., this is the only one that falls within our stellar and planetary cuts. We think this object was missed by the *Kepler* pipeline because strong stellar variability occurs on the same timescale as the transit duration. We include all these candidates in our sample. In the case of KIC 6805414, we use detrended data provided to us by Chelsea Huang (2012, private communication).

7.9 Assumptions that Cannot Explain a Lower than Expected Number of Super-eccentric Proto-hot Jupiters

These assumptions cannot explain observing fewer than expected super-eccentric proto-hot Jupiters, either because a violation would result in *more* super-eccentric progenitors (1) or because they are unlikely to be violated (2-5).

1. *The evolution of the planet's radius due to tidal inflation is negligible, and no planets are disrupted by tides.* However, if the planet's radius were to expand over the course of HEM due to tidal inflation, then the tidal dissipation rate would be even lower during the earlier stages of HEM, causing planets to spend even

longer at high eccentricities. Therefore, this effect could only increase the expected number of super-eccentric proto-hot Jupiters. The prevalence of tidal disruption does not affect the S12 prediction, because the prediction is based on the survivors. Depending on the timescale of tidal disruption, we may observe additional doomed proto-hot Jupiters that will not survive their HEM.

2. *Angular momentum is not exchanged between the planet and star.* If planets were to typically transfer angular momentum to stars, we would expect more super-eccentric hot Jupiters than predicted and vice versa. However, Penev et al. (2012) argue that stellar tidal dissipation is likely unimportant, because if it were, most hot Jupiters would be subsumed by their stars on short timescales. We note that although a star can add or remove angular momentum from the planet's orbit as the star rapidly expands on the giant branch (e.g. Santerne et al. 2012), we strictly restrict our samples to main-sequence stars so we can ignore this effect. We note that the Sun's spin angular momentum ranges from about 10% ($P_{\rm final}$ = 3 days) to 6% ($P_{\rm final}$ = 10 days) the orbital angular momentum of a proto-hot Jupiter.

3. *The planet's orbital angular momentum and spin angular momentum are not exchanged*. We neglect this effect because we assume that the planet maintains a pseudo-synchronous spin throughout its evolution. If the ratio of the planet's orbital angular momentum to its spin angular momentum is large, the planet's spin quickly (compared to the circularization timescale) evolves to this pseudo-synchronous state, in which the planet's spin rate is similar to the orbital frequency at periapse. We expect the ratio of orbital to spin angular momentum is indeed typically large, because the planet's distance from the star is very large compared to the planetary

radius.

4. *Moderately-eccentric calibration Jupiters ($N_{\mathrm{mod},0}$) truly have $e > 0.2$; they are not low-eccentricity planets that appear eccentric due to eccentricity bias.* Eccentricity bias occurs when noise masquerades as eccentricity. Because the eccentricity cannot be negative, it is biased toward higher values. If one decomposes the RV signal caused by an eccentric planet into sinusoidal harmonics of the planet's orbital frequency, one finds that the signal due to eccentricity is primarily embedded in the second harmonic and has an amplitude of eK, where K is the RV amplitude (e.g. Anglada-Escudé et al. 2010). Eccentricity bias is primarily a concern when eK is near the noise level, i.e. for low-mass and/or long-period planets with small K. In contrast, Jupiter-mass planets on short-period orbits have large K. For an RV precision of a few m/s and a typical hot Jupiter $K \sim 100$ m/s, a signal of amplitude $e \times K = 0.2 \times 100$ m/s $= 20$ m/s is well above the noise level. Moreover, an even tighter constraint on the planet's eccentricity is possible through a joint fit to the RVs and transit light curve, as performed for each member of the calibration sample. Therefore we expect that the calibration sample moderately-eccentric Jupiters (which have orbital periods ranging from 3 - 15 days) truly do have $e > 0.2$.

5. *Only a small fraction of* Kepler *hot Jupiters are false positives.* The expected number of proto-hot Jupiters is proportional to the true rate of *Kepler* hot Jupiters $\overline{N}_{P=P\mathrm{final}}$ (Equation 7.6). For example, if half the *Kepler* hot Jupiters were false positives, the predicted number of proto-hot Jupiters should be cut in half. Morton & Johnson (2011b) and Desert et al. (2012) find low false-positive rates for *Kepler* candidates ($< 10\%$). Santerne et al. (2012), Colón et al. (2012), and Fressin et al.

(2013) find higher false-positive rates. However, Santerne et al. (2012) focused on a population with high a priori false-positive probabilities because of their V-shaped light curves. Moreover, the false positive discoveries by Colón et al. (2012) were for planets with $P < 3$ days, which Colón et al. (2012) suggested can be expected from the period distribution of binaries, and we do not include planets with $P < 3$ days in our sample here. We have removed known false-positives from the computations in Section 7.3. Finally, the false positive rate derived by Fressin et al. (2013) is somewhat larger (18%). However, this rate was based on the Bolmont et al. (2013) sample and, since then, roughly 25% of hot Jupiters have been removed from the *Kepler* sample and marked as false positives Burke et al. (2013), so we expect the false positive rate of the Burke et al. (2013) sample that we use is significantly lower.

7.10 Avoiding Problems Due to Incorrect Stellar Parameters

Characterizing the entire planetary eccentricity distribution from transit light curve parameters can be complicated by systematic errors and uncertainties in the stellar parameters (e.g. Moorhead et al. 2011; Kane et al. 2012; Plavchan et al. 2012). Instead, we simply aim to determine whether or not there are light curves for which $\rho_{\rm circ}$ is physically unlikely. For example, a planet transiting at periapse with $e = 0.95$ would have $\rho_{\rm circ} = 244\rho_\star$. Such a high density would be astrophysically implausible based on our knowledge of stellar evolution.

We consider three potential problems caused by incorrect stellar parameters. First, we could mistakenly identify a planet as being highly eccentric even if it had $\rho_{\rm circ} \sim \rho_\odot$ if we were to underestimate $\rho_\star$ as being very low. Second, we could miss an eccentric planet if we thought its host star had $\rho_\star \sim \rho_\odot$ but the true stellar density were much smaller. However, we avoid both these problems by restricting our samples to exclude giants. All of the $\rho_\star$ we derive for *Kepler* hosts in Section 7.4 are of order 1. Moreover, by excluding giants from the well-characterized, calibration sample of stars with both transits and RV measurements (Figure 7.1), we did not make any predictions for super-eccentric planets orbiting giants, and therefore cannot miss any.

The third potential problem is that we used the number of hot Jupiters in the *Kepler* sample, $N_{P=P\rm final}$, as an input for predicting $N_{\rm sup}$ (Equation 7.6). If a large fraction of the *Kepler* hot Jupiters orbits stars that are secretly giants but slipped past our stellar parameter cuts, then we might overpredict the expected number of super-eccentric proto-hot Jupiters. As shown by Mann et al. (2012) and Dressing & Charbonneau 2013, some of the stars classified as M or K dwarfs might be giants. However, Mann et al. (2012) find that imposing a cut of $\log g > 4$, as we do, helps avoid this misclassification. With the cut imposed, 97% of cool stars dimmer than $Kp = 14$ are dwarves (Mann et al. 2012). Among our sample of *Kepler* hot Jupiters, all the stars with $T_{\rm eff} < 5714$ K have $Kp > 14$, so it is very unlikely our sample harbors many giants masquerading as M or K dwarves.

7.11 Excluded and Exceptional Candidates

Based on our fits to the transit light curves, we find that three candidates are likely eclipsing binaries: KOI-772.01, KOI-1193.01, and KOI-1587.01 and exclude them from the rest of this work.The orbital periods of KOI-1477.01, KOI-1486.01, and KOI-211.01 were incorrectly reported, perhaps because of missing transits; their true orbital periods are 169.54 days,127.2824 days, and 124.03599 days respectively respectively. KOI-211.01 is on the list of *Kepler* eclipsing binaries but this may be an error so we keep it in our sample.

The transits of KOI-1095.01 were particularly noisy. We applied co-detrending vectors before processing with `AutoKep` and imposed a normal prior on the limb darkening parameters using the routine provided by Sing (2010). Typically we can distinguish between a large eccentricity and a large impact parameter for Jupiter-sized planets (DJ12), but in this case, we could not tell whether the transit is grazing. To more easily explore parameter space, we fit the parameter $\ln \rho_{\rm circ}$ instead of $\rho_{\rm circ}$. In order to maintain a uniform prior on e and ω, we correspondingly use the parameter $\ln \rho_{\rm circ}$ when performing the MCMC fit to obtain the eccentricity posterior (Section 7.4.2). Including or excluding this candidate only affects the significance of the results by 0.1%.

KOI-433.02 (Figure 5) has an anomalously *low* $\rho_{\rm circ}$, but it has a companion in the system. If KOI-433.02 had $P_{\rm final} < 10$ days, its orbit would cross that of KOI-433.01. Therefore, likely either: a) the candidate has a large eccentricity but $P_{\rm final} > 10$ days, and is not part of the prediction, or b) the host star's density is overestimated. Fortunately, as discussed in Appendix 7.10, we have designed our approach so that it is not a problem for our assessment of the prediction if some host stars have much lower densities than we

estimate.

As part of our spectroscopic survey, we measured spectroscopic parameters using `SpecMatch` for KOI-44, KOI-193, KOI-211, KOI-686, and KOI-1474, which we use instead of the KIC parameters. For these candidates only, we impose a prior on the stellar mass, metallicity, and age from a TRILEGAL (TRIdimensional modeL of thE GALaxy; Girardi et al. 2005) synthetic *Kepler* field population, as described in Section 3.3 of D12.

The Takeda et al. (2007) evolution models only include stars with $M_\star > 0.7 M_\odot$. For a subset of low-mass host stars — KOI-398, KOI-433, KOI-806, KOI-855, KOI-918, KOI-1095, KOI-1466, KOI-1477, and KOI-1552 — we use the Dartmouth stellar evolution models (Dotter et al. 2008) instead, sampling to maintain a uniform prior on stellar age, mass, and metallicity.

Chapter 8

Giant Planets Orbiting Metal-rich Stars Show Signatures of Planet-planet Interactions

R. I. Dawson & R. A. Murray-Clay *The Astronomical Journal*, Vol. 767, id. L14, 2013

Abstract

Gas giants orbiting interior to the ice line are thought to have been displaced from their formation locations by processes that remain debated. Here we uncover several new metallicity trends, which together may indicate that two competing mechanisms deliver close-in giant planets: gentle disk migration, operating in environments with a range of metallicities, and violent planet-planet gravitational interactions, primarily triggered in metal-rich systems in which multiple giant planets can form. First, we

show with 99.1% confidence that giant planets with semi-major axes between 0.1 and 1 AU orbiting metal-poor stars ([Fe/H]<0) are confined to lower eccentricities than those orbiting metal-rich stars. Second, we show with 93.3% confidence that eccentric proto-hot Jupiters undergoing tidal circularization primarily orbit metal-rich stars. Finally, we show that only metal-rich stars host a pile-up of hot Jupiters, helping account for the lack of such a pile-up in the overall *Kepler* sample. Migration caused by stellar perturbers (e.g. stellar Kozai) is unlikely to account for the trends. These trends further motivate follow-up theoretical work addressing which hot Jupiter migration theories can also produce the observed population of eccentric giant planets between 0.1 and 1 AU.

8.1 Introduction

Approximately 1% of stars host hot Jupiters, ousted from their birthplaces to short-period orbits (Wright et al. 2012) via mechanisms that remain debated. Proposed theories fall into two classes: smooth disk migration (e.g. Goldreich & Tremaine 1980), and migration via gravitational perturbations, either by stars (e.g. stellar binary Kozai, Wu & Murray 2003) or sibling planets (including planetary Kozai, e.g. Naoz et al. 2011; scattering, e.g. Rasio & Ford 1996; and secular chaos, e.g. Wu & Lithwick 2011). (See Dawson et al. 2013, DMJ13 hereafter, for additional references.) We consider the latter class as also encompassing gravitational perturbations preceeded by disk migration (e.g. Guillochon et al. 2011).

Migration processes must not only produce hot Jupiters — heavily studied, extensively observed gas giants orbiting within 0.1 AU of their host stars — but also populate the region from 0.1 to 1 AU. This region is outside the reach of tidal damping

forces exerted by the host star but interior to both the ice line and the observed pile-up of giant planets at 1 AU, one of which likely indicates where large, rocky cores can grow and accrete. We call this semi-major axis range the "Valley," because it roughly corresponds to the "Period Valley" (e.g. Jones et al. 2003), the observed dip in the giant planet orbital period (P) distribution from roughly $10 < P < 100$ days. The Valley houses gas giants both on highly eccentric and nearly circular orbits. Gas disk migration is unlikely to excite large eccentricities (e.g. Dunhill et al. 2013) whereas dynamical interactions are unlikely to produce a substantial population of circular orbits. Therefore this eccentricity distribution may point toward intermixing between two different migration mechanisms, one gentle and one violent. Another orbital feature — the bimodal distribution of spin-orbit alignments among hot Jupiters — is sometimes interpreted as evidence for two migration mechanisms (Fabrycky & Winn 2009; Morton & Johnson 2011a; Naoz et al. 2012). However, it may result from stellar torques on the proto-planetary disk (Batygin 2012), gravity waves that misalign the star's spin axis (Rogers et al. 2012), or two regimes for tidal realignment (Winn et al. 2010; Albrecht et al. 2012). Because tides are negligible in the Valley (except at the most extreme periastron, e.g. HD-80606-b, HD-17156-b), we can interpret trends more easily. Excited inclinations and eccentricities cannot have been erased by tidal damping.

If *two* common mechanisms indeed deliver close-in giant planets, physical properties of the proto-planetary environment may determine which is triggered. A decade ago, Santos et al. (2001, 2004) discovered that giant planets more commonly orbit metal-rich stars, supporting the core accretion formation theory. Independent and follow-up studies confirmed this trend for giant planets (e.g. Fischer & Valenti 2005, Sozzetti et al. 2009 Johnson et al. 2010, Sousa et al. 2011, Mortier et al. 2012) but not small planets (Ribas

& Miralda-Escudé 2007; Buchhave et al. 2012). Neither the Santos et al. (2004) nor the Fischer & Valenti (2005) samples exhibited correlations between stellar metallicity and planetary period or eccentricity, but now the radial-velocity (RV) sample has quadrupled. It is time to revisit the planet-metallicity correlation, but now to gain insight into the dynamical evolution of planetary systems *following* planet formation.

Another motivation is the puzzlingly low occurrence rate of hot Jupiters in the *Kepler* vs. RV sample (Youdin 2011; Howard et al. 2012b; Wright et al. 2012). *Kepler* targets have systematically lower metallicities than RV targets. We will show that differences in the planetary period distribution — not just the overall occurrence rate — between metal-rich and metal-poor stars may account for the discrepancy.

We uncover new stellar metallicity trends in the eccentricities of giant Valley planets (Section 8.2), eccentricities of giant planets tidally circularizing (Section 8.3), and giant planet period distribution (Section 8.4). These correlations point toward planet-planet interactions as one of two mechanisms for delivering close-in gas giants (Section 8.5).

8.2 Eccentric Valley Planets Orbit Metal-rich Stars

Valley gas giants are unlikely to have formed in situ (Rafikov 2006) and exhibit a range of eccentricities (e) (Figure 1). Here we consider giant planets discovered by radial-velocity surveys with $m \sin\ i > 0.1 M_{\rm Jup}$, (queried from the Exoplanet Orbit Database[1] [EOD] on March 1st, 2013, Wright et al. 2011). We restrict the sample to

[1]Five planets fulfilling our selection criteria have eccentricities fixed at 0 in the EOD fits. We perform Monte Carlo Markov Chain fits to the RVs of 14-And-b ($e = 0.026^{+0.016}_{-0.013}$), HD-81688-b ($e = 0.031^{+0.020}_{-0.015}$),

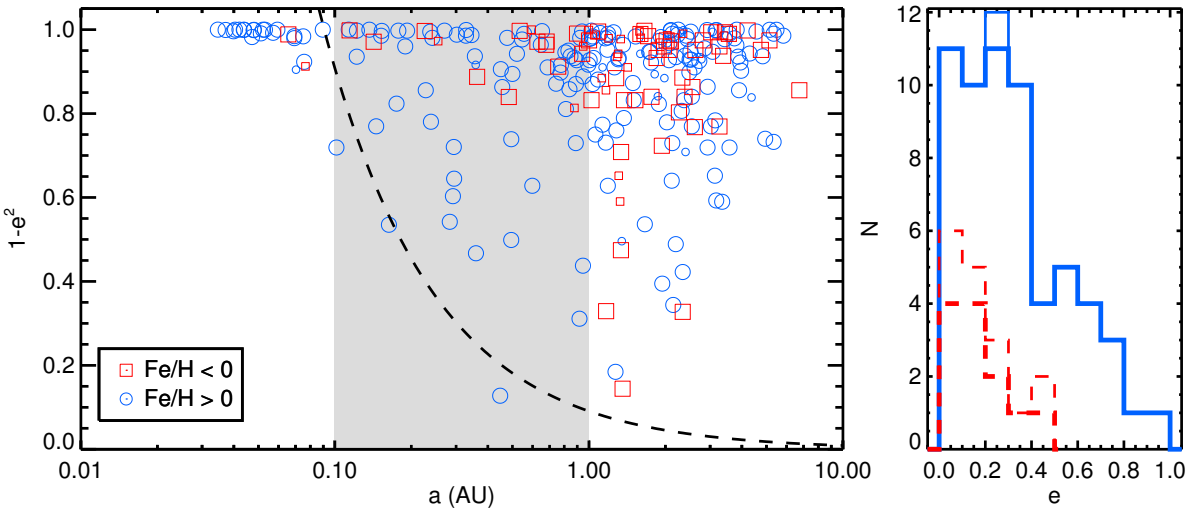

Figure 8.1.—: Left: Valley (gray region) giant planets orbiting metal-rich stars ([Fe/H]≥0, blue circles) have a range of eccentricities; those orbiting metal-poor stars ([Fe/H]<0, red squares) are confined to low eccentricities. Small symbols represent stars with $\log g < 4$. For reference, above the dashed line (a tidal circularization track ending at 0.1 AU) planets are unlikely to experience significant tidal circularization. We plot the quantity $1 - e^2$ to emphasize high-eccentricity planets. Right: Eccentricity distributions of Valley planets orbiting metal-rich (blue solid) and metal-poor (red dashed) stars. The bold distributions omit stars with $\log g < 4$.

FGK stars ($0.4 < M_\star < 1.4 M_\odot$).

Under the two migration mechanisms hypothesis, Valley planets on nearly circular orbits moved in smoothly through the gaseous proto-planetary disk, whereas those on eccentric orbits were displaced through multi-body interactions. In Figure 1, we emphasize planets with large eccentricities by plotting $1 - e^2$. This quantity is related to the specific orbital angular momentum, $h = \sqrt{a(1-e^2)}$, an important parameter for dynamical interactions. This scale also minimizes eccentricity bias. For example, as a result of noise and eccentricity bias, a planet truly on a circular orbit could have a measured $e \sim 0.1$. However, on this scale, $e = 0.1$ would be nearly indistinguishable from $e = 0$.

We divide the sample into planets orbiting metal-rich stars ([Fe/H]$\geq$0, blue circles) vs. metal-poor stars ([Fe/H]$<$0, red squares). Only the metal-rich stars host Valley planets with large eccentricities. The eccentricities of these 61 planets extend up to 0.93. In contrast, the 17 Valley planets orbiting metal-poor stars are confined to low eccentricities ($e \leq 0.43$). Overall, 28% of Valley planets orbiting metal-rich stars have eccentricities exceeding that of the most eccentric one orbiting a metal-poor star.

We assess the statistical significance of the low eccentricities of Valley planets orbiting metal-poor stars. We perform a Kolmogorov-Smirnov (K-S) test on the null hypothesis that the eccentricities of the metal-rich and metal-poor sample are drawn from the same distribution. We reject the null hypothesis with 95.1% confidence. Using a test more sensitive to the tails of distributions, Anderson-Darling (A-D), we reject

and Xi-Aql-b ($e = 0.26 \pm 0.04$) using Sato et al. (2008)'s data; adopt Johnson et al. (2011c)'s $e = 0.03 (< 0.28)$ for HD-96063-b; and remove HD-104067-b because the RVs are unavailable.

the null hypothesis with 96.9% confidence. Finally the probability that the maximum eccentricity of the 17 planets is less than or equal to the observed $e = 0.43$ is the ratio of combinations:

$$\frac{\begin{pmatrix} 61 \text{ Valley } e \leq 0.43 \\ 17 \text{ Valley } [Fe/H] < 0 \end{pmatrix}}{\begin{pmatrix} 78 \text{ Valley} \\ 17 \text{ Valley } [Fe/H] < 0 \end{pmatrix}} = 0.86\%$$

The results are insensitive to the exact metallicity cut and significant at 95% confidence or higher for any cut located between -0.15 and 0.03 dex. Therefore, with 99.14% confidence, we reject the hypothesis that the confinement to low eccentricities of the planets orbiting metal-poor stars results from chance. Although the exact statistical significance is somewhat sensitive to the definition of the Valley, which defines the sample size, it is evident in Figure 1 that the trend occurs throughout the Valley, and the significance of the results is 95% or higher for cuts from $0.6 < a < 1.16$ AU. The significance is 99.86% without the stellar cuts and 97.8% with an additional cut of $\log g > 4$ to remove evolved stars.

As suggested by Johansen et al. (2012) in the context of the mutual inclinations of *Kepler* multi-planet systems, one might expect a threshold metallicity to trigger instability. Decreasing planets' semi-major axes (a) via gravitational perturbations requires interactions between at least two (and probably more) closely-spaced giant planets. It may be that only metal-rich proto-planetary environments can form such

systems.[2] In contrast, planets on circular orbits would have arrived via disk migration, which can occur regardless of metallicity.

We note that beyond 1 AU, the metal-rich and metal-poor sample have similar eccentricity distributions. Planets with $a > 1$ AU have not necessarily changed their semi-major axes: they may have formed where we observe them. These planets on eccentric orbits near their formation location may have exchanged angular momentum with another planet or star without requiring the abundance of closely-packed giant planets necessary to drastically alter a.

8.3 Proto-hot Jupiters Orbit Metal-rich Stars

We turn to planets experiencing significant tidal dissipation, detected[3] by non-*Kepler* transit surveys (Figure 2) and followed up with RV measurements. We use the stellar and

[2]RV systems containing multiple known giant planets do appear to have systematically higher metallicities than those containing one, but the statistical significance is marginal. We note that planets may be scattered to distances beyond current RV detection or ejected, so systems with only one known giant planet perhaps originally had more.

[3]Some planets have e fixed at 0 in EOD fits. We remove those with poorly-constrained eccentricities: CoRoT-7-b, HAT-P-9-b, OGLE-TR-10-b, OGLE-TR-111-b, TrES-1-b, TrES-4-b, WASP-13-b, WASP-39-b, WASP-58-b, XO-1-b, XO-5-b. We include planets whose eccentricities are constrained to be small ($e < 0.2$), by our fits (CoRoT-13-b, CoRoT-17-b, WASP-16-b) or the literature (CoRoT-7-b, HAT-P-1-b, HAT-P-4-b, HAT-P-8-b, HAT-P-12-b, HAT-P-27-b, HAT-P-39-b, OGLE-TR-211-b, KELT-2-Ab, WASP-7, WASP-11-b, WASP-15-b, WASP-21-b, WASP-25-b, WASP-31-b, WASP-35-b, WASP-37-b, WASP-41-b, WASP-42-b, WASP-47-b, WASP-61-b, WASP-62-b, WASP-63-b, WASP-67-b). See the EOD for each planet's orbital reference.

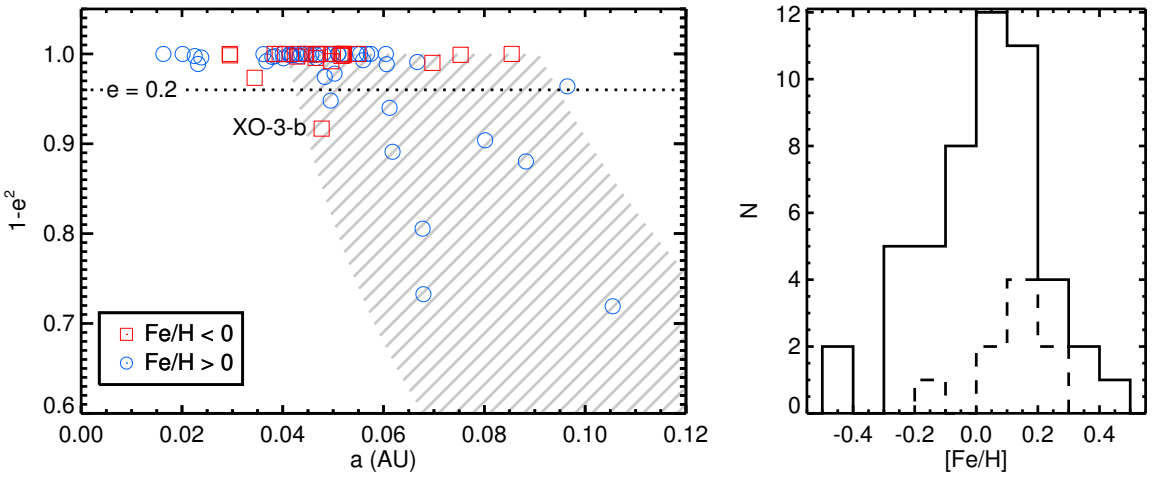

Figure 8.2.—: Left: Giant planets discovered by non-*Kepler* transit surveys, orbiting metal-rich (blue circles) and metal-poor (red squares) stars. The striped region encloses planets undergoing tidal circularization to $3 < P_{\rm final} < 10$ days. Planets below the dotted line have $e > 0.2$, most of which orbit metal-rich stars. Right: Distribution of host star metallicities for planets in the striped region (left) with e >0.2 (dotted line) and $e < 0.2$ (solid line).

planetary cuts described in Section 8.2 (except for XO-3-b, see below). Socrates et al. (2012b) and DMJ13 used this sample to calculate the abundance of moderately-eccentric proto-hot Jupiters. Advantageously for this sample, transit surveys are less inclined to target metal-rich stars, yielding planets orbiting metal-poor stars for comparison. To be consistent with Socrates et al. (2012b) and DMJ13 and to avoid eccentricity bias, we classify planets with $e > 0.2$ as eccentric.

The striped region contains planets undergoing tidal circularization along tracks of constant angular momentum (see Socrates et al. 2012b, DMJ13) to final orbital periods $P_{\rm final}$ between 2.8 and 10 days. (The traditional boundary for hot Jupiters is 10 days, and 2.8 days is the limit above which we still see eccentric giant planets. Those with $P_{\rm final} < 2.8$ days have much faster tidal circularization rates.) Most observed eccentric planets orbit metal-rich stars (blue circles). We suggest that only giant planets forming in metal-rich systems with multiple giant planets are likely to be scattered onto eccentric orbits that bring them close enough to the star to undergo tidal circularization (e.g. Ford & Rasio 2006).

The probability of randomly selecting eight planets orbiting stars with $[Fe/H] \geq 0$ and one planet (i.e. XO-3-b) orbiting a star with $[Fe/H] \geq -0.18$ is the ratio of combinations:

$$\frac{\left(\begin{array}{c} 38 \\ 8 \end{array} \right) \times 14 + \left(\begin{array}{c} 38 \\ 9 \end{array} \right)}{\left(\begin{array}{c} 59 \\ 9 \end{array} \right)} = 6.7\%$$

where, among the 59 stars in the $P_{\rm final}$ range, 38 have $[Fe/H] \geq 0$ and 14 have $-0.18 \leq [Fe/H] < 0$. XO-3 has $M_\star = 1.41 M_\odot$, just above our stellar mass cut; the

high mass of the star (corresponding to a more massive disk and more metals to form giant planets) may account for the presence of a proto-hot Jupiter despite the star's low metallicity. Without this star, the statistical significance is 98.3%. We also perform a K-S (A-D) test, rejecting with 95.5% (92.1%) confidence the null hypothesis that the host star metallicities of planets in the striped region with $e > 0.2$ are drawn from the same distribution as those with $e < 0.2$.

8.4 The Short-period Pile-up is a Feature of Metal-rich Stars

Howard et al. (2012b) found a surprisingly low *Kepler* hot Jupiter occurrence rate ($f_{\rm HJ,Kepler}$) — the expected number of giant planets per star with $P < 10$ days — compared to RV surveys ($f_{\rm HJ,RV}$), a trend confirmed by Wright et al. (2012) and Fressin et al. (2013); all suggested that the systematically lower metallicities of *Kepler* host stars may contribute to the discrepancy. In Figure 3, we compare the period distribution of transiting giant planet candidates detected by the *Kepler* survey (Burke et al. 2013; see also Borucki et al. 2011 and Batalha et al. 2013) — applying a radius cut of $8 < R_{\rm planet} < 20 R_{\rm earth}$ — to that expected from the RV sample,[4] using a normalization constant $C_{\rm norm}$ (defined below). The RV sample includes only planets discovered by RV surveys, not transit surveys. For both samples, we follow DMJ13 and impose cuts

[4] The RV sample is not uniform; we plot it for qualitative comparison. The expected distribution derived from the period distribution reported by Cumming et al. (2008) appears similar. We therefore interpret the short-period pile-up as real, not due to preferential detection. For the quantitative calculations in this section, we use the uniform Fischer & Valenti (2005) sample.

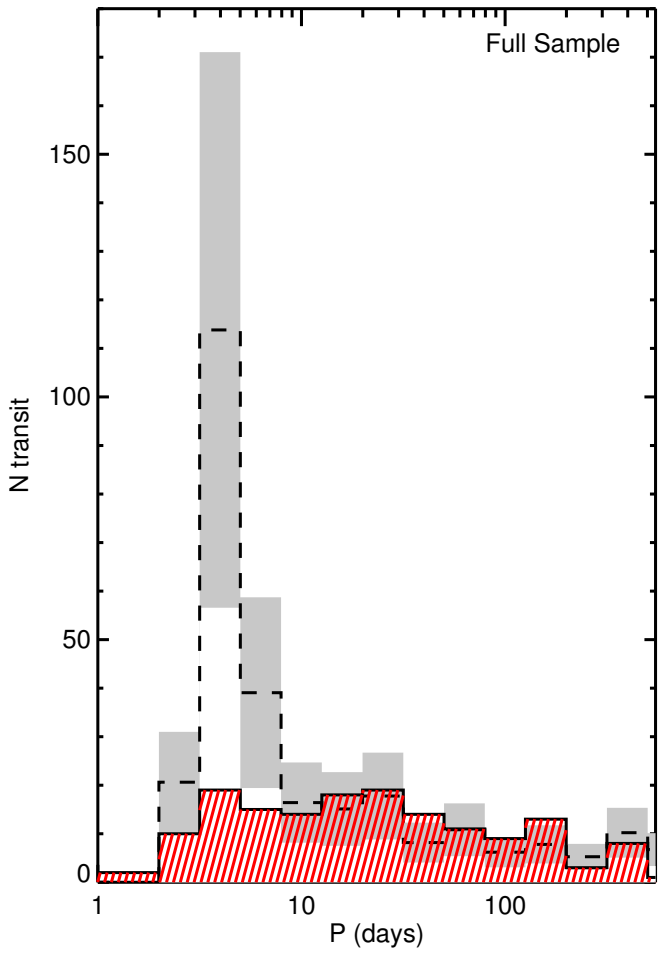

Figure 8.3.—: Red striped: number of transiting giant planets detected by *Kepler*. Black dashed: expected number based on the RV-discovered (i.e. excluding planets discovered by transit surveys) sample[4]. The gray error bars are from uncertainties in $C_{\rm norm}$, not the Poisson uncertainties of each individual bin. The two distributions are consistent at long periods, but the *Kepler* sample lacks a short period pile-up.

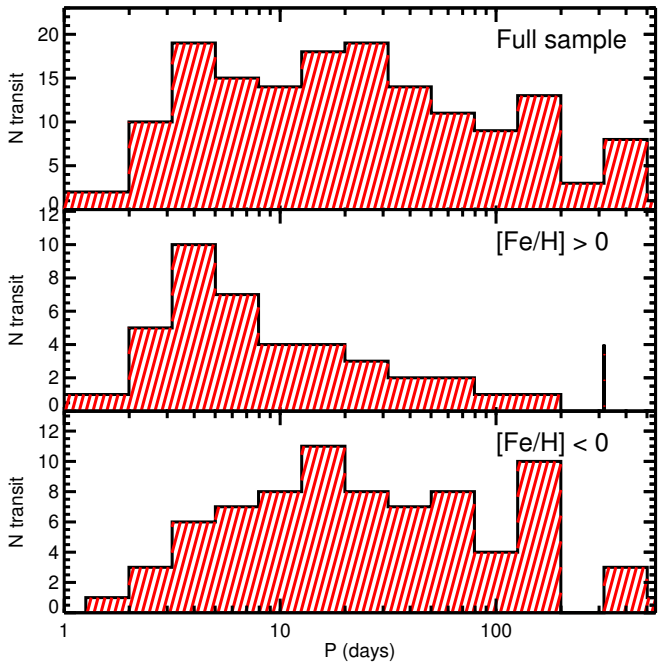

Figure 8.4.—: Number of transiting giant planets observed by *Kepler* without a stellar metallically cut (top), with [Fe/H]≥0 (middle), and with [Fe/H]<0 (bottom). In the metal-rich sample (middle), we recover the shape of the short-period pile-up seen in the RV sample (black-dashed line, Figure 3). In contrast, the metal-poor sample (bottom) is depleted in short-period giants.

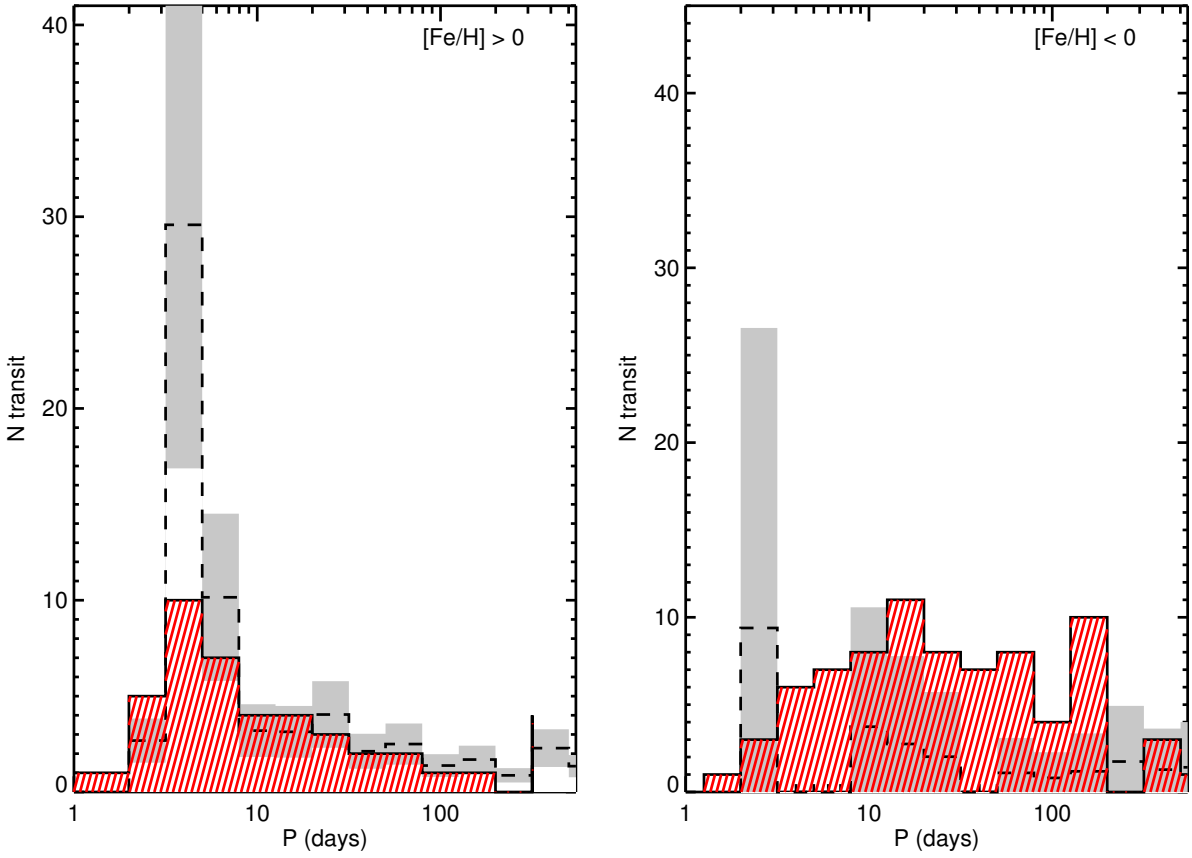

Figure 8.5.—: Same as Figure 3 but for metal-rich (left) and metal-poor (right) subsamples. Left: Metal-rich *Kepler* sample (red striped) exhibits a short-period pile-up, but falls below RV expectations in the 3-5 day bin. Right: Metal-poor *Kepler* sample is not inconsistent with the metal-poor RV sample, but the latter is difficult to characterize due to small numbers.

of stellar temperature $4500 < T < 6500K$ and surface gravity $\log g > 4$ to restrict the sample to well-characterized Kepler host stars (Brown et al. 2011b). The two distributions appear consistent beyond 10 days but differ strikingly at short orbital periods: the *Kepler* period distribution lacks a short-period pile-up (in fact, the absolute *Kepler* giant planet occurrence declines toward short orbital periods, as modeled by Youdin 2011 and Howard et al. 2012b).

Although *Kepler* Input Catalog (KIC) metallicity estimates are known to be uncertain (Brown et al. 2011b), we can roughly divide the *Kepler* sample into metal-rich ([Fe/H]$\geq$0) and metal-poor ([Fe/H]$<$0). In Figure 4, we compare the period distributions for *Kepler* giant planets orbiting metal-rich vs. metal-poor stars. When we limit the sample to [Fe/H]$\geq$ 0 (row 2), we recover the missing short-period pile-up, which the metal-poor sample (row 3) lacks. Performing a K-S test, we reject with 99.95% confidence the hypothesis that the metal-rich sample and metal-poor sample are drawn from the same distribution. The results are insensitive to the exact metallicity cut.

We compare the *Kepler* metal-rich(poor) sample to the RV metal-rich(poor) sample in Figure 5. In Figures 3 and 5, we compare the observed number of transiting *Kepler* giant planets (red striped) to the number expected (black dashed) based on the RV sample,

$$N_{\mathrm{RV,trans}} = C_{\mathrm{norm}} N_{\mathrm{RV}} \mathrm{prob}_{\mathrm{trans}},$$

where N_{RV} is the observed number of RV planets per bin and $\mathrm{prob}_{\mathrm{trans}}(P)$ is the transit probability. We set the normalization constant, C_{norm}, using the values (computed below) of $f_{\mathrm{HJ,Kepler}}$ and $f_{\mathrm{HJ,RV}}$:

$$C_{\mathrm{norm}} = \frac{f_{\mathrm{HJ,RV}}}{f_{\mathrm{HJ,Kepler}}} \frac{\sum_{P=0}^{10\mathrm{days}} N_{\mathrm{trans,Kep}}(P)/\mathrm{prob}_{\mathrm{trans}}(P)}{\sum_{P=0}^{10\mathrm{days}} N_{\mathrm{RV}}(P)}.$$

Each error bar is due to the uncertainty in $f_{\rm HJ,RV}/f_{\rm HJ,Kepler}$. To compute $f_{\rm HJ,Kepler}$, we follow Howard et al. (2012b), using our own stellar and planetary cuts and the latest sample of *Kepler* candidates (Burke et al. 2013). The Barbara A. Mikulski Archive for Space Telescopes (MAST) supplied the stellar parameters and the NExSci Exoplanet Archive the transit shape parameters (duration, depth, $a/R_\star$, $R_{\rm planet}/R_\star$). We obtain[5] $f_{\rm HJ,Kepler} = 0.38^{+0.08}_{-0.07}\%$ for giant planets with P <10 days (consistent with Howard et al. 2012b and Fressin et al. 2013), $1.08^{+0.33}_{-0.27}\%$ for the metal-rich sample, and $0.25^{+0.08}_{-0.06}\%$ for the metal-poor sample. To compute $f_{\rm HJ,RV}$, we use the stellar and planetary sample from the iconic planet-metallicity correlation (Fischer & Valenti 2005) and associated stellar parameters (Valenti & Fischer 2005), the last RV target list to be publicly released. We obtain $f_{\rm HJ,RV} = 1.03^{+0.34}_{-0.32}\%$ for giant planets with P <10 days (in agreement with Wright et al. 2012), $1.74^{+0.67}_{-0.54}\%$ for those orbiting stars with [Fe/H]≥0, and $0.07^{+0.23}_{-0.06}\%$ for [Fe/H]<0. With no metallicity cut, $f_{\rm HJ,Kepler}$ is inconsistent with $f_{\rm HJ,RV}$ at the 2.0σ level.

In the metal-rich comparison (Figure 5, left), we see greater consistency between the *Kepler* and RV distribution than in the full sample (Figure 3). The metal-rich *Kepler* sample exhibits a short-period pile-up; the discrepancy between $f_{\rm HJ,Kepler}$ vs. $f_{\rm HJ,RV}$ is now only 1.0σ, with the greatest discrepancy in the 3-5 day bin. This improvement motivates a detailed follow-up analysis, including a more precise estimate of $f_{\rm HJ,RV}$ using the latest RV target lists. If follow-up studies find a significant discrepancy between the metal-rich *Kepler* and radial velocity samples, it could be due to the KIC metallicity estimates. Using spectroscopic metallicity measurements by Buchhave et al. (2012), we find that high metallicities do correspond linearly to high spectroscopic metallicities

[5]We estimate the occurrence rates and uncertainties based on the Poisson likelihood and a Jeffrey's prior, following DMJ13.

(with a scatter of about 0.2 dex about a best-fit line with slope 0.3), but the spectroscopic metallicities have a systematic offset corresponding to 0.1 dex at KIC [Fe/H] = 0, consistent with the discussion by Brown et al. (2011b). However, we attribute the systematic offset to the fact that stars targeted for spectroscopic follow-up are bright, main-sequence stars in our solar neighborhood and thus have systematically higher metallicities; in contrast, the KIC metallicities were computed assuming a low-metallicity prior, due to the *Kepler* targets being above the galactic plane. The planetary radius cut may also contribute to the discrepancy. The $8R_{\rm earth}$ cut for the *Kepler* sample corresponds to the RV cut of $m \sin i = 0.1 M_{\rm Jup}$ for a planet made of pure hydrogen at a low effective temperature (e.g. Seager et al. 2007). However, close-in, low-mass planets may be inflated to $> 8R_{\rm earth}$ and may have a different period distribution, contaminating the sample. In the metal-poor comparison (Figure 5, right), the *Kepler* and RV distributions do not appear inconsistent, but it is difficult to judge given the very small sample of RV-detected planets orbiting metal-poor stars.

8.5 Conclusion

We found three ways in which the properties of hot Jupiters and Valley giants depend on host star metallicity:

1. Gas giants with $a < 1$AU orbiting metal-rich stars have a range of eccentricities, whereas those orbiting metal-poor stars are restricted to lower eccentricities.

2. Metal-rich stars host most eccentric proto-hot Jupiters undergoing tidal circularization.

3. The pile-up of short-period giant planets, missing in the *Kepler* sample, is a feature of metal-rich stars and is largely recovered for giants orbiting metal-rich *Kepler* host stars.

Hot Jupiters and Valley giants are both thought to have been displaced from their birthplaces. Therefore these metallicity trends can be understood if smooth disk migration and planet-planet scattering both contribute to the early evolution of systems of giant planets. We expect disk migration could occur in any system, but only systems packed with giant planets – which most easily form around metal-rich stars – can scatter giant planets inward to large eccentricities (Trend 1). Some of these tides shrink and circularize (Trend 2), creating a pile-up of short-period giants (Trend 3). Moreover, these trends support planet-planet interactions (e.g. scattering, secular chaos, or Kozai) as the dynamical migration mechanism for delivering close-in giant planets, rather than stellar Kozai. This is consistent with previous work by DMJ13 arguing that stellar Kozai does not produce most hot Jupiters, based on the lack of super-eccentric proto-hot Jupiters. We would not expect planet-planet scattering to typically result in nearby companions to hot Jupiters, which have been ruled out in the *Kepler* sample by Steffen et al. (2012a). (See also Latham et al. 2011.)

One possible challenge for our interpretation is the lack of apparent correlation between spin-orbit misalignment and metallicity. However, spin-orbit misalignments are not necessary caused by dynamical perturbations, and their interpretation is complicated because measurements have primarily been performed for close-in planets subject to tidal realignment. We recommend spin-orbit alignment measurements, via spectroscopy (McLaughlin 1924; Rossiter 1924; Queloz et al. 2000) or photometry (Nutzman et al.

2011; Sanchis-Ojeda et al. 2011), of *Kepler* candidates in the Valley, which are typically too distant to be tidally realigned.

To support or rule-out the interpretation that these metallicity trends are signatures of planet-planet interactions, we further recommend: 1) theoretical assessments of whether planet-planet interaction mechanisms designed to account for hot Jupiters can simultaneously produce the observed population of eccentric Valley planets, and 2) more sophisticated assessments of the trends we report here, using the target lists of recent RV surveys and, as undertaken by Fressin et al. (2013), a careful treatment of *Kepler* false-positives and detection thresholds.

Note added in proof: We thank readers for alerting us to references we missed. Gonzalez (1997) first pointed out the planet-metallicity correlation, Gould et al. (2006) that RV surveys are biased toward higher metallicities, and, in a submitted conference proceedings, Taylor (2012) a correlation between eccentricity and metallicity for close-in giant planets.

Chapter 9

Conclusion

9.1 Summary

The surprisingly dynamical architectures of extra-solar planetary systems and of our own solar system's Kuiper belt have necessitated looking beyond the simple "clockwork" picture of planetary system evolution. Four centuries after Kepler declared planetary systems to be "not like a divine animal but like a clock," new discoveries have left us struggling to make sense of the animal-like properties of the growing menagerie of extra-solar planets and Kuiper belt objects. This thesis investigated the migratory behavior of planetary systems, in which giant planets leave behind the icy regions where they formed for warmer and/or more exotic climes. We sought to distinguish whether planetary migration is a smooth or violent process through a two-pronged approach: 1) reconstructing the migratory behavior of planets based on the debris disks they sculpted in the process (Chapters 2 - 3) and 2) developing new methods for characterizing modern planetary orbits, which we used to understand the histories of planetary systems

(Chapters 4 - 8).

In Chapter 2, we investigated planetary migration in our own solar system, addressing the question of whether Neptune underwent smooth, planetesimal-driven migration or violent planet-planet scattering. We made use of the fact that Neptune's migration created several dynamical populations in our solar system's debris disk, the Kuiper belt. These populations include one of dynamically "hot" high-inclination objects overlying another flat, dynamically "cold" population with distinct physical properties. We presented a new observational constraint: the cold population is confined to eccentricities well below the limit dictated by long-term survival. Thus Neptune must deliver hot KBOs into the Kuiper belt without excessively exciting the cold KBOs eccentricities. We explored the parameter space for Neptune's migration history, developing analytical expressions that allowed us thoroughly explore this parameter space without the need for a computationally-prohibitive number of simulations. We ruled out much of parameter space, except where Neptune is scattered to a moderately eccentric orbit (e$>$ 0.15), experiences eccentricity-damping from the dynamical friction of planetesimals, and subsequently migrates a distance Δ a = 1-6 AU. Therefore Neptune likely experienced both planet-planet scattering and smooth disk migration.

Next (Chapter 3), we modeled the warping of the extra-solar debris disk, β Pictoris, by a planet on inclined orbit. The known planet in the system, β Pictoris b, was reported by Currie et al. (2011) to be on an orbit aligned with the system's flat outer disk and therefore unable to produce the observed warp in the disk. We showed that if planet b were aligned with the flat outer disk, it would prevent another planet from creating a warp with the observed properties; therefore planet b itself must be responsible for the warp. Next, we demonstrated that, at the extremes of the uncertainties, planet b is

sufficiently inclined to produce the observed warp. Finally, we showed that planet b's inclination could have been damped by dynamical friction and still produce the observed disk morphology, but the feasibility of such damping depends on the disk properties and the presence of other planets.

Knowing a planet's true orbital period is essential for understanding the dynamics and migration history of its planetary system. In Chapter 4, we developed and applied a new approach for correctly identifying a planet's orbital frequency from radial-velocity data and avoid confusion with alias frequencies, which can cause severe mischaracterization of the planet. Our approach makes use of the fact that ground-based observations contain gaps on multiple timescales, leading to a predictable pattern of aliases that can be compared with the data. We examined six cases of orbital ambiguity and found in particular that the orbital period 55 Cnc e is 0.7365 days, not the 2.817 days reported in the literature.

In Chapters 5, 6, and 7, we searched for hot Jupiters' posited progenitors: Jupiters on long-period, highly-eccentric orbits undergoing migration through tidal damping of their orbits. Socrates et al. (2012b) had predicted that the *Kepler* Mission should discover a significant number of these super-eccentric Jupiters if hot Jupiters achieve their close-in orbits via strong gravitational interactions. In Chapter 5, We presented a new approach for measuring a planet's eccentricity from its transit light curve, preventing the need for radial-velocity follow-up. In Chapter 6, we applied this approach to *Kepler* candidate KOI-1474.01, finding that this Jupiter-sized planet has a large eccentricity and exhibits transit timing variations due to a massive outer companion. However, its periapse is probably too far for the star for tidal friction to transform it to a hot Jupiter over its host star's lifetime. Therefore we consider KOI-1474.01 a failed hot

Jupiter. Then we applied our approach to the other giant planets discovered by the *Kepler* Mission and found a lack of super-eccentric hot Jupiter progenitors, allowing us to place an upper limit on the fraction of hot Jupiters produced by the Kozai mechanism. Therefore most hot Jupiters are likely produced by disk migration and/or some form of planet-planet interactions that do not require the hot Jupiter progenitor to undergo a super-eccentric phase.

Finally, we proposed in Chapter 8 that if both planet-disk and multi-body interactions commonly cause giant planet migration, physical properties of the proto-planetary environment may determine which is triggered. We identified three trends in which giant planets orbiting metal rich stars show signatures of planet-planet interactions: (1) gas giants orbiting within 1 AU of metal-rich stars have a range of eccentricities, whereas those orbiting metal-poor stars are restricted to lower eccentricities; (2) metal-rich stars host most eccentric proto-hot Jupiters undergoing tidal circularization; and (3) the pile-up of short-period giant planets, missing in the *Kepler* sample, is a feature of metal-rich stars and is largely recovered for giants orbiting metal-rich *Kepler* host stars.

The results of this thesis suggest that both disk migration and planet-planet interactions may be widespread, with the latter occurring primarily in metal-rich planetary systems where multiple giant planets can form.

9.2 Follow-up

The work presented in thesis has spurred a variety of follow-up work by us and others. We are continuing to investigate Neptune's migration history by focusing on the origin of the Kuiper belt's bimodal inclination distribution (Brown 2001; Gulbis et al. 2010; Volk & Malhotra 2011). To date no simulations have been able to produce both the high and low inclination classical Kuiper belt objects while qualitatively matching their observed eccentricity distribution. We are expanding the framework we developed in Chapter 2 to explore whether the large inclinations of many Kuiper belt objects could be the result of Neptune undergoing a period of high inclination during the early period of solar system upheaval (Dawson & Murray-Clay, in preparation). We are also assessing whether our constraints hold if the Kuiper belt was quite massive during the period of upheaval.

Since the publication of Chapter 3 in 2011, more observations of β Pictoris have been conducted. We had found that either β Pictoris b must either be on an inclined orbit misaligned with the flat, outer disk or that its orbit was inclined in the past and subsequently damped. We argued that the apparent alignment of β Pictoris b with the flat outer disk reported by Currie et al. (2011) could be the result of uncertainty in the measured sky position of the planet and disk, which were measured in separate images, and had recommended endeavoring to measure the position of the planet and the disk in the same image. Lagrange et al. (2012) made this measurement and found that the planet is indeed misaligned with the flat outer disk and thus has sufficient inclination to produce the observed warp.

Our revised period for the radial-velocity-discovered super-Earth 55 Cnc e (Chapter 4) resulted in an enhanced transit probability, motivating new searches for its transit.

We collaborated in campaign led by Joshua Winn to photometrically monitor 55 Cnc with the MOST satellite, and the planet was found to transit (Winn et al. 2011). The transit was concurrently discovered with Spitzer by Demory et al. (2011). A super-Earth transiting a bright star, 55 Cnc e is now a laboratory for composition and atmospheric studies, both theoretical (e.g. Castan & Menou 2011; Madhusudhan et al. 2012; Lopez et al. 2012) and observational (e.g. Crossfield 2012; Demory et al. 2012; Ehrenreich et al. 2012). The new period also led to new insights on the dynamics of the system (Kaib et al. 2011; Van Laerhoven & Greenberg 2012; Bolmont et al. 2013). Our de-aliasing approach was recently employed to distinguish the true orbital period of an Earth-mass planet orbiting our stellar neighbor Alpha Centauri B (Dumusque et al. 2012, supplementary material).

With the new *Kepler* data collected since the publication of Chapter 6 and radial-velocity measurements conducted by John Johnson, we are measuring the highly eccentric KOI-1474.01's mass and pinning down the identity of its perturber. Combining the transit timing variations and radial-velocity measurements, we are constraining the mutual inclinations of the planets. We can also better constrain the projected rotational velocity of the star and therefore the transiting planet's projected spin-orbit alignment. This combined orbital knowledge will hopefully reveal a three-dimensional view of this planetary system. The "photo-eccentric effect" (Chapter 5) was recently applied by Sanchis-Ojeda et al. (2013, submitted to the Astrophysical Journal) to constrain the eccentricity of a misaligned planet.

9.3 Future Directions

Although we have made process toward understanding the migratory behavior of planetary systems, a number of open questions remain, including:

1. Which of several proposed mechanisms for migration via planet-planet interactions is most common?

2. What is the role of planetesimal-driven migration, an important process in our own solar system, in extra-solar systems?

3. What effects does planetary migration have on the composition and, ultimately, habitability of planets in the system, including those not directly involved in the migration?

Planetary migration models have previously been crafted and fine-tuned to reproduce the regions of exoplanet parameter space well-populated with early discoveries. Therefore, we may be able to leap forward by targeting exoplanet exceptions, those lying in under-populated regions of parameter space, as a new test ground for migration theories, allowing us to distinguish the contributions of the potpourri of proposed migration mechanisms. Because a complete migration theory must account for these exoplanet exceptions and their occurrence rates, exoplanet exceptions promise either to be the exceptions that prove the rule, or to demand the incorporation of migration processes previously considered unimportant.

One promising class of planets for future investigations are those located in the "Period Valley," interior to the ice line but exterior to hot Jupiters. These are the giant

planets for which we found a correlation between eccentricity and metallicity in Chapter 8. In this region, there is an observed drop in the occurrence rate of giant planets, but radial-velocity surveys and the *Kepler* Mission have found exoplanet exceptions here (e.g. Wright et al. 2009; Borucki et al. 2011), many on eccentric orbits. Migration models, designed to produce hot Jupiters from Jupiters formed at or beyond the ice line, can populate the Period Valley as a side effect (e.g. Ida & Lin 2008; Matsumura et al. 2010; Wu & Lithwick 2011). Focusing on migration models involving strong gravitational interactions among planets, which have the greatest potential to produce the observed eccentric orbits of Period Valley planets, we can perform computer simulations and develop analytical expressions to predict the typical orbital properties of planets in the Period Valley, which we expect to vary significantly among migration models. The following orbital properties may be particularly important for distinguishing which mechanisms of planet-planet interactions cause migration:

- Eccentricities: We can make predictions for the eccentricities of Period Valley planets based on different models for creating hot Jupiters via planet-planet interactions, including: 1) planet-planet scattering (e.g. Rasio & Ford 1996; Matsumura et al. 2010), in which planets undergo random walks through the Period Valley, resulting in a broad range of eccentricities, and 2) secular (long timescale) mechanisms in which planets transverse the Period Valley primarily on high eccentricity orbits (e.g. Wu & Murray 2003; Wu & Lithwick 2011). We can compare these predictions to eccentricities measured by radial-velocity surveys, and expand the collection of eccentricities measured from Kepler data using the photo-eccentric effect described in Chapter 5. Radial-velocity surveys are biased against highly eccentric planets (O'Toole et al. 2009), which the photoeccentric

effect is most effective for identifying, so combining these complementary datasets would allow us disentangle selection effects.

- Inclinations: Migration caused by perturbations from other stars and planets can tilt a planets orbit out of the plane it formed in. Migration models have previously been used to make predictions for the orbital inclinations of hot Jupiters (e.g. Fabrycky & Tremaine 2007b; Naoz et al. 2011). However, due to their close-in orbits, hot Jupiters experience strong tidal dissipation that can erase inclination signatures of migration (e.g. Winn et al. 2010; Albrecht et al. 2012). We can predict inclinations for the pristine period-valley planets (i.e. most are too distant from their stars to be affected by tides) and compute how these inclinations translate to projected obliquities between the planets orbit and host stars spin axis, measurements of which should be feasible among the subset of bright Kepler host stars via the Rossiter-McLaughlin effect (Rossiter 1924; McLaughlin 1924)) and the Sanchis-Nutzman effect (Sanchis-Ojeda et al. 2011; Nutzman et al. 2011).

- Interplanetary interactions: Strong interplanetary gravitational interactions in a planetary system lead to orbital variations, which cause a planet to transit its host star at intervals that deviate from a constant orbital period (Holman & Murray 2005; Agol et al. 2005). *Kepler* has detected such transit timing variations for many period-valley planets (Ford et al. 2012). We can use the typical magnitudes and timescales of these observed variations to distinguish migration models in which Period Valley planets decouple from their perturbers after reaching their final orbital positions vs. remaining coupled, as well as distinguishing between models featuring distant perturbers vs. nearby perturbers, which cause stronger transit timing variations.

Through the comparisons above, we can make progress toward distinguishing between a subset of planetary migration models that all involve gravitational interactions among planets but which range qualitatively from more gentle, long-timescale perturbations to more violent, short-timescale upheaval.

Another class of "exoplanets exceptions" may provide new insights about disk migration. Within the Period Valley itself, gas disk migration models predict an even more striking depletion: a total lack of super-Earth and Neptune-mass planets (Alibert et al. 2005; Ida & Lin 2008). This so-called "Planet Desert" arises because as planets migrate through the Period Valley, they undergo runaway gas accretion and end up Jupiter-mass. Although early radial-velocity surveys were consistent with this prediction, recent, more sensitive radial-velocity surveys, as well as *Kepler* , have discovered a number of exceptions (Howard et al. 2010, 2012b). We should explore whether debris from planet formation can cause migration (e.g. Fernandez & Ip 1984) that populates the Planet Desert after the gas disk dissipates and allows Neptune-mass planets to move interior to the ice line without undergoing run-away gas accretion. To investigate the role of planetesimal-driven migration in populating the Planet Desert, we are developing a code (gadgetbelt; based on gadget, Springel 2005), that fully models the gravitational interactions between planets and debris disks, rather than the analytical prescriptions typically used. This approach is necessary because we expect that early in a planetary systems history, the participating debris disk may have a mass comparable to Neptunes.

Finally, the TESS Mission will provide a rich sample of well-characterized planets essential for investigating links between the dynamics and composition of planets. For example, consider a Super-Earth orbiting near its star. We might expect it to have a different bulk and/or atmospheric composition if: a) plowed through a disk of gas

and/or planetesimals, accreting along the way; b) was scattered inward during an upheaval caused by giant planets in the system; or c) formed *in situ*, a theory of origin for Super-Earths and mini-Neptunes that has recently been growing in popularity (e.g. Chiang & Laughlin 2012). Moreover, when the first Earth-analogs are discovered, it will be essential to understand the migratory history of any giant planets in the system, who may caused an upheaval with profound effects on habitability.

References

Agol, E., Steffen, J., Sari, R., & Clarkson, W. 2005, MNRAS, 359, 567

Albrecht, S., et al. 2011, ApJ, 738, 50

—. 2012, ApJ, 757, 18

Alibert, Y., Mordasini, C., Benz, W., & Winisdoerffer, C. 2005, A&A, 434, 343

Anglada-Escudé, G., López-Morales, M., & Chambers, J. E. 2010, ApJ, 709, 168

Augereau, J. C., Nelson, R. P., Lagrange, A. M., Papaloizou, J. C. B., & Mouillet, D. 2001, A&A, 370, 447

Aumann, H. H., et al. 1984, ApJ, 278, L23

Bakos, G. Á., et al. 2007, ApJ, 670, 826

—. 2009, ApJ, 707, 446

Ballard, S., et al. 2011, ApJ, 743, 200

Barbieri, M., et al. 2007, A&A, 476, L13

—. 2009, A&A, 503, 601

Barnes, J. W. 2007, PASP, 119, 986

Barnes, R., & Raymond, S. N. 2004, ApJ, 617, 569

Barnes, R., Raymond, S. N., Greenberg, R., Jackson, B., & Kaib, N. A. 2010, ApJ, 709, L95

Batalha, N. M., et al. 2010, ApJ, 713, L109

—. 2013, ApJS, 204, 24

Batygin, K. 2012, Nature, 491, 418

Batygin, K., & Brown, M. E. 2010, ApJ, 716, 1323

Batygin, K., Brown, M. E., & Fraser, W. C. 2011, ApJ, 738, 13

Beaugé, C., & Nesvorný, D. 2012, ApJ, 751, 119

Bernardo, J., & Smith, A. 2000, Bayesian Theory

Bitsch, B., & Kley, W. 2011, A&A, 530, A41

Boccaletti, A., Augereau, J.-C., Baudoz, P., Pantin, E., & Lagrange, A.-M. 2009, A&A, 495, 523

Boley, A. C., Payne, M. J., & Ford, E. B. 2012, ApJ, 754, 57

Bolmont, E., Selsis, F., Raymond, S. N., Leconte, J., Hersant, F., Maurin, A.-S., & Pericaud, J. 2013, ArXiv e-prints

Bonfils, X., et al. 2005, A&A, 443, L15

Bonnefoy, M., et al. 2011, A&A, 528, L15

Bonomo, A. S., et al. 2010, A&A, 520, A65

Borkovits, T., Csizmadia, S., Forgács-Dajka, E., & Hegedüs, T. 2011, A&A, 528, A53

Borkovits, T., Érdi, B., Forgács-Dajka, E., & Kovács, T. 2003, A&A, 398, 1091

Borkovits, T., Forgács-Dajka, E., & Regály, Z. 2004, A&A, 426, 951

Borucki, W. J., et al. 2010, Science, 327, 977

—. 2011, ApJ, 736, 19

Bowler, B. P., et al. 2010, ApJ, 709, 396

Bromley, B. C., & Kenyon, S. J. 2011, ApJ, 735, 29

Brown, M. E. 2001, AJ, 121, 2804

Brown, M. E., Schaller, E. L., & Fraser, W. C. 2011a, ApJ, 739, L60+

Brown, T. M. 2003, ApJ, 593, L125

Brown, T. M., Latham, D. W., Everett, M. E., & Esquerdo, G. A. 2011b, AJ, 142, 112

Brucker, M. J., Grundy, W. M., Stansberry, J. A., Spencer, J. R., Sheppard, S. S., Chiang, E. I., & Buie, M. W. 2009, Icarus , 201, 284

Bryan, M. L., et al. 2012, ApJ, 750, 84

Buchhave, L. A., et al. 2012, Nature, 486, 375

Burke, C. J. 2008, ApJ, 679, 1566

Burke, C. J., Bryson, S., Christiansen, J., Mullally, F., Rowe, J., Science Office, K., & Kepler Science Team. 2013, in American Astronomical Society Meeting Abstracts, Vol. 221, American Astronomical Society Meeting Abstracts, #216.02

Burke, C. J., et al. 2007, ApJ, 671, 2115

Butler, R. P., Marcy, G. W., Williams, E., Hauser, H., & Shirts, P. 1997, ApJ, 474, L115+

Carter, J. A., & Winn, J. N. 2009, ApJ, 704, 51

Castan, T., & Menou, K. 2011, ApJ, 743, L36

Chambers, J. E. 1999, MNRAS, 304, 793

Charbonneau, D., Brown, T. M., Latham, D. W., & Mayor, M. 2000, ApJ, 529, L45

Chatterjee, S., Ford, E. B., Matsumura, S., & Rasio, F. A. 2008, ApJ, 686, 580

Chatterjee, S., Ford, E. B., & Rasio, F. A. 2011, in IAU Symposium, Vol. 276, IAU Symposium, ed. A. Sozzetti, M. G. Lattanzi, & A. P. Boss, 225–229

Chiang, E., & Choi, H. 2008, AJ, 136, 350

Chiang, E., Kite, E., Kalas, P., Graham, J. R., & Clampin, M. 2009, ApJ, 693, 734

Chiang, E., & Laughlin, G. 2012, ArXiv e-prints

Chiang, E., & Youdin, A. N. 2010, Annual Review of Earth and Planetary Sciences, 38, 493

Chib, S., & Greenberg, E. 1995, American Statistician, 49, 327

Colón, K. D., Ford, E. B., & Morehead, R. C. 2012, ArXiv e-prints

Correia, A. C. M., et al. 2010, A&A, 511, A21+

Crossfield, I. J. M. 2012, A&A, 545, A97

Cumming, A., Butler, R. P., Marcy, G. W., Vogt, S. S., Wright, J. T., & Fischer, D. A. 2008, PASP, 120, 531

Cumming, A., Marcy, G. W., & Butler, R. P. 1999, ApJ, 526, 890

Currie, T., Lada, C. J., Plavchan, P., Robitaille, T. P., Irwin, J., & Kenyon, S. J. 2009, ApJ, 698, 1

Currie, T., Thalmann, C., Matsumura, S., Madhusudhan, N., Burrows, A., & Kuchner, M. 2011, ApJ, 736, L33

Dawson, R. I., & Johnson, J. A. 2012, ApJ, 756, 122

Dawson, R. I., Johnson, J. A., Morton, T. D., Crepp, J. R., Fabrycky, D. C., Murray-Clay, R. A., & Howard, A. W. 2012, ApJ, 761, 163

Dawson, R. I., & Murray-Clay, R. 2012, ApJ, 750, 43

Dawson, R. I., Murray-Clay, R. A., & Fabrycky, D. C. 2011, ApJ, 743, L17

Dawson, R. I., Murray-Clay, R. A., & Johnson, J. A. 2013, ArXiv e-prints

Deeming, T. J. 1975, Ap&SS, 36, 137

—. 1976, Ap&SS, 42, 257

Demory, B.-O., Gillon, M., Seager, S., Benneke, B., Deming, D., & Jackson, B. 2012, ApJ, 751, L28

Demory, B.-O., & Seager, S. 2011, ApJS, 197, 12

Demory, B.-O., et al. 2011, A&A, 533, A114

Desert, J.-M., Charbonneau, D., Fressin, F., & Torres, G. 2012, in American Astronomical Society Meeting Abstracts, Vol. 219, American Astronomical Society Meeting Abstracts #219, #414.02

Désert, J.-M., et al. 2011, ApJS, 197, 14

Dong, S., Katz, B., & Socrates, A. 2013, ApJ, 763, L2

Dotter, A., Chaboyer, B., Jevremović, D., Kostov, V., Baron, E., & Ferguson, J. W. 2008, ApJS, 178, 89

Dressing, C. D., & Charbonneau, D. 2013, ArXiv e-prints

Dressing, C. D., Spiegel, D. S., Scharf, C. A., Menou, K., & Raymond, S. N. 2010, ApJ, 721, 1295

Dumusque, X., et al. 2012, Nature, 491, 207

Dunhill, A. C., Alexander, R. D., & Armitage, P. J. 2013, MNRAS, 428, 3072

Edelson, R. A., & Krolik, J. H. 1988, ApJ, 333, 646

Eggleton, P. P., Kiseleva, L. G., & Hut, P. 1998, ApJ, 499, 853

Ehrenreich, D., et al. 2012, A&A, 547, A18

Eyer, L., & Bartholdi, P. 1999, A&AS, 135, 1

Fabrycky, D., & Tremaine, S. 2007a, ApJ, 669, 1298

—. 2007b, ApJ, 669, 1298

Fabrycky, D. C., & Winn, J. N. 2009, ApJ, 696, 1230

Fabrycky, D. C., et al. 2012a, ArXiv e-prints

—. 2012b, ApJ, 750, 114

Fabrycky, D. F. 2010, Non-Keplerian Dynamics of Exoplanets, ed. Seager, S., 217–238

Farr, W. M., Gair, J. R., Mandel, I., & Cutler, C. 2013, ArXiv e-prints

Fernandez, J. A., & Ip, W. 1984, Icarus , 58, 109

Fischer, D. A., & Valenti, J. 2005, ApJ, 622, 1102

Fischer, D. A., et al. 2005, ApJ, 620, 481

—. 2007, ApJ, 669, 1336

—. 2008, ApJ, 675, 790

Ford, E. B. 2008, AJ, 135, 1008

Ford, E. B., & Chiang, E. I. 2007, ApJ, 661, 602

Ford, E. B., Quinn, S. N., & Veras, D. 2008, ApJ, 678, 1407

Ford, E. B., & Rasio, F. A. 2006, ApJ, 638, L45

—. 2008, ApJ, 686, 621

Ford, E. B., et al. 2012, ApJ, 756, 185

Foreman-Mackey, D., Hogg, D. W., Lang, D., & Goodman, J. 2012, ArXiv e-prints

Fortney, J. J., Saumon, D., Marley, M. S., Lodders, K., & Freedman, R. S. 2006, ApJ, 642, 495

Foster, G. 1995, AJ, 109, 1889

Fraser, W. C., Brown, M. E., & Schwamb, M. E. 2010, Icarus, 210, 944

Fressin, F., et al. 2013, ApJ, 766, 81

Gaidos, E., Conrad, C. P., Manga, M., & Hernlund, J. 2010, ApJ, 718, 596

Galland, F., Lagrange, A.-M., Udry, S., Chelli, A., Pepe, F., Beuzit, J.-L., & Mayor, M. 2006, A&A, 447, 355

Gaudi, B. S., Seager, S., & Mallen-Ornelas, G. 2005, ApJ, 623, 472

Gazak, J. Z., Johnson, J. A., Tonry, J., Dragomir, D., Eastman, J., Mann, A. W., & Agol, E. 2012, Advances in Astronomy, 2012

Gelman, S. E., Elkins-Tanton, L. T., & Seager, S. 2009, in Lunar and Planetary Inst. Technical Report, Vol. 40, Lunar and Planetary Institute Science Conference Abstracts, 1338–+

Giguere, M. J., et al. 2012, ApJ, 744, 4

Gilliland, R. L., McCullough, P. R., Nelan, E. P., Brown, T. M., Charbonneau, D., Nutzman, P., Christensen-Dalsgaard, J., & Kjeldsen, H. 2011, ApJ, 726, 2

Gingerich, O., ed. 1993, Masters of Modern Physics, Vol. 7, The eye of the heaven. Ptolemy, Copernicus, Kepler.

Girardi, L., Groenewegen, M. A. T., Hatziminaoglou, E., & da Costa, L. 2005, A&A, 436, 895

Gladman, B. 1993, Icarus , 106, 247

Gladman, B., Marsden, B. G., & Vanlaerhoven, C. 2008, Nomenclature in the Outer Solar System, 43–57

Goldreich, P., Lithwick, Y., & Sari, R. 2004, ARA&A, 42, 549

Goldreich, P., & Rappaport, N. 2003, Icarus , 162, 391

Goldreich, P., & Sari, R. 2003, ApJ, 585, 1024

Goldreich, P., & Tremaine, S. 1980, ApJ, 241, 425

Golimowski, D. A., et al. 2006, AJ, 131, 3109

Gomes, R. S. 2003, Icarus , 161, 404

Gonzalez, G. 1997, MNRAS, 285, 403

Gould, A., Dorsher, S., Gaudi, B. S., & Udalski, A. 2006, Acta Astronomica, 56, 1

Gray, D. F. 2008, The Observation and Analysis of Stellar Photospheres

Gregory, P. C. 2005, ApJ, 631, 1198

Guillochon, J., Ramirez-Ruiz, E., & Lin, D. 2011, ApJ, 732, 74

Gulbis, A. A. S., Elliot, J. L., Adams, E. R., Benecchi, S. D., Buie, M. W., Trilling, D. E., & Wasserman, L. H. 2010, AJ, 140, 350

Hahn, J. M., & Malhotra, R. 2005, The Astronomical Journal, 130, 2392

Hansen, B. M. S. 2010, ApJ, 723, 285

—. 2012, ApJ, 757, 6

Hansen, B. M. S., & Murray, N. 2012, ApJ, 751, 158

Heap, S. R., Lindler, D. J., Lanz, T. M., Cornett, R. H., Hubeny, I., Maran, S. P., & Woodgate, B. 2000, ApJ, 539, 435

Hebb, L., et al. 2009, ApJ, 693, 1920

Hébrard, G., et al. 2008, A&A, 488, 763

Hernández, J., et al. 2007, ApJ, 662, 1067

Hill, G. W. 1897, AJ, 17, 81

Hillenbrand, L. A., Massey, P., Strom, S. E., & Merrill, K. M. 1993, AJ, 106, 1906

Hirano, T., Sanchis-Ojeda, R., Takeda, Y., Narita, N., Winn, J. N., Taruya, A., & Suto, Y. 2012, ApJ, 756, 66

Holman, M. J., & Murray, N. W. 2005, Science, 307, 1288

Howard, A. W., et al. 2010, Science, 330, 653

—. 2011, ApJ, 726, 73

—. 2012a, ApJ, 749, 134

—. 2012b, ApJS, 201, 15

Huang, X., Bakos, G. Á., & Hartman, J. D. 2013, MNRAS, 429, 2001

Hut, P. 1981, A&A, 99, 126

Ida, S., & Lin, D. N. C. 2008, ApJ, 673, 487

Ivanov, P. B., & Papaloizou, J. C. B. 2011, Celestial Mechanics and Dynamical Astronomy, 111, 51

Jackson, B., Greenberg, R., & Barnes, R. 2008a, ApJ, 678, 1396

—. 2008b, ApJ, 681, 1631

Jackson, B., Miller, N., Barnes, R., Raymond, S. N., Fortney, J. J., & Greenberg, R. 2010, MNRAS, 407, 910

Jewitt, D., & Luu, J. 1993, Nature, 362, 730

Johansen, A., Davies, M. B., Church, R. P., & Holmelin, V. 2012, ApJ, 758, 39

Johnson, J. A., Aller, K. M., Howard, A. W., & Crepp, J. R. 2010, PASP, 122, 905

Johnson, J. A., et al. 2006, ApJ, 647, 600

—. 2011a, ApJ, 735, 24

—. 2011b, ApJ, 730, 79

—. 2011c, ApJS, 197, 26

—. 2012, AJ, 143, 111

Jones, H. R. A., Butler, R. P., Tinney, C. G., Marcy, G. W., Penny, A. J., McCarthy, C., & Carter, B. D. 2003, MNRAS, 341, 948

Jurić, M., & Tremaine, S. 2008, ApJ, 686, 603

Kaib, N. A., Raymond, S. N., & Duncan, M. J. 2011, ApJ, 742, L24

Kalas, P., & Jewitt, D. 1995, AJ, 110, 794

Kane, S. R. 2007, MNRAS, 380, 1488

Kane, S. R., Ciardi, D. R., Gelino, D. M., & von Braun, K. 2012, MNRAS, 425, 757

Kane, S. R., & von Braun, K. 2009, PASP, 121, 1096

Kataria, T., Showman, A. P., Lewis, N. K., Fortney, J. J., Marley, M. S., & Freedman, R. S. 2011, in EPSC-DPS Joint Meeting 2011, 573

Kavelaars, J. J., Petit, J.-M., Gladman, B., & Marsden, B. G. 2009, Minor Planet Electronic Circ., 75

Kennedy, G. M., & Kenyon, S. J. 2008, ApJ, 673, 502

Kenyon, S. J., & Bromley, B. C. 2008, ApJS, 179, 451

Kenyon, S. J., & Luu, J. X. 1998, AJ, 115, 2136

Kipping, D. M. 2008, MNRAS, 389, 1383

—. 2010a, MNRAS, 408, 1758

—. 2010b, MNRAS, 407, 301

Kipping, D. M., Dunn, W. R., Jasinski, J. M., & Manthri, V. P. 2012, MNRAS, 2413

Kipping, D. M., Fossey, S. J., & Campanella, G. 2009, MNRAS, 400, 398

Kipping, D. M., & Tinetti, G. 2010, MNRAS, 407, 2589

Knežević, Z., & Milani, A. 2000, Celestial Mechanics and Dynamical Astronomy, 78, 17

—. 2003, A&A, 403, 1165

Knezevic, Z., Lemaître, A., & Milani, A. 2002, Asteroids III, 603

Kozai, Y. 1962, AJ, 67, 591

Lagrange, A.-M., et al. 2009, A&A, 493, L21

—. 2010, Science, 329, 57

—. 2012, A&A, 542, A40

Latham, D. W., Stefanik, R. P., Mazeh, T., Mayor, M., & Burki, G. 1989, Nature, 339, 38

Latham, D. W., et al. 2011, ApJ, 732, L24

Lee, M. H., & Peale, S. J. 2003, ApJ, 592, 1201

Léger, A., et al. 2009, A&A, 506, 287

Levison, H. F., & Duncan, M. J. 1994, Icarus , 108, 18

Levison, H. F., & Morbidelli, A. 2003, Nature, 426, 419

Levison, H. F., Morbidelli, A., Vanlaerhoven, C., Gomes, R., & Tsiganis, K. 2008, Icarus, 196, 258

Levison, H. F., & Stern, S. A. 2001, AJ, 121, 1730

Lissauer, J. J., et al. 2011, ApJS, 197, 8

Lithwick, Y., & Naoz, S. 2011, ApJ, 742, 94

Lomb, N. R. 1976, Ap&SS, 39, 447

Lopez, E. D., Fortney, J. J., & Miller, N. 2012, ApJ, 761, 59

Lunine, J. I. 2001, Proceedings of the National Academy of Science, 98, 809

Lykawka, P. S., & Mukai, T. 2005, Earth, 97, 107

Lykawka, P. S., & Mukai, T. 2007, Icarus , 186, 331

—. 2008, AJ, 135, 1161

Madhusudhan, N., Lee, K. K. M., & Mousis, O. 2012, ApJ, 759, L40

Malhotra, R. 1993, Nature, 365, 819

—. 1995, AJ, 110, 420

Malhotra, R., Fox, K., Murray, C., & Nicholson, P. 1989, Astronomy and Astrophysics, 221, 348

Mandel, K., & Agol, E. 2002, ApJ, 580, L171

Mann, A. W., Gaidos, E., Lépine, S., & Hilton, E. J. 2012, ApJ, 753, 90

Marcy, G. W., Butler, R. P., Fischer, D., Vogt, S. S., Lissauer, J. J., & Rivera, E. J. 2001, ApJ, 556, 296

Marcy, G. W., Butler, R. P., Fischer, D. A., Laughlin, G., Vogt, S. S., Henry, G. W., & Pourbaix, D. 2002, ApJ, 581, 1375

Marcy, G. W., Butler, R. P., Vogt, S. S., Fischer, D., & Lissauer, J. J. 1998, ApJ, 505, L147

Marcy, G. W., Butler, R. P., Williams, E., Bildsten, L., Graham, J. R., Ghez, A. M., & Jernigan, J. G. 1997, ApJ, 481, 926

Mardling, R. A. 2007, MNRAS, 382, 1768

Markwardt, C. B. 2009, in Astronomical Society of the Pacific Conference Series, Vol. 411, Astronomical Data Analysis Software and Systems XVIII, ed. D. A. Bohlender, D. Durand, & P. Dowler, 251

Marzari, F., & Nelson, A. F. 2009, ApJ, 705, 1575

Matsumura, S., Peale, S. J., & Rasio, F. A. 2010, ApJ, 725, 1995

Mayor, M., & Queloz, D. 1995, Nature, 378, 355

Mayor, M., et al. 2009, A&A, 507, 487

—. 2011, ArXiv e-prints

McArthur, B. E., Benedict, G. F., Barnes, R., Martioli, E., Korzennik, S., Nelan, E., & Butler, R. P. 2010, ApJ, 715, 1203

McArthur, B. E., et al. 2004, ApJ, 614, L81

McClellan, J. H., Schafer, R. W., & Yoder, M. A. 1999, DSP First: A Multimedia Approach (Prentice Hall)

McLaughlin, D. B. 1924, ApJ, 60, 22

Minton, D. A., & Malhotra, R. 2011, ApJ, 732, 53

Miralda-Escudé, J. 2002, ApJ, 564, 1019

Moorhead, A. V., et al. 2011, ApJS, 197, 1

Morbidelli, A., Levison, H. F., & Gomes, R. 2008, The Dynamical Structure of the Kuiper Belt and Its Primordial Origin, ed. Barucci, M. A., Boehnhardt, H., Cruikshank, D. P., Morbidelli, A., & Dotson, R., 275–292

Mortier, A., Santos, N. C., Sozzetti, A., Mayor, M., Latham, D., Bonfils, X., & Udry, S. 2012, A&A, 543, A45

Morton, T. D. 2012, ApJ, 761, 6

Morton, T. D., & Johnson, J. A. 2011a, ApJ, 729, 138

—. 2011b, ApJ, 738, 170

Mouillet, D., Larwood, J. D., Papaloizou, J. C. B., & Lagrange, A. M. 1997, MNRAS, 292, 896

Moutou, C., et al. 2009, A&A, 498, L5

Murray, C. D., & Dermott, S. F. 2000, Solar System Dynamics

Murray-Clay, R. A., & Chiang, E. I. 2006, ApJ, 651, 1194

Murray-Clay, R. A., & Schlichting, H. E. 2011, ApJ, 730, 132

Naef, D., Mayor, M., Beuzit, J. L., Perrier, C., Queloz, D., Sivan, J. P., & Udry, S. 2004, A&A, 414, 351

Naef, D., et al. 2001, A&A, 375, L27

Nagasawa, M., & Ida, S. 2011, ApJ, 742, 72

Naoz, S., Farr, W. M., Lithwick, Y., Rasio, F. A., & Teyssandier, J. 2011, Nature, 473, 187

Naoz, S., Farr, W. M., & Rasio, F. A. 2012, ApJ, 754, L36

Nesvorný, D., Kipping, D. M., Buchhave, L. A., Bakos, G. Á., Hartman, J., & Schmitt, A. R. 2012, Science, 336, 1133

Noll, K. S., Grundy, W. M., Stephens, D. C., Levison, H. F., & Kern, S. D. 2008, Icarus, 194, 758

Nutzman, P. A., Fabrycky, D. C., & Fortney, J. J. 2011, ApJ, 740, L10

O'Toole, S. J., Tinney, C. G., Jones, H. R. A., Butler, R. P., Marcy, G. W., Carter, B., & Bailey, J. 2009, MNRAS, 392, 641

Parker, A. H., & Kavelaars, J. J. 2010, ApJ, 722, L204

Peixinho, N., Lacerda, P., & Jewitt, D. 2008, AJ, 136, 1837

Penev, K., Jackson, B., Spada, F., & Thom, N. 2012, ApJ, 751, 96

Pinsonneault, M. H., An, D., Molenda-Żakowicz, J., Chaplin, W. J., Metcalfe, T. S., & Bruntt, H. 2012, ApJS, 199, 30

Pinsonneault, M. H., DePoy, D. L., & Coffee, M. 2001, ApJ, 556, L59

Plavchan, P., Bilinski, C., & Currie, T. 2012, ArXiv e-prints

Plavchan, P., Jura, M., Kirkpatrick, J. D., Cutri, R. M., & Gallagher, S. C. 2008, ApJS, 175, 191

Quanz, S. P., et al. 2010, ApJ, 722, L49

Queloz, D., Eggenberger, A., Mayor, M., Perrier, C., Beuzit, J. L., Naef, D., Sivan, J. P., & Udry, S. 2000, A&A, 359, L13

Queloz, D., et al. 2009, A&A, 506, 303

Quillen, A. C. 2006, MNRAS, 372, L14

Quinn, S. N., et al. 2012, ApJ, 756, L33

Rafikov, R. R. 2006, ApJ, 648, 666

Ragozzine, D., & Holman, M. J. 2010, ArXiv e-prints

Rasio, F. A., & Ford, E. B. 1996, Science, 274, 954

Reegen, P. 2007, A&A, 467, 1353

—. 2011, Communications in Asteroseismology, 163, 3

Reiners, A., & Schmitt, J. H. M. M. 2003, A&A, 412, 813

Ribas, I., & Miralda-Escudé, J. 2007, A&A, 464, 779

Rivera, E. J., et al. 2005, ApJ, 634, 625

Roberts, D. H., Lehar, J., & Dreher, J. W. 1987, AJ, 93, 968

Robinson, S. E., et al. 2007, ApJ, 670, 1391

Rogers, T. M., Lin, D. N. C., & Lau, H. H. B. 2012, ApJ, 758, L6

Rossiter, R. A. 1924, ApJ, 60, 15

Sanchis-Ojeda, R., Winn, J. N., Holman, M. J., Carter, J. A., Osip, D. J., & Fuentes, C. I. 2011, ApJ, 733, 127

Santerne, A., et al. 2012, A&A, 545, A76

Santos, N. C., Israelian, G., & Mayor, M. 2001, A&A, 373, 1019

—. 2004, A&A, 415, 1153

Sari, R., & Goldreich, P. 2004, ApJ, 606, L77

Sato, B., et al. 2008, PASJ, 60, 1317

Saunders, E. S., Naylor, T., & Allan, A. 2006, A&A, 455, 757

Scargle, J. D. 1982, ApJ, 263, 835

Schlaufman, K. C. 2010, ApJ, 719, 602

Seager, S., & Deming, D. 2009, ApJ, 703, 1884

Seager, S., Kuchner, M., Hier-Majumder, C. A., & Militzer, B. 2007, ApJ, 669, 1279

Sing, D. K. 2010, A&A, 510, A21

Siverd, R. J., et al. 2012, ApJ, 761, 123

Smith, B. A., & Terrile, R. J. 1984, Science, 226, 1421

Socrates, A., & Katz, B. 2012, ArXiv e-prints

Socrates, A., Katz, B., & Dong, S. 2012a, ArXiv e-prints

Socrates, A., Katz, B., Dong, S., & Tremaine, S. 2012b, ApJ, 750, 106

Sousa, S. G., Santos, N. C., Israelian, G., Mayor, M., & Udry, S. 2011, A&A, 533, A141

Sozzetti, A., Torres, G., Latham, D. W., Stefanik, R. P., Korzennik, S. G., Boss, A. P., Carney, B. W., & Laird, J. B. 2009, ApJ, 697, 544

Spiegel, D. S., Raymond, S. N., Dressing, C. D., Scharf, C. A., & Mitchell, J. L. 2010, ApJ, 721, 1308

Springel, V. 2005, MNRAS, 364, 1105

Steffen, J. H., et al. 2012a, Proceedings of the National Academy of Science, 109, 7982

—. 2012b, ApJ, 756, 186

Stephens, D. C., & Noll, K. S. 2006, AJ, 131, 1142

Stern, S. A., & Colwell, J. E. 1997, AJ, 114, 841

Sumi, T., et al. 2011, Nature, 473, 349

Takeda, G., Ford, E. B., Sills, A., Rasio, F. A., Fischer, D. A., & Valenti, J. A. 2007, ApJS, 168, 297

Taylor, S. F. 2012, ArXiv e-prints

Tegler, S. C., & Romanishin, W. 2000, Nature, 407, 979

Thommes, E. W., Duncan, M. J., & Levison, H. F. 1999, Nature, 402, 635

—. 2002, AJ, 123, 2862

Thommes, E. W., & Lissauer, J. J. 2003, ApJ, 597, 566

Tinney, C. G., Butler, R. P., Marcy, G. W., Jones, H. R. A., Laughlin, G., Carter, B. D., Bailey, J. A., & O'Toole, S. 2006, ApJ, 647, 594

Tinney, C. G., Butler, R. P., Marcy, G. W., Jones, H. R. A., Penny, A. J., McCarthy, C., Carter, B. D., & Bond, J. 2003, ApJ, 587, 423

Torres, G., Andersen, J., & Giménez, A. 2010, A&A Rev., 18, 67

Torres, G., et al. 2011, ApJ, 727, 24

Triaud, A. H. M. J. 2011, A&A, 534, L6

Triaud, A. H. M. J., et al. 2010, A&A, 524, A25

Udry, S., Mayor, M., & Santos, N. C. 2003, A&A, 407, 369

Udry, S., et al. 2007, A&A, 469, L43

Valencia, D., O'Connell, R. J., & Sasselov, D. 2006, Icarus, 181, 545

Valenti, J. A., & Fischer, D. A. 2005, ApJS, 159, 141

Valenti, J. A., & Piskunov, N. 1996, A&AS, 118, 595

Van Laerhoven, C., & Greenberg, R. 2012, Celestial Mechanics and Dynamical Astronomy, 113, 215

Veras, D., Crepp, J. R., & Ford, E. B. 2009, ApJ, 696, 1600

Verner, G. A., et al. 2011, ApJ, 738, L28

Vidal-Madjar, A., Lecavelier des Etangs, A., & Ferlet, R. 1998, Planet. Space Sci., 46, 629

Vogt, S. S., et al. 1994, in Society of Photo-Optical Instrumentation Engineers (SPIE) Conference Series, Vol. 2198, Society of Photo-Optical Instrumentation Engineers (SPIE) Conference Series, ed. D. L. Crawford & E. R. Craine, 362

Volk, K., & Malhotra, R. 2011, ApJ, 736, 11

Wang, J., et al. 2013, ArXiv e-prints

Ward, W. R. 1997, Icarus , 126, 261

Welsh, W. F. 1999, PASP, 111, 1347

Winn, J. N. 2010, Exoplanet Transits and Occultations, ed. Seager, S., 55–77

Winn, J. N., Fabrycky, D., Albrecht, S., & Johnson, J. A. 2010, ApJ, 718, L145

Winn, J. N., Johnson, J. A., Albrecht, S., Howard, A. W., Marcy, G. W., Crossfield, I. J., & Holman, M. J. 2009a, ApJ, 703, L99

Winn, J. N., et al. 2009b, ApJ, 700, 302

—. 2009c, ApJ, 703, 2091

—. 2009d, ApJ, 693, 794

—. 2011, ApJ, 737, L18

Wisdom, J. 2005, in Bulletin of the American Astronomical Society, Vol. 37, Bulletin of the American Astronomical Society, 525

Wisdom, J., & Holman, M. 1991, AJ, 102, 1528

Wittenmyer, R. A., O'Toole, S. J., Jones, H. R. A., Tinney, C. G., Butler, R. P., Carter, B. D., & Bailey, J. 2010, ApJ, 722, 1854

Wolff, S., Dawson, R. I., & Murray-Clay, R. A. 2012, ApJ, 746, 171

Wright, J. T., Marcy, G. W., Howard, A. W., Johnson, J. A., Morton, T. D., & Fischer, D. A. 2012, ApJ, 753, 160

Wright, J. T., Upadhyay, S., Marcy, G. W., Fischer, D. A., Ford, E. B., & Johnson, J. A. 2009, ApJ, 693, 1084

Wright, J. T., et al. 2011, PASP, 123, 412

Wu, Y., & Lithwick, Y. 2011, ApJ, 735, 109

Wu, Y., & Murray, N. 2003, ApJ, 589, 605

Youdin, A. N. 2011, ApJ, 742, 38

Zahn, J.-P. 1975, A&A, 41, 329

Zechmeister, M., & Kürster, M. 2009, A&A, 496, 577

Zuckerman, B., Song, I., Bessell, M. S., & Webb, R. A. 2001, ApJ, 562, L87